Technical Physics, Vol. 49, No. 3, 2004, pp. 283–286. Translated from Zhurnal Tekhnicheskoĭ Fiziki, Vol. 74, No. 3, 2004, pp. 1–4.
Original Russian Text Copyright © 2004 by Gladkov, Kashcheev, Petrov, Rumyantsev.

THEORETICAL AND MATHEMATICAL PHYSICS

Diffusion of a Low-Soluble Impurity in a Solid Matrix

V. P. Gladkov, V. A. Kashcheev, V. I. Petrov, and I. M. Rumyantsev

Moscow Engineering Physics Institute (State University), Kashirskoe sh. 31, Moscow, 115409 Russia

e-mail: ivanr@sim.ru

Received June 11, 2003

Abstract—An analytical expression for the concentration profile of a low-soluble diffusant in a sample is derived for a high-capacity diffusion source. The model is checked by determining the diffusion coefficient of yttrium in beryllium. © *2004 MAIK "Nauka/Interperiodica".*

The long-term behavior of solids is often controlled by diffusion redistribution of impurities, which is characterized by the diffusion coefficient D of an impurity in the material. Mathematically, diffusion experiments are described by Fick's equation, which is an analogue of the heat conduction equation [1, 2].

The mathematical problem of diffusion, which involves Fick's equation and boundary conditions (as a rule, an "instantaneous" impurity source [1, 2]), formally does not impose constraints on the diffusant concentration in a matrix. However, the impurity concentration in the matrix always depends on the solubility limit. In [3], a constraint on the diffusant concentration in the matrix was imposed by assuming that the time of action of the diffusant (impurity) source is finite. In other words, it was assumed that the impurity source at the initial step of the process is of a finite (rather than infinite) capacity. The higher the diffusant–matrix mutual solubility, the smaller the error introduced into the diffusion coefficient when the solubility limit of the impurity in the matrix is ignored. A great body of reliable data has been obtained for systems with a high mutual solubility. However, there are numerous examples of systems with a low mutual solubility [4], to which the methods mentioned above [2, 3] are inapplicable. In these cases, the solubility limit of the impurity has to be taken into account in mathematical simulation of impurity diffusion. In this paper, an attempt to describe the diffusion of a low-soluble impurity in a material is made.

Let the diffusion of an impurity into a solid matrix be controlled by the solubility limit c^*. We assume, as usual, that the process is one-dimensional case and consider the linear problem of impurity diffusion into a semi-infinite sample, neglecting the dependence of the diffusion coefficient on the diffusant concentration (D = const). In differential form, the problem is stated as [1]

$$\frac{\partial}{\partial t}c(x,t) = D\frac{\partial^2}{\partial x^2}c(x,t) + \delta(x)f(t), \quad x \geq 0,\ t \geq 0; \tag{1}$$

$$c(x, t=0) = 0, \quad x \geq 0,$$

where $c(x, t)$ is the impurity concentration at a distance x from the boundary of the matrix at a time t (the coordinate of the boundary is $x = 0$), $f(t)$ is the impurity source strength on the surface $x = 0$ of the matrix (i.e., the amount of the impurity entering the matrix per unit area per unit time), and $\delta(x)$ is the Dirac delta function.

The analytical expression for the concentration profile $c(x, t)$ is given by the well-known general solution of (1)

$$c(x,t) = \frac{1}{\sqrt{\pi D}}\int_0^t \frac{f(t)}{\sqrt{t-\tau}}\exp\left[-\frac{x^2}{4D(t-\tau)}\right]d\tau, \tag{2}$$

$$x \geq 0,\ t \geq 0.$$

We assume that (i) the diffusant source (layer) is so thin that the time it takes for any impurity atom from the source to reach the surface is negligibly small compared with the duration of the diffusion experiment, (ii) the source–matrix interface is perfectly permeable, and (iii) the equilibrium number of impurity atoms that can diffuse from the source into the matrix (i.e., the number of activated atoms) is proportional to the total number of atoms in the source by a time t.

Consider the case when the source capacity Q (the number of atoms in the source) is much greater than the number of atoms entering the sample during diffusion annealing; i.e., $Q(t)$ = const. Such a situation is common, e.g., for diffusion from the gas phase. In the case of diffusion from a solid, the source may be considered as having an infinite capacitance only if the solubility limit of a diffusant is very low (the diffusion of yttrium into beryllium is an example). Our early experiments [5] showed that the overwhelming majority of yttrium atoms (95%) did not pass into the solid matrix upon the diffusion annealing of the beryllium sample covered by a layer of the ^{90}Y isotope (the experiment lasted 67.5 h at 1220°C). This result is explained by the low solubility limit of yttrium in beryllium [4].

In the approximation $Q(t)$ = const, the expression for the source strength can be represented in the form

$$f(t) = \alpha Q_0 \eta(t), \tag{3}$$

1063-7842/04/4903-0283$26.00 © 2004 MAIK "Nauka/Interperiodica"

where $\alpha = 1/\theta$, θ is the characteristic dissociation (activation) time of diffusant atoms in the source [3], Q_0 is the total number of diffusant atoms in the source layer per unit surface area of the sample,

$$\eta(t) = 1 - c(0, t)/c^* \quad (4)$$

is the dimensionless parameter taking into account the fraction of "vacant sites" for impurity atoms in the surface layer of the sample, $c(0, t)$ is the actual concentration of atoms dissolved in the surface layer of the sample by a time t, and c^* is the solubility limit of the diffusant in the matrix.

Then, having determined $c(0, t)$ from general solution (2) at $x = 0$ and using Eqs. (3) and (4), we find an equation for the function $f(t)$:

$$f(t) = \alpha Q_0\left[1 - \frac{1}{\sqrt{\pi D}c^*}\int_0^t \frac{f(t)}{\sqrt{t-\tau}}d\tau\right], \quad (5)$$

which is the linear integral Volterra equation of the second kind with the kernel in the form of convolution [1].

A solution to Eq. (5) can be found by applying the Laplace transformation:

$$f(t) = \alpha Q_0 \exp(\xi^2 t)\operatorname{erfc}(\xi\sqrt{t}), \quad (6)$$

where $\xi = \alpha Q_0/c^*\sqrt{D}$ is a parameter of dimension $[t^{-1/2}]$ and $\operatorname{erfc}(\xi\sqrt{t})$ is the probability integral.

Substituting $f(t)$ in the form of (6) into (2) at $x = 0$, one finds the time dependence of the impurity concentration in the "zero" layer, i.e., at the boundary $x = 0$:

$$c(0, t) = c^*(1 - \exp(\xi^2 t)\operatorname{erfc}(\xi\sqrt{t})). \quad (7)$$

This dependence is shown in Fig. 1. From expression (7), it follows that, at the early stages of the diffusion process, when the impurity present in subsurface layers of the matrix as yet does not prevent other impurity atoms from penetrating into the matrix ($\xi^2 t \ll 1$), the function $c(0, t)$ is representable in the form

$$c(0, t) \approx \alpha Q_0\sqrt{\frac{2t}{\pi D}}. \quad (8)$$

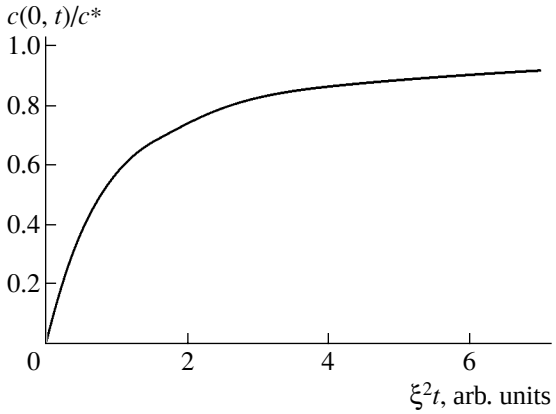

Fig. 1. Diffusant concentration as a function of time in the zero layer.

Dependence (8) is typical of the case when a steady source of strength αQ_0 (an infinite-capacity source) acts on the matrix surface.

With time, the effect of the solubility limit shows up, which appears as though the impurity source was nearly exhausted.

Therefore, the expansion of the function $\operatorname{erfc}(\xi\sqrt{t})$ at large times ($\xi^2 t \gg 1$) results in

$$c(0, t) \approx c^*\left(1 - \frac{1}{\sqrt{\pi\xi^2 t}}\right); \quad (9)$$

i.e., the impurity concentration in the subsurface layers of the matrix tends to the limiting value c^*.

An expression for the concentration profile $c(x, t)$ is obtained by substituting (6) into general solution (2) of the diffusion problem:

$$c(x, t) = c^*\operatorname{erfc}(z)\left[1 - \frac{\Phi(z + \xi\sqrt{t})}{\Phi(z)}\right], \quad x \geq 0,\ t > 0, \quad (10)$$

where $\Phi(z) = \operatorname{erfc}(z)\exp(z^2)$ and $z = x/(2\sqrt{Dt})$.

Expression (10) involves the functions $\Phi(z)$ taken at different values of the argument z. This function decreases monotonically at $z \geq 0$: $\Phi(0) = 1$ and $\Phi(z \longrightarrow \infty) = 0$.

Under the constraint $t \gg \max\{\xi^{-2},\ x/(2\sqrt{D}\,\xi)\}$, expression (10) simplifies to

$$c(x, t) \approx c^*\operatorname{erfc}(z), \quad x \geq 0,\ t > 0 \quad (11)$$

and takes the form of the concentration profile for the case when the impurity concentration at the surface is held constant: $c(0, t) = c^*$.

Note that, in diffusion experiments with radioactive isotopes, one determines an impurity-concentration-related quantity in solid matrices instead of the impurity concentration itself. This quantity is the integral activity $N(x, t)$ of the sample, which is related to the concentration $c(x, t)$ as follows:

$$N(x, t) = A\int_x^L c(x', t)\exp[-\mu(x' - x)]dx', \quad (12)$$

where μ is the linear coefficient of radioactive radiation absorption (cm^{-1}), A is a constant relating the activity of the sample with the diffusant concentration (counts/(cm^2 s)), L is the length of the sample (cm), and x' is the variable of integration (cm).

In experiments, the impurity diffusion depth $(Dt)^{1/2}$ is usually substantially shorter than the length of the sample: $(Dt)^{1/2}/L \ll 1$. Then, the upper limit of integration in (12) may be taken at infinity:

$$N(x, t) = A\int_x^\infty c(x', t)\exp[-\mu(x' - x)]dx'. \quad (13)$$

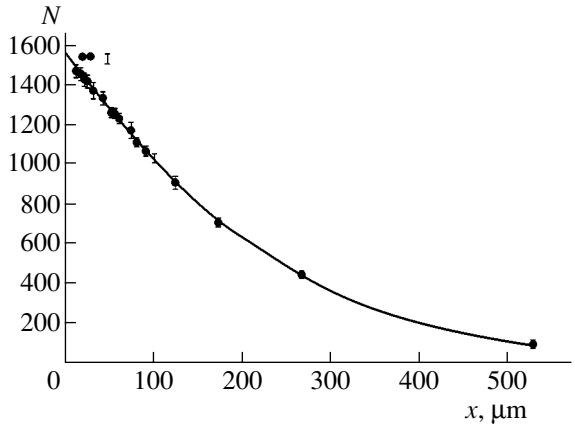

Fig. 2. Integral activity profile for yttrium diffusion in beryllium (1200°C, 67.5 h).

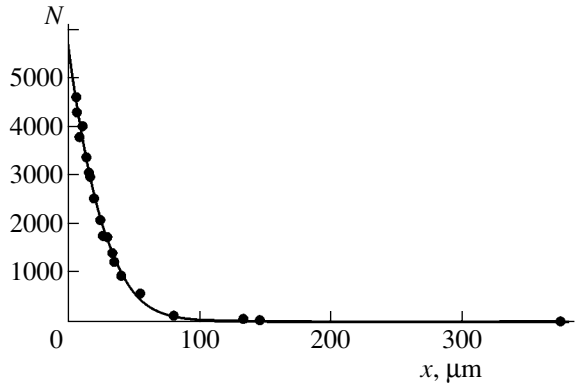

Fig. 3. Integral activity profile for yttrium diffusion in the beryllium–0.05% Y alloy (1150°C, 36 h).

If the absorption of isotope radiation in the sample is neglected, expression (13) greatly simplifies:

$$N(x, t) = A\int_{x}^{\infty} c(x', t)dx'. \qquad (14)$$

The case of low absorption of isotope radiation is widely met in practice. In particular, the absorption of ^{90}Y radioactive radiation by a 300-μm-thick beryllium layer may be neglected.

If the impurity concentration in the matrix is described by (10), expression (14) for the total activity takes the form

$$N(x, t) = A\frac{2c^*\sqrt{Dt}}{\sqrt{\pi}}\exp(-z^2)\left\{[1 - \sqrt{\pi}z\Phi(z)] + \frac{\sqrt{\pi}}{2\xi\sqrt{t}}[\Phi(z + \xi\sqrt{t}) - \Phi(z)]\right\}, \qquad (15)$$

where $\Phi(z) = \exp(z^2)\mathrm{erfc}(z)$.

Let us apply result (15) to process experimental data for ^{90}Y diffusion in Be. Figure 2 shows the experimental distribution of the integral activity of ^{90}Y in the beryllium sample after diffusion annealing at 1220°C (67.5 h); Fig. 3, the distribution of the integral activity in the beryllium sample with 0.05% yttrium after diffusion annealing at 1150°C (36 h). The simulation curves corresponding to Eq. (15) are also shown in both figures. The deviations of the data points for the activity from the curves do not exceed the measurement error (in Fig. 3, the measurement error is within the size of the data points). Hence, the simulation curves give a good fit to the experimental results.

The diffusion coefficients determined from the above experimental curves are listed in the table.

For comparison, we also calculated the diffusion coefficients for two limiting cases that may occur at the interface between an impurity source and a sample if the impurity solubility is finite and the source is inexhaustible: the steady diffusion flux condition (short-

Diffusion coefficients for yttrium in beryllium

Material	Temperature, °C	Model used to process experimental data	D, cm^2/s	$\sigma^2 \times 10^2$
Beryllium–0.05% yttrium	1150	Constant concentration	$(4.7 \pm 0.4) \times 10^{-11}$	5.53
		Equation (15)	$(6.7 \pm 0.4) \times 10^{-11}$	5.51
		Steady flux	$(8.0 \pm 0.5) \times 10^{-11}$	7.14
		Work [5]	$(3.8 \pm 0.4) \times 10^{-11}$	12.6
Beryllium	1220	Constant concentration	$(2.1 \pm 0.2) \times 10^{-9}$	1.76
		Equation (15)	$(2.3 \pm 0.2) \times 10^{-9}$	1.73
		Steady flux	$(3.0 \pm 0.2) \times 10^{-9}$	2.09
		Work [5]	$(2.8 \pm 0.3) \times 10^{-9}$	3.29

term diffusion annealing, see (8)) and the constant concentration condition (long-term annealing, see (9)).

The table also lists the minimum standard deviations σ^2 of the data points for the total activity from the simulation curves corresponding to different models of the process.

It follows from the table that formula (15) provides the most accurate approximation.

Using Eq. (15), one can determine the degree of saturation of a sample with an impurity in a particular experiment. As applied to our experiment, the standard deviations (the last column in the table) calculated for various models imply that yttrium diffusion in both samples resembles one of the limiting cases, namely, the case of constant concentration. Hence, the surface layer is close to saturation.

REFERENCES

1. V. Ya. Arsenin, *Basic Equations and Special Functions of Mathematical Physics*, 2nd ed. (Nauka, Moscow, 1984; Iliffe Books, London, 1968).
2. B. S. Bokshteĭn, *Diffusion in Metals* (Metallurgiya, Moscow, 1976).
3. V. P. Gladkov, V. A. Kashcheev, and A. V. Chervyakov, Izotopy SSSR, No. 2 (71), 42 (1986).
4. *Phase Diagrams of Binary Metallic Systems: A Handbook*, Ed. by N. P. Lyakishev (Mashinostroenie, Moscow, 1996), Vol. 3.
5. V. M. Anan'in, V. S. Zotov, V. P. Gladkov, and D. M. Skorov, *Diffusion in Beryllium* (Énergoizdat, Moscow, 1981).

Translated by M. Fofanov

Technical Physics, Vol. 49, No. 3, 2004, pp. 287–295. Translated from Zhurnal Tekhnicheskoĭ Fiziki, Vol. 74, No. 3, 2004, pp. 5–13.
Original Russian Text Copyright © 2004 by Belonozhko, Grigor'ev.

GASES AND LIQUIDS

Nonlinear Periodic Waves on the Charged Surface of a Deep Low-Viscosity Conducting Liquid

D. F. Belonozhko and A. I. Grigor'ev

Demidov State University, Sovetskaya ul. 14, Yaroslavl, 150000 Russia

e-mail: grig@uniyar.ac.ru

Received May 26, 2003; in final form, August 11, 2003

Abstract—An analytical expression for the profile of a finite-amplitude wave on the free charged surface of a deep low-viscosity conducting liquid is derived in an approximation quadratic in wave amplitude-to-wavelength ratio. It is shown that viscosity causes the wave amplitude to decay with time and makes the wave profile asymmetric at surface charge densities subcritical in terms of Tonks–Frenkel instability. At supercritical values of the surface charge density, taking account of viscosity decreases the growth rate of emissive protrusions on the unstable free surface, slightly broadens them for short waves, and narrows for long ones. Analytical expressions for the wave frequencies, damping rates, and instability growth rates with regard to viscosity are found.
© 2004 MAIK "Nauka/Interperiodica".

INTRODUCTION

Studies of nonlinear periodic capillary–gravitational waves traveling on the free surface of a liquid date back to the end of the 19th century (see, for example, [1]). Throughout the 20th century, this problem was solved in only the ideal liquid approximation [2–7]. The few attempts to take into account viscosity were not quite correct (see, e.g., [8, 9]). A rigorous solution to the problem of finite-amplitude waves on the free surface of a deep finite-viscosity liquid has been found only recently [10–13]. However, the solution is so awkward that it is impossible to write explicit expressions for the wave profile and liquid velocity field. Accordingly, numerical methods are invoked to analyze results obtained. Therefore, the finding of asymptotic analytical expressions for the solutions [10–13] in the lower viscosity limit seems to be of importance. Generalization of the problem of nonlinear waves in a viscous liquid for the case of a conducting liquid with the uniformly charged free surface is also of great scientific and applied interest. The aforesaid is the aim of this article.

MATHEMATICAL STATEMENT OF THE PROBLEM

As in [10–13], we assume that an incompressible Newtonian liquid with a kinematic viscosity ν, density ρ, and surface tension coefficient γ occupies the half-space $z \le 0$ in the Cartesian coordinate system $Oxyz$ with the z axis directed upward in the gravitational field ($\mathbf{g} \parallel -\mathbf{e}_z$). The environment is a vacuum. The liquid is assumed to be an ideal conductor uniformly charged over its free surface. Above the free surface distorted by wave flow, the surface charge induces an electric field that has a uniform strength $E_0\mathbf{e}_z$ in the limit $z \longrightarrow \infty$. Our aim is to study the evolution of the initial deformation of the free surface in time.

Let $u = u(x, z, t)$ and $v = v(x, z, t)$ be the horizontal and vertical components of the velocity field of wave flow in the liquid that, for simplicity, are assumed to be y independent, and $\mathbf{e}_x$ and $\mathbf{e}_z$ be unit vectors along the Ox and Oz axes, respectively. Then, the deviation $\xi = \xi(x, t)$ of the free liquid surface from its equilibrium (in the gravity field) shape $z = 0$ due to the virtual initial deformation, the velocity field $\mathbf{U} = u\mathbf{e}_x + v\mathbf{e}_z$, and the electric potential Φ above the liquid are given by

$$z > \xi: \Delta\Phi = 0; \tag{1}$$

$$z < \xi: \partial_t\mathbf{U} + \operatorname{curl}\mathbf{U} \times \mathbf{U} = -\operatorname{grad}\left(\frac{1}{\rho}p + \frac{U^2}{2} + gz\right) + \nu\Delta\mathbf{U}; \tag{2}$$

$$\operatorname{div}\mathbf{U} = 0; \tag{3}$$

$$z = \xi: \partial_t\xi + u\partial_x\xi = v; \tag{4}$$

$$p - 2\rho\nu\mathbf{n} \cdot ((\mathbf{n} \cdot \nabla)\mathbf{U}) = \frac{1}{8\pi}(\nabla\Phi)^2 = \gamma\operatorname{div}(\mathbf{n}); \tag{5}$$

$$\boldsymbol{\tau} \cdot ((\mathbf{n} \cdot \nabla)\mathbf{U}) + \mathbf{n} \cdot ((\boldsymbol{\tau}\nabla)\mathbf{U}) = 0; \tag{6}$$

$$\Phi = 0; \tag{7}$$

$$z \longrightarrow +\infty: -\nabla\Phi \longrightarrow E_0\mathbf{e}_z; \tag{8}$$

$$z \longrightarrow -\infty: \mathbf{U} \longrightarrow 0. \tag{9}$$

Here t is time, p is the pressure in the liquid; ∂_t and ∂_x are the partial derivatives with respect to time and x coordinate, respectively; $\boldsymbol{\tau}$ and $\mathbf{n}$ are the unit vectors tangential and normal to the liquid surface, respec-

tively; and Δ is the Laplacian. The derivation of the related expressions and also the expression for div(**n**) can be found elsewhere [13].

To close the mathematical statement of the problem, we must supplement relationships (1)–(9) by initial conditions for the deviation of the surface from its equilibrium shape and for the distribution of the velocity field. As is commonly accepted in the theory of finite-amplitude periodic waves [1–7], the initial conditions will be defined during solving of the problem so as to obtain such types of free surface oscillations that are simple to treat analytically and to discover the basic nonlinearity-associated properties of the wave.

Let the maximal height of the virtual perturbation of the wave with a length λ over the equilibrium surface $z = 0$ at the zero time be A. In most of the earlier calculations for finite amplitude waves on the free surface of an ideal liquid (see, for example, [1–13]), the initial conditions were imposed on the amplitude of the nonlinear-wave component that is linear in the small parameter. In this case, the maximal deviation A of the resultant nonlinear wave from the plane surface $z = 0$ at the initial time remains uncertain and is calculated after the entire problem has been solved. At the same time, the measurable physical quantity is A, so it is natural to use this parameter in the initial conditions. Moreover, if A is defined *a priori*, one may avoid the situation [5, 6, 10–13] where the amplitude coefficient of a nonlinear correction to the final solution (this coefficient has resonant form under certain conditions) causes the amplitude of the nonlinear wave to grow indefinitely. This is inconsistent with the initial condition and breaks the asymptotics of the solution found.

SOLUTION OF THE PROBLEM

Let the initial perturbation $\xi(x, t)$ be periodic in x and form a wavy pattern with a wavelength λ and amplitude A. As a small parameter, we choose $\varepsilon = kA$, where $k = 2\pi/\lambda$ is the wavenumber.

In an approximation quadratic in ε, a solution to problem (1)–(9) is sought in the form of expansions:

$$\mathbf{U} = \mathbf{U}_1 + \mathbf{U}_2 + O(\varepsilon^3), \quad \mathbf{U}_1 \sim O(\varepsilon), \quad \mathbf{U}_2 \sim O(\varepsilon^2);$$

$$p = p_0 + p_1 + p_2 + O(\varepsilon^3), \quad p_0 \sim O(1),$$

$$p_1 \sim O(\varepsilon), \quad p_2 \sim O(\varepsilon^2);$$

$$\Phi = \Phi_0 + \Phi_1 + \Phi_2 + O(\varepsilon^3), \quad \Phi_0 \sim O(1);$$

$$\Phi_1 \sim O(\varepsilon), \quad \Phi_2 \sim O(\varepsilon^2);$$

$$\xi = \xi_1 + \xi_2 + O(\varepsilon^3), \quad \xi_1 \sim O(\varepsilon), \quad \xi_2 = O(\varepsilon^2).$$

Substituting these relations into (1)–(3) and applying the boundary conditions to the undisturbed liquid surface $z = 0$, one splits initial problem (1)–(9) into subproblems of the zeroth, first, and second orders of smallness (for details, [13]).

In the zeroth approximation in ε, the problem is reduced to finding the hydrostatic pressure distribution in the liquid:

$$u_0 = 0; \quad v_0 = 0; \quad p_0 = -\frac{E_0^2}{8\pi} - \rho g z; \quad \Phi_0 = -E_0 z.$$

As in [13], we will use the following notation for linear differential operators:

$$\mathcal{L} \equiv \begin{bmatrix} \partial_t - \nu(\partial_{xx} + \partial_{zz}) & 0 & (1/\rho)\partial_x & 0 \\ 0 & \partial_t - \nu(\partial_{xx} + \partial_{zz}) & (1/\rho)\partial_z & 0 \\ \partial_x & \partial_z & 0 & 0 \\ 0 & 0 & 0 & \partial_{xx} + \partial_{zz} \end{bmatrix};$$

$$\mathcal{R} \equiv \begin{bmatrix} \partial_t \\ -\rho g + \gamma \partial_{xx} \\ 0 \\ -E_0 \end{bmatrix};$$

$$\mathcal{B} \equiv \begin{bmatrix} 0 & -1 & 0 & 0 \\ 0 & -2\rho\nu\partial_z & 1 & -E_0/(4\pi)\partial_z \\ \partial_z & \partial_x & 0 & 0 \\ 0 & 0 & 0 & 1 \end{bmatrix}_{z=0}$$

and for column matrices with their components:

$$\hat{O} \equiv \begin{bmatrix} 0 \\ 0 \\ 0 \\ 0 \end{bmatrix}; \quad \hat{Y}_j \equiv \begin{bmatrix} u_j \\ v_j \\ p_j \\ \Phi_j \end{bmatrix}; \quad \begin{aligned} Y_j[1] &\equiv u_j; \\ Y_j[2] &\equiv v_j; \\ Y_j[3] &\equiv p_j; \\ Y_j[4] &\equiv \Phi_j. \end{aligned}$$

Operator $\mathcal{B}$ acts on objects of Y_j type according to the following rule: first, the matrix operations are fulfilled; then, all differentiations and arithmetic operations are done; and, finally, it is assumed that $z = 0$. Operator $\mathcal{B}$ transforms a column vector of four functions dependent on the variables x, z, and t into a column of four z-independent functions.

PROBLEM OF THE FIRST ORDER OF SMALLNESS

In the notation adopted, the complete mathematical formulation of the problem for the quantities of the first order of smallness in ε has the form

$$\mathcal{L}\hat{Y}_1 = \hat{O}; \tag{10}$$

$$\mathcal{B}\hat{Y}_1 + \mathcal{R}\xi_1 = \hat{O}; \tag{11}$$

$$z \longrightarrow +\infty: \Phi_1 \equiv Y_1[4] \longrightarrow 0; \quad (12)$$

$$z \longrightarrow -\infty: u_1 \equiv Y_1[1] \longrightarrow 0; \quad v_1 \equiv Y_1[2] \longrightarrow 0; \quad (13)$$

$$\begin{aligned} t = 0: \xi_1 &= \eta\cos(kx); \\ z \le 0: Y_1[1]_{t=0} &= u_1^0; \quad Y_1[2]_{t=0} = v_1^0. \end{aligned} \quad (14)$$

For simplicity, the initial deformation is approximated by a cosine curve in a first approximation. The functions $u_1^0 \equiv u_1^0(x, z)$ and $v_1^0 \equiv v_1^0(x, z)$ are chosen in the course of the solution. These functions must provide a solution that is easy to treat analytically. Eventually, the solution to the first-order problem takes the well-known form [14]

$$\xi_1 = \eta\cos(\theta)\exp(T); \quad (15)$$

$$\begin{aligned} u_1 = \eta((&S_2\exp(kz) - 2\nu k(q_2\cos(q_2z) + q_1\sin(q_2z)) \\ &\times \exp(q_1z))\cos(\theta) + (D\exp(kz) - 2\nu k(q_1\cos(q_2z) \\ &- q_2\sin(q_2z))\exp(q_1z))\sin(\theta))\exp(T); \end{aligned} \quad (16)$$

$$\begin{aligned} v_1 = \eta((&D\exp(kz) - 2\nu k^2\cos(q_2z)\exp(q_1z))\cos(\theta) \\ &- (S_2\exp(kz) - 2\nu k^2\sin(q_2z)\exp(q_1z))\sin(\theta))\exp(T); \end{aligned} \quad (17)$$

$$\begin{aligned} p_1 = \eta\rho k^{-1}&((-S_1D + S_2^2)\cos(\theta) \\ &+ 2S_2(S_1 + \nu k^2)\sin(\theta))\exp(kz)\exp(T); \end{aligned} \quad (18)$$

$$\Phi_1 = \eta E_0\cos(\theta)\exp(T); \quad (19)$$

$$\nu^2(k^2 + q^2)^2 + k\left(g + \frac{k^2\gamma}{\rho} - \frac{k}{\rho}\frac{E_0^2}{4\pi}\right) = 4\nu^2k^3q; \quad (20)$$

$$q_1 = \mathrm{Re}q \ge 0; \quad q_2 = \mathrm{Im}(q) \ge 0; \quad (21)$$

$$S = \nu(q^2 - k^2); \quad S_1 = \mathrm{Re}S; \quad S_2 = \mathrm{Im}S; \quad (22)$$

$$\theta = S_2t - kx; \quad T = S_1t; \quad D = S_1 + 2\nu k^2. \quad (23)$$

In these relationships, the parameter q is calculated as the root of dispersion relation (20) that satisfies (21). These relationships dictate the selection of the root corresponding to a wave flow with a velocity tending to zero at $z \longrightarrow -\infty$ (see condition (13)). The root chosen is assigned a wave travelling to the right. Conditions (21) provide the uniqueness of the complex frequency S. The coefficient η specifies the wave amplitude component that is linear in ε.

Relationships (15)–(23) represent the solution to the first-order problem if one takes u_1 and v_1 ((16) and (17), respectively) at $t = 0$ as $u_1^0 \equiv u_1^0(x, z)$ and $v_1^0 \equiv v_1^0(x, z)$ entering in (14).

Since the first-order problem is linear, any superposition of solutions of form (15)–(19) with different k will be a solution to the initial problem. In the linear approximation, the waves corresponding to these solutions propagate without interaction between each other. Any solution to the linear problem is obtained from solutions (15)–(19) by superposition, which can be chosen in such a way as to meet any reasonable initial conditions.

SECOND-ORDER PROBLEM

Using the same approach to finding the initial conditions as in the first-order problem, we will not write their specific form when formulating the second-order problem:

$$\begin{aligned} \mathcal{L}\hat{Y}_2 = \eta^2\mathrm{Re}\Bigg(\Bigg(&\begin{bmatrix}\hat{A}_1\\0\end{bmatrix}\exp(2q_1z) + \begin{bmatrix}\hat{A}_2\\0\end{bmatrix}\exp(2kz) \\ &+ \begin{bmatrix}\hat{A}_3\\0\end{bmatrix}\exp((k+q)z)\Bigg)\exp(2T) \\ &+ \begin{bmatrix}\hat{A}_4\\0\end{bmatrix}\exp((k+q)z)\exp(2(T+i\theta))\Bigg); \end{aligned} \quad (24)$$

$$\begin{aligned} \mathcal{B}\hat{Y}_2 + \mathcal{R}\xi_2 = \eta^2\mathrm{Re}\Bigg(&\begin{bmatrix}\hat{A}_5\\ \frac{1}{2}kE_0\end{bmatrix}\exp(2T) \\ &+ \begin{bmatrix}\hat{A}_6\\ \frac{1}{2}kE_0\end{bmatrix}\exp(2(T+i\theta))\Bigg); \end{aligned} \quad (25)$$

$$z \longrightarrow +\infty: \Phi_2 \equiv Y_2[4] \longrightarrow 0; \quad (26)$$

$$z \longrightarrow -\infty; u_2 \equiv Y_2[1] \longrightarrow 0; \quad v_2 \equiv Y_2[2] \longrightarrow 0. \quad (27)$$

Here, $\hat{A}_1$ – $\hat{A}_6$ are three-component columns with complex coefficients that are independent of coordinates and time:

$$\hat{A}_1 = -4\nu^2k^3q_1\begin{bmatrix}q_2\\k\\0\end{bmatrix}; \quad \hat{A}_2 = \begin{bmatrix}0\\-k(S_2^2 + D^2)\\0\end{bmatrix};$$

$$\hat{A}_3 = \nu k\begin{bmatrix}2(\bar{S}_1 - iS_2 + 2\nu k^2)q_1q_2 + (S_2 + iD)(q_2^2 - q_1^2 + k^2)\\-2ik(k+q)(S_2 + iD)\\0\end{bmatrix};$$

$$\hat{A}_4 = \begin{bmatrix}-i\nu k(q-k)^2(S + 2\nu k^2)\\0\\0\end{bmatrix};$$

$$\hat{A}_5 = \begin{bmatrix}0\\N_0\\M_0\end{bmatrix}; \quad \hat{A}_6 = \begin{bmatrix}\Omega\\N\\M\end{bmatrix}; \quad \begin{aligned}\Omega &= \Omega_1 + i\Omega_2; \\ N &= N_1 + iN_2; \\ M &= M_1 + iM_2;\end{aligned}$$

$$i^2 = -1;\ \Omega_1 = k(D - 2\nu k q_1);\ \Omega_2 = k(S_2 - 2\nu k q_2);$$

$$N_0 = \frac{1}{2}\rho(S_1^2 - S_2^2 + 4\nu k^2 S_1 + 4\nu^2 k^2 (k^2 - q_1^2 + q_2^2));$$

$$N_1 = N_0 + \frac{1}{2}k^2\frac{E_0^2}{4\pi};$$

$$N_2 = \rho(S_2 D - 4\nu^2 k^2 q_1 q_2);$$

$$M_0 = k(kS_2 - q_2(3k^2 + q_2^2 - 3q_1^2));$$

$$M_1 = -k(3kS_2 - q_2(5k^2 - q_2^2 + 3q_1^2)\nu);$$

$$M_2 = k(2kS_1 + \nu(6k^3 - 5k^2 q_1 + 3q_2^2 q_1 - q_1^3)).$$

Relationships (24)–(27) are equations for the complex components entering into the column $\hat{Y}_2$. Only the real part of these components is physically meaningful.

With the approach described in [13], one can find a second-order nonlinear correction to the wave profile:

$$\xi_2 = \eta^2(\zeta_1\cos(2\theta) - \zeta_2\sin(2\theta))\exp(2T) + \text{LWSs}, \quad (28)$$

where the abbreviation LWSs stands for linear wave solutions (the same as in the linear theory).

These linear wave solutions are solutions to the homogeneous problem corresponding to inhomogeneous problem (24)–(27) considered. Accurate to notation, this homogeneous problem coincides with the first-order problem. As LWSs, one may take any superposition of travelling waves $\eta\cos(\Sigma_2 t \pm \kappa x + \varphi)\exp(\Sigma_1 t)$ with an amplitude η and wavenumber κ such that $\kappa\eta = O(\varepsilon^2)$. The complex frequency $\Sigma = \Sigma_1 + i\Sigma_2$ and the wavenumber κ of these waves are related by the same dispersion relation (20) as the quantities S and k appearing in the expressions for the variables $\theta = S_2 t - kx$ and $T = S_1 t$. When propagating, LWS-related waves do not interact with each other and with the solution to the first-order problem. Therein lies the main distinction of the LWSs from the first part of expression (28) for ξ_2, which involves the amplitude coefficients ζ_1 and ζ_2 depending on k, ρ, γ, g, ν, and W, that is, on the physical parameters entering in the expressions for the frequency and wavenumber in the first-order problem. As these physical parameters (that is, the properties of the first-order solution) vary, so do the amplitude coefficients ζ_1 and ξ_2. In other words, this nonlinear part of the second-order solution will interact with the solution to the problem linear in ε. While the solution to the first-order problem was chosen for simplicity of analysis, in the nonlinear problem the part of its solution that describes interaction between wave flows is taken into consideration and LWSs are omitted in subsequent analysis.

PROFILE OF THE NONLINEAR WAVE

Summing the solutions to the first- and second-order problems and normalizing the amplitude η in such a way that the maximum of the initial surface deviation equals A, we obtain an expression for the profile of a nonlinear periodic capillary–gravitational wave in an approximation quadratic in ε:

$$\xi(x, t) = \xi(\theta, t) = \eta\cos(\theta) + \eta^2[\zeta_1\cos(2\theta) - \zeta_2\sin(2\theta)]\exp(2T), \quad (29)$$

where η is chosen such that

$$A = \max\xi(\theta, 0) \quad \text{at} \quad \theta \in [0, 2\pi]. \quad (30)$$

This relation is the normalization condition for the amplitude.

The complete analytical expressions for ζ_1 and ζ_2 are not given here, because they are extremely awkward. Below, we derive asymptotic expressions for ζ_1 and ζ_2 in the low viscosity approximation. Note only that ζ_1 and ζ_2 depend on the wavenumber k, as well as on ρ, ν, γ, g, and the surface charge density. The last-named parameter determines the value of the Tonks–Frenkel dimensionless parameter

$$W \equiv \frac{E_0^2}{4\pi\sqrt{\rho g\gamma}},$$

which characterizes the stability of the charged liquid surface against its self-charge [15]. From the linear theory, it is well known that the condition

$$W > \alpha k + \frac{1}{\alpha k}, \quad (31)$$

where $\alpha = (\gamma/(\rho g))^{1/2}$ is the capillary constant, provides, at a given αk, the positiveness of the parameter $S_1 \equiv \mathrm{Re}S$ entering into the solutions to the first- and second-order problems. In this case, the charged free surface of the liquid becomes unstable [15]. Then, S_1 takes on the meaning of the wave amplitude growth rate in the first approximation in ε (the term linear in η in (29)) and $2S_1$, the growth rate of the term nonlinear in amplitude η. If the value of W is not large enough to meet condition (30), $S_1 < 0$ and characterizes the exponential damping rate of the term linear in amplitude η in (29), and $2S_1$ characterizes the damping rate of the nonlinear term. Later on, the values of W that meet and do not meet condition (31) will be called supercritical and subcritical, respectively.

The constant η is chosen so that normalization condition (30) is valid at zero time. This condition means that the interval $[0, 2\pi]$ has a value of θ such that $\xi(\theta, 0) = A$ and that the function $f(\theta) = \xi(\theta, 0)$ reaches a maximum at this θ. Since expression (29) implies a finite number of extrema of $f(\theta)$, including a maximum, nor-

malization can be accomplished using the set of equations

$$\begin{cases}\eta\cos(\theta)+\eta^2(\zeta_1\cos(2\theta)-\zeta_2\sin(2\theta)) = A\\ -\sin(\theta)+2\eta(-\zeta_1\sin(2\theta)+\zeta_2\cos(2\theta)) = 0\end{cases}$$

for θ and η. The first equation of this set is the condition under which $\xi(\theta, 0)$ equals A at a certain θ; the second, the necessary condition for the existence of an extremum of the function $f(\theta)$. Among a finite number of pairs of solutions (η, θ) to this set, there necessarily exists that which maximizes $\xi(\theta, 0)$. The value of η from this pair should be taken.

It is important to note that use of the wave amplitude A (containing the components of the first and second orders in ε) as the initial parameter discriminates the problem definition in this work from previous papers [1–13], where the parameter denoted here as η was taken to be input.

REPRESENTATION OF THE COMPLEX FREQUENCY IN THE FORM OF A SERIES IN POWERS OF DIMENSIONLESS VISCOSITY

Consider the quantities

$$\begin{aligned}\omega_0 &= \sqrt{kg(1+\alpha^2k^2-\alpha kW)};\\ r_0 &= \sqrt{kg(\alpha kW-1-\alpha^2k^2)}.\end{aligned} \tag{32}$$

The values of ω_0 and r_0 are real at subcritical and supercritical W, respectively. Physically, ω_0 is the frequency of the wave flow on the surface of an ideal liquid, while r_0 is the growth rate of instability against the excess surface charge for an ideal liquid at supercritical W.

Let us divide both sides of dispersion relation (20) by ω_0^2 and r_0^2 when W is subcritical and supercritical, respectively:

$$(\beta+2\chi)^2+\begin{Bmatrix}1\\-1\end{Bmatrix} = 4\chi^{3/2}\sqrt{\beta+\chi}; \tag{33}$$

$$\mathrm{Re}(\sqrt{\beta+\chi}) = 0;$$

$$\beta = \begin{Bmatrix}S/\omega_0\\ S/r_0\end{Bmatrix};\quad \chi = \begin{Bmatrix}\nu k^2/\omega_0\\ \nu k^2/r_0\end{Bmatrix}. \tag{34}$$

Hereafter, we use the designation

$$\begin{Bmatrix}Q\\R\end{Bmatrix} = \begin{cases}Q, & \text{if} \quad W<\alpha k+(\alpha k)^{-1}\\ R, & \text{if} \quad W>\alpha k+(\alpha k)^{-1}.\end{cases} \tag{35}$$

Along with numerical coefficients, (33) contains only two dimensionless variables: the dimensionless frequency β and the dimensionless viscosity χ.

For definiteness, consider dispersion relation (33) at subcritical W:

$$(\beta+2\chi)^2+1 = 4\chi^{3/2}\sqrt{\beta+\chi};\quad \mathrm{Re}(\sqrt{\beta+\chi}) = 0. \tag{36}$$

Let $\chi \ll 1$. We will expand the root of dispersion relation (36) that tends to $\beta = i$ at $\chi \longrightarrow 0$ in powers of χ. To do this, we assume that

$$\beta = i+\sigma;\quad \lim_{\chi\to 0}\sigma = 0.$$

The square root of the right-hand side of (36) has two analytical branches

$$\sqrt{\beta+\chi} = \sqrt{i}\sqrt{1-i(\chi+\sigma)} = \pm\frac{i+1}{\sqrt{2}}\sqrt{1-i(\chi+\sigma)}, \tag{37}$$

which are series in integer powers of the small parameter $(\chi + \sigma)$ (when calculating the square root $\sqrt{1-i(\chi+\sigma)}$ we, for definiteness, select the branch where the root equals unity at $\chi + \sigma = 0$). Selecting the branch of the function $\sqrt{\beta+\chi}$ with the real part positive at $(\chi + \sigma)$ much smaller than unity (including zero), we obtain the dispersion relation in the form

$$(i+\sigma+2\chi)^2+1 = 2\sqrt{2}(i+1)\chi^{3/2}\sqrt{1+i(\chi+\sigma)}.$$

Represent σ as the sum of two terms: $\sigma = \sigma_1 + \sigma_2$, where $\sigma_2 \sim o(\chi)$ and σ_1 remains undefined. Upon substituting $\sigma = \sigma_1 + \sigma_2$ into Eq. (36), its left-hand side takes the asymptotic form $2i(\sigma_1 + 2\chi) + o(\chi)$, while the right-hand one is on the order of $\chi^{3/2}$. Eventually, in the linear approximation in χ, we obtain $\sigma_1 = -2\chi$ and

$$\beta = i-2\chi+\sigma_2;\quad \sigma_2 = o(\chi). \tag{38}$$

Upon substituting (37) and (38) into (36), we arrive at the relationship

$$\sigma_2(\sigma_2+2i) = 2\sqrt{2}(i+1)\chi^{3/2}\sqrt{1+i(\chi-\sigma_2)}. \tag{39}$$

For the right-hand side of (39) subject to (38), we have

$$\begin{aligned}&2\sqrt{2}(i+1)\chi^{3/2}\sqrt{1+i(\chi-\sigma_2)}\\ &= 2\sqrt{2}(i+1)\chi^{3/2}+\sqrt{2}i(i+1)\chi^{5/2}+o(\chi^{5/2}).\end{aligned}$$

Thus, two leading terms, which are proportional to $\chi^{3/2}$ and $\chi^{5/2}$, have been separated out. This means that the leading terms in the asymptotic representation of the left-hand side of (39) must be of the same orders. Eventually, two first principal orders separate out in the asymptotic representation of σ_2:

$$\sigma_2 = \beta_3\chi^{3/2}+\beta_5\chi^{5/2}+o(\chi^{5/2}).$$

Substituting σ_2 with the separated leading terms into (39) again, we find that the least possible order of χ in the third term of expansion (39) for the square root is three ($O(\chi^3)$). Hence, terms of the same order must be

present in the asymptotic representation of the left-hand side of (39):

$$\sigma_2 = \beta_3\chi^{3/2} + \beta_5\chi^{5/2} + \beta_6\chi^3 + o(\chi^3).$$

The procedure of successive isolation of the leading terms in the representation for σ_2 can be continued by induction.

In the foregoing, we said nothing about the values of β_3 and β_5, through which the coefficients multiplying higher order terms are expressed (these coefficients may vanish, of which β_6 is an example). In the procedure of isolating principal orders in the representation for σ_2, terms of each succeeding order are isolated by powering or multiplying orders isolated at the previous step. The process starts from $\chi^{3/2}$ and $\chi^{5/2}$. Therefore, the orders of all subsequent terms in the expansion must be expressed by integer powers of $\chi^{1/2}$. This means that, without loss of generality, we may represent σ_2 in the form

$$\sigma^2 = \sum_{n=3}^{\infty}\beta_n\chi^{n/2}, \tag{40}$$

where some β_n may be zero.

The root of (36) that turns into imaginary unity at $\chi = 0$ should be sought in the form of the series

$$\beta = i + \sum_{n=2}^{N}\beta_n\chi^{n/2}. \tag{41}$$

Substituting (41) into (36), expanding both sides of (36) into a series in integer powers of $\chi^{1/2}$, and equating the coefficients multiplying the same powers of this parameter yields a set of equations for β_n.

To find the coefficients β_n in expansions (40) and (41), we will apply the theorem on the differentiation of a composite function to $\beta = \beta(\delta)$, where $\delta = \chi^{1/2}$. This function is defined in implicit form by (36). Proceeding in this way, we can find derivatives $d^n\beta/d\delta^n$ of any order n, which will be used to express the coefficients of Taylor series (41).

Similar reasoning applies to the dispersion relation at supercritical values of W. Eventually, for the complex frequency S, we obtain the expression

$$S = \begin{Bmatrix}\omega_0\\ r_0\end{Bmatrix}\left(\begin{Bmatrix} i\\ 1\end{Bmatrix} + \sum_{n=2}^{\infty}\beta_n\chi^{n/2}\right), \tag{42}$$

where

$$\beta_n = -\left(\frac{1}{n!}\frac{d^{n-1}}{d\delta^{n-1}}\left(\frac{\partial_\beta F(\beta,\delta)}{\partial_\delta F(\beta,\delta)}\right)\right)_{\substack{\{\beta = i\}\\ \{\beta = 1\}\\ \delta = 0}} \tag{43}$$

$$F(\beta,\delta) = (\beta + 2\delta^2)^2 - 4\delta^3(\sqrt{\beta + \delta^2}).$$

The braces are used here in the sense of (35). When calculating β_n by formula (43), one should take into account the following. First, in the successive calculation of total derivatives with respect to δ, the derivative $\beta' = \beta'(\delta)$ resulting from the differentiation of the composite function must be replaced by the expression

$$\beta' = -\frac{\partial_\beta F(\beta,\delta)}{\partial_\delta F(\beta,\delta)} = \frac{2\delta(-3\beta\delta - 4\delta^3 + (\beta+\delta)^{3/2})}{\delta^3 - (\beta+\delta)^{3/2}}.$$

Second, the expression obtained after calculating the final derivative is a fractional rational function of β, δ, and $\sqrt{\beta + \delta^2}$. To calculate this expression at $\beta = i$ and $\delta = 0$, one should replace $\sqrt{i}$ by $(i+1)/\sqrt{2}$. In this case, the coefficient β_n calculated corresponds to the root of Eq. (36) that meets the condition $\mathrm{Re}(\sqrt{\beta + \chi}) > 0$.

When constructing series (41), we represented the square root of the right-hand side of (37) in the form of a series. This series converges inside the domain $|\chi + \sigma| < 1$.

Instead of analyzing the convergence of series (41) in the general case, we studied the possibility of representing the root of Eq. (33) by the end part of series (42). Below are given approximate expressions for the frequency S_2 and parameter $r = S_1$, which characterizes the damping rate (at $r < 0$) and growth rate (at $r > 0$) of instability. These expressions are obtained from (42) by rejecting terms on the order of $O(\chi^5)$ and higher:

$$S_2 = \begin{Bmatrix}\omega_0\left(1 - \sqrt{2}\chi^{3/2} + \frac{1}{\sqrt{2}}\chi^{5/2} - \frac{1}{4\sqrt{2}}\chi^{7/2} + 2\chi^4\frac{9}{8\sqrt{2}}\chi^{9/2}\right)\\ 0\end{Bmatrix}, \tag{44}$$

$$S_1 = \begin{Bmatrix}\omega_0\left(-2\chi - \sqrt{2}\chi^{3/2} + \frac{1}{\sqrt{2}}\chi^{5/2} + \frac{1}{4\sqrt{2}}\chi^{7/2} - \frac{9}{8\sqrt{2}}\chi^{9/2}\right)\\ r_0\left(1 - 2\chi + 2\chi^{3/2} - \chi^{5/2} - \frac{1}{4}\chi^{7/2} + 2\chi^4 - \frac{9}{8}\chi^{9.2}\right)\end{Bmatrix}. \tag{45}$$

Numerical calculations show that the fractional error in formula (44) at $\chi = 0.1$ reaches 10^{-6} and 0.002 if we take into account, respectively, all six terms and the terms of orders not higher than $\chi^{3/2}$. For formula (45), the fractional error is 10^{-5} with all terms taken into account. The error amounts to 0.015 for the damping rate and 0.004 for the growth rate with the terms of orders higher than $\chi^{3/2}$ rejected. Therefore, at $\chi \le 0.1$, the order $\chi^{3/2}$ in (44) and (45) provides the accuracy sufficient for practical calculations.

The terms in formulas (44) and (45) are significant with χ close to 0.5. For $\chi = 0.5$, the fractional error in formula (44) is 0.03. In formula (45), the error is 0.1 for the damping rate and 0.02 for the growth rate. The error grows noticeably with increasing χ.

APPROXIMATE FORMULA FOR THE NONLINEAR WAVE PROFILE IN THE LOW VISCOSITY LIMIT

From exact solution (29) for the amplitude parameters ζ_1 and ζ_2, it is easy to derive asymptotic formulas in the low viscosity limit:

$$\zeta_1 = \frac{1}{4}k\frac{(1+\alpha^2k^2-2\alpha kW)}{0.5-\alpha^2k^2} + \begin{Bmatrix} o(\nu) \\ \dfrac{r_0}{g}\dfrac{2k^2}{0.5-\alpha^2k^2}\nu \end{Bmatrix}; \quad (46)$$

$$\zeta_2 = \begin{Bmatrix} \dfrac{k^2\omega_0}{g}\dfrac{(2-\alpha^2k^2-2\alpha kW)}{(0.5-\alpha^2k^2)^2}\nu + o(\nu) \\ 0 \end{Bmatrix}. \quad (47)$$

Here, the braces have the same sense as in the previous section. At $W = 0$ and $\nu = 0$, we come to the same solution as in [5, 6] if the condition imposed on η is taken as the initial condition. From (46) and (47), it is seen that the amplitude factors ζ_1 and ζ_2 tend to infinity at $\alpha k \longrightarrow 1/\sqrt{2}$. Because of this, the value $k = k_* = 1/\sqrt{2}$ was considered resonant in [5, 6].

As was already noted, the statement of the problem in this work implies that the amplitude η is normalized. In other words, the value of η is chosen in such a way that solution (29) meets initial condition (30) at zero time. In the ideal liquid approximation ($\nu = 0$), the shape of the nonlinear wave at zero time has the form $\xi = \eta\cos(kx) + \eta^2\zeta\cos(2kx)$. Adding up these solutions at the origin of coordinates and meeting normalization condition (30), one easily derives a quadratic equation for η with the positive solutions

$$\eta = \begin{cases} \dfrac{\sqrt{1+4A\zeta}-1}{2\zeta}, & \text{if} \quad \zeta \ge 0 \\ -\dfrac{\sqrt{1+4A\zeta}+1}{2\zeta}, & \text{if} \quad \zeta < 0, \end{cases} \quad (48)$$

$$\zeta = \frac{1}{4}k\frac{(1+\alpha^2k^2-2\alpha kW)}{0.5-\alpha^2k^2}.$$

Such an approach assures that the amplitude of the wave on the surface of an ideal liquid,

$$\xi = \eta\cos(\theta) + \eta^2\zeta\cos(2\theta)$$

will not grow at $k \longrightarrow k_*$. As the wavenumber approaches the resonant value, the amplitude of the term linear in the small parameter in (29) tends to zero, while the amplitude of the nonlinear term tends to A. Although the wave profile height under resonance is finite, expansion (29) at $k = k_*$ loses its asymptotic property: the leading term in (29) becomes infinitesimal compared with the correction quadratic in the small parameter.

Since ζ may take both positive and negative values, it is necessary that $4A|\zeta| \le 1$ in order to employ formulas (48).

INFLUENCE OF VISCOSITY ON THE FREE SURFACE SHAPE

Viscosity influences the evolution of the wave profile in two ways. On the one hand, viscosity appears in the formula for S_1, which describes the damping rate or growth rate of the wave amplitude (in the first approximation in ε for the term linear in η in (28) and in the second approximation for the nonlinear term) depending on whether W is subcritical or supercritical. Also, it is easy to see that the ratios S_2/ω_0 and S_1/r_0 are functions of only the dimensionless viscosity χ.

On the other hand, viscosity affects the amplitude coefficients ζ_1 and ζ_2, through which the solution to the second-order problem is expressed.

From asymptotic expressions (46) and (47), it follows that, at subcritical values of W, the viscosity affects $\zeta_2 \sim O(\nu)$ to the greatest extent. The constant-sign conditions for this parameter are as follows:

$$\zeta_2 > 0, \quad \text{if} \quad \begin{cases} W < (\alpha k)^{-1} - 0.5\alpha k \\ \alpha^2k^2 > 0.5 \end{cases} \quad \text{or} \quad \begin{cases} W > (\alpha k)^{-1} - 0.5\alpha k \\ \alpha^2k^2 < 0.5, \end{cases}$$

$$\zeta_2 < 0, \quad \text{if} \quad \begin{cases} W > (\alpha k)^{-1} - 0.5\alpha k \\ \alpha^2k^2 > 0.5 \end{cases} \quad \text{or} \quad \begin{cases} W < (\alpha k)^{-1} - 0.5\alpha k \\ \alpha^2k^2 < 0.5. \end{cases}$$

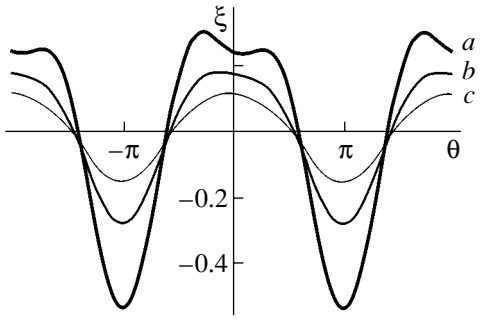

Fig. 1. Nonlinear wave profiles calculated using expression (29) at $k = 1$, $\nu = 0.03$, and $A = 0.3$ for dimensionless time $t =$ (*a*) 0, (*b*) 10, and (*c*) 20. The surface charge density $W = 0$.

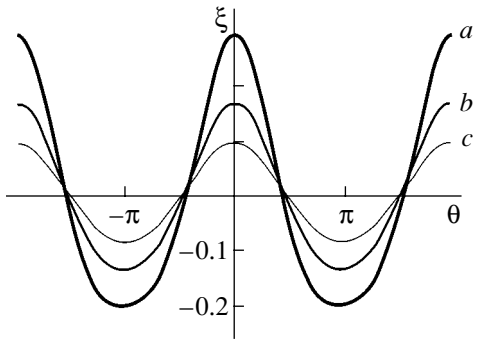

Fig. 3. Same as in Fig. 1 at $W = 1.7$.

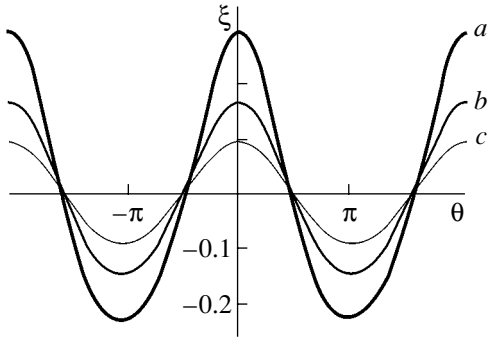

Fig. 2. Same as in Fig. 1 at $W = 0.5$.

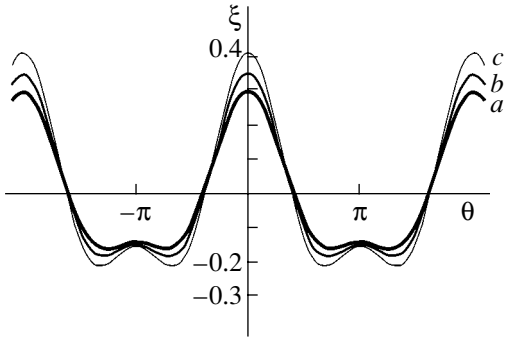

Fig. 4. Shape of an emissive protrusion developing from the initial deformation (see (29)) of the equilibrium flat surface at $k = 1$, $\nu = 0.1$, $A = 0.3$, and $W = 4$ for dimensionless time $t =$ (a) 0, (b) 0.1, and (c) 0.2. At larger times, the amplitude of the protrusion increases rapidly because of a major contribution from the nonlinear correction.

Let us recast the solution for ξ in the form

$$\xi = [\eta\cos(\theta)\exp(S_1 t) + \eta^2\zeta_1\cos(2\theta)\exp(2S_1 t)] - \eta^2\zeta_2\sin(2\theta)\exp(2S_1 t).$$

Here, the bracketed term is the profile symmetric about the vertical line passing through the crest of the wave. The second term is the profile shifted by $\pm\pi/2$ (depending on the sign of ζ_2) relative to the first one. The resultant profile is asymmetric about the vertical line passing through the crest of the wave. The skewness is related to ζ_2, which depends on ν; hence, the skewness depends on viscosity. The direction of asymmetry (along or counter to the wave flow) is determined by the sign of ζ_2.

At supercritical *W*, viscosity influences the shape of the free surface in a quite different manner, as follows from (46) and (47): an additional term proportional to viscosity appears in the expression for ζ_1. This addition is positive for long waves, $\alpha k < 0.5$, and negative for short waves, $\alpha k > 0.5$. The value of ζ_2 at $W \geq 2$ is equal to zero. This means that, at supercritical *W*, the wave profile is symmetric and viscosity increases the contribution of the second-order correction in the expression for ξ.

Figures 1–3 show the calculation results for the wave profile evolution at $k = 1$ and $\nu = 0.03$ (the ordinate and abscissa are dimensionless variables such that $\rho = g = \gamma = 1$). In the absence of the electric charge, the wave traveling to the right is skewed opposite to the direction of wave propagation (Fig. 1). Such behavior is typical of waves for which $\zeta_2 > 0$. At other *k*, ζ_2 may be less than 0. An increase in *W* up to $W = 0.5$ eliminates the asymmetry (Fig. 2). As *W* increases further, the leading front of the wave steepens insignificantly, which can be judged from only the shape of the valleys (Fig. 3). When the parameter *W* reaches its critical value $W = 2$, the conclusions based on the analysis of the low-viscosity expressions become invalid, because the dimensionless viscosity $\chi = \nu k^2/\omega_0^2 \longrightarrow \infty$ at $k = 1$ and $W = 2$. However, calculations using the exact formulas show that the wave profile is symmetric in the vicinity of $W = 2$.

Figure 4 demonstrates the initial stage of the evolution of the free surface profile at supercritical $W = 4$ ($k = 1$, $\nu = 0.1$); Fig. 5, the shape of a protrusion on the free surface for $W = 4$ ($\nu = 0$ and 0.1) within a certain time after the beginning of growth. The times and viscosities are selected so as to provide the same final height of the protrusion. At $\nu = 0$, this height is reached

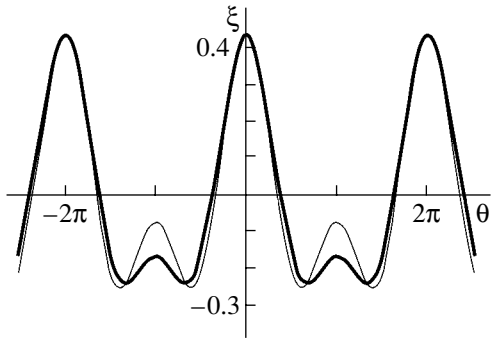

Fig. 5. Shape of the emissive protrusion developing from the initial deformation (see (29)) of the equilibrium flat liquid surface at $k = 1$, $A = 0.3$, and $W = 4$. The thick line is drawn for the viscous liquid: $\nu = 0.1$ and $t = 0.25$; the thin line, for the ideal liquid: $\nu = 0$ and $t = 0.2$.

in $t = 0.20$; at $\nu = 0.1$, the process lasts longer: $t = 0.25$. It is seen that the protrusion on the surface of the viscous liquid is somewhat more flattened and its peak in the valley is less pronounced. This is because $\alpha^2 k^2 > 0.5$ and the factor multiplying ν in (46) is negative at dimensionless value $k = 1$. For k yielding $\alpha^2 k^2 < 0.5$, this factor is positive; that is, ζ_1 will be larger than in the case of an ideal liquid and the emissive protrusion will slightly narrow.

CONCLUSIONS

The behavior of nonlinear periodic capillary–gravitational waves on the charged free surface of a viscous conducting liquid is appreciably different from that of nonlinear waves on the charged surface of an ideal liquid. This distinction is due to surface charge and viscosity. When the surface charge density is subcritical in terms of free surface stability against excess electric charge, viscosity causes asymmetry of the wave profile about the vertical line passing through the crest of the wave. This asymmetry increases with the viscosity. At supercritical surface charge densities, the effect of viscosity changes the shape of emissive protrusions on the free charged surface at the initial stage of instability. The top of a protrusion developing from a virtual short-wave (long-wave) perturbation turns out to be flatter (sharper) than the top of a protrusion on the surface of the ideal liquid. It is noteworthy that the damping rate of a nonlinear correction to the wave profile is twice as large as the damping rate of its component linear in a small parameter.

ACKNOWLEDGMENTS

This work was supported by the President of the Russian Federation (grant no. MK-929.2003.01) and the Russian Foundation for Basic Research (grant no. 03-01-00760).

REFERENCES

1. J. H. Michel, Philos. Mag. **36**, 430 (1893).
2. H. Lamb, *Hydrodynamics* (Cambridge Univ. Press, Cambridge, 1932; Gostekhizdat, Moscow, 1947).
3. J. J. Stoker, *Water Waves* (Wiley, New York, 1957; Inostrannaya Literatura, Moscow, 1959).
4. G. B. Whitham, *Linear and Nonlinear Waves* (Wiley, New York, 1974; Mir, Moscow, 1977).
5. A. H. Nayfeh, J. Fluid Mech. **48**, 385 (1971).
6. L. F. McGoldric, J. Fluid Mech. **52**, 725 (1972).
7. I. Shugan and K. Voliak, J. Fluid Mech. **368**, 321 (1998).
8. W. J. Harison, Proc. London Math. Soc., Ser. 2 **7**, 107 (1908).
9. J. R. Wilton, Philos. Mag. **29**, 688 (1915).
10. D. F. Belonozhko, A. I. Grigor'ev, and S. O. Shiryaeva, Pis'ma Zh. Tekh. Fiz. **28** (19), 1 (2002) [Tech. Phys. Lett. **28**, 795 (2002)].
11. D. F. Belonozhko and A. I. Grigor'ev, Izv. Ross. Akad. Nauk, Mekh. Zhidk. Gaza, No. 2, 184 (2003).
12. D. F. Belonozhko and A. I. Grigor'ev, Pis'ma Zh. Tekh. Fiz. **29** (8), 1 (2003) [Tech. Phys. Lett. **29**, 309 (2003)].
13. D. F. Belonozhko and A. I. Grigor'ev, Zh. Tekh. Fiz. **73** (4), 28 (2003) [Tech. Phys. **48**, 404 (2003)].
14. V. G. Levich, *Physicochemical Hydrodynamics* (Fizmatgiz, Moscow, 1959).
15. Ya. I. Frenkel, Zh. Éksp. Teor. Fiz. **6**, 348 (1936).

Translated by N. Mende

Technical Physics, Vol. 49, No. 3, 2004, pp. 296–301. Translated from Zhurnal Tekhnicheskoĭ Fiziki, Vol. 74, No. 3, 2004, pp. 14–19.
Original Russian Text Copyright © 2004 by Svirkova.

SOLIDS

Effect of Grain-Boundary Electron Scattering in Magnetic Layers on the Magnetoresistive Ratio of a Polycrystalline Sandwich under Transverse Charge Transfer

N. N. Svirkova

Institute of Laser and Information Technologies, Russian Academy of Sciences, Shatura, Moscow Oblast, 140070 Russia

e-mail: center@laser.nictl.msk.su

Received March 17, 2003; in final form, August 4, 2003

Abstract—For a polycrystalline magnetic sandwich, an analytical expression that relates the electron scattering by grain boundary roughness, the conductivity of ferromagnetic layers, and the grain size is derived for the case of a transverse charge transfer. The effect of this scattering mechanism on the giant magnetoresistance of the sandwich is studied with account taken for the dispersity of the ferromagnetic layers and the length of grain-boundary diffusion of nonmagnetic spacer atoms into the layers. © *2004 MAIK "Nauka/Interperiodica".*

INTRODUCTION

The discovery (1918) of the giant magnetoresistance (GMR) [1] in the Fe/Cr superlattice has provoked considerable interest in multilayer ferromagnet–nonmagnetic metal systems. On the one hand, this effect has given us great insight into the nature of magnetism, especially into the magnetism of surface and quasi-two-dimensional systems. On the other hand, it has stimulated the industrial use of new magnetic storage, sensor, etc., technologies.

For applications, it is necessary to provide the magnetoresistive ratio $(\rho - \rho_s)/\rho$ of superlattices as high as possible (ρ is the maximal resistivity of the superlattice and ρ_s is the resistivity of the superlattice at saturation). The highest magnetoresistive ratios are offered by epitaxial structures grown along particular crystallographic directions. However, the complexity of epitaxial processes has given impetus to studying the GMR effect in nonoriented highly disperse polycrystalline superlattices, which are much easier to fabricate.

In these structures, the GMR effect has a number of intriguing features due to unique properties of thin polycrystalline films. For example, the character of charge transfer in the films affects considerably the conductivity and, hence, the magnetoresistive ratio of polycrystalline superlattices. In the film with columnar grains oriented normally to its surface, charge transfer both along (parallel transfer) and across (transverse transfer) the film should be considered. The conductivity due to parallel transfer naturally depends heavily on the grain boundary (GB) properties. The effect of GB scattering on the longitudinal conductivity of the layers becomes of special importance when the grain size is comparable to the mean free path of carriers in the bulk metal. Quantitatively, a decrease in the longitudinal conductivity with decreasing grain size is described well in terms of the Mayadas–Shatzkes theory for internal size effect [2].

The transverse conductivity is affected by GBs only slightly. However, in the immediate vicinity of the boundary, where the grains are in contact, there always exist stationary domains with a high concentration of unoccupied vacancies even at very low temperatures [3]. Accordingly, in ferromagnetic layers of polycrystalline superlattices, these domains are heavily enriched by diffused nonmagnetic metal atoms [4]. In ferromagnetic transition metals, the electron scattering by impurity atoms may depend appreciably on the spin sign. In single-crystal iron, the scattering probabilities for electrons with opposite spins differ sixfold [1]. As a result, electrons with a particular spin that fall into the domains adjacent to the nonmagnetic spacer will be scattered by GBs much more strongly than in the rest of the layer. Such spin-dependent electron scattering may have a significant effect both on the conductivity of the layers and on the magnetoresistive ratio of the polycrystalline multilayer structure even in the case of the CPP (Current Perpendicular to the Plane) geometry (charge carries move perpendicularly to the surface of the layers).

It is logical to assume that the effect associated with this scattering mechanism will depend on the grain size much as the GMR of a superlattice depends on the ferromagnetic layer thickness. Moreover, if diffusion is localized within GB regions (which is possible at very low temperatures and extremely short diffusion annealings [4]) and so changes the magnetic parameters insignificantly [5], the dispersity of the ferromagnetic layers and the length of GB diffusion have a decisive effect on the GMR in noncrystalline superlattices.

1063-7842/04/4903-0296$26.00 © 2004 MAIK "Nauka/Interperiodica"

In this work, we estimate the influence of spin-dependent electron scattering by nonmagnetic spacer atoms diffused into the ferromagnetic layers on the magnetoresistance for a polycrystalline sandwich with the CPP geometry. The parameters of the problem are the mean grain size (morphology parameter) and the length of GB diffusion.

CPP CONDUCTIVITY OF THE FERROMAGNETIC LAYER VERSUS SPIN-DEPENDENT SCATTERING OF ELECTRONS BY GRAIN-BOUNDARY ROUGHNESS AND MORPHOLOGY PARAMETER

The magnetic sandwich configuration is shown in Fig. 1. We assume for simplicity that (i) grains in the ferromagnetic layer are rectangular columns of the square section of side d (mean grain size) running normally to its surface; (ii) the magnetizations of the columns are aligned with one another; and (iii) the transition (boundary) region between two grains is a continuous domain of the nonmagnetic metal with a thickness equal to the GB diffusion length δ, so that the electrons in the boundary region have the same energy (velocity) as in the nonmagnetic spacer of the sandwich.

Consider a series of the columns in the ferromagnetic layer and direct the coordinate axis as shown in Fig. 2. Then, within the GB diffusion length h, a section made by cutting the layer by the plane $x0z$ can be considered as a structure periodic along the z axis, i.e., as a kind of one-dimensional magnetic superlattice with a ferromagnetic configuration period equal to two columns (Fig. 3). The thickness of the "ferromagnetic layer" of such a "superlattice" equals the grain size d; that of the nonmagnetic spacer, to the GB diffusion length δ.

Certainly, the above assumptions greatly simplify the actual pattern. However, they allow us to consider on a qualitative basis how spin-dependent electron scattering by the GB roughness (i.e., by nonmagnetic metal atoms diffused) in the ferromagnetic layers of polycrystalline superlattices affects the CPP conductivity of these layers in view of their morphology. To this end, we invoke theoretical models used to estimate the effect of various factors, such as layer thickness, on the magnetoresistance of multilayer crystalline structures.

In this work, the effect of spin-dependent electron scattering by GB roughness in a ferromagnetic layer on its CPP conductivity with regard for the morphology parameter d was studied in terms of the model put forward in [6, 7] (which is a generalization of the Fuchs–Sondheimer theory of size effect in a single metallic layer [8]) and its associated technique of deriving an expression for the admittance [9]. This model was selected, because, first, it is intended for studying the magnetoresistance of crystalline superlattices to current passing parallel to the plane of the layers and, second, it includes spin-dependent coefficients that

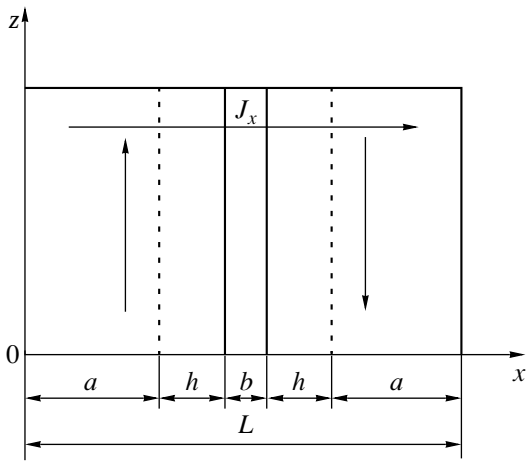

Fig. 1. Magnetic sandwich: L, the length of the sample along the x axis; $a + h$, the thickness of the magnetic layer; h, the length of GB diffusion of nonmagnetic metal atoms; and b is the nonmagnetic spacer thickness. The vertical arrows indicate the direction of the magnetization vector in the ferromagnetic layers for the antiferromagnetic configuration; the horizontal arrows, the direction of the current in the case of the CPP geometry.

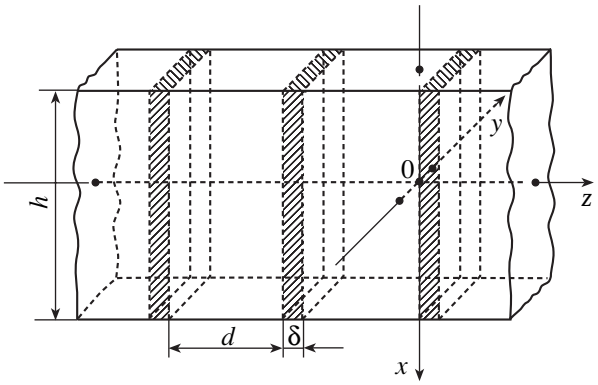

Fig. 2. Direction of the coordinate axes in columnar grains of the ferromagnetic layer. Grain boundaries are hatched.

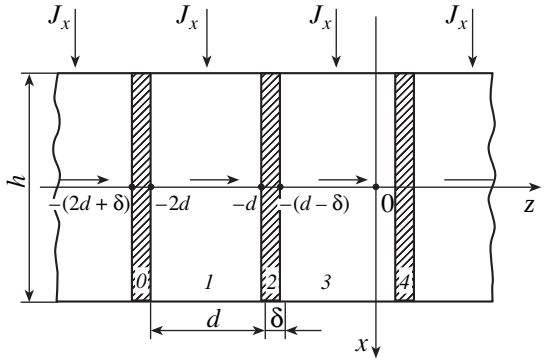

Fig. 3. Ferromagnetic configuration of a one-dimensional magnetic superlattice. Nonmagnetic spacers are hatched. The horizontal arrows indicate the magnetization direction in the ferromagnetic layers; the vertical arrows, the direction of the longitudinal current J_x in each of these layers.

account for specular reflection, transmission, and diffuse scattering of conduction electrons by rough inner interfaces.

Let a uniform electric field of strength E be applied along the x axis. Then, in each jth layer of the superlattice shown in Fig. 3, there exists a longitudinal current $J_{xj}(z)$. This current is the sum of two currents due to electrons with the spins oriented parallel and antiparallel to the magnetization vector of the ferromagnetic layer. The expression for $J_{xj}(z)$ has the form [9]

$$J_{xj}(z) = \frac{e}{4\pi}\int_0^\infty \rho_j v_j dW \int_0^\pi \psi_j \sin^2\theta_j d\theta_j. \quad (1)$$

Here, e is the charge of an electron, ρ_j is the density of states, v_j is the magnitude of the electron mean velocity, W is the electron potential energy, θ_j is the angle of incidence of the electrons on the interface, and ψ_j is a correction to the Fermi–Dirac equilibrium distribution function f_0 that takes into account electron scattering by GB roughness.

An expression for the mean conductivity of a jth ferromagnetic layer (let $j = 1$ for the definiteness) for electrons with a given spin orientation will be found by the technique described in [9]. The boundary condition is assumed to have the form $\psi_1^-(-d) = P_{12}\psi_1^+(-d) + Q_{21}\psi_2^-(-d)$ (Fig. 3). In view of the equalities $\psi_1^+(-d) = \psi_1^-(-2d)$ and $\psi_2^-(-d)\psi_0^-(-2d - \delta) \approx \psi_1^-(-2d)$, which follow from the symmetry and periodicity of the boundary values ψ_j, we have

$$\psi_1^-(-d) \approx P_{12}\psi_1^-(-2d) + Q_{21}\psi_1^-(-2d), \quad (2)$$

where $\psi_j^+(z)$ and $\psi_j^-(z)$ are the nonequilibrium distribution functions depending on the sign of the projection of the velocity v_j onto the z axis, P_{12} is the transparency coefficient (the probability that an electron specularly reflects from the interface between layers 1 and 2), $Q_{21} = Q_{12}$ is the transmission coefficient (the probability that an electron passes from layer 1 into layer 2 through the interface), and d is the mean size of a columnar grain.

Without going into details of calculation, we give the desired expression:

$$\sigma_{x1} = \sigma_1(1 - \gamma_1), \quad (3)$$

where

$$\sigma_1 = \frac{e^2 m_1^2 \tau_1 v_{f1}^3}{6\pi^2\hbar^3}, \quad (4)$$

$$\gamma_1 = \frac{3l_1}{2d}\int_0^{\pi/2} \frac{(1 - P_{12} - Q_{12})(1 - \exp(-d/l_1\cos\theta_1))}{(1 - (P_{12} + Q_{12})\exp(-d/l_1\cos\theta_1))} \times \sin^3\theta_1\cos\theta_1 d\theta_1. \quad (5)$$

Here, σ_1 is the volumetric conductivity of layer 1, τ_1 is the relaxation time, v_{f1} is the velocity of Fermi electrons, m_1 is the effective mass of an electron, and $l_1 = \tau_1 v_{f1}$ is the electron free path. The second term in (3) takes into account the deviation of the conductivity of layer 1from its volumetric value because of the presence of inner interfaces. According to [9], the transparency coefficient P_{12} and the transmission coefficient Q_{12} are quantitatively determined with formulas that represent these coefficients through the electron parameters in explicit form and include the roughness of the interfaces:

$$P_{12} = R_{12}\exp\left[-\left(\frac{2\eta}{\hbar}m_1 v_{f1}\cos\theta_1\right)^2\right],$$
$$Q_{12} = (1 - R_{12}) \times \exp\left[-\frac{\eta^2}{\hbar^2}(m_1 v_{f1}\cos\theta_1 - m_2 v_{f2}\cos\theta_2)^2\right], \quad (6)$$
$$R_{12} = \left(\frac{v_{f1}\cos\theta_1 - v_{f2}\cos\theta_2}{v_{f1}\cos\theta_1 + v_{f2}\cos\theta_2}\right)^2,$$

where R_{12} is the reflection coefficient; v_{f2} and m_2 are, respectively, the Fermi velocity and the effective mass of electrons in the nonmagnetic spacer; θ_1 and θ_2 are the angles of incidence of electrons from layer 1 and layer 2, respectively, on the interface between these layers; and η is a parameter that includes the roughness of the interfaces.

The angle θ_2 is related to the angle θ_1, over which the integral in (5) is taken, by the relationship

$$\frac{\sin\theta_1}{\sin\theta_2} = \frac{m_2 v_2}{m_1 v_1}. \quad (7)$$

When the angle of incidence θ_j exceeds a critical value

$$Q_{j\max} = \arcsin\sqrt{m_k v_k / m_j v_j}, \quad \text{if} \quad m_j v_j > m_k v_k, \quad (8)$$

the electrons may experience total internal reflection. Then, the reflection coefficient $R_{jk} = 1$ and the transmission coefficient $q_{jk} = 0$ [9].

It should be noted that the electrons in each of the columnar grains in a given series will experience scattering by lateral faces that are normal not only to the z axis but also to the y axis (Fig. 2), as opposed to the usual magnetic superlattices. This additional scattering in the expression for the mean conductivity is taken into account as follows:

$$\sigma_{x\text{grain}} = \sigma_{x1}(1 - \gamma_1) = \sigma_1(1 - \gamma_1)^2. \quad (9)$$

Since the GB thickness in thin metallic films is small (δ = 0.5–1.0 nm [4]), the conductivity of the ferromagnetic layer domain of thickness h that is adjacent to the nonmagnetic spacer may be approximated by formula (9) with an acceptable accuracy. As follows from calculations performed in [9] for a Fe/Cu/Fe sandwich (parameters of electrons and geometrical dimensions of the sandwich are given below), the inclusion of nonmagnetic spacers between the grains changes the final result by less than 4%, while the amount of computation grows significantly because of the need for using four boundary conditions.

Now let us determine the conductivity of the entire ferromagnetic layer. Within a ferromagnetic layer domain of thickness a, electrons move parallel to GBs, which are, in this case, free of roughness in the form of nonmagnetic atoms (Fig. 1). Therefore, diffuse scattering by GBs in this domain may be ignored and its conductivity may be taken to be roughly equal to the bulk conductivity of the material (formula (4)). Then, for electrons with a given spin orientation, the conductivity of the entire ferromagnetic layer of the sandwich is given by [10]

$$\sigma_{x\max} = \frac{a + h}{a + h/(1 - \gamma_1)^2}\sigma_1. \qquad (10)$$

Expressions (4)–(7) make it possible to estimate the contribution of spin-dependent electron GB scattering in a ferromagnetic layer to the CPP conductivity of this layer in view of its dispersity. Consider a Fe/Cu/Fe sandwich as an example, for which the Fermi velocities of electrons with oppositely oriented spins in the magnetic ($v_{f1}^{\uparrow}$, $v_{f1}^{\downarrow}$) and nonmagnetic (v_{f2}) layers have been determined: $v_{f1}^{\uparrow} = 7.1 \times 10^5$ m/s, $v_{f1}^{\downarrow} = 8.51 \times 10^5$ m/s, and $v_{f2} = 8.67 \times 10^5$ m/s [9]. The effective masses of electrons are taken to be the same: $m_1 = m_2 = 4m_0$, where m_0 is the electron mass at rest. The parameters with the arrow pointing up (down) refer to electrons with the spins parallel (antiparallel) to the magnetization of the ferromagnetic layer. The relaxation times are assumed to be the same: $\tau_1 = \tau_2 = 10^{-13}$ s. The roughness parameter η is taken to be equal to 0.1 nm (on the order of the atomic size). The thickness $a + h$ of the iron layer is 10 nm, i.e., exceeds the free path length of conduction electrons in a metal, and the length of GB diffusion of copper atoms into the magnetic layer is h = 3 nm. The thickness b of the copper spacer is taken to be equal to 2.2 nm (the second antiferromagnetic maximum).

Figure 4 shows the CPP conductivity $\sigma_{x\text{mm}}$ of the magnetic layer in the Fe/Cu/Fe polycrystalline sandwich versus the grain size d for electrons with oppositely oriented spins (calculation by formulas (4)–(7) and (10)). The value of d varies between 5 nm and 100 μm. As follows from the curves, the scattering probability for the electrons with the spin directed parallel to the magnetization is much higher than for the electrons with the spin directed antiparallel. Note that electron scattering by GB roughness affects the conductivity of the layer until the grain size reaches a spin-orientation-dependent critical value. For the electrons with the spin pointing up (down), $d_c^{\uparrow} \approx 0.5$ μm ($d_c^{\downarrow} \approx 0.03$ μm). As the grain size increases, so does the conductivity, reaching a maximum that is equal to the bulk conductivity of the magnetic material. The values of d_c for electrons with a spin up and down are shown in Fig. 4 by arrows.

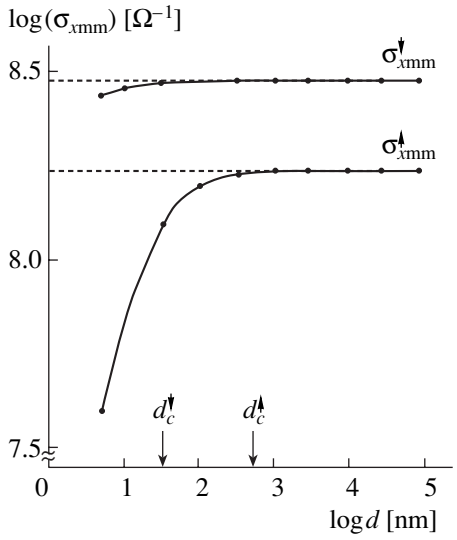

Fig. 4. CPP conductivity of the ferromagnetic layer in the polycrystalline sandwich vs. grain size for electrons with oppositely oriented spins: $\sigma_{x\text{mm}}^{\uparrow}$, the conductivity for electrons with the spin parallel to the magnetization vector; $\sigma_{x\text{mm}}^{\downarrow}$, the conductivity for electrons with the spin antiparallel to the magnetization vector.

SPIN-DEPENDENT SCATTERING OF CONDUCTION ELECTRONS BY GRAIN-BOUNDARY ROUGHNESS WITH REGARD FOR THE FERROMAGNETIC LAYER MORPHOLOGY AND GRAIN-BOUNDARY DIFFUSION LENGTH

Let the ferromagnet–nonmagnetic spacer interface be ideal. Then, the contribution of the spin-dependent electron scattering by this interface to the magnetoresistive ratio of the sandwich may be neglected and we can write for the antiferromagnetic configuration of the sandwich conductivity

$$\sigma_{\text{AF}} = \sigma_{\text{AF}}^{\uparrow} + \sigma_{\text{AF}}^{\downarrow} = \frac{2L}{a/\sigma_1^{\uparrow} + h/\sigma_1^{\uparrow}(1 - \gamma_1^{\uparrow})^2 + b/\sigma_{\text{nm}} + h/\sigma_1^{\downarrow}(1 - \gamma_1^{\downarrow})^2 + a/\sigma_1^{\downarrow}}, \qquad (11)$$

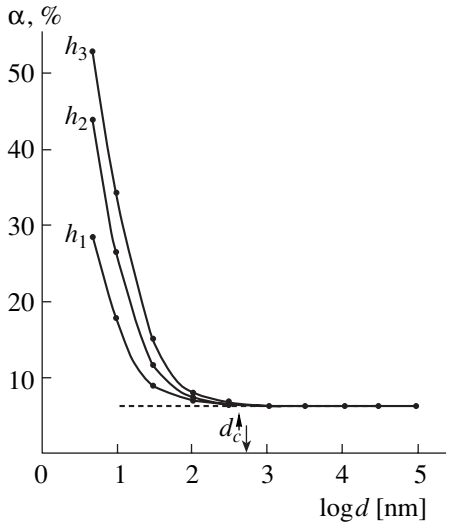

Fig. 5. Contribution of spin-dependent scattering of conduction electrons by GB roughness (continuous curves) and in the bulk of the ferromagnetic grains (dashed line) to the CPP magnetoresistance of the polycrystalline sandwich vs. the dispersity of the layers for the GB diffusion length h_1 = 1 nm, h_2 = 2 nm, and h_3 = 3 nm.

since $\sigma_{AF}^{\uparrow} = \sigma_{AF}^{\downarrow}$. For the ferromagnetic configuration, $\sigma_F^{\uparrow} \neq \sigma_F^{\downarrow}$; therefore,

$$\sigma_F = \sigma_F^{\uparrow} + \sigma_F^{\downarrow} = \frac{L}{2a/\sigma_1^{\uparrow} + 2h/\sigma_1^{\uparrow}(1-\gamma_1^{\uparrow})^2 + b/\sigma_{nm}} + \frac{L}{2a/\sigma_1^{\uparrow} + 2h/\sigma_1^{\downarrow}(1-\gamma_1^{\uparrow})^2 + b/\sigma_{nm}}. \quad (12)$$

The CPP conductivity of the nonmagnetic metal layer, σ_{nm}, is also taken to be roughly equal to its bulk conductivity and may be calculated from formula (4) by substituting the values of the electron parameters (v_{f2}, m_2, and τ_2) into it. The effect of spin-dependent scattering of conduction electrons in the bulk of the grains and due to GB roughness in the ferromagnetic layers on the magnetoresistive ratio of the sandwich is determined by the relationship

$$\alpha = 1 - \frac{\sigma_{AF}}{\sigma_F}. \quad (13)$$

Expressions (11)–(13) make it possible to estimate the effect of spin-dependent electron scattering by GB roughness on the GMR for different values of the morphology parameter of the ferromagnetic layer in the case of the CPP geometry of the polycrystalline sandwich. Figure 5 plots α against the grain size in the ferromagnetic layers of the Fe/Cu/Fe sandwich for three GB diffusion lengths. For subcritical grain sizes ($d_c^{\uparrow} \approx 0.5$ μm), charge carrier diffuse scattering by GB roughness (continuous curves) makes a much greater contribution to the magnetoresistive ratio of the sandwich than scattering in the bulk of the iron grains (dashed line). The latter contribution increases with GB diffusion length. As the grain size grows, scattering by GB roughness becomes less significant and, at $d > d_c^{\uparrow}$, only grain-size-independent scattering in the bulk contributes to α.

It should be noted that the above reasoning is of a qualitative character because of a great number of simplifying assumptions. It is interesting to contrast them with experimental data [11] for the magnetoresistance of Co/Cu/Co three-layer polycrystalline films of grain size less than 5 nm. The films were thermomagnetically processed, i.e., kept for 30 min at a number of temperatures ranging from 20 to 500°C. In this interval, the Co/Cu system is temperature stable [5]; therefore, structure transformations in the films annealed do not cause magnetic degradation.

In the films exhibiting the GMR under transverse charge transfer, the magnetoresistive ratio at T = 20°C was found to be ≈0.7%. As the annealing temperature rises, the ratio increases, reaching a maximum of ≈4% at T = 240°C, and then drops to ≈0.5% (i.e., below the initial value) at T = 380°C. Simultaneously, the grain size increases two- to threefold. It was conjectured [11] that the increase in the GMR is associated with cobalt and copper stratification at the interface. This makes the interface smoother, and copper spacer thickness fluctuations diminish. As a result, the magnetostatic coupling between cobalt layers loosens while the antiferromagnetic coupling strengthens. A further decline in the GMR is related to grain coarsening, which disturbs the continuity of the copper layer and establishes direct exchange coupling between the cobalt layers. However, it is not improbable that electron scattering by GBs in the magnetic layers also affects the behavior of the magnetoresistive ratio in the Co/Cu/Co system. The possible scenario is as follows. As the annealing temperature grows, the length of diffusion of copper atoms into the cobalt layers increases and the role of spin-dependent scattering by GBs in the GMR effect is enhanced. Accordingly, the magnetoresistive ratio of the film rises. Annealing of extra vacancies in the cobalt layers (the process going in parallel with the diffusion) prevents the zone of GB roughness from penetrating deeper into the layers. At the same time, it causes a slight increase in the GMR, raising the flux of spin-polarized electrons toward the interface. As the annealing temperature grows further, the grains start coarsening and the contribution of spin-dependent scattering by GBs to the magnetoresistive ratio of the film eventually drops below the initial value.

CONCLUSIONS

It is shown that, when studying the magnetoresistance of multilayer polycrystalline (especially finely disperse) structures to the current passing normally to

the surfaces of the layers, one should take into account a possible decline in the ferromagnetic layer conductivity and a rise in the magnetoresistive ratio. The latter fact may be associated with spin-dependent electron scattering in ferromagnetic domains adjacent to the nonmagnetic spacer. The scattering mechanism in this case is scattering by GB roughness in the form of nonmagnetic impurity atoms. The effect of this scattering mechanism grows with decreasing grain size in ferromagnetic layers and increasing the length of GB diffusion of nonmagnetic atoms into the grains. Thus, the properties of polycrystalline superlattices can be controlled by varying the fabrication and GB diffusion conditions.

REFERENCES

1. M. N. Baibich, J. M. Broto, A. Fert, *et al.*, Phys. Rev. Lett. **61**, 2472 (1988).
2. A. F. Mayadas and M. Shatzkes, Phys. Rev. B **1**, 1382 (1970).
3. S. M. Klotsman, V. N. Kaĭgorodov, M. I. Kurkin, *et al.*, Fiz. Met. Metalloved. **85** (3), 134 (1998).
4. I. Kaur and W. Gust, *Fundamentals of Grain and Interphase Boundary Diffusion* (Ziegler, Stuttgart, 1988; Mashinostroenie, Moscow, 1991).
5. A. V. Boltushkin, V. M. Fedosyuk, and O. I. Kasyutich, Fiz. Met. Metalloved. **75** (6), 58 (1993).
6. R. Q. Hood and L. M. Falicov, Phys. Rev. B **46**, 8287 (1992).
7. J. Barnas, A. Fuss, R. E. Camley, *et al.*, Phys. Rev. B **42**, 8110 (1990).
8. K. Fuchs, Proc. Cambridge Philos. Soc. **34**, 100 (1938); E. H. Sondheimer, Adv. Phys. **1**, 1 (1952).
9. N. F. Kubrakov, A. K. Zvezdin, K. A. Zvezdin, *et al.*, Zh. Éksp. Teor. Fiz. **114**, 1101 (1998) [JETP **87**, 600 (1998)].
10. S. Zhang and P. M. Levy, J. Appl. Phys. **69**, 4786 (1991).
11. L. A. Chebotkevich, Yu. D. Vorob'ev, I. N. Burkova, *et al.*, Fiz. Met. Metalloved. **89** (3), 56 (2000).

Translated by V. Isaakyan

Technical Physics, Vol. 49, No. 3, 2004, pp. 302–305. Translated from Zhurnal Tekhnicheskoĭ Fiziki, Vol. 74, No. 3, 2004, pp. 20–23.
Original Russian Text Copyright © 2004 by Kiselev, Akashev, Kononenko.

SOLIDS

Effective Electron Mass in Melts of Aluminum, Cerium, and Al–3 at.% Ce Binary System

A. I. Kiselev, L. A. Akashev, and V. I. Kononenko

Institute of Solid-State Chemistry, Ural Division, Russian Academy of Sciences, Pervomaĭskaya ul. 91, Yekaterinburg, 620019 Russia

e-mail: Kononenko@ihim.uran.ru

Received June 2, 2003

Abstract—If the effective mass of an electron is taken into account in the Drude classical equation for light-induced conductivity, the conductivity can be estimated from optical experiment data. © *2004 MAIK "Nauka/Interperiodica".*

INTRODUCTION

From measured values of optical parameters, one may extract valuable information on the electron energy band structure in rare-earth metals, for which the theory and experiment give quantitatively different results for the position of the 4*f* levels [1]. It is conjectured that the effect of magnetic ordering on the optical properties of rare-earth metals in the molten state disappears. One may also assume that secondary magnetization effects due to *s–f* exchange between conduction electrons are suppressed when cerium dissolves in molten aluminum. In REM melts, exchange interaction between conduction electrons and 4*f* electrons causes an extra periodicity in the conduction electron energy with the formation of new gaps in the energy spectrum [1].

The wavelength (λ) dependences of the refractive index *n* and absorption coefficient *k* for pure aluminum and Al–3 at.% Ce alloy are given in [2]. They were spline-approximated into the dependence of the light-induced conductivity on the photon energy with a step of 0.05 eV. The results of approximation are shown in Fig. 1 (curve *1*, pure aluminum; curve *2*, Al–3 at.% Ce alloy).

Miller [3] ellipsometrically measured the optical properties of molten aluminum in the range 0.77–5.0 eV. It was found that the light-induced conductivity maximum at 1.5 eV, which is observed in aluminum crystals, disappears upon melting. The light-induced conductivity spectrum in Fig. 1 does not contain clear-cut absorption bands. It is also seen that the light-induced conductivity spectrum of the alloy is similar to the associated spectrum of cerium melt; namely, it has a sharp peak at a photon energy of 1.2 eV and an extended peak, which starts at a threshold energy of 1.9 eV [4].

At low frequencies, the wavelength dependences of the permittivity and light-induced conductivity σ may be described adequately in terms of the almost-free-electron model. At high frequencies, the quantum character of interaction between electromagnetic radiation and electrons that are in various energy states becomes of crucial importance. Measuring the optical parameters, one visualizes the electron energy spectrum and the density of states within a certain interval in the vicinity of the Fermi level.

OPTICAL CHARACTERISTICS OF ALUMINUM, CERIUM, AND Al–3 at. % Ce ALLOY MELTS IN THE ALMOST-FREE-ELECTRON MODEL

When describing electromagnetic processes in real solids, electrodynamics of continuous media disregards the complex distribution of the charge density and fields over the electron–ion system. The medium is assumed to be electrically quasi-neutral; that is, the mean charge density in it equals zero. Metallic systems of this type are adequately characterized by the almost-free-electron model. Charge transport under the action of an external force is described by the Drude–Zener equations for the real, ε_1, and imaginary, ε_2, parts of the

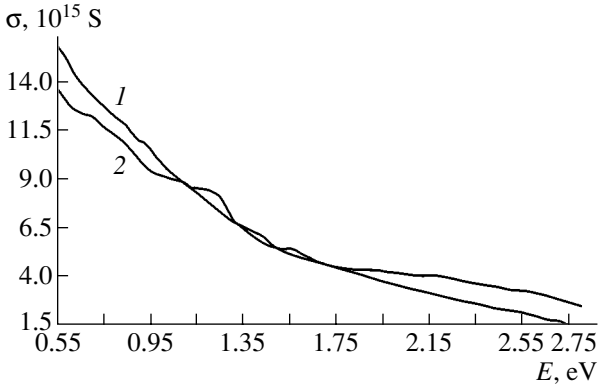

Fig. 1. Light-induced conductivity σ vs. photon energy for molten (*1*) Al and (*2*) Al–3 at. % Ce.

1063-7842/04/4903-0302$26.00 © 2004 MAIK "Nauka/Interperiodica"

Table 1. Plasma oscillation frequency ω_p, resistivity ρ, relaxation frequency ω_0, and effective electron mass m_{eff}

	$\omega_p \times 10^{-16}$, s^{-1}		$\rho \times 10^8$, Ω m	$\omega_0 \times 10^{-15}$, s^{-1}		m_{eff}
Al	2.2130	2.033 [2]	28.53 [5]	1.24	1.58 [2]	1.16
Ce	1.6314	1.6575 [8]	129.0 [9]	3.03	3.6 [8]	1.38
Al–Ce	2.2432	2.023 [2]	34.01 [10]	1.51	2.06 [2]	1.23

permittivity:

$$\varepsilon_1 = 1 - \frac{\omega_p^2}{\omega^2 + \omega_0^2}, \quad (1)$$

$$\varepsilon_2\omega = 4\pi\sigma = \frac{\omega_0\omega_p^2}{\omega^2 + \omega_0^2}, \quad (2)$$

where ω_p is the plasma oscillation frequency and ω_0 is the quantity that numerically equals the inverse relaxation time τ. The plasma frequency in the Drude model is given by

$$\omega_p^2 = 4\pi e^2 N_e/m_e, \quad (3)$$

where e and m_e are the charge and mass of an electron.

The concentration of conduction electrons is $N_e = z/\Omega$, where z is the valence and Ω is the atomic volume.

Table 1 lists the plasma frequencies in Al, Ce, and Al–3 at.% Ce melts that were calculated by Eq. (3). The valence was taken to be equal to three. The atomic volume was found from experimental data for the densities of molten aluminum [5], cerium [6], and Al–Ce alloy [7]. Table 1 also shows the plasma frequencies measured ellipsometrically [2, 8]. The calculated and experimental plasma frequencies for molten cerium are seen to be close to each other. For the aluminum and alloy melts, these values differ by no more than 10%.

In the limit of constant field ($\omega = 0$), the light-induced conductivity σ turns into the static conductivity

$$\sigma(0) = \rho^{-1} = \frac{N_e e^2}{m_e\omega_0}. \quad (4)$$

Table 1 lists the relaxation frequencies calculated by (4) using experimental values of the resistivity from [9, 10]. It also shows the relaxation frequencies determined in [2, 8] under the assumption that the experimental and calculated values of the light-induced conductivity in the IR range are close to each other.

The same result may be obtained by introducing the notion of the effective mass of an electron rather than by varying the relaxation frequency. When passing from the almost-free-electron model to the more realistic model of metal, the electron mass, which is present in explicit form in many equations, is replaced by the effective electron mass. Specifically, Eq. (3) is recast as

$$\omega_p^2 = 4\pi e^2 N_e/m^*, \quad (5)$$

where m^* is the absolute effective mass of an electron.

Subsequently, we will use for simplicity the dimensionless coefficient m_{eff} defined as m^*/m_e (relative effective mass). Designating the plasma frequency in the free electron approximation as ω_{ep}, one can recast Eq. (5) in the form

$$\omega_p^2 = \omega_{ep}^2/m_{eff}.$$

The relaxation frequency in the free electron approximation will be designated as ω_{e0}. With experimental values of the resistivity substituted into Eq. (4), the effective mass is taken into account indirectly; that is, from this equation, the relationship $\omega_{e0} = \omega_0/m_{eff}$ can be derived. It was suggested [11] that the dependence of the relaxation time on the effective electron mass be included in the Drude equation for the light-induced conductivity. Then, the expression for ω_{e0} takes the form $\omega_{e0} = \omega_0/m_{eff}^2$. In this case, we arrive at the Drude equation for the light-induced conductivity that follows from Eq. (2):

$$\sigma = \frac{\omega\varepsilon_2}{4\pi} = \frac{m_{eff}}{4\pi}\frac{\omega_{e0}\omega_{ep}^0}{\omega^2 + m_{eff}^4\omega_{e0}^2}. \quad (6)$$

Expression (1) for the real part of the permittivity is then recast as

$$\varepsilon_1 = 1 - \frac{1}{m_{eff}}\frac{\omega_{ep}^2}{\omega^2 + m_{eff}^2\omega_{e0}^2}. \quad (7)$$

Varying the effective electron mass value, one may bring the experimentally found parts of the permittivity into coincidence with the calculated values in the IR range of the spectrum. The results of such a variation with the effective electron mass taken from Table 1 are shown in Fig. 2. The curves were constructed based on Eq. (7) with the plasma oscillation frequency ω_{ep} coincident with calculated ω_p (Table 1) and ω_{e0} obtained from the relationship $\omega_{e0} = \omega_0/m_{eff}^2$, where the relaxation frequency ω_0 is also obtained by calculation. From Fig. 2, it follows that the experiment and calculation by Eq. (7) coincide in far infrared.

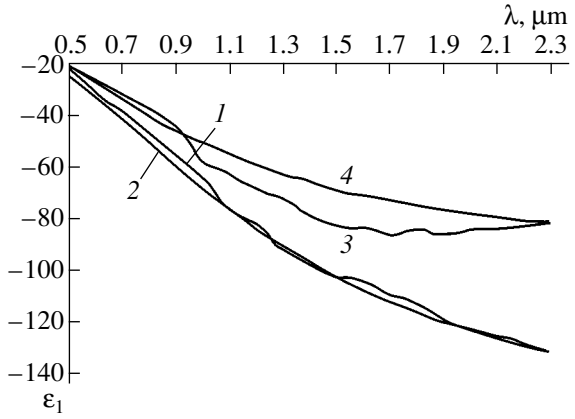

Fig. 2. Experimental wavelength dependences of the real part of the permittivity for (*1*) Al and (*3*) Al–Ce. (*2*, *4*) The same curves for Al and Al–Ce, respectively, calculated by Eq. (7).

ELECTRONIC CHARACTERISTICS OF Al, Ce, AND Al–3 at.% Ce MELTS IN VIEW OF THE EFFECTIVE ELECTRON MASS

Molten cerium intensely absorbs photons in the wavelength interval from 0.5 to 1.7 μm or in the energy interval from 0.7 to 2.5 eV [2]. The deviation of the behavior of the permittivity parts in the visible range from that predicted by the Drude–Zener model is usually explained by induced interband electron transitions. However, prior to determining the electronic parameters of such transitions, it is necessary to separate out the contributions of conduction electrons and electrons participating in these transitions to the optical constants measured.

A relationship between the optical parameters and those used in the electron theory is most clearly demonstrated in the case of the light-induced conductivity σ.

Table 2. Electronic parameters of the conduction electron line and interband transition lines for molten aluminum with $m_{\text{eff}} = 1.132$

j	Δ_j, eV	$\omega_{pj} \times 10^{-15}$, s^{-1}	$\omega_{0j} \times 10^{-15}$, s^{-1}	z_j
0	0	15.485	0.559	1.740
1	0.441	8.334	0.200	0.504
2	0.556	1.518	0.022	0.017
3	0.762	6.563	0.186	0.313
4	0.935	2.485	0.068	0.045
5	1.125	3.594	0.100	0.094
6	1.364	3.031	0.118	0.067
7	1.583	2.328	0.064	0.039
8	1.768	2.213	0.068	0.035
9	1.962	1.871	0.058	0.025
10	2.157	1.118	0.020	0.009

The contributions responsible for the experimental dependence of the light-induced conductivity on the photon energy [12] are those from conduction electrons and electrons participating in interband transitions:

$$\sigma(\omega) = \sum_{j=0}^{N} \sigma_j(\omega), \tag{8}$$

where N is the total number of interband transition lines (the subscript $j = 0$ refers to the line of conduction electrons; $j = 1, \ldots, N$ refer to interband transition lines).

The problem of finding the partial additive functions was solved graphically [4] by appropriately selecting three parameters: the plasma oscillation frequency ω_{pj} (an analogue of the peak height), the position ω_j of the peak (where the interband transition gap is $\Delta_j = \hbar\omega_j$), and the relaxation frequency ω_{0j} (an analogue of the peak width). Nine contributions will suffice to fit the experimental curve for the light-induced conductivity of molten cerium [4].

In [4], based on the rule of sum, we derived a relationship for the partial numbers of electrons per atom, z_j, that make a contribution to the light-induced conductivity:

$$z_j = z\omega_{pj}^2/\omega_p^2. \tag{9}$$

In terms of the effective electron mass, the equation for the contributions of electrons participating in interband transitions to the light-induced conductivity [4] can be written in the form

$$\sigma_j(\omega) = \frac{m_{\text{eff}}}{4\pi}\frac{\omega^2\omega_j\omega_{e0j}\omega_{epj}^2}{(\omega^2 + m_{\text{eff}}^4\omega_{e0j}^2)^2} \times\left(\frac{\omega^2 - m_{\text{eff}}^4\omega_{e0j}^2}{A_jB_j} - \frac{2B_j}{A_j} + \frac{2}{\omega_j}\right), \tag{10}$$

where ω_j is the position of a jth interband transition on the curve $\sigma(\omega)$,

$$A_j = \sqrt{\gamma_j^4 + 4\omega^2 m_{\text{eff}}^4\omega_{e0j}^2},$$

$$B_j = \sqrt{(A_j + \gamma_j^2)/2}$$

and

$$\gamma_j^2 = \omega_j^2 - \omega^2 + m_{\text{eff}}^4\omega_{e0j}^2.$$

A most stringent criterion of validity for the optical properties of metals is the coincidence of light-induced conductivity (8) with the static conductivity in the limit $\omega \longrightarrow 0$. Using Eq. (4), one can represent this test as

$$\left.\frac{\sigma(\omega)}{\sigma(0)}\right|_{\omega\to 0} = \frac{z_0\omega_0}{zm_{\text{eff}}^2\omega_{e00}}. \tag{11}$$

Here, z_0 obtained from (9) serves as the effective valence, i.e., stands for the number of electrons providing the static conductivity in a molten metal.

Table 3. Electronic parameters of the conduction electron line and interband transition lines for molten cerium with $m_{\text{eff}} = 1.336$

j	Δ_j, eV	$\omega_{pj} \times 10^{-15}$, s^{-1}	$\omega_{0j} \times 10^{-15}$, s^{-1}	z_j
0	0	12.661	0.991	1.750
1	0.522	3.071	0.085	0.103
2	0.902	8.292	0.305	0.751
3	1.167	4.245	0.100	0.197
4	1.660	6.227	0.245	0.423
5	1.696	6.705	0.283	0.491
6	1.743	7.687	0.374	0.645
7	2.046	4.200	0.164	0.193
8	2.340	4.163	0.114	0.189
9	2.732	3.966	0.120	0.172
10	2.925	2.624	0.133	0.075
11	2.938	3.444	0.150	0.129

Table 4. Electronic parameters of the conduction electron line and interband transition lines for molten Al–3 at.% Ce alloy with $m_{\text{eff}} = 1.206$

j	Δ_j, eV	$\omega_{pj} \times 10^{-15}$, s^{-1}	$\omega_{0j} \times 10^{-15}$, s^{-1}	z_j
0	0	14.648	0.544	1.557
1	0.389	6.422	0.075	0.299
2	0.667	8.395	0.191	0.511
3	0.833	2.195	0.064	0.035
4	1.039	4.500	0.092	0.147
5	1.185	3.993	0.059	0.116
6	1.512	1.320	0.020	0.013
7	1.639	2.046	0.076	0.030
8	1.884	4.632	0.166	0.156
9	2.166	4.891	0.183	0.174
10	2.437	2.304	0.097	0.038
11	2.562	1.409	0.034	0.014

Tables 2–4 list the electronic parameters of the melts of aluminum, cerium, and the alloy that were determined by varying m_{eff} with a minimal step of 0.001 provided that the right of (11) deviated from unity by no more that 1%. The effective masses thus obtained, though being somewhat smaller than those listed in Table 1, are in fairly good agreement with them.

At the same time, the concentration dependence of the effective mass in the binary metallic alloy differs substantially from the additive dependence. This fact suggests that the electron energy band structure is modified significantly upon alloying. From Tables 2 and 4, it follows that the alloy exhibits all interband transitions typical of pure aluminum. However, the energy gap for most of the transitions in the alloy exceeds that in the metals by about 0.1 eV. At high photon energies, the optical properties of the alloy exhibit energy transitions characteristic of cerium.

CONCLUSIONS

(1) If the effective mass of an electron is taken into account in the Drude classical equation for light-induced conductivity, the conductivity can be estimated from optical experiment data. Tentatively, the effective electron mass can be estimated from the experimental wavelength dependence of the real part of the permittivity.

(2) The effective mass varies with component concentration in the Al–3 at.% Ce alloy nonadditively.

ACKNOWLEDGMENTS

This work was supported by the Russian Foundation for Basic Research (project no. 02-02-17579).

REFERENCES

1. M. M. Noskov, *Electronic Structure and Physical Properties of Rare-Earth Metals and Actinides* (Ural. Nauch. Tsentr Akad. Nauk SSSR, Sverdlovsk, 1981), pp. 3–22.
2. L. A. Akashev and V. I. Kononenko, Teplofiz. Vys. Temp. **39**, 412 (2001).
3. J. C. Miller, Philos. Mag. **20**, 1115 (1969).
4. A. I. Kiselev, V. I. Kononenko, and L. A. Akashev, Teplofiz. Vys. Temp. **40**, 50 (2002).
5. V. E. Zinov'ev, *Thermophysical Properties of Metals at High Temperatures: A Handbook* (Metallurgiya, Moscow, 1989).
6. V. I. Kononenko, A. L. Sukhman, S. L. Gruverman, and V. V. Torokin, Phys. Status Solidi A **84**, 423 (1984).
7. E. V. Semenov, Candidate's Dissertation (Inst. Khim., Ural. Otd. Akad. Nauk SSSR, Sverdlovsk, 1984).
8. L. A. Akashev and V. I. Kononenko, Rasplavy, No. 5, 115 (1991).
9. H.-J. Guntherodt, E. Hauser, and H. U. Kunzi, in *Proceedings of the 3rd International Conference on Liquid Metals* (Metallurgiya, Moscow, 1980), pp. 176–239.
10. S. V. Golubev and V. I. Kononenko, Rasplavy, No. 5, 35 (1988).
11. E. Faber, in *Electrons*, Vol. 1: *The Physics of Metals*, Ed. by J. Ziman (Cambridge Univ. Press, Cambridge, 1969; Mir, Moscow, 1972).
12. G. P. Motulevich, Tr. Fiz. Inst. Akad. Nauk SSSR **55**, 3 (1971).

Translated by V. Isaakyan

Technical Physics, Vol. 49, No. 3, 2004, pp. 306–309. Translated from Zhurnal Tekhnicheskoĭ Fiziki, Vol. 74, No. 3, 2004, pp. 24–27.
Original Russian Text Copyright © 2004 by Antonets, Kotov, Nekipelov, Golubev.

SOLID-STATE ELECTRONICS

Nanostructure and Conductivity of Thin Metal Films

I. V. Antonets*, L. N. Kotov*, S. V. Nekipelov*, and Ye. A. Golubev**

** Syktyvkar State University, Syktyvkar, 167001 Russia*

e-mail: kotov@syktsu.ru

*** Institute of Geology, Komi Scientific Center, Ural Division, Russian Academy of Sciences, Syktyvkar, 167982 Russia*

Received April 15, 2003

Abstract—Amorphous silver, copper, gold, and iron films of a thickness between 6 and 350 nm are grown on polymeric substrates by vacuum evaporation. The nanostructure of the films is investigated. The dependence of the conductivity on the film thickness is obtained, and a correlation between the surface morphology and the conductivity is established. © *2004 MAIK "Nauka/Interperiodica".*

INTRODUCTION

The recent advancements in micro- and optoelectronics, as well as in optics and a number of other fields, are closely associated with the progress in thin-film processes [1–4]. Current technology places stringent requirements on the film quality and on the effective use of their specific properties [2–4]. The structure, conductivity, surface condition, and stability of the material properties [1–7], all are responsible for the quality of the films.

Today's explosive development of nanotechnologies stimulates interest in films whose thickness is several tens of nanometers or even several nanometers. In addition, the amorphous state of materials has attracted much attention in recent years [7–10]. The electrical parameters of amorphous films (such as the conductivity) are usually much lower than those of crystalline films. This is because the concentration and mean free path of free electrons in the former drop due to scattering by defects [8, 11, 12]. At the same time, the conductivity is the basic parameter governing the electrodynamic properties of the films.

At present, thin films are used in many fields of the industry, in particular, in optics (antireflection coatings and multilayer interference systems), in microelectronics (active and passive film elements), and in spaceborne instrument making (surface films for controlling the temperature of satellites) [2, 4, 7].

The aim of this work is to investigate the surface of thin amorphous metal films (Ag, Cu, Au, and Fe) and to find a correlation between the structure and conductivity of the films.

PROPERTIES OF TEST FILMS

We investigated silver, gold, copper, and iron films produced by vacuum evaporation. The films were deposited on polymeric substrates at room temperature under pressure of about 10^{-5} Torr with a rate of 10 nm/s. Such a high deposition rate provides growth of pure metal films with a minor amount of impurities under a medium vacuum and is commonly used in the industrial production of thin-film materials. The film thicknesses ranged from 6 to 350 nm.

The examination of the films by X-ray diffraction showed that diffraction reflections typical of the crystalline state are completely absent. Hence, one can conclude that the films are amorphous in terms of X-ray diffraction. With regard to the method of growing polycrystalline films [13], the reasons for the amorphous state of our films may be rapid condensation, a polymeric substrate, or low substrate temperature (T = 300 K). As a substrate, we used a 0.5-mm-thick polymeric X-ray film.

EXPERIMENTAL

(i) Surface morphology. The surface morphology of the film was examined with an ARIS-3500 atomic force microscope (AFM) with a maximal scan area of 70 × 70 μm (Burleigh Instrument Co, USA). As a probe, we used a standard pyramidal silicon cantilever (Burleigh) with a radius of curvature of the tip of ≈10 nm and a stiffness of 0.1 N/m. The microscope produces three-dimensional topographic images of solid surfaces with a lateral resolution comparable to that of a scanning electron microscope. In addition, since an AFM offers a higher sensitivity in the vertical direction, one can visualize finer morphological features of solids uniform in composition. Surface imaging was carried out under normal conditions both at a constant probe–substrate spacing and at a constant probe–substrate interaction force in the contact mode (the force was roughly equal to 10^{-9} N). Prior to investigation, the films were rinsed in alcohol. Special chemical methods making it possible to reveal the finer structure were not employed. To take accurate measurements in the *XY*

1063-7842/04/4903-0306$26.00 © 2004 MAIK "Nauka/Interperiodica"

plane and in the vertical direction, we calibrated the scales of the images using certified test samples.

(ii) Thickness and conductivity of the films. To monitor the film thickness during deposition, we used a calibrator based on a quartz resonator. The material evaporated was simultaneously deposited on the substrate and on the faces of the quartz crystal, which was inserted in the high-frequency oscillatory circuit of an oscillator. The application of an ac electric field generates resonant vibrations across the quartz plate. As the weight of the film increases, the resonant frequency of the oscillator shifts by a value of Δf, which is related to the film thickness (provided that the film thickness is no more than 1% of the thickness of the quartz plate) by the relationship $d = B\Delta f/\rho$, where ρ is the density of the film and B is a constant. Down to a film thickness on the order of several hundred nanometers, the relationship between the frequency shift and the film thickness is linear with an accuracy of 1% or higher. The quartz calibrator was graduated by simultaneously depositing copper from a Mo boat on the calibrator and aluminum foil. The copper layer deposited on the foil was weighed using a VLR-200 precision analytical balance (the accuracy is no worse than 0.05 mg), and the frequency shift was found from the frequency difference before and after deposition. The graduation of the calibrator and the experiments were performed under the same conditions. Knowing the frequency shift Δf and having the calibration curve at hand, we determined the surface density of the thin film. Under the assumption that the surface and bulk densities differ insignificantly, the thickness of the film was calculated.

The conductivity of the films was measured with a setup consisting of a B5-43 dc power supply, Ch3-57 digital frequency meter, Shch-34 digital ohmmeter, and a detector with the quartz calibrator. The detector was level with the substrate in the vacuum chamber. In this experiment, the substrate was made of textolite and had silver-plated contacts at its ends. In the course of the experiment, the resistance of the film was measured after each deposition. Knowing the geometrical sizes and resistance of the thin film, one can find its conductivity.

RESULTS AND DISCUSSION

The basic results of our experiments are illustrated in Figs. 1–3. Figure 1 shows typical surface images of silver, copper, gold, and iron films 63, 120, 74, and 130 nm in thickness, respectively.

As can be seen from Fig. 1, the morphology of the metal films is irregular and consists of clusters (blocks). The apparent sizes of the clusters correlate, in general, with the thickness of the films, and the clusters have a nonisometric rounded shape. Facets are not seen. However, when closely packed, the clusters may take on the shape of polyhedrons. Sporadically, one can observe individual crystal-like faceted objects.

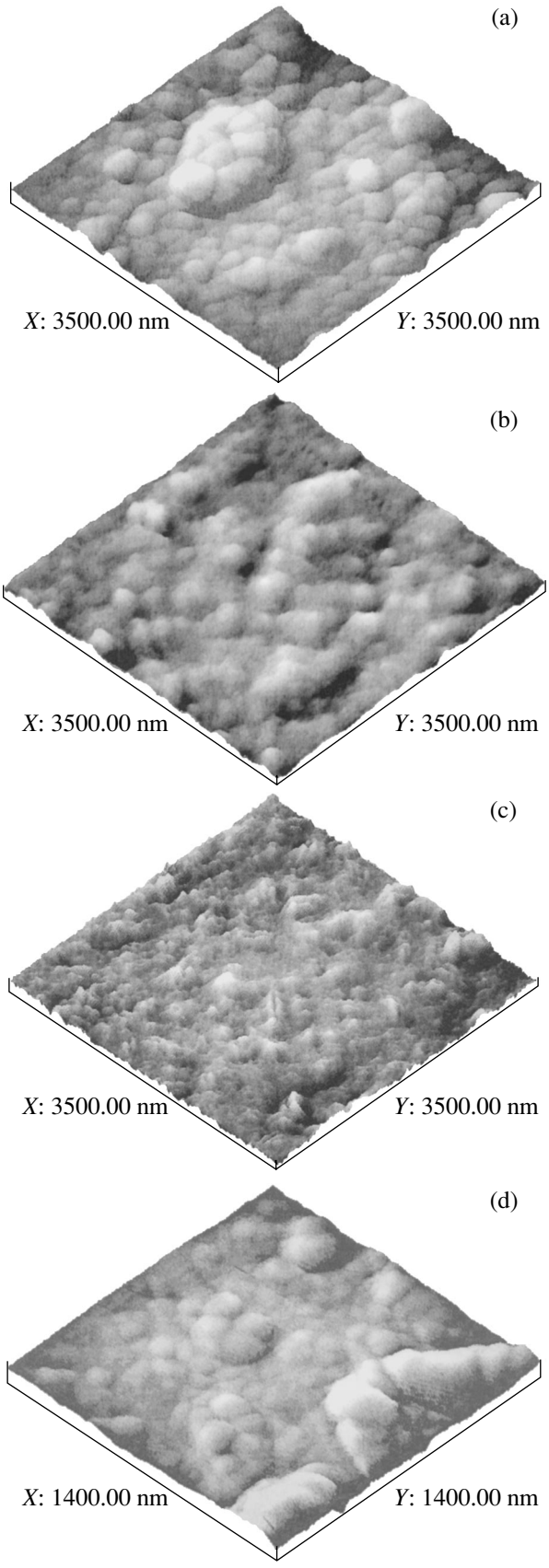

Fig. 1. AFM images of the film surfaces: (a) silver, (b) copper, (c) gold, and (d) iron.

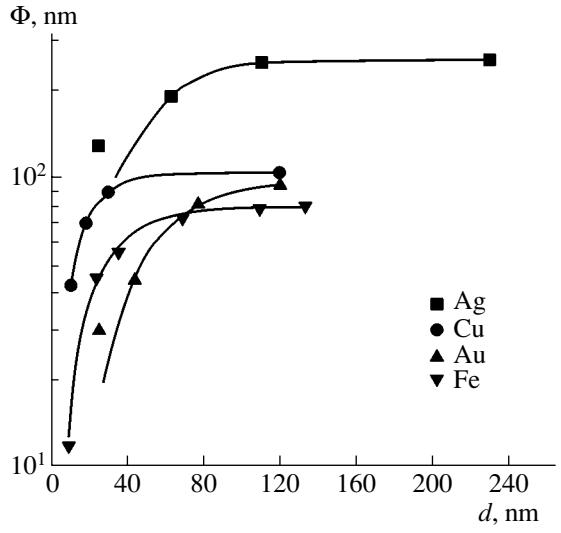

Fig. 2. Mean cluster size vs. the film thickness.

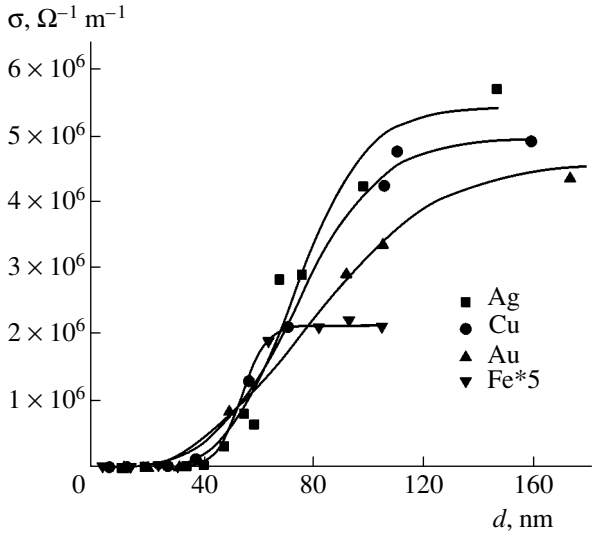

Fig. 3. Conductivity vs. the film thickness.

The cluster structure of the iron and silver films is distinctly visualized, and individual clusters are well resolved (the films appear fractured). The statistical straggling of the sizes is relatively small. Some of these films exhibit regions consisting of rodlike structures formed by cluster chains. The length of these structures reaches several hundred nanometers, and they are frequently orderly oriented.

On the gold films, the clusters are also well resolved but have the most irregular shape. Therefore, because of a high statistical straggling, the apparent sizes of clusters in the gold films are more difficult to analyze than in the other films. On these films, the clusters sometimes merge into curved fibers.

The morphology of the copper films on the AFM images is fairly smooth: blocks are observed only under high magnification. The clusters tend to merge, producing islands or hills with diffuse boundaries in between, in contrast to the other films.

On the surfaces of the silver, gold, and iron films, there are many macroislands (drops) formed during deposition. They are up to several micrometers in size and also consist of rounded clusters. On the copper films, such islands were not observed.

Our data indicate that the majority of the clusters in the silver and copper films are much larger than those in the other films, their thicknesses being equal.

It was also found that the size of the clusters depends considerably on the film thickness. In Fig. 2, the cluster mean size Φ is plotted against the thickness of the films. As the thickness grows, so does the size of the cluster. For copper and iron films less than 40 nm thick, the growth is nearly linear and the lateral size of a cluster exceeds the film thickness by a factor of 1.5–2. However, from thicknesses of about 40–50 nm on, the growth of the clusters slows and virtually stops at 100–120 nm. Such behavior pertains equally to the copper and iron films, but the size of copper clusters invariably exceeds iron ones by 30–50%.

For the silver films, a significant growth of the clusters (from 130 to 250 nm) is observed up to thicknesses of 100–120 nm. Above 120 nm, the growth of the copper and iron clusters ceases. For thicker silver films, the cluster size is virtually independent of the film thickness and roughly equals 250 nm, which exceeds the mean size of copper and iron clusters by a factor of 2.5 and 4, respectively (for identical thicknesses).

Figure 3 shows the conductivity versus the metal film thickness (for the iron films, the values of the conductivity are increased fivefold). The data points are approximated by the Boltzmann function. From Fig. 3, it follows that the conductivity depends on the thickness only slightly when the films are less than 40 nm thick. It is likely that, for thicknesses below 40 nm, the films have an island structure [13–15]. A thin film represents a system of conducting domains (islands) separated by nonconducting (or low-conductivity) regions; hence, the conductivity is very low. As the film thickens and the conducting domains merge together, the conductivity sharply rises (the percolation effect). Experimentally, one observes a sharp dependence of the conductivity on the film thickness in this case (the range 40–120 nm for the Ag, Cu, and Au films and the range 40–70 nm for the Fe films). As the film grows, the dependence $\sigma(d)$ becomes weaker. In the ranges $d >$ 70 nm for the iron films and $d >$ 120 nm for the others, the conductivity is close to the maximal value.

Note that the maximal conductivity of the films differs considerably (almost by one order of magnitude) from the bulk value. The amorphism of the films may decrease significantly their conductivity as compared with the crystalline state. This is because free electrons are pinned at cluster boundaries [16] or scattered by

defects [8, 11, 12]. Typically, the conductivity of amorphous metal alloys is on the order of $10^6\ \Omega^{-1}\ m^{-1}$ [8], which also follows from Fig. 3 (in our case, σ ranges from 4×10^6 to $6 \times 10^6\ \Omega^{-1}\ m^{-1}$ for the gold, copper, and silver films, and reaches $5 \times 10^5\ \Omega^{-1}\ m^{-1}$ for the iron films).

Indeed, to obtain the amorphous state of pure metals (for example, iron) is generally a challenge, whereas a medium working vacuum (10^{-4}–10^{-5} Torr, exactly as in this study) simplifies the problem [8]. In contaminated metals, the conductivity may be even lower. The foregoing reasoning to some extent explains such a low conductivity in our experiments. However, a particular mechanism of this phenomenon calls for special investigation.

CONCLUSIONS

Amorphous silver, copper, gold, and iron films from 6 to 350 nm in thickness are grown on polymer substrates at room temperature by evaporation under a medium vacuum. The films have a cluster structure. The dependence of the conductivity of the films on their thickness and, as a consequence, on the cluster size is found. For very thin (as yet discontinuous) films of thickness less than 40 nm, this dependence is insignificant. Reasons for the low conductivity of the films in comparison with the bulk crystals are analyzed. It is shown that a small thickness and the cluster structure of the films may be partially responsible for the above effects when the films are thinner than 40 nm, while for thicker films these factors do not work. The amorphism of the films may to some extent explain the low conductivity of the films, but the detailed mechanism behind this phenomenon needs refinement.

REFERENCES

1. F. Abeles, in *Physics of Thin Films*, Ed. by G. Hass and R. E. Thun (Academic, New York, 1971; Mir, Moscow, 1973), Vol. 6.
2. *Physics of Thin Films*, Ed. by G. Hass and R. E. Thun (Academic, New York, 1963; Mir, Moscow, 1967), Vol. 1.
3. L. I. Maissel and R. Glang, *Handbook of Thin Film Technology* (McGraw-Hill, New York, 1970; Sov. Radio, Moscow, 1977).
4. M. I. Elinson, Radiotekh. Élektron. (Moscow), No. 1, 3 (1968).
5. A. V. Sokolov, *Optical Properties of Metals* (Fizmatlit, Moscow, 1961).
6. R. F. Soohoo, *Magnetic Thin Films* (Harper and Row, London, 1965; Mir, Moscow, 1967).
7. H. J. Güntherodt and H. Beck, *Glassy Metals* (Springer-Verlag, Berlin, 1981; Mir, Moscow, 1983).
8. J. M. Ziman, *Models of Disorder: The Theoretical Physics of Homogeneously Disordered Systems* (Cambridge Univ. Press, Cambridge, 1979; Mir, Moscow, 1982).
9. V. A. Polukhin and N. A. Vatolin, *Simulation of Amorphous Metals* (Nauka, Moscow, 1985).
10. A. S. Andreenko and S. A. Nikitin, Usp. Fiz. Nauk **167**, 605 (1997) [Phys. Usp. **40**, 581 (1997)].
11. G. Marchal, P. Mangin, and C. Janot, Thin Solid Films **23**, 17 (1974).
12. R. Hasegava, Phys. Rev. Lett. **28**, 1376 (1972).
13. H.-D. Liu, Y.-P. Zhao, G. Ramanath, *et al.*, Thin Solid Films **384**, 151 (2001).
14. A. K. Sarychev, D. J. Bergman, and Y. Yagil, Phys. Rev. B **51**, 5366 (1995).
15. R. Levy-Nathansohn and D. J. Bergman, Phys. Rev. B **55**, 5425 (1997).
16. G. I. Frolov, V. S. Zhigalov, A. I. Pol'skiĭ, and V. G. Pozdnyakov, Fiz. Tverd. Tela (St. Petersburg) **38**, 1208 (1996) [Phys. Solid State **38**, 668 (1996)].

Translated by Yu. Vishnyakov

Technical Physics, Vol. 49, No. 3, 2004, pp. 310–317. Translated from Zhurnal Tekhnicheskoĭ Fiziki, Vol. 74, No. 3, 2004, pp. 28–36.
Original Russian Text Copyright © 2004 by Bespalov, Vorontsov, Gorbatsevich, Egorkin, Zhigal'skiĭ, Il'ichev, Kulakov, Nalbandov, Pantuev, Rasputnyĭ, Sveshnikov, Shmelev.

SOLID-STATE ELECTRONICS

Electrophysical Properties of GaAs Layers and the Characteristics of Fast Particle GaAs Detectors

V. A. Bespalov*, A. V. Vorontsov, A. A. Gorbatsevich*, V. I. Egorkin*, G. P. Zhigal'skiĭ*, É. A. Il'ichev***, A. V. Kulakov*, B. G. Nalbandov*, V. S. Pantuev*, V. N. Rasputnyĭ*, Yu. N. Sveshnikov**, and S. S. Shmelev***

** Moscow State Institute of Electronic Technology (Technical University), Zelenograd, Moscow, 124498 Russia*

*** Joint-Stock Venture Élma-Malakhit, Zelenograd, Moscow, 124460 Russia*

**** State Unitary Enterprise Lukin Research Institute of Physical Problems, Zelenograd, Moscow, 124460 Russia*

e-mail: edward@qdn.miee.ru

Received April 16, 2003; in final form, August 11, 2003

Abstract—Results of complex experiments aimed at finding a relationship between the properties of initial GaAs single-crystal wafers and epitaxial films and the threshold spectrometric characteristics of ionizing radiation detectors are reported. © *2004 MAIK "Nauka/Interperiodica".*

INTRODUCTION

The present-day market of fast-particle and gamma-radiation solid-state detectors is dominated by high-resistivity silicon devices [1, 2]. Yet, extensive research for alternative materials that are capable of effectively withstanding severe temperature and radiation conditions for a long time is being carried out. Among those holding the attention of researchers, such as high-purity Ge, PbSeEu, carbon (diamond), and GaAs [2–6], diamond offers the highest radiation resistance [2]. However, because of the small charge number of carbon ($Z = 6$), diamond detectors are bound to be surpassed in efficiency of converting the energy of gamma quanta to the generation of electron–hole pairs by the others. Conversely, high-purity Ge ($Z = 32$) detectors, as well as detectors based on PbSeEu solid solutions ($Z \approx 55$), are extremely attractive because of a higher charge number and, hence, gamma absorption coefficient. However, the application of pure germanium and lead-based solid solutions is greatly limited by their narrow energy gap and difficulties in creating good *p–n* junctions (which have low leakage currents, a high dielectric strength, and high operating temperatures). Thus, each of the materials mentioned may compete with silicon only in narrow niches of ionizing radiation detection.

Of the materials listed above gallium arsenide is today the most technologically developed. Until recently, the high radiation hardness of this material has been considered as its basic advantage. However, detailed analysis of using GaAs in gamma-radiation and fast-particle detectors has shown that high radiation hardness by no means exhausts the list of points in its favor. Below, we give theoretical and experimental estimates convincingly demonstrating that the noise parameters and conversion efficiency of GaAs detectors are as good as those of high-resistivity silicon detectors. Moreover, at temperatures between 40 and 50°C, the former significantly outperform their silicon counterparts for ionizing radiation detection.

ANALYSIS

Detection of fast particles and gamma radiation by solid-state detectors is based on determining the energy loss of a particle (quantum) when it passes through the material. In detecting particles with energies ranging from 10 keV to 10 MeV, the first-order effect is ionization, which generates electron–hole pairs (see, e.g., [7]). This is also true for X-ray gamma quanta, since most of their energy is spent on the generation of nonequilibrium electron–hole pairs [8].

Therefore, when detecting particles with energies from this range and also soft X-ray radiation, one effectively detects the current of nonequilibrium charge carries, which appears as a result of ionization losses.

Comparing the process of interaction between fast particles and the material of solid-state detectors, we draw the reader's attention to the following experimental observations. (i) The ionization efficiency in GaAs exceeds that in silicon by a factor of 1.5 [9, 10]; (ii) the absorption coefficient for the gamma radiation energy may be approximately expressed as $\gamma \approx cZ^4\lambda^3$ (λ is the wavelength, Z is the charge number of the matrix, and c is the speed of light), and the scattering coefficient is $\sigma \approx (8\pi/3)q^4Z/m^2c^4$ (m is the atomic mass of the matrix) [7, 8]; (iii) the radiation hardness of GaAs ICs far exceeds that of silicon ICs [11–13]; and (iv) the upper limit of the critical power for GaAs ICs is much higher than that for silicon ICs [14]. Note also that, for microparticles, the absorption coefficient is proportional to

the charge number and the number of pairs of nonequilibrium carriers arising in a solid is proportional to the ratio of the particle energy to the mean energy of pair generation, as follows from many experiments (these energies are almost the same in silicon and gallium arsenide).

Accordingly, in the energy range mentioned above, the efficiency of energy conversion to the generation of nonequilibrium electron–hole pairs per unit thickness of the layer in GaAs is expected to be higher than in Si by a factor of $(Z_{GaAs}/Z_{Si})^4$ for gamma radiation and by a factor of (Z_{GaAs}/Z_{Si}) for microparticles, where $Z_{Si} = 14$ and $Z_{GaAs} = 32$. Since the vast majority of δ electrons have an energy that is sufficient for the generation of gamma quanta from the X-ray range and the cross section of this process is fairly high, one may anticipate the following sequence: microparticles give rise to gamma quanta and the gamma quanta generate electron–hole pairs. Therefore, it may be anticipated with a high probability that the conversion efficiency ratio for microparticles will equal to $(Z_{GaAs}/Z_{Si})^\beta$, where $\beta > 1$.

The detector efficiency η depends not only on the microparticle (quantum)-to-nonequilibrium pair conversion efficiency but also to a great extent on the ratios of the lifetimes of the nonequilibrium carriers to their transit times: $\eta \sim \tau_n/t_n^* + \tau_p/t_p^*$, where $t_{p,n}^* = L^2/V\mu_{p,n}$ are the times the carries take to transit the gap L between the detector contacts, V is the voltage between the contacts, $\mu_{p,n}$ are the carrier mobilities, and $\tau_{n,p}$ are the lifetimes of the carriers in bands of nonlocalized states. Thus, not the lifetimes as such (in GaAs, they are three to four orders of magnitude lower than in pure Si) but the lifetime to the transit time ratios are of primary importance.

The power dependence of the absorption coefficient on the serial number of an element ($\gamma \sim Z^\beta$, where $\beta > 1$) allows the designers of the GaAs detectors to employ active layers that are much thinner than in the Si devices (by a factor of $(Z_{GaAs}/Z_{Si})^4$ for X-ray radiation) and, hence, cut the transit time of the nonequilibrium carriers in comparison with the Si devices (by a factor of $(Z_{GaAs}/Z_{Si})^8\mu_{GaAs}/\mu_{Si}$, i.e., by more than 10^3 times), with the efficiency of absorbing ionizing radiations being the same. It is hoped that the great difference in the charge number will totally compensate a loss in photoelectric amplification in the GaAs detectors, where the carrier lifetimes in bands of nonlocalized states are shorter than in the silicon devices.

The photoelectric amplification η of the detector must be high and stable. Instability may be due to radiation-induced defects, which cause charge losses and, hence, change the kinetic parameters ($\mu_{p,n}$ and $\tau_{n,p}$) in the active area of the device. As a result, the photoelectric efficiency drops (the device degrades under operation). GaAs ICs far outperform their Si counterparts in radiation hardness [15, 16]; therefore, with the detection efficiency of GaAs and Si detectors being the same, the former material seems more promising for fast particle detectors.

The potentialities of GaAs are extended still further in view of its wide energy gap, which allows for operation under high temperatures and high radiation doses (in nuclear reactors, high-energy accelerators, or in geology under logging conditions).

EXPERIMENTAL RESULTS

Below, we perform a comparative analysis of the devices based on compensated GaAs crystals, pure GaAs epitaxial films, and high-resistivity silicon by example of detecting fast α particles. The detectors measure the current of nonequilibrium carriers generated by the ionizing radiation flux. The vertical designs of both barrier- (metal–semiconductor junction or *p–n* junction) and resistive-type GaAs detectors were used. The barrier-type detectors were made on variously doped epitaxial layers (Table 1) grown by the chloride CVD method on *n*-GaAs substrates doped to degeneracy. The resistive-type devices were made on commercial semi-insulating GaAs wafers (compensated by EL2 defects or deep-seated chromium- and chromium-

Table 1. Electrophysical parameters of the detectors

Types of detectors	Electrophysical parameters of detecting layers					
	N_n, cm^{-3}	d, μm	μ, cm^2/(V s)	Deep trap parameters		
				E_t	S_t	fN_t
Type I: *M*–n^-GaAs–n^+GaAs	3×10^{13}	29	4400	0.23*D*	2×10^{-17}	10^{13}
Type II: *M*–p^+GaAs–n^-GaAs	10^{13}	29	4400	0.23*D*	2×10^{-17}	10^{13}
Type III: *M*–n^-GaAs–n^+GaAs–	3×10^{14}	29	3900	0.6*D*	5×10^{-13}	5×10^{13}
Type IV: *M*–*i*GaAs–*M*(Cr–CrO)	7×10^6	≈150	4300	0.48*D*	2×10^{-14}	7×10^{14}
Type V: *M*–*i*GaAs–*M*(EL2)	10^7	≈150	5000	0.78		10^{15}

Note: N_n (cm^{-3}) is the electron concentration in the pure layer; d (μm) is the thickness of the pure layer; μ (cm^2/(V s)) is the electron mobility in the pure layer; E_t (eV), S_t (cm^2), f and N_t (cm^{-3}) are, respectively, the initial energy level, capture cross section, fill factor, and concentration of traps in the pure layer; *D* is the deep donor; and *M* is a metal.

Table 2. Operating parameters of the detectors

Detector type	Electrophysical parameters					
	SPD, V^2/Hz		Optimal operating conditions			
	20 Hz	1330 Hz	U, V	I_l, nA	R, keV	S, keV
I	4.6×10^{-12}	8.36×10^{-16}	–22	<15	35	18.7
II	3.33×10^{-11}	2.38×10^{-15}	–30	45	15.1	8.3
III	6.27×10^{-11}	1.6×10^{-14}	–30	6–7	141	9.1
IV	–	–	–50	90	287	–
V	$>10^{-8}$	3.56×10^{-9}	–70	140	40	–

Note: U is the depletion-mode voltage, I_l is the leakage current of a detector cell, R is the energy resolution, and S is the energy equivalent of noise. Alpha source: type 1, E = 5.147 MeV and E = 5.499 MeV; type 2, E = 5.499 MeV and E = 5.456 MeV.

oxide-related energy centers) by the membrane technology: a 500 μm-thick platelet measuring 6 × 8 mm was thinned (down to 100 μm) in its 5 × 5-mm central part on the back side, and an Au/Ge/Ni ohmic contact to the back side and a 4 × 4-mm Au/V contact to the front side of the platelet in its central part were made.

The electrophysical properties of the detector materials are listed in Table 1. The kinetic coefficients, which govern the lifetimes, transit times, and dark currents of nonequilibrium carriers, were determined by Hall measurements (in the van der Pauw configuration) and relaxation measurements (with the contactless nondestructive method of deep-level optoelectronic relaxation spectroscopy [17, 18]). By taking C–V curves, we found the depletion width of the device's active areas as a function of the reverse bias voltage. From the field and temperature dependences of the current through the detector cells, we established that the current is limited by the volume of the detecting layer. Typical energies of activation and dark currents through the cells were experimentally determined in the 15–150°C temperature range. With these parameters at hand, we can predict the behavior of the cells at temperatures above 150°C. The electrophysical parameters thus measured were used to select the optimal power supply conditions (see Table 2) and analyze the operation of the detectors in the spectrometric mode. For the optimal (in terms of spectrometric characteristics) reverse bias voltage applied to the barriers of the detector cells, the mean dark currents for the devices with an active surface area of ≈0.12 cm^2 are given in Table 2. In the detectors on the semi-insulating (compensated) GaAs, they reach 90 nA; for the detectors on the pure (epitaxial) GaAs with metal–semiconductor barriers, 10 nA; for those on the lightly doped GaAs (3×10^{14} cm^{-3}) with metal–semiconductor (m/s) barriers, 6.5 nA; and for the devices on the pure GaAs with a depleted p–n junction barrier contact, 45 nA. Thus, the best results are offered by the device on the lightly doped GaAs (type III) presumably because of the much deeper energy position of traps (0.6 eV versus 0.23 eV for the pure material).

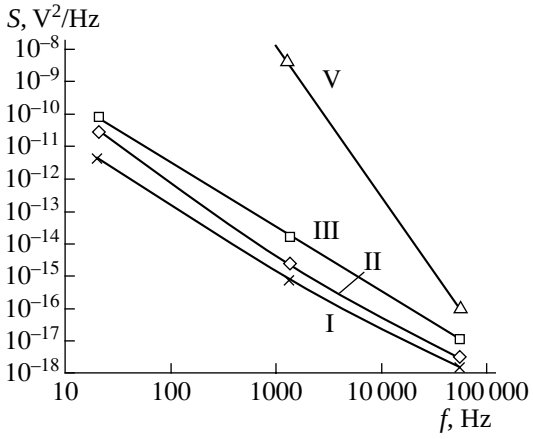

Fig. 1. SPD of $1/f^{\gamma}$ noise vs. frequency under reverse bias voltages for various types of detectors. γ = (I) 1.86, (II) 2.04, (III) 1.94, and (V) 4.63.

The measurements of the excess noise spectral power density (SPD) S are shown in Table 2 and Fig. 1. The SPD grows with increasing background dopant concentration: in the material compensated by intrinsic defects (type V), it is several orders of magnitude higher than in the pure material.

The operation of the detectors in the spectrometric mode is represented graphically in the form of histograms. All the devices were tested under the operating voltages, which provide total depletion of the detecting layer in majority carriers. Two types of alpha sources were used, each having two radiation lines: 5.147 and 5.499 MeV (the first) and 5.456 and 5.499 MeV (the second). The current of nonequilibrium carriers that are generated by alphas absorbed in the active layer was integrated by a charge preamplifier. Signal processing was accomplished in such a way that the amplitude of the signal from an ADC was proportional to the charge absorbed over a reference time interval. Since the concentration of electron–hole pairs generated is proportional to the alpha energy, such a processing makes it possible to obtain an uncalibrated absorption spectrum (histogram of events), where the ordinate and abscissa

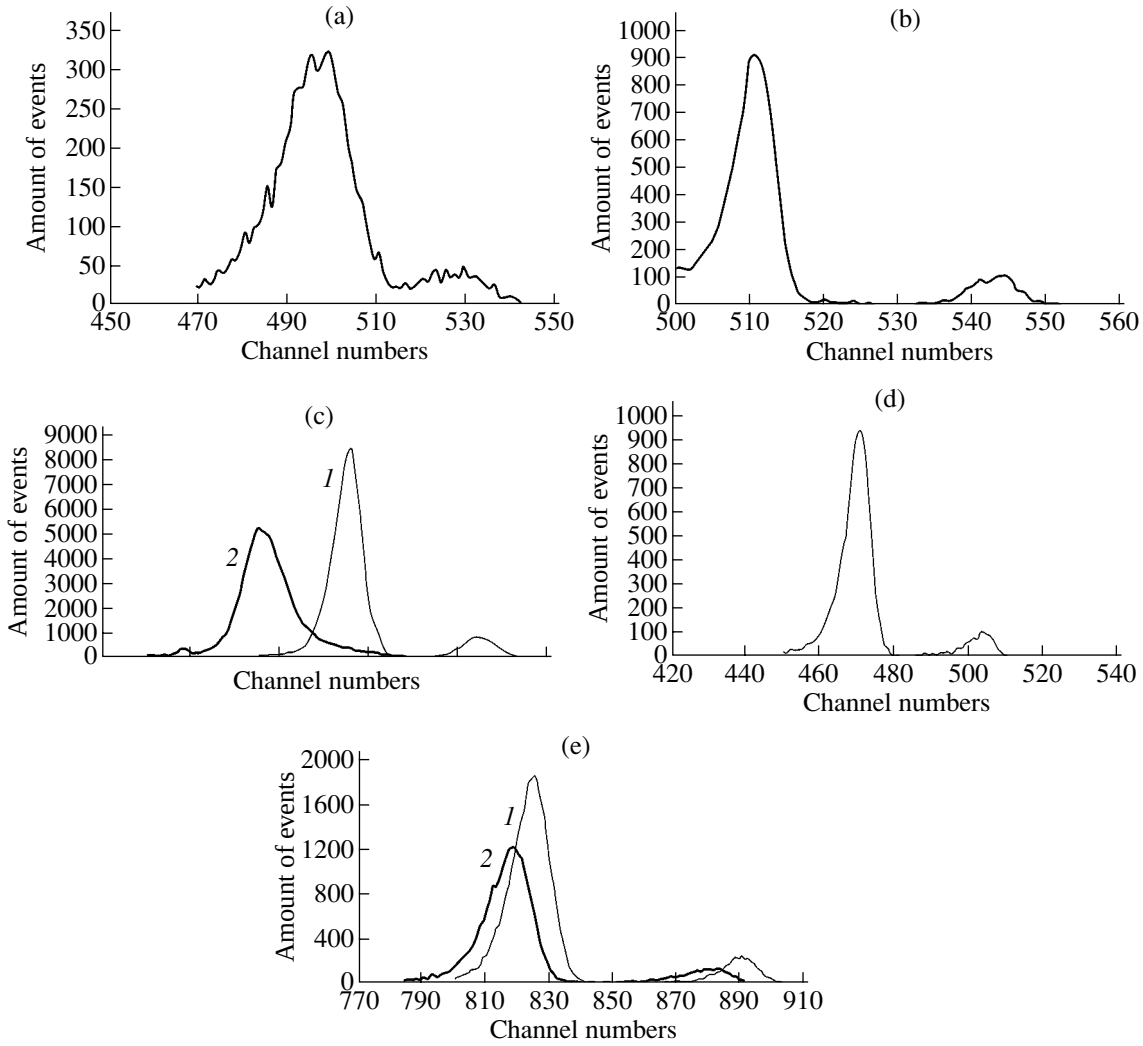

Fig. 2. Histograms of events for cells of the (a) high-resistivity Si detectors ($U = -17$ V, $T = 295$ K) and GaAs detectors on (b) semi-insulating substrate ($U = -115$ V, $T = 295$ K), (c) with m/s barrier ($n = 3 \times 10^{14}$ cm^{-3}; $T = 295$ K; $U = (1)$ 70 and (2) 50 V), (d) with p^+–n^- junction ($U = -15$ V, $T = 295$ K), and (e) with m/s barrier ($n = 3 \times 10^{13}$ cm^{-3}; $T = 295$ K; $U = (1)$ 60 and (2) 25 V).

are, respectively, the number of events of pair generation and the energy channel number. The energy width of each of the channels is the same and is easily found by using an energy mark (the reference spacing between the two spectral lines of the associated alpha source), which is present in each of the runs.

Typical results for the GaAs detectors operating in the spectrometric mode under the optimal conditions and at different temperatures are demonstrated by the histograms in Fig. 2 and by the curves shown in Figs. 3 and 4. The threshold and spectrometric characteristics are listed in Table 2. The best results were obtained for the pure GaAs layer ($N \approx 3 \times 10^{13}$ cm^{-3}) with the p–n junction (type II) in the optimal depletion mode (≈30 V). At an intrinsic noise level of ≈8.3 keV, the energy resolution was ≈15.1 keV; the leakage current of the junction detector, ≈44 nA. The lowest leakage current was observed in type-III structures; however, their energy resolution was poor (≈140 keV). The high-resistivity silicon detectors optimized and the GaAs detectors have nearly the same detection efficiency. Spectrometric measurements with the source of the second type demonstrated that the spectrometric parameters of the high-resistivity silicon detectors are somewhat higher than those of the GaAs devices: the energy resolution is ≈10 keV and the energy equivalent of noise is ≈2 keV.

Thus, the experiments supported the analytical results for the efficiency of the GaAs and Si detectors: the photoelectric gain of the latter is comparable to that of the optimized commercial high-resistivity silicon counterparts. However, the silicon devices still outperform the GaAs ones in room-temperature energy equivalent of noise ($S \approx 2$ keV) and energy resolution (≈10 keV). A plausible reason is a higher generation–recombination noise of the GaAs active layer, which is

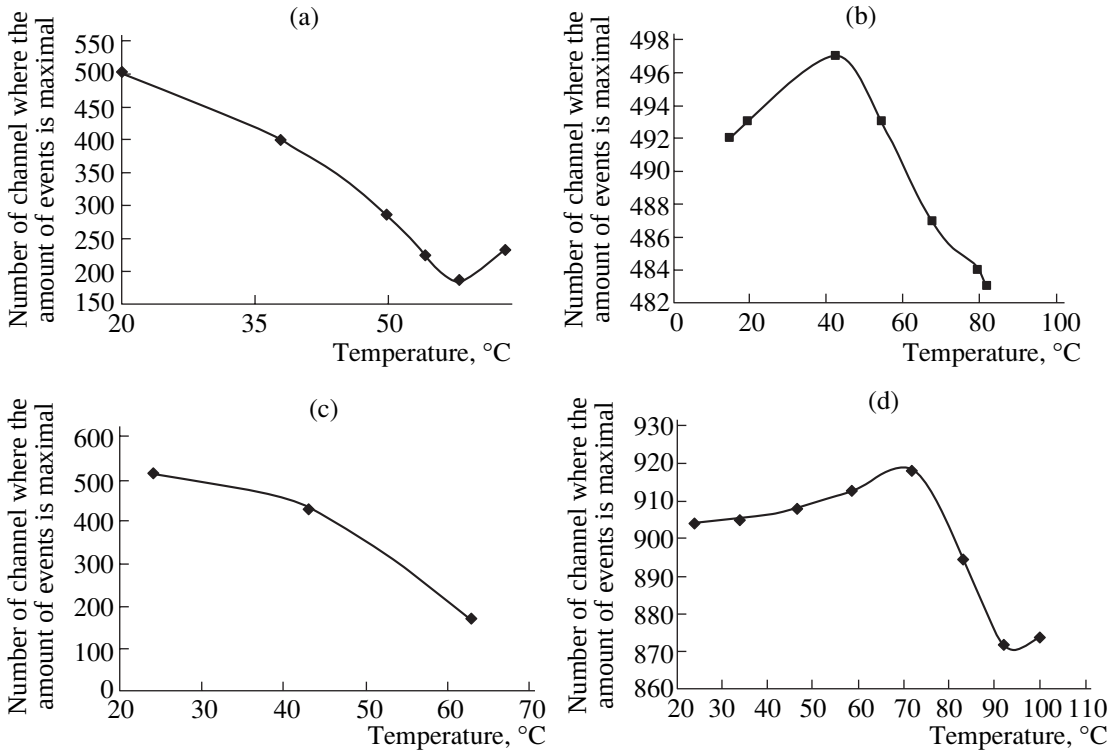

Fig. 3. Temperature dependences of the position of the peak of events for the (a) Si detectors (U = –17 V) and GaAs detectors (b)with p–n junction (U = –22 V), (c) on semi-insulating substrate (U = –115 V), and (d) with m/s barrier (U = –28 V).

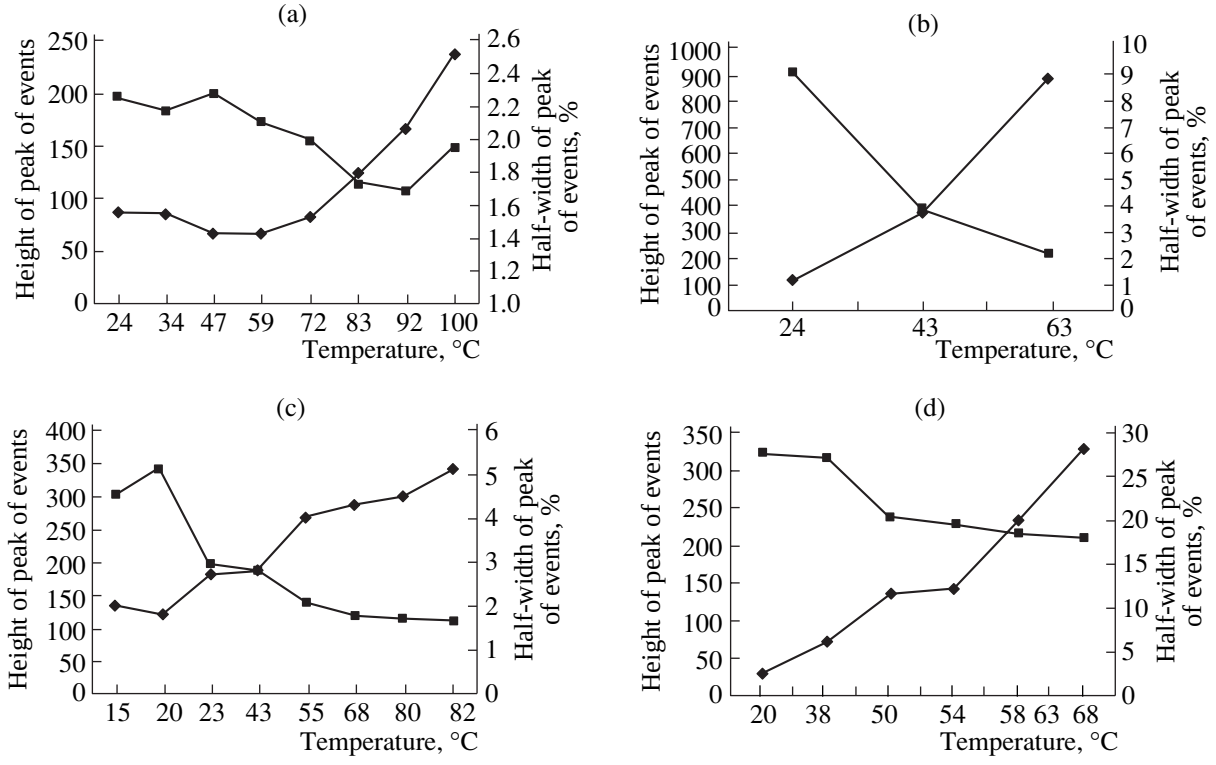

Fig. 4. Temperature dependences of the (◆) half-width and (■) height of the peak of events for the GaAs detectors (a) with m/s barrier (U = –20 V), (b) on semi-insulating substrate (U = –115 V), (c) with p^+–n junction (U = –22 V), and (d) for the Si detectors (U = –17 V).

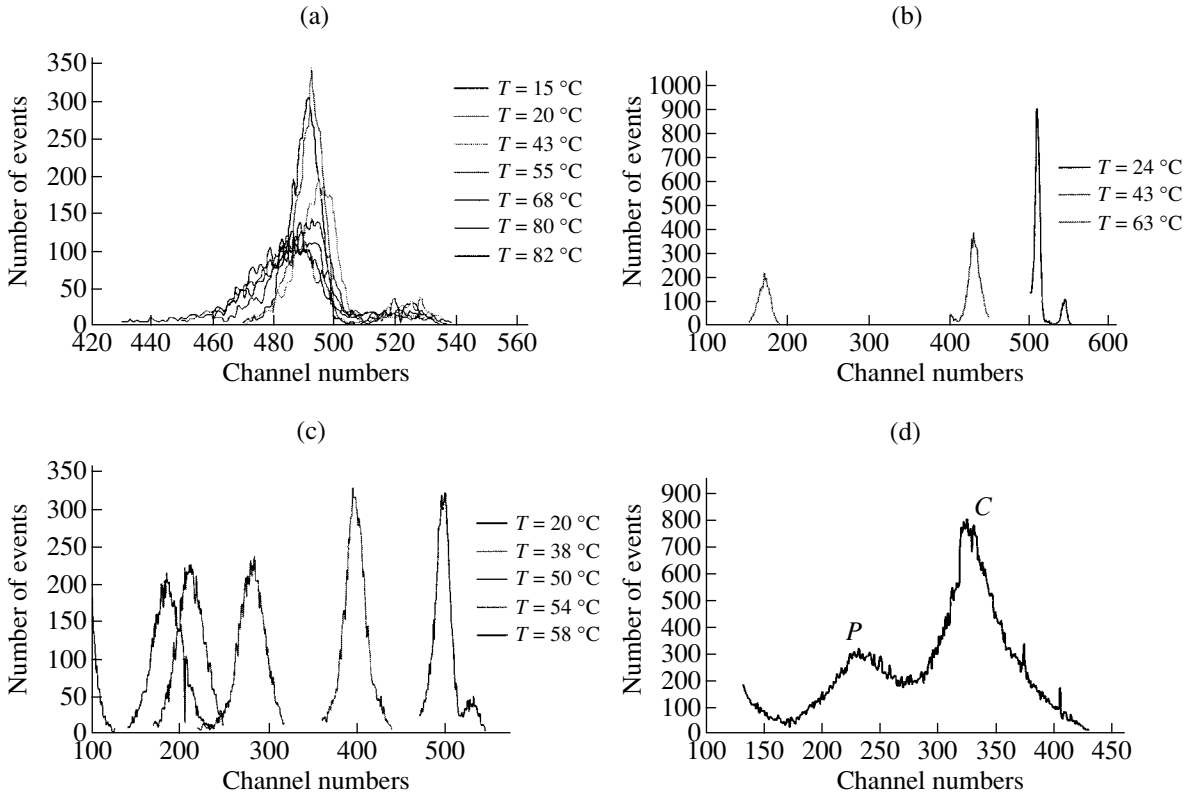

Fig. 5. Histograms of events at different temperatures for the GaAs detectors (a) with *p*–*n* junction (U = –22 V) and (b) on semi-insulating substrate (U = –115 V) and for the silicon detectors with (c) U = –17 V and (d) U = –17 V and a fixed temperature T = 73°C.

much more heavily contaminated by background impurities (Table 1).

For both detectors, the temperature range of stable operation is governed by generation–recombination processes and, eventually, by barrier-contact and detecting-layer leakages. In practice, the detectors may also be placed in hot areas, so that problems associated with heat release and detector overheating may arise. The same problems appear when the energy of the particles is very high (for example, in accelerators designed for particle energies of >1 GeV) or the particle beam has a high density. This has stimulated us to perform a comparative study of the detectors operating under elevated temperatures (up to 100°C). The results are presented in the form of the voltage and temperature dependences of the histograms (Fig. 5), positions of the peaks of events (Fig. 6), and height and half-width of the peaks (Figs. 3, 4). It is seen that the efficiency of the

N

Table 3. Effect of radiation on the electrophysical parameters of test transistors and circuits

Types of structures	High-energy electrons (4 MeV, 10^7 rad)			Co^{60} (1.25 MeV, 3×10^7 rad)				
	$\Delta I/I$	$\Delta V/V$	$\Delta S/S$	$\Delta I/I$	$\Delta V/V$	$\Delta S/S$	$\Delta k/k$	$\Delta\tau/\tau$
Uniform doping	−0.7	−0.4	−0.6	+0.25	+0.15	−0.10	–	−0.3
δ–10^{-12}/3	−0.4	−0.25	−0.10	–	–	–	–	–
δ–3×10^{-12}/1	−0.3	−0.18	−0.07	+0.18	+0.10	~0.02	<0.02	<0.02
n^-GaAs epitaxial layer	Before 0.6 eV, $\sim 8 \times 10^{13}$ cm^{-3}			Before 0.6 eV, $\sim 8 \times 10^{13}$ cm^{-3}				
	After 0.35 eV, 2×10^{14} cm^{-3}			After 0.20 eV, 10^{14} cm^{-3}, $\delta\tau/\tau \approx 0.3$				
Semi-insulating substrate	Before 0.82 eV, 7×10^{14} cm^{-3}			E_{ta} and E_{td} spectra unchanged				
	After 0.87 eV, 0.38 eV							

Note: I and ΔI are the drain current and its change; V and ΔV, the threshold voltage and its change; S and ΔS, the transconductance of the field-effect transistor and its change; k and Δk, the gain of the transistor and its change; and τ and $\Delta\tau$, the photovoltage relaxation time and its change. δ–10^{12}/3 designates a δ structure with three δ layers doped to a level of 10^{12} cm^{-2} and spaced 150 Å apart.

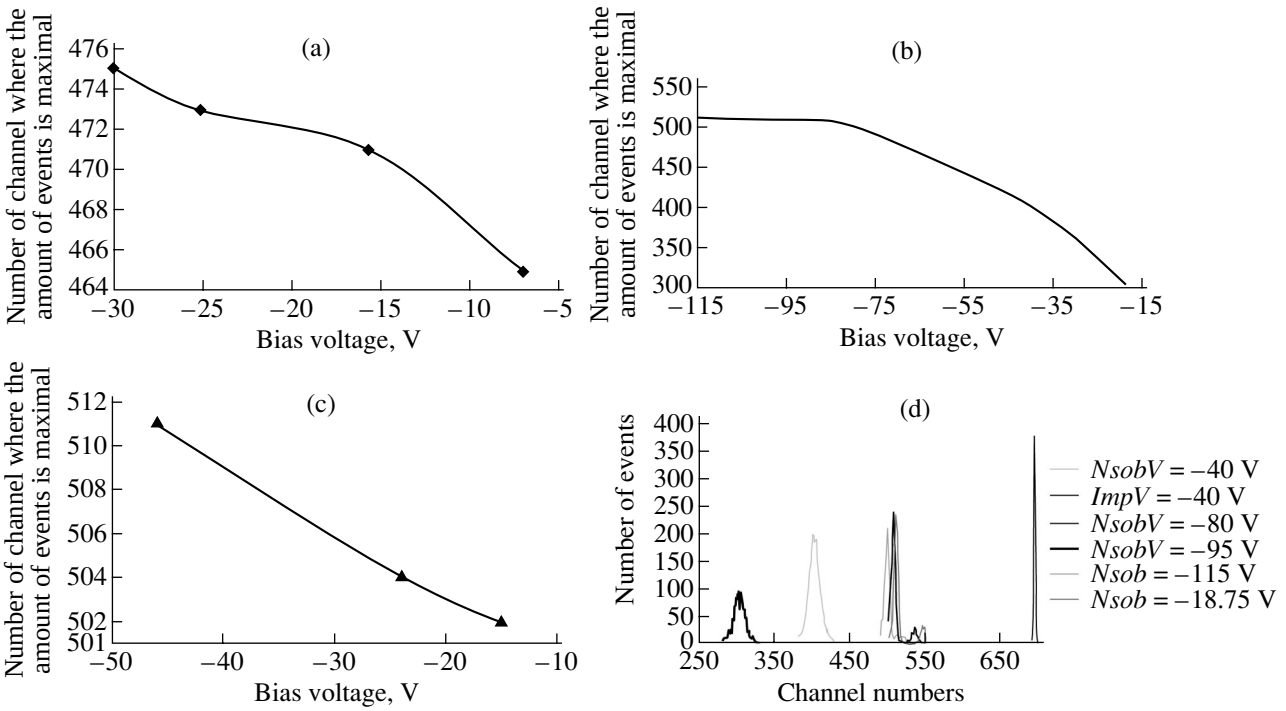

Fig. 6. Dependence of the position of the peak of events on the bias voltage for the (a) GaAs detectors with *p–n* junction (T = 300 K), (b) GaAs detectors on semi-insulating substrate (T = 300 K), and the (c) Si detectors (T = 300 K). (d) Histogram of events for the GaAs detectors on the semi-insulating substrate for different voltages.

silicon detectors and those on the semi-insulating GaAs is degraded considerably with rising temperature. Specifically, the relative charge loss in both detectors is ≈300% at ≈50°C, while in the devices on the pure GaAs (types I and II), it is as low as 4% even at 100°C. As for the energy resolution, the silicon devices lose their advantage even at ≈40°C and are degraded catastrophically at temperatures above 50°C. In particular, the calibration peak (marked by *C* in the histograms for the silicon detectors, Fig. 5), which occupies two energy channels at room temperature, covers as many as 50 channels at 50°C. Therefore, preference should be undoubtedly given to the GaAs detectors on the pure GaAs epitaxial layers (the peak marked by *P* in Fig. 5) at operating temperatures above 40°C.

The effect of radiation (high-energy electrons and Co^{60} electromagnetic radiation) on the GaAs materials used was studied with various test transistors and circuits (Table 3). The radiation of both types affects most significantly the parameters of the GaAs devices made on pure or uniformly doped layers. The semi-insulating GaAs offers the highest radiation hardness (resistance to failure); however, use of the semi-insulating material leads to a high noise level (Fig. 1) and necessitates forced cooling of the detectors, as follows from the data mentioned above.

CONCLUSIONS

Thus, the complex experimental and analytical study leads us to conclude that undoped GaAs is a promising material for detectors of gamma radiation and microparticles with energies ranging from 10 keV to 10 MeV. Possessing virtually the same sensitivity and spectral resolution as their high-resistivity Si counterparts, the GaAs detectors allow for a considerable reduction of operating voltages (by 20 to 30 V for alpha detectors) and offer a much higher radiation and thermal stability.

Our analysis was restricted to the energy range from 10 keV to 10 MeV. At higher energies of the particles (or gamma quanta), the effect of overheating and radiation-induced defects is enhanced and the dependence of the absorption coefficient on the charge number becomes still stronger. For particle energies higher than 10 GeV, detecting modules with alternate detecting and moderating (i.e., tungsten) layers (platelets) appear the most appropriate. Gamma quanta or delta electrons and photoelectrons generated in a moderator strike the detecting platelet immediately adjacent to the moderator. In view of the specific energy losses by fast particles in a solid-state detector due to stopping (Bethe–Heitler estimates for bremsstrahlung [19]) or ionization (Bohr estimates [20]), the idea that ionization due to gamma radiation prevails seems quite plausible. Hence, one might expect the nonlinear dependence of the absorption coefficient on the charge number of detector

material atoms. Both sides of a GaAs detector platelet adjacent to a tungsten moderator will be exposed not only to delta electrons but also to photoelectrons, soft X-ray radiation, and hard gamma radiation. The last-named radiation escapes the moderators from depths that are shorter than its radiation length. Thus, for ionizing radiation of energy above the range considered, the need for a detecting material with a high charge number (e.g., GaAs) becomes still more obvious.

REFERENCES

1. Yu. K. Akimov, O. V. Ignat'ev, A. I. Kalinin, and V. F. Kushniruk, *Semiconductor Detectors in Experimental Physics* (Énergoatomizdat, Moscow, 1989).
2. *EG&G Ortec Catalogue: Instruments and Systems for Nuclear Spectroscopy. Modular Pulse-Processing Electronics and Semiconductor Radiation Detectors* (ORTEC, Berthold, 1995), pp. 408–409.
3. S. Arbari, W. Braunschweig, Z. Chu, *et al.*, in *Proceedings of the 3rd International Scientific–Technological Conference on Actual Problems of Electronic Instrument Engineering, Nosib, 1996*, Vol. 1, p. 1.
4. V. N. Brudnyĭ, A. I. Potapov, and O. P. Tolbanov, Élektron. Prom., No. 2/3, 29 (2002).
5. G. I. Aĭzenshtat, V. P. Germogenov, S. M. Gushchin, *et al.*, in *Proceedings of the 8th Russian Conference on Gallium Arsenide and III–V Semiconductor Compounds, 2002*, pp. 278–280.
6. É. A. Il'ichev, V. I. Egorkin, A. V. Kulakov, *et al.*, in *Proceedings of the 8th Russian Conference on Gallium Arsenide and III–V Semiconductor Compounds, 2002*, pp. 266–268.
7. H. A. Bethe, Ann. Phys. **5**, 325 (1930).
8. V. B. Berestetskii, E. M. Lifshitz, and L. P. Pitaevskii, *Relativistic Quantum Theory* (Nauka, Moscow, 1968; Pergamon, Oxford, 1971), Part 1.
9. E. R. Astvatsetur'yan, O. N. Golotyuk, Yu. A. Popov, *et al.*, *The Design of Radiation-Resistant Electronic Circuits* (Moscow, 1984).
10. V. S. Vavilov, *Effects of Radiation on Semiconductors* (Fizmatgiz, Moscow, 1963; Consultants Bureau, New York, 1965).
11. D. M. Newell, P. T. Ho, R. L. Mencik, and J. R. Pelos, IEEE Trans. Nucl. Sci. **28**, 4403 (1981).
12. Y. Kadowaki, V. Mitsni, T. Takebe, *et al.*, in *Technical Digest of the IEEE Gallium Arsenide Integrated Circuit Symposium, 1982*, pp. 83–86.
13. H. H. Derley, T. W. Houston, and L. R. Hite, IEEE Trans. Nucl. Sci. **30**, 4277 (1983).
14. R. Zully and J. K. Notthoff, IEEE Trans. Nucl. Sci. **29**, 656 (1982).
15. J. K. Notthoff, IEEE Trans. Nucl. Sci. **32**, 1 (1985).
16. W. N. Sheld, J. L. Sampson, and D. C. La Pierre, IEEE Trans. Nucl. Sci. **30**, 83 (1983).
17. É. A. Il'ichev and A. I. Luk'yanchenko, RF Patent No. 2079853 (1993).
18. É. A. Il'ichev, Zh. Tekh. Fiz. **68** (5), 41 (1998) [Tech. Phys. **43**, 611 (1998)].
19. W. Heitler, *The Quantum Theory of Radiation*, 3rd ed. (Clarendon, Oxford, 1954; Inostrannaya Literatura, Moscow, 1956).
20. N. Bohr, *The Penetration of Atomic Particles through Matter*, 3rd ed. (Munksgaard, Copenhagen, 1960; Inostrannaya Literatura, Moscow, 1965).

Translated by V. Isaakyan

Technical Physics, Vol. 49, No. 3, 2004, pp. 318–324. Translated from Zhurnal Tekhnicheskoĭ Fiziki, Vol. 74, No. 3, 2004, pp. 37–43.
Original Russian Text Copyright © 2004 by Zvezdin, Khvalkovskii.

SOLID-STATE ELECTRONICS

Magnetoresistance of a Planar Nanobridge

K. A. Zvezdin and A. V. Khvalkovskii

General Physics Institute, Russian Academy of Sciences, Moscow, 119991 Russia

e-mail: khvalkov@ran.gpi.ru

Received June 2, 2003

Abstract—This work pursues the two-dimensional study of the spin accumulation effect in film magnetic nanobridges between two planar electrodes. Such a structure is of considerable interest for different applications in microelectronics. The dependence of the magnetoresistance, as well as of the spin density nonequilibrium distribution, on the geometric parameters of the system is obtained. © *2004 MAIK "Nauka/Interperiodica".*

INTRODUCTION

In recent years, the transport properties of spin-polarized electrons and the related field of science, spintronics, have attracted much attention [1-4]. The effect of giant magnetoresistance in multilayer films and superlattices [2], tunnel junctions [3], nanocontacts [4], nanobridges [5], and nanowires with domain walls [6, 7] holds the lead among the subjects spintronics covers.

Magnetic nanocontacts and nanobridges are also of special interest. A number of new intriguing effects, which have much potential for application in microelectronics, have been discovered in these systems. Among them, the effect of extremely high magnetoresistance found experimentally in nanocontacts ranks first. The value of magnetoresistance may reach several hundreds of percent at room temperature. For example, experiments [4] were performed with a system of two macroscopic ferromagnetic rods that were connected and disconnected in such a way that a point nanocontact formed at the time of connection or disconnection. Such a system has been demonstrated to have a magnetoresistance as high as 700% at room temperature. Investigations of the magnetoresistance in nanowires are also noteworthy. It was shown, in particular [6], that domain walls in nanowires make a significant contribution to the magnetoresistance.

Until recently, the geometry of nanocontacts has been poorly controlled. Works [4] are, in essence, a statistical investigation of nanocontacts randomly formed by connecting or disconnecting two oppositely magnetized rods. In [8], a micromagnetic study of the configurations arising in nanocontacts that bridge massive rods (similar to the ones used in works [4]) were performed. It was shown that the magnetic structure of such nanocontacts is extremely sensitive even to slight changes in the geometry. Obviously, for more reliable experimentation and practical use, it is required that nanocontacts have a well-defined geometry.

As such contacts, we propose film nanobridges consisting of two planar electrodes (banks) connected by a nanowire (bridge) (Fig. 1). It was shown [5] that a domain wall in magnetic nanobridges may be both on and off the bridge center depending on the material parameters. For different configurations of the system, the transition from the symmetric to the asymmetric state may be continuous (like second-order phase transitions) or discrete (like first-order phase transitions). Due to this fact, nanobridges are very promising for use in spintronics.

The mechanism behind the effect of giant magnetoresistance in magnetic nanocontacts and nanowires has been the subject of many theoretical papers [9]. An important mechanism that should be taken into account when analyzing the magnetoresistance of such systems is spin accumulation [10–16]: the occurrence of a nonequilibrium spin density near the domain wall when the electric current passes through it. As a consequence, an additional resistance arises.

The reason for the spin accumulation effect is that the band structure of ferromagnets is different for carrirs whose spin is parallel and antiparallel to the magnetization. As a result, the transport properties (the density of states at the Fermi level and the conductivity) for carriers with one spin polarization are much higher than for carrirs with the opposite spin polarization. The

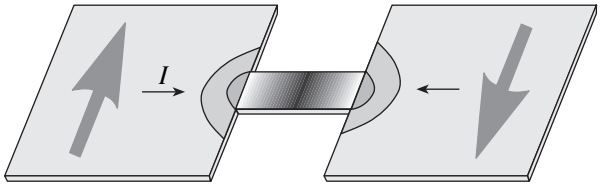

Fig. 1. Nanobridge with a domain wall inside. The nonequilibrium spin density appearing near the domain wall when the current passes through it is shown in gray. The small and large arrows indicate the directions of the current and electrode magnetizations, respectively.

1063-7842/04/4903-0318$26.00 © 2004 MAIK "Nauka/Interperiodica"

former have been named majority carrirs; the latter, minority carrirs. The spin accumulation effect and its contribution to the magnetoresistance of an infinite one-dimensional magnetic nanowire with a domain wall were investigated in [15, 16]. The potential distribution and the surface resistance due to the domain wall were calculated as a function of the skewness of the transport properties for majority and minority carriers.

For practical use, as well as for quantitative processing of experimental data, one should know the dependence of the transport properties of nanobridges on their physical and geometric parameters. This paper is devoted to the theoretical investigation of the spin accumulation effect in a finite-length (on the order of the spin diffusion length) magnetic nanobridge at the center of which a so-called linear domain boundary [17, 18] is located. The result of this work is the construction of a two-dimensional model of spin accumulation in a planar nanobridge. This allowed us to find the dependence of the magnetoresistance on the system's geometry.

BASIC EQUATIONS

The current flowing through a planar magnetic nanobridge generates a nonequilibrium spin density near the domain wall (Fig. 1) and, hence, causes the resistance to grow as in the case of a nanowire [16].

Let us write the set of equations [11, 16] for the spin density and electric potential in a ferromagnet through which the current with a density J passes. The quantities governing the nonequilibrium distribution of majority and minority electrons in the system are electrochemical potentials μ_α

$$\mu_\alpha = \zeta_\alpha - eU. \tag{1}$$

Here, $\alpha \in \{+, -\}$ are the spin indices for two opposite polarizations, ζ_α is the nonequilibrium chemical potential of the electron subsystem with a spin α, and U is the electrical potential at a given point. The chemical potentials are related to the nonequilibrium density n_α as

$$n_\alpha = g_\alpha \zeta_\alpha, \tag{2}$$

where g_α is the density of states for electrons with a spin α on the Fermi surface and n_α obeys the neutrality condition

$$\sum_\alpha n_\alpha = n_+ + n_- = 0. \tag{3}$$

The values of n_α and ζ_α are measured relative to their equilibrium values (the Fermi level for ζ_α). The spin currents j_α are given by the equations

$$\mathbf{j}_\alpha = \sigma_\alpha \frac{1}{e} \nabla \mu_\alpha, \tag{4}$$

where σ_α are the conductivities of the spin subsystems.

The currents j_α and densities n_α are related via the continuity condition:

$$\operatorname{div} \mathbf{j}_\alpha = \frac{e n_\alpha}{\tau_s}, \tag{5}$$

where τ_s is the longitudinal time of electron spin relaxation.

Below, we use the symmetrized variables

$$\begin{gathered} \mu_t = \mu_+ + \mu_-, \quad \mu_s = \mu_+ - \mu_-, \\ \zeta_t = \zeta_+ + \zeta_-, \\ J = j_+ + j_-, \quad j_s = j_+ - j_-, \end{gathered} \tag{6}$$

and the quantities

$$\sigma_\pm = \frac{\sigma}{2}(1 \pm \beta) = \frac{1}{2\rho}(1 \pm \beta), \quad g_\pm = \frac{g}{2}(1 \pm \delta), \tag{7}$$

where σ, ρ, and g are the conductivity, resistivity, and density of states of the nanowire, respectively; β and δ are dimensionless parameters characterizing the skewness of the related parameters.

Equations (4)–(6) imply that the spin potential μ_s is continuous. From Eqs. (1)–(3), it follows that [15]

$$\mu_s = n_+(g_+^{-1} + g_-^{-1}), \tag{8}$$

i.e., μ_s is proportional to the nonequilibrium spin density. The distribution of μ_s in the bridge and banks is given by a solution to the diffusion equation [16]

$$\Delta \mu_s = \frac{\mu_s}{L_s^2}. \tag{9}$$

Here, $L_s = (D_s \tau_s)^{1/2}$ is the spin diffusion length and

$$D_s = \frac{1}{e^2} \frac{g_+^{-1} + g_-^{-1}}{\sigma_+^{-1} + \sigma_-^{-1}}$$

is the diffusion coefficient of the material. To Eq. (9), there corresponds the functional

$$2E(\mu_s) = \iint_{NB} \left(\left(\frac{\mu_s}{L_s} \right)^2 + \left(\frac{d\mu_s}{dx} \right)^2 + \left(\frac{d\mu_s}{dy} \right)^2 \right) dx\,dy, \tag{10}$$

where the integral is taken over the nanobridge (the axes are shown in Fig. 2, where the origin is placed at the bridge center). Differential equation (9) is the Euler–Lagrange equation for this functional.

We assume that the domain wall is placed at the bridge center $x = 0$. Hence, a solution $\mu_s(x, y)$ to Eq. (9) is a function symmetric about the system's center and with respect to change of sign of μ_s. Therefore, for simplicity, we designate the value of the functional as $2E(\mu_s)$, where $E(\mu_s)$ corresponds to the integral in Eq. (10) taken over half the nanobridge (over the right half for definiteness).

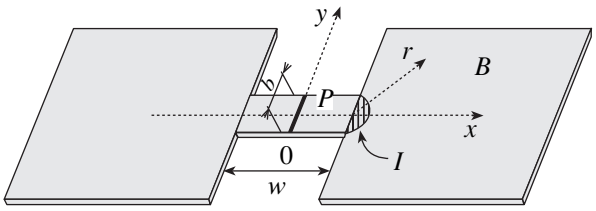

Fig. 2. Nanobridge with the designations used in the calculations.

To exactly solve Eq. (9) for the nanobridge is a challenge; therefore, we search for a solution in an approximate form. To this end, we construct a function $\mu_s(x, y)$ so that it satisfies both Eq. (9) (individually in the bridge and in the electrodes) and the boundary conditions on the domain wall and at the bridge edges. Under general assumptions, this function, as is shown below, depends on a single parameter (at a given current). To find this parameter, we apply the variational principle to functional (10), i.e., assume that integral (10) during the solution of Eq. (9) reaches a minimum.

In view of the geometry of the nanobridge, it is natural to partition it into three areas (Fig. 2) and search for a solution for each of them. Area *P* is half of the bridge; area *I*, a semicircle with its base lying on the face end of the bridge; and area *B*, a part of the right bank of the bridge (without area *I*). The length and thickness of the bridge are designated as *w* and *b*, respectively.

Let the bridge be sufficiently long and narrow, so that the distribution of μ_s in area *P* may be considered one-dimensional. Then, a solution to Eq. (9) for this area can be expressed as

$$\mu_s = Ae^{-x} + Be^{x}, \tag{11}$$

where *A* and *B* are coefficients.

Equation (11) can be conveniently expressed in the form

$$\mu_s(x) = \frac{\mu_1 - \mu_0 e^{-w/2}}{2\sinh(w/2)}e^{x} + \frac{-\mu_1 + \mu_0 e^{w/2}}{2\sinh(w/2)}e^{-x}, \quad 0 \le x \le w/2, \tag{12}$$

where μ_0 and μ_1 are the spin potentials at the center and edge of the bridge and

$$x \longrightarrow x/L_s \tag{13}$$

is the dimensionless length. We assume that the μ_s distribution in the banks is radially symmetric starting from a distance to the bridge. Let this distance be equal to half *b* for definiteness. Then, in view of (13), Eq. (9) for area *B* in the polar coordinates can be expressed as

$$\frac{d^2\mu_s}{dr^2} + \frac{1}{r}\frac{d\mu_s}{dr} - \mu_s = 0, \tag{14}$$

where *r* is the coordinate on the polar axis, which originates at the point where the bridge and bank meet (Fig. 2).

The modified Bessel function of the second type $K_0(r)$ is a limited-at-infinity solution to Eq. (14). This function monotonically approaches zero at infinity and logarithmically diverges at the point $r = 0$. Thus, a solution to Eq. (9) in area *B* will have the form

$$\mu_s(r) = \frac{a}{\pi}K_0(r), \quad r \ge b/2, \tag{15}$$

where *a* is an arbitrary constant defined by the boundary conditions.

To calculate the unknown coefficients *a*, μ_0, and μ_1, we should join together the solutions at the boundaries between the areas and on the domain wall. First, *a* is expressed in terms of μ_0 and μ_1. Let us take the integral S_I of Eq. (9) over area *I*:

$$S_I \equiv \iint_I (\Delta\mu_s)dxdy = \iint_I \mu_s dxdy. \tag{16}$$

The upper estimate of the right-hand side is

$$S_I = \pi(b/2)^2\mu_1. \tag{17}$$

Since expression (17) is a quantity of the second order of smallness in *b*, the value of the integral S_I may be neglected. Then, transforming the right of Eq. (16) into a surface integral and using Eqs. (12) and (15), we express the constant *a* through μ_0 and μ_1:

$$a(\mu_0, \mu_1) = -\frac{1}{K_0'(b/2)}\frac{\mu_0 - \mu_1\cosh(w/2)}{\sinh(w/2)}. \tag{18}$$

Since $K_0(r)$ is a monotonically decreasing function, its derivative is negative.

Now let us find a relationship between μ_0 and μ_1. We neglect the reflection and relaxation of polarized carriers at the domain wall; therefore, the spin currents and densities are continuous at it. The spin current takes the form

$$j_s = \beta J + \frac{2(1-\beta^2)}{e}\mu_s'. \tag{19}$$

With regard to current continuity at the domain wall, we obtain μ_0 as a function of μ_1 from Eq. (12):

$$\mu_0(\mu_1) = e\frac{\beta}{2(1-\beta^2)}\tanh(w/2)\rho J + \frac{\mu_1}{\cosh(w/2)}. \tag{20}$$

Thus, all the coefficients can be expressed through each other and only one of them is independent. In this case, μ_1 is most conveniently taken as an independent coefficient. This parameter uniquely (for a given current) defines a solution, where functional (10) reaches a minimum according to the variational principle. Thus,

μ_1 is obtained from the equation

$$\frac{dE(\mu_s(\mu_1))}{d\mu_1} = 0. \quad (21)$$

The functional $E(\mu_s)$ can be expressed as the sum of three terms:[1]

$$E(\mu_s) = E_P + E_I + E_B, \quad (22)$$

each being found by integration over the related areas into which the nanobridge is divided. In areas *P* and *B*, a solution was found in one-dimensional form (see (12) and (15)); hence, E_P and E_B are expressed as one-dimensional integrals. To estimate E_I, we integrated a linear function that relates the spin potential at the edge of the bridge to that on the bank of radius $r = b/2$ along a rectangle $b/2 \times \pi b/4$. Thus, the model spin potential in this rectangle joins linearly solutions (12) and (15) at the extreme points and is given by

$$\mu_{\text{mod}}(z) = \mu_1 - \frac{\mu_1 - \frac{a}{\pi}K_0(b/2)}{b/2}z, \quad 0 \le z \le b/2. \quad (23)$$

Accordingly, E_I is the integral of function (23) along this rectangle (the dimensions of this rectangle are taken so that its surface area equals that of area *I*).

RESISTANCE OF THE NANOBRIDGE

Using the technique described in the previous section, we determined the spin potential distribution in the nanobridge for different lengths and widths of the bridge. In this way, one can estimate how the geometry of the nanobridge influences its magnetoresistance.

Let us calculate a potential drop across the nanobridge due to the spin accumulation effect. According to [16], the parameter μ_t (see (6)) is given by

$$\mu_t = \delta\mu_s - 2eU. \quad (24)$$

Thus, since the chemical potentials are continuous functions, the expression for voltage drop ΔU_1 across the domain wall in the nanobridge has the form

$$\Delta U_1 = \frac{1}{e}\delta\mu_s(0). \quad (25)$$

Spin accumulation results in an extra voltage drop ΔU_2 along the length of the bridge and across the banks. Set (1)–(5) yields the expression for the total current

$$J = \frac{\sigma_+}{e}\nabla\mu_+ + \frac{\sigma_-}{e}\nabla\mu_-. \quad (26)$$

Expressing the right of Eq. (26) through the chemical and spin potentials, we obtain

$$\nabla U + \frac{\mathbf{J}}{2\sigma} = \frac{1}{2e}\nabla\zeta_t + \frac{\beta}{2e}\nabla\mu_s. \quad (27)$$

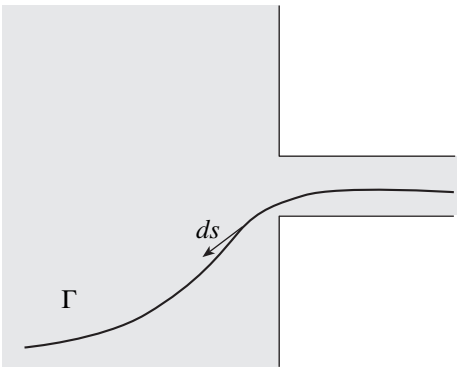

Fig. 3. Curve Γ along which integral (28) is taken. The resistance due to the domain wall does not depend on the choice of the curve.

The value of ΔU_2 is determined by integrating vector equation (27) along any curve Γ that connects the domain wall with one of the electrodes (Fig. 3) and does not cross the current source:[2]

$$\Delta U_2 = 2\int_0^\infty \left(\nabla U + \frac{\mathbf{J}}{2\sigma}\right)d\mathbf{s}, \quad (28)$$

where $d\mathbf{s}$ is the differential of an arc of the curve Γ. The factor 2 in Eq. (28) means integration over both sides of the domain wall. Set (1)–(5) also yields a correlation between ξ_t and μ_s at any point of the curve Γ:

$$\xi_t = -\delta\mu_s. \quad (29)$$

Eventually, from Eqs. (27)–(29), we find

$$\Delta U_2 = \frac{1}{e}\int_0^\infty (\beta - \delta)\frac{d\mu_s}{ds}ds. \quad (30)$$

Since μ_s goes to zero at infinity, the total voltage drop ΔU_b due to the presence of the domain wall is equal to, in view of (25),

$$\Delta U_b = \Delta U_1 + \Delta U_2 = \frac{\beta}{e}\mu_0. \quad (31)$$

In this case, a value given by Eq. (31) does not depend on the choice of the curve Γ.

Let us designate the spin potential on the domain wall in the case of an infinite nanowire as μ_0^{nw} and

[1] The argument on the right is omitted for brevity.

[2] For definiteness, the upper limit of integration is taken to be infinity, since it is of no significance because of a fast decrease of the spin potential with distance.

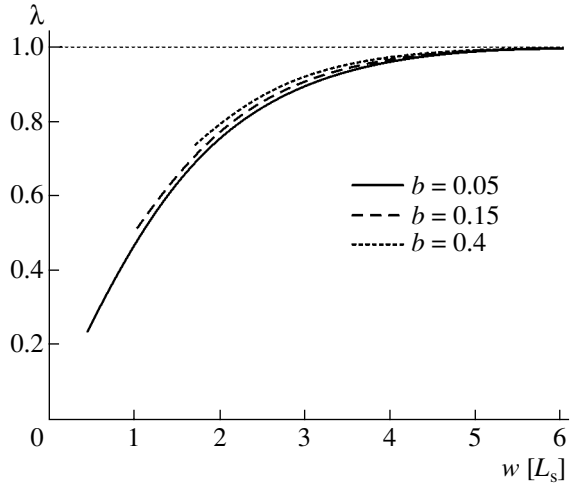

Fig. 4. $\lambda(w, b)$ as a function of the bridge length for several values of the thickness b. The lengths are expressed in units of the spin relaxation length L_s.

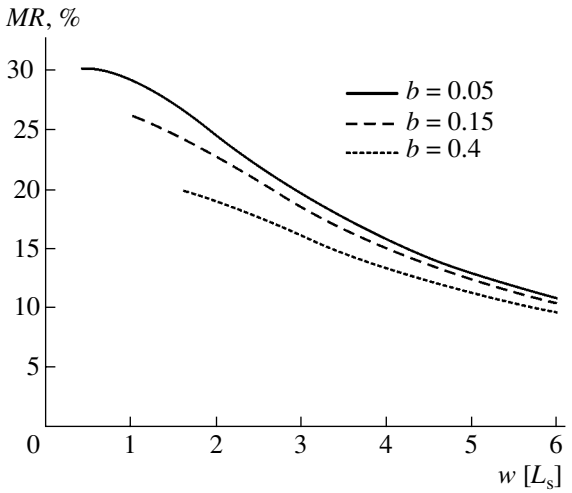

Fig. 5. Magnetoresistance of the nanobridge as a function of its length for several values of the thickness b. The lengths are expressed in units of L_s.

introduce a function

$$\lambda(w, b) = \frac{\mu_0}{\mu_0^{nw}}. \quad (32)$$

The resistivity of the domain wall in the case of a nanowire, ρ_{nw}, [16] can be obtained from (20) and (31) in the limit of an infinitely long bridge:

$$R_{nw} = \rho\frac{2\beta^2}{1-\beta^2}L_s. \quad (33)$$

(here, the length is given in dimensional units.) Then, according to (31)–(33), the total resistance of the domain wall in a nanobridge is given by

$$R_b = \lambda(w, b)\rho\frac{2\beta^2}{1-\beta^2}L_s. \quad (34)$$

Thus, $\lambda(w, b)$ is the ratio between the resistances of the domain wall in the nanobridge and the nanowire. Figure 4 plots λ versus the bridge length w for different thicknesses b. As the length and thickness of the bridge increase, its resistance grows monotonically, approaching the resistance of the nanowire.

Let us calculate the magnetoresistance of the nanobridge using the expression

$$MR = \frac{R_{AP} - R_P}{R_P}, \quad (35)$$

where R_{AP} and R_P are the resistances of the nanobridge with the banks magnetized antiparallel and parallel to each other, respectively. R_P, the ohmic resistance of the nanobridge, can be expressed as

$$R_P = 2\frac{L_x}{L_y c}\rho + \frac{w}{bc}\rho. \quad (36)$$

Here, L_x and L_y are the length and width of the banks, respectively (their values are usually as large as hundreds of nanometers), and c is the thickness of the nanobridge. The first item in expression (36) is the resistance of the banks; the second one, the ohmic resistance of the bridge.

In the case of a nanobridge with oppositely magnetized domains, its resistance equals the sum of R_P and the resistance due to the spin accumulation effect:

$$R_{AP} = R_P + \frac{R_b}{bc}. \quad (37)$$

As a result, summing Eqs. (35)–(37) yields an expression for the magnetoresistance of the nanobridge:

$$MR = \lambda(b, w)\frac{2\beta^2}{1-\beta^2}\frac{L_s}{2b\frac{L_x}{L_y} + w}. \quad (38)$$

The dependence of the magnetoresistance MR on the length w of the bridge is shown in Fig. 5 for different values b of its thickness. The value of β is taken to be 0.5, which coincides with that for transition metals in order of magnitude. L_x and L_y are taken to be equal to each other. As is seen from the graphs in Fig. 5, the magnetoresistance MR of the nanobridge increases as its length and thickness decrease, while the resistance of the domain wall falls, as was mentioned above. The apparent contradiction is explained by the fact that the magnetoresistance of the nanocontact depends both on the absolute value of the spin resistance of the system and on the contribution of the spin resistance to the total resistance. The first term (represented by the factor $\lambda(w, b)$) decreases with decreasing length and thickness of the bridge, while the contribution from the domain

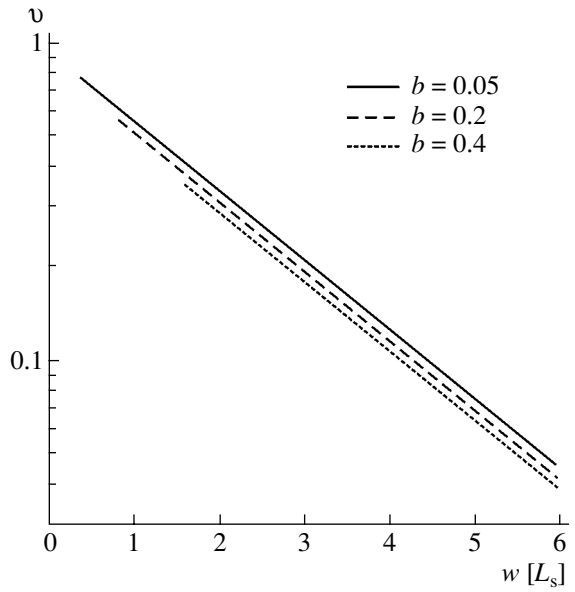

Fig. 6. υ as a function of the bridge length for several values of the bridge thickness *b*. The lengths are expressed in units of L_s.

wall (represented by the last factor in Eq. (38)) increases faster than λ decreases under the same conditions.

NUMERICAL SIMULATION

The results obtained vary weakly with the model parameters. To investigate the stability of the results, we varied (i) the linear dimensions of the rectangle along which the function μ_{mod} in Eq. (23) was integrated to estimate E_I and (ii) the lower limit of integration in the one-dimensional integral determining the value of E_B (this limit equals $b/2$). Also (iii), in Eqs. (16)–(18), from which the coefficient a as a function of μ_0 and μ_1 was derived, the value of the left-hand side of the integral in (16) was taken in the form of (17) (as the upper bound).

The results of variations are as follows. A twofold change in the lengths mentioned in (i) and (ii), as well as the substitution made in (iii), changed λ by no more than 2–3%. Such a value (i.e., several percent when all the variables are varied simultaneously) may be taken as the accuracy of the model presented.

Using the parameters μ_0 and μ_1, one can construct a dimensionless fraction designated as υ:

$$\upsilon = \frac{\mu_1 - \mu_0 e^{-w/L_s}}{\mu_0 - \mu_1 e^{-w/L_s}}. \quad (39)$$

This fraction, like λ, describes the effect of the banks on the spin resistance. The value of υ equals zero in the case of an infinitely long bridge and unity if the bridge is infinitely short. This quantity is of interest because it is well described by the exponential dependence on the length of the bridge (Fig. 6):

$$\upsilon = -\nu(b)\exp(-w/L_s). \quad (40)$$

Here, ν(*b*) is the coefficient depending on the bridge thickness. The deviation from dependence Eq. (40) is negligible (about 1–2%) for lengths several times greater than the bridge thickness:

$$w > (2-3)b. \quad (41)$$

The right of condition (41) may be taken as the lower applicability bound of simulation, above which, in particular, corrections of the second order of smallness in *b* (see, for example, expressions (16)–(18)) may be neglected. The same condition may be taken as the validity bound for the assumption that the current in the bridge is uniform and in the banks radially symmetric.

CONCLUSIONS

Thus, we investigated the behavior of a planar magnetic nanobridge and developed a model allowing one to derive the nonequilibrium spin density distribution in a set of bridged electrodes. The model is shown to be stable; i.e., calculation results vary only slightly with the model parameters.

Using the data obtained, we calculated a nanobridge resistance increment induced by the presence of a domain wall. The dependence of the magnetoresistance on the geometric parameters of the bridge was obtained. According to calculations based on our model, the magnetoresistance reaches 20–30%. As the length and thickness of the bridge decrease, the magnetoresistance of the nanobridge increases monotonically.

ACKNOWLEDGMENTS

This work was supported by the Russian Foundation for Basic Research (project nos. 02-02-17389 and 01-02-16595) and INTAS (project no. 99-01839).

REFERENCES

1. G. A. Prinz, Science **282**, 1660 (1998); I. Zutic, cond-mat/0112368 (2001).
2. M. A. M. Gijs and G. E. W. Bauer, Adv. Phys. **46**, 285 (1997).
3. R. Meservey and P. M. Tedrow, Phys. Rep. **238**, 173 (1994).
4. N. Garcia, M. Muñoz, and Y.-W. Zhao, Phys. Rev. Lett. **82**, 2923 (1999); G. Tatara, Y.-W. Zhao, M. Muñoz, *et al.*, Phys. Rev. Lett. **83**, 2030 (1999); M. Muñoz *et al.*, Appl. Phys. Lett. **79**, 2946 (2001); N. Garcia, M. Muñoz, G. G. Qian, *et al.*, Appl. Phys. Lett. **79**, 4550 (2001); N. Garcia, Appl. Phys. Lett. **77**, 1351 (2000); N. Garcia, M. Muñoz, and Y.-W. Zhao, Appl. Phys. Lett. **76**, 2586 (2000); S. H. Chung, M. Muñoz, N. Garcia, *et al.*, Phys. Rev. Lett. **89**, 287203 (2002).
5. A. A. Zvezdin and K. A. Zvezdin, Pis'ma Zh. Éksp. Teor. Fiz. **75**, 613 (2002) [JETP Lett. **75**, 517 (2002)].

6. R. C. Giordano, Physica B **194**, 1009 (1994); Phys. Rev. B **51**, 9855 (1995).
7. S. Dubois, L. Piraux, J. M. George, *et al.*, Phys. Rev. B **60**, 477 (1999); U. Ebels, A. Radulescu, Y. Henry, *et al.*, Phys. Rev. Lett. **84**, 983 (2000).
8. A. K. Zvezdin, A. F. Popkov, K. A. Zvezdin, *et al.*, Phys. Met. Metallogr. **9**, S165 (2001).
9. H. Imamura, N. Kobayashi, S. Takahashi, *et al.*, Phys. Rev. Lett. **84**, 1003 (2000); A. K. Zvezdin and A. F. Popkov, Pis'ma Zh. Éksp. Teor. Fiz. **71**, 304 (2000) [JETP Lett. **71**, 209 (2000)]; L. R. Tagirov, B. P. Vodopyanov, and K. B. Efetov, Phys. Rev. B **63**, 104428 (2001); V. V. Osipov, E. V. Ponizovskaya, and N. Garsia, Appl. Phys. Lett. **79**, 2222 (2001); L. L. Savchenko, A. K. Zvezdin, A. F. Popkov, and K. A. Zvezdin, Fiz. Tverd. Tela (St. Petersburg) **43**, 1449 (2001) [Phys. Solid State **43**, 1509 (2001)]; J. M. Coey, L. Berger, and Y. Labaye, Phys. Rev. B **64**, 020407 (2001).
10. M. Johnson and R. H. Silsbee, Phys. Rev. B **35**, 4959 (1987); M. Johnson, Science **260**, 320 (1993); P. C. van Son, H. van Kempen, and P. Wyder, Phys. Rev. Lett. **58**, 2271 (1987); M. V. Tsoi, A. G. M. Jansen, J. Bass, *et al.*, Phys. Rev. Lett. **80**, 4281 (1998).
11. T. Valet and A. Fert, Phys. Rev. B **48**, 7099 (1993).
12. A. K. Zvezdin and S. Utochkin, Pis'ma Zh. Éksp. Teor. Fiz. **57**, 418 (1993) [JETP Lett. **57**, 433 (1993)].
13. A. Aronov, Pis'ma Zh. Éksp. Teor. Fiz. **24**, 37 (1976) [JETP Lett. **24**, 32 (1976)]; M. Johnson and R. H. Silsbee, Phys. Rev. Lett. **55**, 1790 (1985).
14. E. I. Rashba, Phys. Rev. B **62**, R16267 (2000).
15. M. Dzero, L. P. Gorkov, A. K. Zvezdin, *et al.*, Phys. Rev. B **67**, 100402 (2003).
16. A. K. Zvezdin and K. A. Zvezdin, Kratk. Soobshch. Fiz. **8**, 3 (2002).
17. V. A. Zhirnov, Zh. Éksp. Teor. Fiz. **35**, 1175 (1958) [Sov. Phys. JETP **8**, 822 (1958)]; L. N. Bulaevskiĭ and V. L. Ginzburg, Pis'ma Zh. Éksp. Teor. Fiz. **11**, 272 (1970) [JETP Lett. **11**, 178 (1970)].
18. A. Hubert, *Theorie der Domanenwande in Geordneten Medien* (Springer-Verlag, Berlin, 1974; Mir, Moscow, 1977).

Translated by M. Astrov

Technical Physics, Vol. 49, No. 3, 2004, pp. 325–329. Translated from Zhurnal Tekhnicheskoĭ Fiziki, Vol. 74, No. 3, 2004, pp. 44–49.
Original Russian Text Copyright © 2004 by Borkovskaya, Dmitruk, Ermolovich, Konakova, Milenin.

SOLID-STATE ELECTRONICS

Effect of γ Radiation from ^{60}Co on the Formation of Metal Contacts to GaAs ($Al_xGa_{1-x}As$) Structures

O. Yu. Borkovskaya, N. L. Dmitruk, I. B. Ermolovich, R. V. Konakova, and V. V. Milenin

Lashkarev Institute of Semiconductor Physics, National Academy of Sciences of Ukraine, pr. Nauki 45, Kiev, 03028 Ukraine

e-mail: konakova@isp.kiev.ua

Received June 2, 2003

Abstract—The properties of nonrectifying AuGe/GaAs ($Al_{0.4}Ga_{0.6}As$) contacts exposed to heat treatment, ^{60}Co γ radiation, and γ radiation combined with the application of an electrical bias are studied. A correlation between the type of interfacial interaction in the contacts and their resistance is found. Results obtained are explained in terms of a diffusion model with a movable boundary of the metal layer. © *2004 MAIK "Nauka/Interperiodica".*

To date, a number of techniques for formation of ohmic contacts (OCs) to GaAs and its solid solutions have been proposed. The available techniques, as well as prospective trends, are considered in reviews and monographs [1–12]. As follows from [1–12], nonrectifying contacts to III–V compounds are usually made by forming a heavily doped layer in the subsurface region of the semiconductor in order to raise the free carrier concentration to the degeneracy level. In this way, a narrow depletion layer in the semiconductor is provided.

Such a layer, being formed prior to metal deposition, is conventionally created by solid-state diffusion, ion implantation, or epitaxy. Otherwise, it may be prepared by crystallizing the eutectic melt appearing after metal deposition. In all cases, high-temperature treatment of the contact structures is necessary. However, heat treatment broadens the metal–semiconductor interface due to mass transfer of the contact pair components and formation of solid solutions and intermetallics. The transition region of the contact becomes disordered and consists of grains, the size, density, and chemical composition of which depend on the heat treatment conditions. Some of the process-related unfavorable factors may be partially or completely eliminated by using laser or electron-beam annealing. Although rapid annealing techniques give good results, vacuum evaporation of metals and alloying-in Au–Ge eutectics covered by different metal layers (Ni, Pt, Ti, or Ag) remain the most-used techniques for preparing low-resistance contacts. The top metal layers influence interfacial interaction during annealing of the contacts and, hence, control their morphological and structural inhomogeneity. The presence of a distinct correlation between phase–structure transformations and the contact resistance value necessitates a reduction of the thermal budget of the process. The time of heat treatment may be cut and its temperature may be decreased by combining heat treatment with exposure to radiation. However, the locality of the irradiation effect and the nonuniformity of temperature distribution over the contact area may lead to troubles. Therefore, combined processing including thermal and athermic techniques is of great interest. Under irradiation, diffusion processes are known to undergo significant modification primarily because the migration of lattice components is related to the radiation-induced variation of the electronic subsystem in the diffusion zone. Heating of the electron gas lowers activation barriers for the motion of defects and impurities, thereby causing their redistribution. Since the OC formation is accompanied by the diffusion redistribution of atoms in the contact area, exposure to radiation may be used as an athermic process.

In this paper, we study the effect of ^{60}Co γ irradiation on the formation mechanism and parameters of OCs to GaAs and $Al_xGa_{1-x}As$.

EXPERIMENTAL

Two types of samples were used in our experiments. The structures of the first type were n–n^+ layers with a concentration of (5–7) × 10^{16} and (1–4) × 10^{18} cm^{-3}, respectively, grown on a semi-insulating GaAs substrate. The structures of the second type were n-$Al_xGa_{1-x}As$ (1×10^{15} cm^{-3})/n^+-GaAs (3.5×10^{18} cm^{-3}) heterostructures with $x \approx 0.4$.

Metallization was carried out under a pressure of 1×10^{-6} Torr by successively evaporating the AuGe eutectic alloy 0.03 (0.05) μm thick and gold 0.27 (0.2) μm thick on the semiconductor surface precleaned in HCl and rinsed in deionized water. The structures obtained were thermally annealed, irradiated by ^{60}Co γ quanta at a dose in the range 10^4–10^9 R, and exposed to γ radia-

1063-7842/04/4903-0325$26.00 © 2004 MAIK "Nauka/Interperiodica"

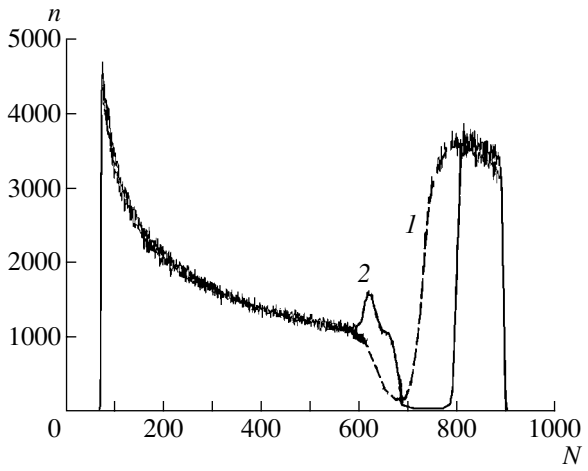

Fig. 1. Energy spectrum of He^+ ions elastically scattered from the AuGe films of different thickness deposited onto GaAs. *d* (*1*) ≥150 and (*2*) ≤100 nm. *n* is the number of counts; *N*, cathode number.

tion with a reverse bias voltage of 2 V applied (the metal was negatively biased).

The contact resistance ρ was measured using the transmission-line method. Its detailed description and requirements for specimens are given in [13].

The chemical composition of the contacts was analyzed by X-ray photoelectron spectroscopy (XPS) combined with ion sputtering (Ar^+, E_i = 1keV) and elastic backscattering of He^+ ion beams with the energy E_0 = 3.0 MeV [14]. The photoelectron spectra were recorded with MgK_α radiation ($h\nu$ = 1253.6 eV). The resolution of the instrument was ≈1.2 eV for the Au 4*f* 1/2 line. The carbon 1*s* line (E = 214.6 eV) and gold 4*f* 7/2 line (E = 13.1 eV) were used as standards. The core-shell electron spectra of C1s, O1s, Au4f, Ga2p, As3d, and Al2p were investigated.

The backscattered ion spectra were recorded by a silicon surface-barrier detector placed at an angle of 135° to the primary ion beam. The energy resolution of the detector was 20 keV. The sample surface examined was ≈1.5 mm^2.

The surface morphology of the structures was studied by atomic force microscopy. Silicon probes with a rated tip size of 10 nm were used in the measurements.

Table 1. Specific resistance of the alloyed Au/AuGe/GaAs contacts

Sample no.	Carriers concentration n, cm^{-3}	Specific contact resistance ρ, Ω cm^2
1	1.25×10^{18}	1.5×10^{-6}
2	1.28×10^{18}	8.6×10^{-6}
3	3.4×10^{18}	8.9×10^{-6}
4	1.8×10^{18}	1.1×10^{-6}

RESULTS AND DISCUSSION

Figure 1 shows the energy spectra of elastically scattered He^+ ions. These spectra characterize the atomic composition of the Au/AuGe/GaAs contacts annealed at T = 300°C for 30 min and the variation of the composition over the thickness. The backscattering spectra from the samples with a metal layer thickness of less than 100 nm (Fig. 1, curve *2*) exhibit a peak, which was assigned to scattering from Ga atoms on the Au surface. In other words, one may expect intense outdiffusion in these structures even under "soft" heat treatment regimes. Experimental evidence for heating-induced migration of Ga atoms from the GaAs into the Au film was found in [4, 15]. In [16], however, the above features of the spectra were related to multiple ion scattering in structures with a disordered surface layer of the semiconductor.

The absence of this peak in the structures with a thicker Au film (Fig. 1, curve *1*), as well as data reported in [17, 18], suggests that the feature (peak) observed in the spectra of backscattered He^+ ions is probably due to local erosion caused by the nonuniform temperature distribution in the semiconductor. Such a mechanism seems quite plausible, because the melting points of eutectics in the sequence Au/Ga/As–Au/Ga–Au/Ge [7] differ insignificantly from the annealing temperature used in this work.

Below, we consider the structures for which the backscattering spectra have the form of curve *1* in Fig. 1.

Table 1 lists the specific contact resistance of these structures annealed at 430°C for 30 s in hydrogen, i.e., under conditions where GaAs–alloy interaction is greatly enhanced because of melting.

The values of ρ obtained are typical of OCs formed in the course of melting and solidification of gold-based eutectics. Such a technique results in the formation of a heavily doped GaAs layer adjacent to the metal–GaAs interface.

Consider now the formation of the contacts and their electrical characteristics in the absence of melting and recrystallization at the interface. In this case, the formation of OCs follows the diffusion model [19], where it is assumed that (i) grain boundary diffusion is responsible for the migration of Ga and As atoms in Au, (ii) the loss of As during low-temperature annealing is negligible; and (iii) prevailing local centers are donors formed by substituting Ge atoms for Ga vacancies $[Ge_{Ga}^+]$.

With a rise in annealing temperature, the solubility of Ga into Au increases and so does the concentration of gallium vacancies V_{Ga}. They are occupied by Ge, which, in turn, raises the donor concentration in the subsurface region of the semiconductor.

The validity of this model can be verified by using XPS in combination with ion sputtering. For this purpose, we constructed the distributions of Ga, As, and

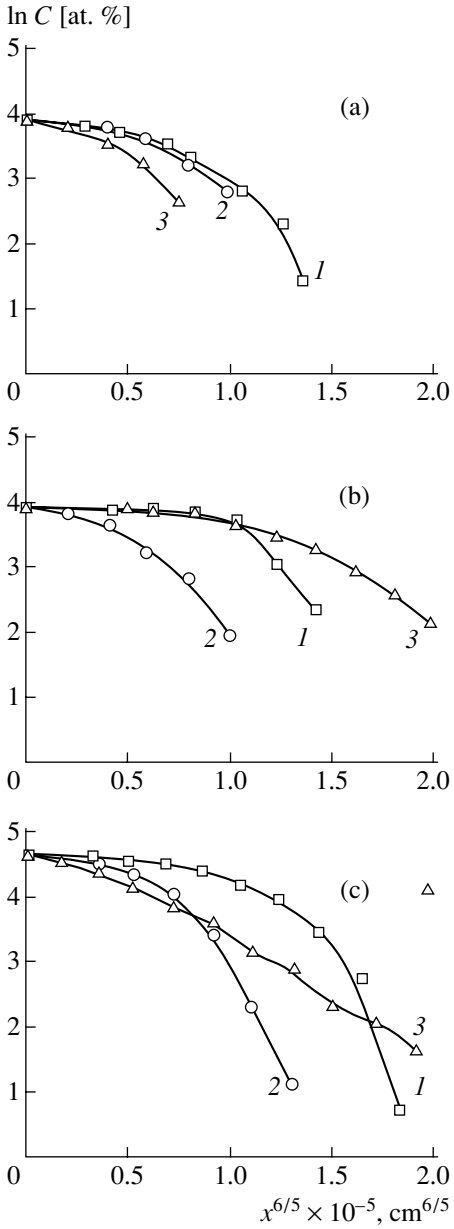

Fig. 2. Distributions of (a) Ga, (b) As, and (c) Au atoms across the AuGe/GaAs contact structure before and after treatments. (*1*) As-prepared sample, (*2*) γ irradiation with a dose of 10^7 R, and (*3*) γ irradiation with a dose of 10^7 under a bias voltage $U = -2$ V.

Au atoms along the normal to the interface in the ln$C$–$x^{6/5}$ coordinates based on layer-by-layer analysis data. Figure 2 shows these distributions for the as-prepared

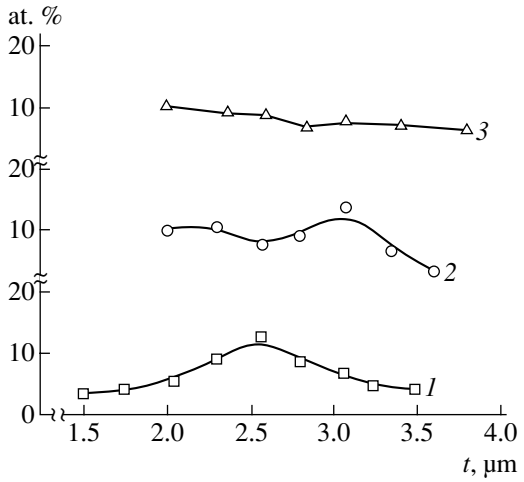

Fig. 3. Ge atom profiles in the AuGe/GaAs contact structures subjected to various treatments. (*1*) As-prepared sample, (*2*) γ irradiation at a dose of 10^7 R, and (*3*) γ irradiation at a dose of 10^7 R under a bias voltage $U = -2$ V.

samples, for the samples exposed to ^{60}Co γ radiation with a dose of 1×10^7 R, as well as for the samples irradiated with the same dose (1×10^7 R) and simultaneously biased at 2 V (the origin corresponds to the maximal signal from one of the components of the contact pair).

As follows from Fig. 2, the linear dependence of ln$C$ on $x^{6/5}$, which is typical of grain boundary diffusion [4], is not observed. Moreover, the profiles of Ga and As are similar to the profile of Au diffusing into the semiconductor substrate. This means that the diffusion mechanism responsible for the distribution of Ga, As, and Au atoms is the same and that grain boundary diffusion does not prevail. As a mechanism of formation of the transition region, it is then reasonable to consider a diffusion model where the metal boundary moves with a constant velocity V. In this case [20], the transition region of the contact is formed by opposing atomic fluxes from the metal layer and from the substrate. As a result, the gold atom concentration is given by

$$C(x, t) = \frac{C_1}{2}\left[\operatorname{erfc}\frac{x - Vt}{2\sqrt{D_1 t}} - \operatorname{erfc}\frac{x + Vt}{2\sqrt{D_1 t}}\right], \qquad (1)$$

and the concentration of semiconductor components,

Table 2. Diffusion parameters of the Au/AuGe/GaAs contacts

Treatment	D_{Au}, cm^2/s	D_{Ga}, cm^2/s	D_{As}, cm^2/s	D_{Ge}, cm^2/s
As-prepared sample	6.8×10^{-12}	6.2×10^{-13}	7.5×10^{-13}	1.7×10^{-11}
1×10^7 R	2.8×10^{-13}	4.5×10^{-15}	1×10^{-14}	1.8×10^{-13}
1×10^7 R, $U = -2$ V	–	1.7×10^{-15}	–	–

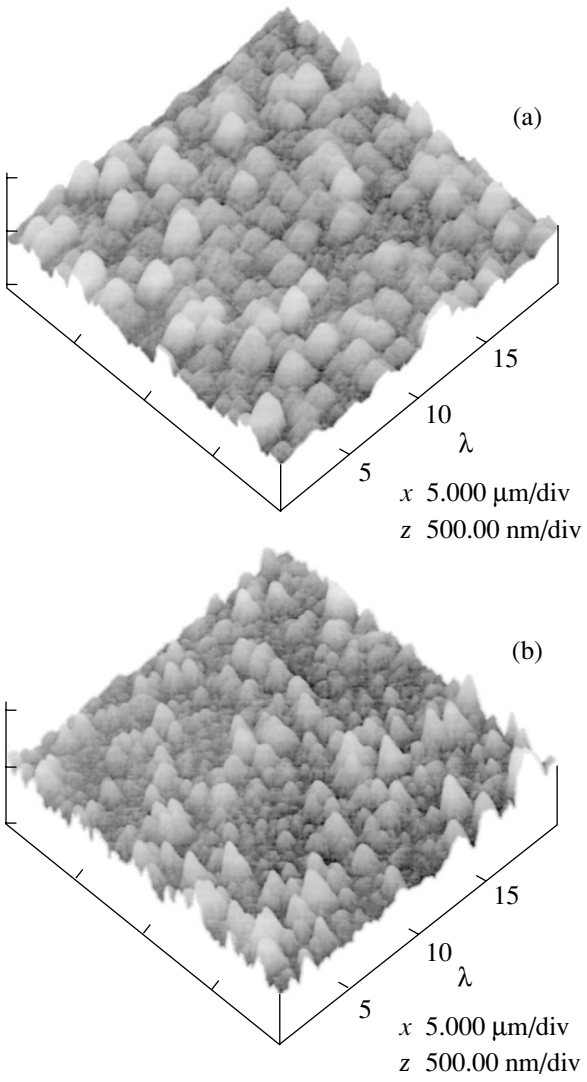

Fig. 4. AFM image of the AuGe/GaAs interface (a) before and (b) after γ irradiation at a dose of 1×10^7 R.

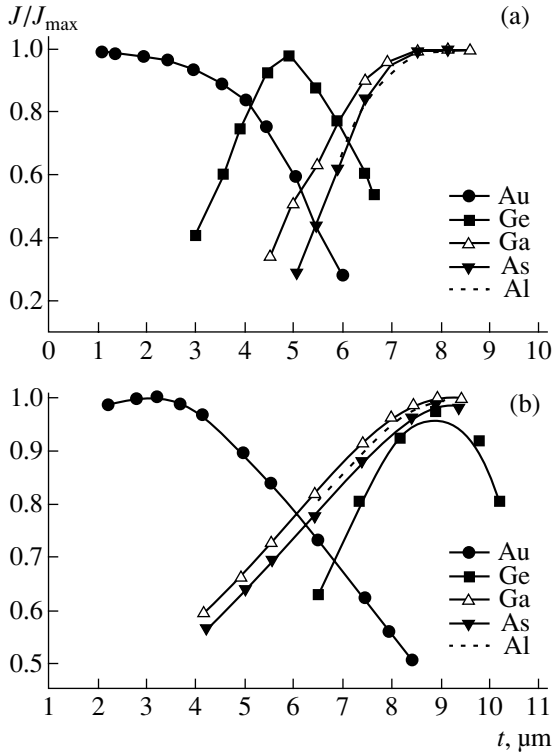

Fig. 5. Component distribution in the transition region of the AuGe/$Al_xGa_{1-x}As$ contact (a) before and (b) after thermal annealing (430°C, 30 s) normalized to the maximal signal from one of the elements.

by

$$C(x, t) = C_2 + \frac{C_2}{2}\left[\operatorname{erfc}\frac{x + Vt}{2\sqrt{D_2 t}} - \operatorname{erfc}\frac{x - Vt}{2\sqrt{D_2 t}}\right]. \quad (2)$$

The values of the diffusion coefficients calculated by (1) and (2) are given in Table 2.

The Ge profiles obtained by layer-by-layer analysis of the contacts are shown in Fig. 3. They differ from the gold profiles and shift toward the GaAs after radiation treatments. Possibly because of this, the value of ρ decreases (see Table 3). These data support the effect of diffusion processes on the OC formation. The diffusion parameters of Ge that are estimated under the assumption of planar-source diffusion [21] are given in Table 2.

The values of the diffusion coefficients for Ga, Ge, and Au in the as-prepared structures are in good agreement with the data of [19]. The decrease in the diffusion coefficients after irradiation is probably a consequence of structural and phase modifications in the contacts. Indeed, as was shown in [22], treatments by radiation may cause the relaxation of internal mechanical strains in the contact, which results in an apparent decrease in the diffusion coefficient. Radiation-induced formation of thin diffusion barriers (e.g., $(GaAs)_{1-x}(Ga_2)_x$ layers, which form during low-temperature thermal treatment [23], or intermetallics [7]) cannot be excluded either.

Table 3. Contact resistance in the Au/AuGe/GaAs structure after irradiation

	γ irradiation, R					γ radiation (R) at $U = -2$ V				
	as-prepared sample	5×10^6	10^7	2×10^7	5×10^7	as-prepared sample	3×10^5	10^7	2×10^7	4×10^7
Contact resistance ρ, Ω cm²	10^{-4}	7×10^{-5}	5×10^{-5}	4×10^{-5}	4×10^{-5}	10^{-4}	4×10^{-5}	2×10^{-5}	2×10^{-5}	2×10^{-5}

Thus, when radiation treatment is combined with heat treatment carried out at temperatures below the eutectic temperature, the mechanism behind OC formation is the superposition of Ge diffusion into the GaAs lattice and solid-phase reactions, which displace the interface. The electronic structure of the newly formed semiconductor surface may differ from the electronic structure of the initial surface. In particular, the Fermi level may be shifted toward the conduction band bottom [24]. As a result, the contact resistance drops.

Since contacts thus produced do not melt, one may expect their high homogeneity. Figure 4 shows the AFM images from the microrelief of the AuGe–GaAs interface (a) before and (b) after γ irradiation. It can be concluded that γ radiation promotes solid-phase reactions, which modify the interface microrelief. However, the modification is not too pronounced to disturb considerably the uniformity of the current passing through the contact.

Consider the effect of γ radiation on the properties of contacts of the second type. Layer-by-layer analysis data for this structure before and after thermal annealing are shown in Fig. 5. At an annealing temperature and time of 430°C and 30 s, respectively, the alloying (solidified) front of the AuGe eutectic penetrates into the subsurface layer of the $Al_{0.4}Ga_{0.6}As$ solid solution, reducing the contact resistance to $7 \times 10^{-5}\ \Omega\ cm^2$. Thus, the OC formation in this case is controlled by the interaction of the solid solution with the melt of the Au–Ge eutectic, and this interaction is responsible for the change in the chemical composition of the interface (Fig. 5). In this situation, the electrical properties of the contact to a great extent depend on the size and composition of forming grains, i.e., on the heat treatment regime. In review [7], a correlation between the grain size and the value of ρ is indicated. This may be a possible explanation for the increase in ρ to $2 \times 10^{-4}\ \Omega\ cm^2$ at an annealing temperature of 450°C. Taking into account that radiation treatment may affect considerably the structure and phase composition at the interface in the contact, we exposed the contacts to γ radiation at doses in the range 10^5–10^8 R. As expected, ρ changed most significantly in the structures that were annealed for a longer time. However, in this case too, the change was small: at doses lower than 10^8 R, ρ decreased approximately twofold, whereas at doses higher than 10^8 R, ρ increased.

Complexity and vagueness of the processes occurring at the interface between metals and III–V semiconductors preclude precision control of the contact formation mechanism. In spite of a great body of data for ohmic contacts, further studies are needed to establish a correlation between the electrical parameters, structure, and chemical composition of the interface. Our work shows that athermic treatments are promising for the formation of good contact structures.

ACKNOWLEDGMENTS

This study was supported by the Ukrainian Center of Science and Technology (project no. UZB-56(J)).

REFERENCES

1. V. L. Rideout, Solid-State Electron. **18**, 541 (1975).
2. V. I. Strikha, G. D. Popova, and E. V. Buzaneva, Poluprovodn. Tekh. Mikroélektron., No. 20, 20 (1975).
3. E. H. Rhoderick, *Metal–Semiconductor Contacts* (Clarendon, Oxford, 1988; Radio i Svyaz', Moscow, 1982).
4. *Thin Films: Interdiffusion and Reactions*, Ed. by J. M. Poate, K. Tu, and J. Meier (Wiley, New York, 1978; Mir, Moscow, 1982).
5. N. Braslau, Thin Solid Films **104**, 391 (1983).
6. A. Piotrowska, A. Guivarch, and G. Pelous, Solid-State Electron. **26**, 179 (1983).
7. B. A. Lapshinov, A. B. Kamnev, L. N. Kravchenko, and V. L. Oplesnin, Zarubezhn. Élektron. Tekh., No. 5 (132), 58 (1987).
8. *GaAs Microelectronics*, Vol. 11 of *VLSI Electronics*, Ed. by N. Einspruch and U. Wisseman (Academic, New York, 1985; Mir, Moscow, 1988).
9. *Ion Implantation and Beam Processing*, Ed. by J. S. Williams and J. M. Poate (Academic, New York, 1984; Naukova Dumka, Kiev, 1988).
10. E. B. Koganovich and S. V. Svechnikov, Optoélektron. Poluprovodn. Tekh., No. 22, 3 (1991).
11. Yu. A. Gol'dberg, Fiz. Tekh. Poluprovodn. (St. Petersburg) **28**, 1681 (1994) [Semiconductors **28**, 935 (1994)].
12. S. Sze, *Physics of Semiconductor Devices* (Wiley, New York, 1981; Mir, Moscow, 1984).
13. M. S. Shur, *GaAs Devices and Circuits* (Plenum, New York, 1987; Mir, Moscow, 1991).
14. L. Feldman and D. Mayer, *Fundamentals of Surface and Thin Film Analysis* (North-Holland, New York, 1986; Mir, Moscow, 1989).
15. S. P. Kwok, J. Vac. Sci. Technol. B **4**, 1383 (1986).
16. N. W. Cheung, P. J. Grunthaner, F. J. Grunthaner, *et al.*, J. Vac. Sci. Technol. **18**, 917 (1981).
17. J. Gynlai, J. W. Mager, V. Rodriquez, *et al.*, J. Appl. Phys. **42**, 3578 (1971).
18. T. S. Kuan, P. E. Batson, T. N. Jackson, *et al.*, J. Appl. Phys. **54**, 6952 (1983).
19. A. K. Kulkarui and C. Lai, J. Vac. Sci. Technol. A **6**, 1531 (1988).
20. G. B. Abdulaev and G. D. Dzhafarov, *Atomic Diffusion in Semiconductors* (Atomizdat, Moscow, 1980).
21. B. I. Boltaks, *Diffusion in Semiconductors* (Fizmatgiz, Moscow, 1961; Academic, New York, 1963).
22. S. A. Grusha, R. V. Konakova, V. V. Milenin, *et al.*, Elektron. Tekh., Ser. 2: Poluprovodn. Prib. **45** (208), 68 (1990).
23. B. Kramer, G. Tomasch, M. Ray, *et al.*, J. Vac. Sci. Technol. A **6**, 1572 (1988).
24. Yu. A. Gol'dberg and E. A. Posse, Fiz. Tekh. Poluprovodn. (St. Petersburg) **32**, 200 (1998) [Semiconductors **32**, 181 (1998)].

Translated by M. Lebedev

Technical Physics, Vol. 49, No. 3, 2004, pp. 330–334. Translated from Zhurnal Tekhnicheskoĭ Fiziki, Vol. 74, No. 3, 2004, pp. 50–54.
Original Russian Text Copyright © 2004 by Ivanov, Kandaurova.

SOLID-STATE ELECTRONICS

Magnetization Reversal in Amorphous Gadolinium–Cobalt Films with a Radial Gradient of Magnetic Properties

V. E. Ivanov and G. S. Kandaurova

Gorkii Ural State University, pr. Lenina 51, Yekaterinburg, 620083 Russia

e-mail: vladimir.ivanov@usu.ru

Received June 30, 2003

Abstract—The integral characteristics of magnetization switching in amorphous gadolinium–cobalt films with perpendicular anisotropy are studied by visualizing the domain structure and measuring magnetooptic hysteresis loops. The films have a radial gradient of magnetic properties that is due to a spatially nonuniform thermal field. Magnetization switching in those film areas where the domain wall motion depends only on the coercive force is simulated in simple terms. In a first approximation, local events of magnetization switching are shown to take place independently of each other and the net hysteresis loop can be represented as a sum of the local loops. © *2004 MAIK "Nauka/Interperiodica".*

The domain structure (DS) in films with perpendicular anisotropy generates both applied [1] and scientific [2, 3] interest. Technical use of iron garnet films is based on the high sensitivity of their DS to a magnetic field, which renders them indispensable in magnetic field visualization [4]. The DS of metallic amorphous films is more sensitive to temperature fields [5]; so, they are used to visualize them [6].

The magnetization of thin multidomain films with perpendicular anisotropy is well studied both theoretically and experimentally. If the coercivity H_C of domain walls is small compared with the maximal stray field $4\pi M_S$ or if the reduced coercivity $h_C = H_C/4\pi M_S < 0.01$, where M_S is the saturation magnetization, the magnetization process is described by the theory developed in [7]. In the case of high-coercivity magnets, hysteresis effects should be taken into account. Then, the ascending and descending branches of the hysteresis loop are satisfactorily described by a solution to the set of equations derived in [8].

As h_C grows, the magnetization switching process is increasingly defined by the coercive force and its dispersion. The transition from the high-coercivity to low-coercivity state may be observed in amorphous Gd–Co films when the temperature is varied within an interval including the temperature of magnetic compensation. In this case, the spatially nonuniform magnetic field causes the magnetization M_S and the coercive force H_C to be space dependent; accordingly, the magnetization curve becomes coordinate sensitive. The question arises as to whether the magnetization process depends only on local magnetic parameters $M_S(x)$ and $H_C(x)$ or there exists a correlation between the magnetizations of adjacent domains. The aim of this work is to experimentally study the integral characteristics of magnetization switching in magnetically nonuniform (in plane) Gd–Co films and to estimate the feasibility of simulating this process (the magnetic nonuniformity is due to the nonuniform spatial temperature distribution generated by a conventional point heat source).

EXPERIMENTAL

Amorphous 0.5- to 1.0-μm-thick Gd–Co films with perpendicular anisotropy were prepared by rf ion–plasma sputtering on glass water-cooled substrates. The free surface of the films was protected by a ≈500 Å thick glass coating. The compensation temperature T_M of the magnetic moment was somewhat higher than room temperature, $T_M \approx 53$°C.

A temperature gradient arose because of a temperature difference between a massive brass "thermostat" and "heat source" (the junction of a copper/constantan thermocouple). The source was heated by passing the current through the constantan leads, and the thermal emf was derived from the copper/constantan thermocouple. In a first approximation, the area of source–amorphous film thermal contact may be considered to be a circle of radius ≈40 μm. Near the contact, the temperature T of the films was assumed to be constant and roughly equal to the source temperature T_S.

The domain structure was visualized by means of the polar magnetooptic Kerr effect through the glass substrate. The magnetization was accomplished at a fixed source temperature T_S and was controlled by measuring surface magnetooptic hysteresis loops in the j–H coordinates at various sites of the sample, where $j(H) = M/M_S$ is the relative magnetization and M is the magnetization in a field H. The measurements were taken by varying the field of vision of the DS with the field stop of a microscope. The hysteresis loops were digitized with the Origin editor.

1063-7842/04/4903-0330$26.00 © 2004 MAIK "Nauka/Interperiodica"

Figure 1 shows the temperature dependences of the saturation magnetization M_S, coercive force H_C, and domain width d_0 in the demagnetized (equilibrium) state. The curves were taken in a uniform thermal field, i.e., without a temperature gradient in the plane of the film. They are necessary for simulating the magnetization process, determining local temperatures from the DS parameters, and recovering the nonuniform temperature field pattern in the plane of the film. The curve H_C in Fig. 1a was constructed by the formula

$$H_C = C/(T - T_M), \quad (1)$$

where the constant $C = 1500$ provides the best fit to experimental data.

The reduced thickness L/l (L is the thickness of the film, $l = \sigma_w/4\pi M_S^2$ is the characteristic length of the material, and σ_w is the energy density of domain walls) that is necessary for calculating the magnetization curves $j(H)$ was found by the Malek–Kambersky equation [9] with the values of d_0/L known.

The hysteretic properties were studied with the well-studied DS [5], which arises in a spatially nonuniform centrosymmetric temperature field produced by a conventional point heat source kept at $T_S = 195$°C (Fig. 2). At the center of the temperature distribution, the temperature of the film far exceeds T_M; therefore, the DS is here fine and hardly observable: the domain width is ≈4 μm. As T approaches the compensation temperature away from the center, the DS coarsens. In Fig. 2 (upper panel), areas (windows) where hysteresis loops were taken are outlined by circles *a*–*d*. In the lower panel, the radial dependences of the temperature T, saturation magnetization M_S, and relative coercivity h_C of domain walls are depicted (the origin is placed at the center of symmetry of the DS pattern). The curves were constructed by the technique suggested in [6]. The hysteresis loops corresponding to these windows are shown in Figs. 3a–3d.

The loops in Figs. 3a and 3c were measured in the window with the minimal possible (under the experimental conditions) diameter, with the center of window *c* being shifted relative to the center of symmetry of the DS under study. It is seen that H_C increases with distance from the heat source, while the nucleation field H_N decreases; that is, the nucleation of the reversed magnetic phase becomes difficult.

As the diameter of the window increases, the coercive force tends to grow and the loop smooths out (cf. Figs. 3a, 3b). Apparently, the field H_C grows when higher coercivity film areas with a temperature approaching T_M start contributing to the magnetization. The loop smooths out near the nucleation field, because this field varies in the radial direction.

The integral hysteresis loop was simulated as follows. The entire film was divided into two regions. One is a circle of diameter D_k centered at the origin (Fig. 2). This region is selected in such a way that the relation-

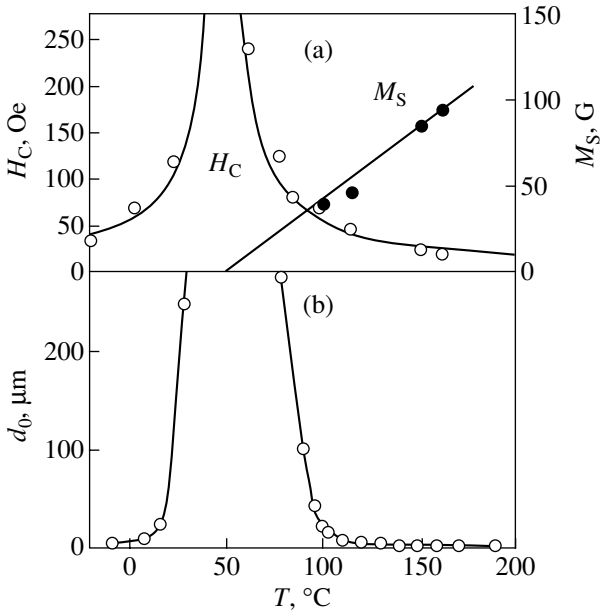

Fig. 1. Temperature dependences of the (a) saturation magnetization M_S and coercive force H_C and (b) domain width d_0 for the Gd–Co film with a temperature of compensation of the magnetic moment $T_M = 53$°C.

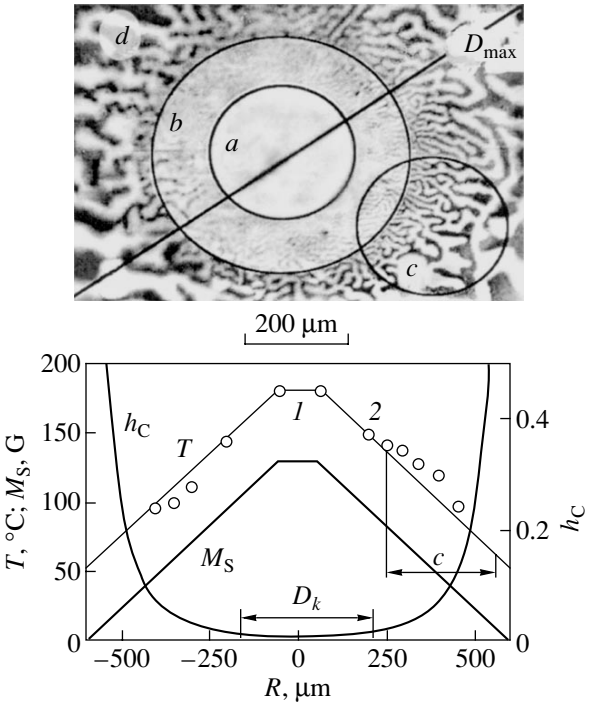

Fig. 2. Domain structure of the Gd–Co film subjected to the spatially nonuniform temperature field (upper panel) and the associated radial dependences of the temperature T, saturation magnetization M_S, and reduced coercive force h_C (lower panel).

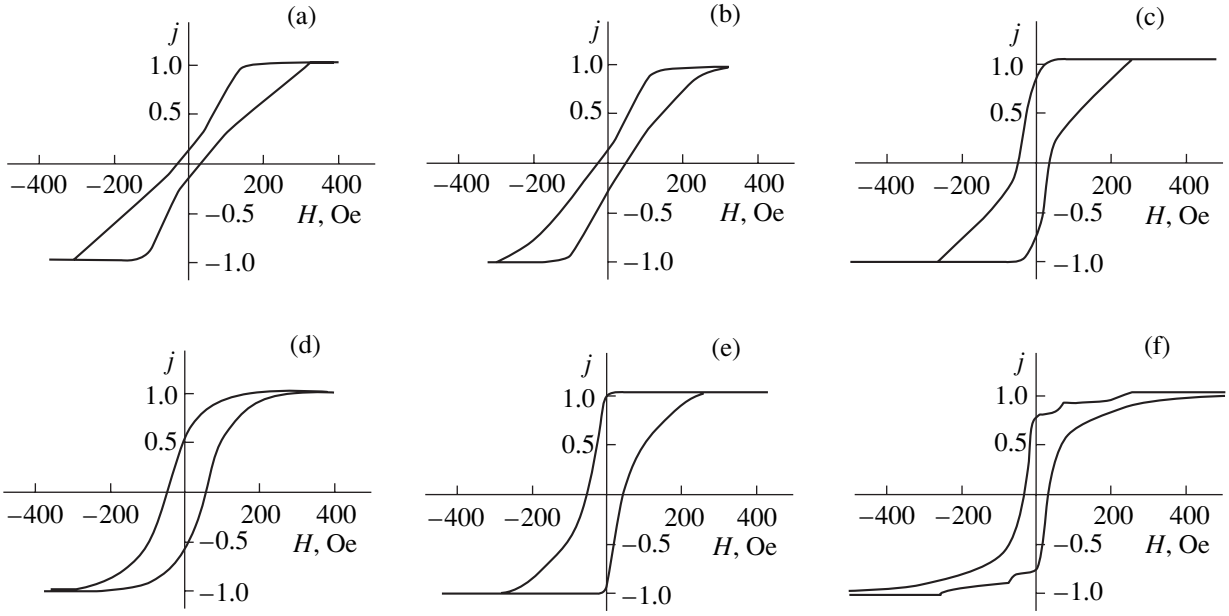

Fig. 3. (a–d) Experimental magnetooptic hysteresis loops taken in the windows shown in Fig. 2 and (f) calculated hysteresis loop.

ship $h_C = H_C/4\pi M_S \le 0.01$ is fulfilled in it. In this region, we calculated local hysteresis loops by the equations derived in [8]. The other region is a higher coercivity ($h_C > 0.01$) ring bounded by the circles with the diameters D_k and D_{max}. In this region, the magnetization switching process was simulated under the assumption that the self-demagnetizing field is absent. The integral hysteresis loop was obtained by summing the local loops with their associated weighting factors.

(1) To construct the hysteresis loops, we, following [6], recovered the coordinate dependence of the temperature, with the origin placed at the center of symmetry of the DS (Fig. 2). The experimental curve $T(R)$ was approximated by the linear dependence $T = T_0 - \alpha R$, where $T_0 = 190$°C and $\alpha = 0.27$°C/μm. It was assumed that the temperature near the film–source contact area is constant, so that there exists a plateau (curve *1* in Fig. 2) directly above the source, where the magnetic properties remain unchanged.

In the low-coercivity region ($h_C < 0.01$), the hysteresis loop $j(H)$ was calculated by the formulas [8]

$$\frac{1}{\tau} = \frac{1}{4\pi^2\alpha^2}\sum_{n=1}^{\infty}\frac{1}{n^3}\sin^2\left[\frac{\pi n(1+j)}{2}\right] \times [1-(1+2\pi n\alpha)\exp(-2\pi n\alpha)] \pm \frac{\pi h_C}{4\alpha}, \quad (2)$$

$$h = j + \frac{1}{\pi^2\alpha}\sum_{n=1}^{\infty}\frac{1}{n^2}\sin[\pi n(1+j)] \times [1-\exp(-2\pi n\alpha)] \pm h_C. \quad (3)$$

Here, $\tau = (4M_S)^2 L/\sigma_w$; $\alpha = L/P = L/(d_1 + d_2)$; $h = H/4\pi M_S$; $j = (d_1 - d_2)/(d_1 + d_2)$ is the relative magnetization; σ_w is the surface energy density of domain walls; and d_1 and d_2 are the widths of domains where the magnetization is, respectively, parallel and antiparallel to the external field. The plus and minus signs correspond to the rise and decline of the external field.

The hysteresis loop shown in Fig. 4a was calculated in terms of the model suggested in [8] with the parameters meeting plateau *1* in Fig. 2: $T = 180$°C, $d_0 = 2$ μm, $M_S = 139$ G, and $h_C = 0.006$. Then, we calculated the loop for $T = 150$°C (Fig. 4b) with $d_0 = 3$ μm, $M_S = 103$ G, and $h_C = 0.01$. The latter case geometrically corresponds to a circular area of radius $R = 190$ μm on the film (point *2* in Fig. 2).

(2) With distance from the center of the pattern (Fig. 2) (approach to the compensation temperature), M_S drops, H_C grows, and eventually the theory [8] becomes inapplicable to this film when $h_C > 0.013$. Therefore, when simulating magnetization switching over window *c* in Fig. 2 (see portion *c* of the curve $T(R)$ in the lower part of Fig. 2), we proceeded as follows. The magnetization process in the annular region of the film, which is bounded by the radii $R_1 = 250$ μm and $R_2 = 550$ μm, was assumed to depend largely on the coercive force of the film. Such an approach is valid, since the saturation magnetization in this region is low; hence, the demagnetizing stray fields, which could generate the DS in the absence of the external magnetic field, are also small. For simplicity, we suppose that two, "white" and "black," domains exists during magnetization switching and that $H = H_C$ at their boundary.

A rectangular window for which calculations were carried out is shown in Fig. 5. With the origin ($x = 0$) placed at the center of the window, the relative magnetization is given by $j = x/a$, where $2a$ is the width of the window along the radius R. The coordinate, in turn, is found from the condition $H = H_C(x)$. The dependence $x(H)$ is determined from the equation

$$H_C(x) = C/(T(x) - T_M) = H(x),$$

in view of (1). Then,

$$j = 1/\alpha a[[T_1 + T_2]/2 - T_k - C/H], \qquad (4)$$

where α is the spatial gradient of the magnetization and T_1 and T_2 are the respective temperatures at the left-hand and right-hand boundaries of the region.

Figure 3e shows the hysteresis loop, the descending and ascending branches of which were calculated by formula (4). In essence, this loop is a theoretical integral hysteresis loop for window *c* in Fig. 2, where magnetization switching proceeds in such a way that the coercive force alone counteracts the external field. Comparing the loop in Fig. 3e with the experimental hysteresis loop (Fig. 3c), we may conclude that our simulation describes the real magnetization switching process adequately (at least, on a qualitative basis).

(3) The theoretical integral hysteresis loop corresponding to window *d* (Fig. 2) with the maximal diameter D_{max} was obtained as follows. The relative magnetization j of the net loop was found by summing the partial magnetizations with the weighting factors proportional to the related areas:

$$j(H) = \sum_{i=1}^{3} j_i(H)\rho_i, \qquad (5)$$

where $i = 1$–3 is the annular region number; j_i is the relative magnetization in an ith region at a given value of H; $\rho_i = S_i/S$; S_i is the surface area of a ring where the hysteresis loop is calculated; and S is the surface area of window *d*, which has the maximal radius.

It was assumed that the hysteretic properties of the annular regions vary along the radius insignificantly, so that the theoretical loops describe the averaged magnetization process in each of the rings. In our case, the surface area ratio is $S_1 : S_2 : S_3 = 1 : 1 : 6$. Comparing the theoretical integral hysteresis loop thus constructed (Fig. 3f) with the experimental magnetooptic loop for maximal window *d* (Fig. 3d) indicates qualitative agreement between the theory and experiment. The jumps on the theoretical loop may be due to the crudeness of the simulation (the small number of steps). This loop may be smoothed out by adding up a greater number of theoretical hysteresis loops calculated with a smaller step in coordinate and, hence, in temperature and magnetic properties.

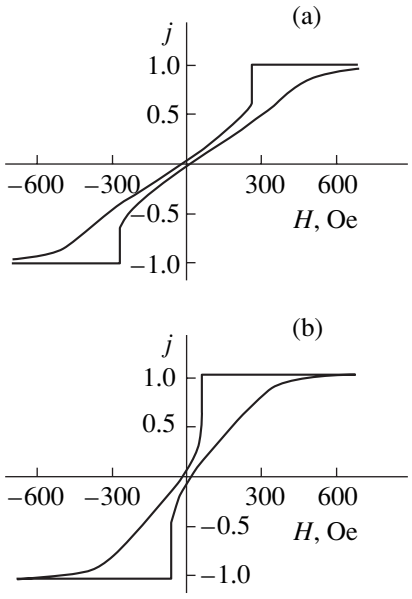

Fig. 4. Hysteresis loops for the Gd–Co film at T = (a) 180 and (b) 150°C. Calculation by the theory [8].

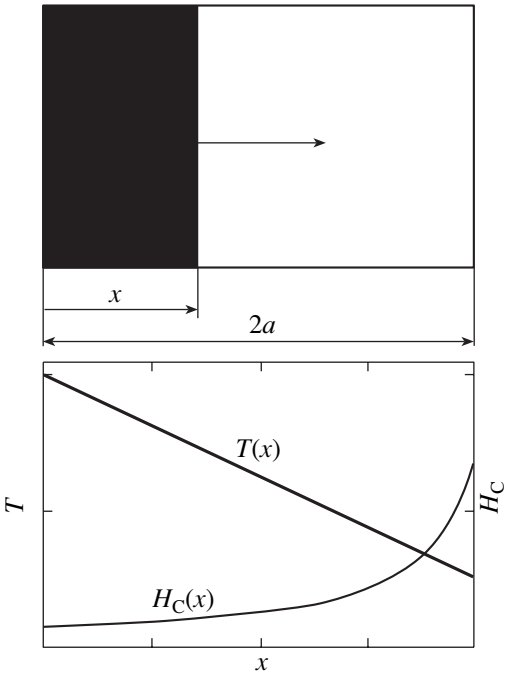

Fig. 5. Simplified (two-domain) structure of a film area and the corresponding coordinate dependences of the temperature and coercive force. The arrow shows the direction of motion of the domain wall.

CONCLUSIONS

Thus, we showed experimentally and theoretically that magnetization reversal in amorphous Gd–Co films

with a domain structure formed in spatially nonuniform (point heat source) and spatially uniform temperature fields proceeds in a much different way. In the latter case, hysteresis loops, as a rule, exhibit steps near the DS nucleation field. In the former case, the resulting coordinate dependence of the magnetic properties of the film smooths out the steps.

The magnetization of domains where the coercive force depends considerably on the coordinate and is the only factor governing the motion of domain walls is described in simple terms. In a first approximation, local processes of magnetization reversal take place independently of each other and the net hysteresis loop is obtained by adding up local loops.

ACKNOWLEDGMENTS

The authors thank L.V. Semenyuk for assistance.

This work was partially supported by the programs "Universities of Russia" and "Fundamental Research in the Field of Natural Sciences" of the Ministry of Education of the Russian Federation, Russian Foundation for Basic Research, and CRDF.

REFERENCES

1. V. V. Randoshkin and A. Ya. Chervonenkis, *Applied Magnetooptics* (Énergoatomizdat, Moscow, 1990).
2. G. S. Kandaurova and A. E. Sviderskij, Zh. Éksp. Teor. Fiz. **97**, 1218 (1990) [Sov. Phys. JETP **70**, 684 (1990)].
3. G. S. Kandaurova, Usp. Fiz. Nauk **172**, 1165 (2002) [Phys. Usp. **45**, 1051 (2002)].
4. N. F. Kubrakov, Trudy Inst. Obshch. Fiz. Ross. Akad. Nauk **35**, 136 (1992).
5. V. E. Ivanov and G. S. Kandaurova, Fiz. Met. Metalloved. **82**, 9674 (1996).
6. V. E. Ivanov, G. S. Kandaurova, and A. V. Svalov, Zh. Tekh. Fiz. **67** (7), 112 (1997) [Tech. Phys. **42**, 823 (1997)].
7. C. Kooy and U. Enz, Philips Res. Rep. **15**, 7 (1960).
8. M. Masuda and S. Yoshino, Res. Rep. Fac. Eng. Mie Univ. **25**, 59 (1980).
9. Z. Malek and V. Kambersky, Czech. J. Phys. **8**, 416 (1958).

Translated by V. Isaakyan

Technical Physics, Vol. 49, No. 3, 2004, pp. 335–337. Translated from Zhurnal Tekhnicheskoĭ Fiziki, Vol. 74, No. 3, 2004, pp. 55–57.
Original Russian Text Copyright © 2004 by Bodnar', Yakushev.

OPTICS, QUANTUM ELECTRONICS

Low-Temperature Photoluminescence in $AgGaSe_2$ Single Crystals

I. V. Bodnar'* and M. V. Yakushev**

** Belarussian State University of Information Science and Radio Electronics, ul. Brovki 17, Minsk, 220072 Belarus*
e-mail: chemzav@gw.bsuir.unibel.by
*** Department of Physics and Applied Physics, Strathclyde University, Glasgow G4 ONG, United Kingdom*

Received May 5, 2003

Abstract—Photoluminescence spectra from a single-crystalline $AgGaSe_2$ ternary compound grown by the Bridgman–Stockbarger method from a nonstoichiometric melt are studied in the temperature interval 8–300 K under various excitation levels. The spectra contain emission bands associated with donor–acceptor recombination, as well as with bound and free excitons. The exciton binding energy and the energy gap of the $AgGaSe_2$ crystals are evaluated. The temperature dependence of the energies of bound and free excitons, as well as of the energy gap of the crystals, is constructed. © *2004 MAIK "Nauka/Interperiodica".*

INTRODUCTION

Silver selenogallate $AgGaSe_2$, as well as other I–III–VI_2 compounds, crystallizes into a chalcopyrite structure (the space group D_{2d}^{12}–I42*d*) and is a chemical electronic analogue of the $Zn_{0.5}Cd_{0.5}Se$ solid solution. The presence of birefringence and an optically isotropic point (the point where the dispersion curves for the ordinary, n_o, and extraordinary, n_e, refractive indices intersect) makes this compound promising for electrooptic modulators and narrow-band filters [1–3].

The aim of this work is to study low-temperature photoluminescence in an $AgGaSe_2$ ternary compound. Earlier, photoluminescence in this compound was investigated elsewhere [4–7].

EXPERIMENTAL

$AgGaSe_2$ single crystals were grown by the Bridgman–Stockbarger method from a nonstoichiometric melt with a seed oriented in the [110] direction. The growth was accomplished in a two-zone vertical furnace. The temperatures in the growth (melt) and annealing zones were kept at ≈1170 and ≈920 K, respectively. The ampoule was pulled with a rate of ≈0.12 mm/h under a temperature gradient of ≈40 K/cm. The single crystals grown were 18 mm in diameter and 35–40 mm in length. They were homogeneous throughout the length (less the 3-mm-long top part), as established by means of X-ray microprobe spectrum analysis and X-ray diffraction.

The composition of the single crystals was determined with a Cameca-MBX microprobe analyzer. The element concentration was determined with an accuracy of 5% or higher. The element ratio (Ag : Ga : Se = 25.36 : 24.39 : 49.26 at.%) was found to be in good agreement with the initial composition of the charge (Ag : Ga : Se = 25.00 : 25.00 : 50.00 at.%). No significant variation of the composition over the crystals was observed, which indicates their high homogeneity.

The structure and equilibrium state of the crystals were determined by X-ray diffraction on a DRON-3M diffractometer (filtered copper radiation). The X-ray data showed that the crystals had the structure of chalcopyrite with the unit cell parameters $a = 5.993 \pm 0.001$ Å and $c = 10.88 \pm 0.01$ Å, which is in good agreement with data in [8, 9]. The fact that high-angle reflections on the diffraction patterns were resolved suggests that the single crystals were in the equilibrium state.

Photoluminescence (PL) spectra were taken from cleavage surfaces with the setup described in [10] at temperatures from 8 to 300 K.

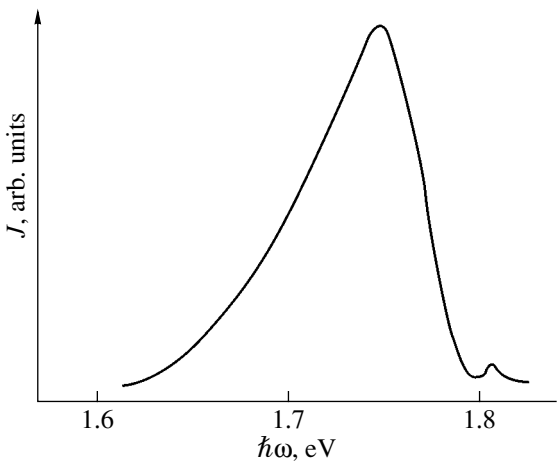

Fig. 1. Stationary PL spectrum taken of the $AgGaSe_2$ single crystals at 8 K.

1063-7842/04/4903-0335$26.00 © 2004 MAIK "Nauka/Interperiodica"

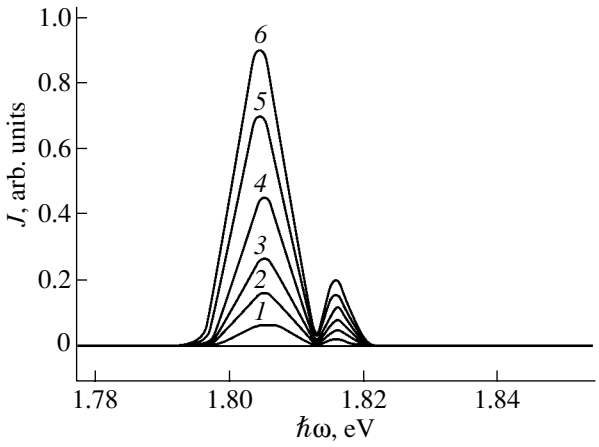

Fig. 2. Normalized emission spectra for free and bound excitons in the $AgGaSe_2$ single crystals under various excitation levels: (*1*) 25, (*2*) 100, (*3*) 150, (*4*) 200, (*5*) 250, and (*6*) 300 mW.

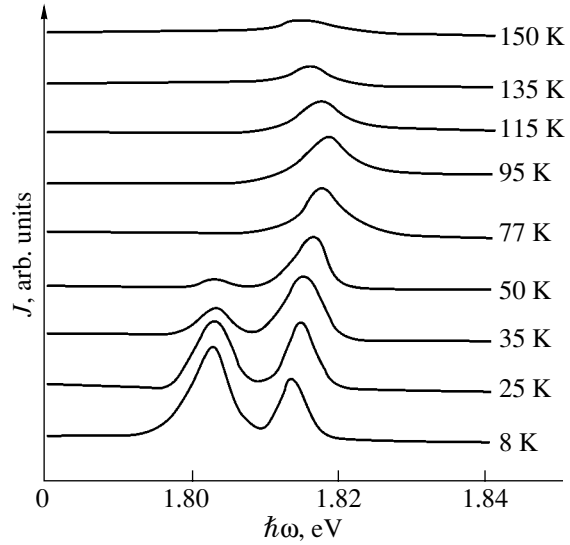

Fig. 3. Temperature behavior of the emission lines for free and bound excitons in the $AgGaSe_2$ single crystals.

Figure 1 shows the PL spectrum taken from $AgGaSe_2$ at 8 K. At this temperature, the spectrum exhibits two lines, one of which (at 1.749 eV) dominates. It is likely that this line is associated with a donor–acceptor recombination where silver acts as a donor and a gallium vacancy, as an acceptor (as for other I–III–VI_2 compounds). The other line with a peak at 1.806 eV seems to be related to the recombination of a free exciton in the ground state. To reliably identify this line, we considered recombinations of a bound exciton, free exciton, and donor–acceptor bond.

As is known, a basic recombination mechanism can be found from the dependence of the PL peak height on the laser excitation power at a fixed temperature. At 8 K, such a dependence for the $AgGaSe_2$ crystals is demonstrated in Fig. 2. At laser outputs above 25 mW, a new line peaking at 1.816 eV appears in the spectrum. The intensity of both lines grows with the laser power, that of the older one increasing more rapidly. It was shown [11] that an exciton-ionized acceptor complex may exist only if $\sigma = m_e/m_h < 0.29$, where m_e and m_h are the effective masses of an electron and hole. For $AgGaSe_2$ ($\sigma = m_e/m_h = 0.17/0.73 = 0.23$), this condition is met. Thus, the first line may be related to a bound exciton (i.e., an exciton-ionized complex); the second, to the ground state of a free exciton.

Figure 3 shows the temperature variation of the exciton lines. The intensity of both lines drops with increasing temperature, the first line (bound exciton) decaying much faster. It is observed at temperatures between 8 and 50 K. At higher temperatures, it disappears because of thermal ionization in $AgGaSe_2$ crystals. The existence interval for the second line is considerably wider: from 8 to 150 K.

In terms of the hydrogen-like atom approximation, the binding energy of a free exciton is calculated by the formula

$$R = m^* e^4/2\hbar^2\varepsilon_0^2, \quad (1)$$

where $m^* = m_e m_h/(m_e + m_h)$ is the reduced effective mass.

In $AgGaSe_2$, $m^* = 0.138m_0$ and the permittivity $\varepsilon_0 = 10.9$ [12]. The binding energy calculated by (1) is $R = 16$ meV, and the energy gap found from the formula

$$E_{ex} = E_g - R/n^2 \quad (2)$$

is $E_g = 1.832$ eV at 8 K.

Figure 4 illustrates the temperature dependences of the binding energy for bound (E) and free (E_{ex}) excitons and of the energy gap. The behavior of E_{ex} is anomalous. In the interval 8–95 K, the free exciton energy first grows with temperature from 1.816 to 1.821 eV and then drops. Such temperature behavior of the binding temperature may be explained by the action of two competing mechanisms: electron–phonon interaction and temperature variation of the $AgGaSe_2$ unit cell parameters [13]. Similar behavior of the free exciton line for $AgGaTe_2$ was also observed in [14].

Thus, one may conclude that the line with the peak at 1.806 eV is associated with the recombination of a bound exciton into an acceptor level. As was shown above, the $AgGaSe_2$ single crystals grown are slightly enriched by silver and depleted by gallium. The deviation from stoichiometry (1 : 1 : 2) causes electroactive intrinsic defects. From the expressions [15] for nonmolecularity,

$$\Delta x = [Ag]/[Ga] - 1 \quad (3)$$

and valence stoichiometry,

$$\Delta y = 2[Se]/[Ag] + 3[Ga] - 1 \quad (4)$$

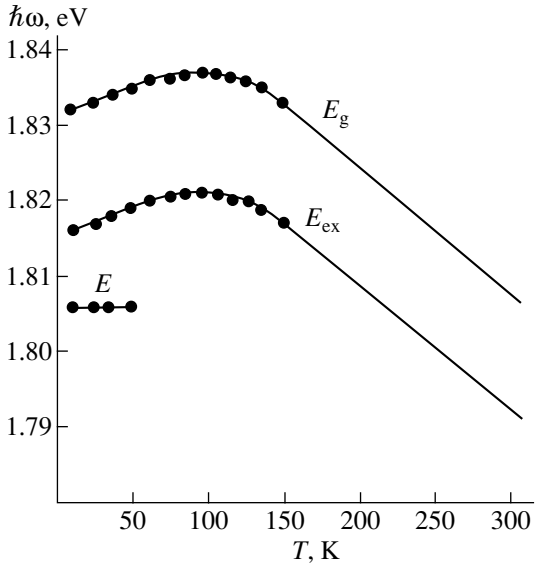

Fig. 4. Temperature dependences of bound- and free-exciton energies (E, and E_{ex}, respectively) and of the energy gap E_g in the $AgGaSe_2$ single crystals.

(where [Ag], [Ga], and [Se] are the concentrations of silver, gallium, and selenium in the $AgGaSe_2$ compound), one finds that $\Delta x > 0$ and $\Delta y > 0$. Since chalcopyrite-like semiconductors are chemically imperfect, it may be inferred that an exciton related to an Ag_{Ga} or Ga_{Ag} acceptor is responsible for the PL line with the peak at 1.806 eV.

The calculated temperature coefficient of the energy gap was $+0.7 \times 10^{-4}$ eV/K in the interval 8–95 K and -1.5×10^{-4} eV/K in the interval 100–150 K.

The extrapolation of E_g to 300 K yields an $AgGaSe_2$ energy gap of 1.807 eV, which agrees well with data reported in [7].

CONCLUSIONS

The study of low-temperature PL spectra taken for a single-crystalline $AgGaSe_2$ ternary compound showed that, at 8 K, they contain two lines at $\hbar\omega = 1.749$ eV and 1.806 eV, the former dominating. The effects of excitation level and temperature on the PL line intensity and position were investigated.

It was shown that the intensity grows with increasing excitation level, while the energy positions of the lines remain unchanged. Temperature variation, however, changes both the intensity and the energy position of the lines. The binding energy of a free exciton first grows from 1.816 to 1.821 eV in the interval 8–95 K and then gradually drops to 1.807 eV at 150 K. The binding energy of a free exciton and the energy gap of $AgGaSe_2$ crystals were calculated.

ACKNOWLEDGMENTS

This work was financially supported by the Ministry of Education of the Republic of Belarus and INTAS (project no. 2001-283).

REFERENCES

1. G. D. Boyd, H. M. Kasper, Y. H. McFee, and F. G. Storz, IEEE J. Quantum Electron. **8**, 900 (1972).
2. V. V. Badikov, I. N. Matveev, and S. M. Pshenichnikov, Kristallografiya **26**, 537 (1981) [Sov. Phys. Crystallogr. **26**, 304 (1981)].
3. N. Yamamoto, H. Takehara, H. Horinaka, and T. Miyauchi, Jpn. J. Appl. Phys. **25**, 1397 (1986).
4. B. Tell and H. M. Kasper, Phys. Rev. B **4**, 4455 (1971).
5. V. F. Agekyan, N. V. Orekhova, D. Radzhab, and A. Yu. Serov, Fiz. Tverd. Tela (Leningrad) **34**, 2272 (1992) [Sov. Phys. Solid State **34**, 1215 (1992)].
6. K.-M. Nigge, F. P. Baumgartner, and E. Bucher, Sol. Energy Mater. Sol. Cells **43**, 335 (1996).
7. M. C. Petcu, N. C. Giles, P. G. Schunemann, and T. M. Pollak, Phys. Status Solidi B **198**, 881 (1996).
8. G. S. C. Abrahams and J. L. Bernstein, J. Chem. Phys. **59**, 5415 (1973).
9. P. Kistaiah, J. C. Venudhar, K. S. Murthy, *et al.*, J. Less-Common Met. **77**, 17 (1981).
10. S. M. Wasim and J. D. Albornoz, Phys. Status Solidi A **110**, 583 (1998).
11. I. V. Bodnar', V. F. Gremenok, R. F. Martin, *et al.*, Zh. Prikl. Spektrosk. **67**, 222 (2000).
12. R. Marquez and C. Rincon, Phys. Status Solidi B **191**, 115 (1995).
13. I. V. Bodnar' and N. S. Orlova, Izv. Akad. Nauk SSSR, Neorg. Mater. **23**, 758 (1987).
14. I. V. Bodnar', V. F. Gremenok, R. B. Martin, and M. V. Yakushev, Opt. Spektrosk. **88**, 424 (2000) [Opt. Spectrosc. **88**, 377 (2000)].
15. J. A. Groenink and P. H. Janse, Phys. Chem. **110**, 17 (1978).

Translated by V. Isaakyan

Technical Physics, Vol. 49, No. 3, 2004, pp. 338–341. Translated from Zhurnal Tekhnicheskoĭ Fiziki, Vol. 74, No. 3, 2004, pp. 58–61.
Original Russian Text Copyright © 2004 by Kalugin, Sobolev.

OPTICS, QUANTUM ELECTRONICS

Optical Properties of CdF_2 in a Wide Energy Range

A. I. Kalugin and V. V. Sobolev

Udmurt State University, Universitetskaya ul. 1, Izhevsk, 426034 Russia

e-mail: sobolev@uni.udm.ru

Received May 20, 2003

Abstract—For either of the two reflection spectra of cadmium difluoride that are known from experiments, a complete set of the fundamental optical functions is calculated in the energy range 4–45 eV with the Kramers–Kronig relationships. The basic features of the optical spectra are established, and a hypothesis for their origin is suggested based on the known theoretical results for the band structure. © *2004 MAIK "Nauka/Interperiodica".*

INTRODUCTION

The researchers engaged in optics and optoelectronics view CdF_2 as a promising material for efficient and inexpensive lasers operating in the visible and UV ranges [1]. CdF_2 is an insulator with a band gap $E_g > 8$ eV that is transparent over a wide energy range. Upon doping and an appropriate thermochemical treatment, it passes to the semiconducting state. It is also important that CdF_2 crystals may be grown to a large enough size and that their cost is low. To completely unveil the potentialities of this material, one must know its energy band structure [2, 3].

It is known that the most comprehensive information on the electron structure of a material can be derived from a variety of its fundamental optical parameters [2] (the reflection coefficient R; the absorption coefficient μ; the real, ε_1, and imaginary, ε_2, parts of the permittivity ε; the refractive index n, the absorption index k, etc.). These parameters are conventionally calculated from the experimental spectra $R(E)$ and $\varepsilon_2(E)$; however, no such calculation for CdF_2 has been carried out.

For cadmium difluoride, which has a fluorite structure, two experimental reflection spectra are today available from literature [4, 5], but the conditions under which these two spectra were taken have not been compared. Since the knowledge of the optical parameters for cadmium difluoride is lacking, its optical properties have not been discussed in detail. The aim of this study is (i) to calculate the complete set of the CdF_2 optical parameters using two reflection spectra obtained in experiments [4, 5], (ii) compare the results of calculation, (iii) visualize the basic features of the optical spectra, and (iv) treat the results in terms of the theoretical models known.

The band structure of CdF_2 was calculated with the empirical pseudopotential method [6], the strong coupling method [7], and also by the strong coupling method for valence bands and by the pseudopotential method for conduction bands [8]. In [6, 7], only a few of the upper valence bands and a few of the lower conduction bands were calculated. The high-lying semicore bands due to the 4*d* states of Cd^{2+} were disregarded. In [8], the valence, core, and semicore bands were calculated near 30 eV along many symmetric directions in the Brillouin zone and near 13 eV for the ΓX and ΓL directions in the conduction band. However, the spectra $\varepsilon_2(E)$ for the crystal studied are still lacking.

In this work, a set of the optical parameters is calculated with the integral Kramers–Kronig relationships and simple analytical formulas relating the optical functions to each other. The methods applied are of frequent use [9, 10] and are described in detail elsewhere [2].

RESULTS AND DISCUSSION

The reflection spectra were taken at 300 K in the range 0–45 eV from as-cleaved samples [4] and from 4 to 56 eV from polished sample [5]. Based on these data, we calculated the fundamental optical functions in the range 4–45 eV.

The two reflection spectra are structurally similar. They contain nine basic bands (see table) and have the same features in the high-energy range (30–45 eV). The distinctions between them are weak band *8'*, which is absent in $R(E)$ obtained in [4], and band *9'*, which is absent in $R(E)$ [5]. In the spectrum obtained in [4], band *2* appears as a broad plateau; in the spectrum taken in [5] it looks like a fairly intense peak. The positions of the basic peaks in the two spectra differ considerably in the energy range 4–15 eV: $\Delta E \approx 0.4$ (for peaks *1*, *4*), 1.2 (peak *2*), and 0.7 eV (peak *3*). At shorter wavelengths, the discrepancies in the energy positions of the peaks decrease ($\Delta E = 0.1$–0.4 eV).

The two spectra are markedly distinct in intensity in the range 4–20 eV and are close to each other at high energies. Peaks *1–5* of the reflection spectrum in [5] are lower than the corresponding peaks in [4] by a factor of 1.6 (peak *1*), 1.4 (peaks *3*, *5*), and 1.3 (peak *4*). The

Peaks (eV) in the spectra of the CdF_2 optical parameters calculated from the experimental $R(E)$ spectra given in [4] (column 1) and [5] (column 2)

No.	R		ε_1		ε_2		n		k		μ		$-\mathrm{Im}\varepsilon^{-1}$		$-\mathrm{Im}(1+\varepsilon)^{-1}$	
	1	2	1	2	1	2	1	2	1	2	1	2	1	2	1	2
1	7.1	7.5	6.9	7.4	7.1	7.6	7.0	7.45	7.15	7.65	7.15	7.65	7.6	7.7	7.5	7.7
2	8.8	10.0	8.6	9.3	8.6	10.3	8.7	9.6	8.7	10.4	8.7	10.5	8.6	10.5	8.6	10.5
3	12.4	13.1	11.9	12.7	12.3	13.2	12.0	12.8	12.4	13.3	12.5	13.3	13.0	13.7	12.9	13.6
4	14.9	15.3	13.9	14.2	14.6	15.05	14.1	14.3	14.9	15.3	14.9	15.4	16.2	16.4	15.8	16.3
5	17.4	17.3	16.5	16.9	17.1	17.3	16.0	16.9	17.3	17.6	17.4	17.7	18.4	18.3	17.6	18.0
6	23.0	22.4	20.6	20.1	21.9	21.9	20.8	20.3	22.5	22.2	22.9	22.3	23.6	23.6	23.0	22.5
7	26.8	26.6	25.5	24.8	26.3	26.1	25.6	24.8	26.5	26.4	26.7	26.5	27.0	27.2	26.8	26.7
8	29.3	29.05	27.7	28.3	28.2	28.7	27.7	28.4	28.8	28.8	29.0	28.9	29.5	29.5	29.2	29.0
8'	–	32.8	–	31.6	–	32.5	–	31.6	–	32.7	–	32.7	–	33.0	–	32.7
9	37.1	36.7	34.6	34.2	36.0	35.9	35.1	34.3	36.3	36.3	36.6	36.5	37.2	36.8	36.7	36.6
9'	42.9	–	41.1	–	42.1	–	41.5	–	42.2	–	42.3	–	42.7	–	42.3	–

reflection coefficient of CdF_2 is low throughout the energy range: ≈0.21 in the highest peak *1* [4]. At $E >$ 0.45 eV, $R \le 2\%$. Comparing the methods and experimental samples used to take the $R(E)$ spectra, we conclude that the discrepancy between the spectra in the range 4–20 eV may be related to an inadequate measuring technique and the poor surface condition of the samples in [5].

Our $\varepsilon_2(E)$ spectra show analogues of the nine basic bands in the reflection spectrum (Fig. 1; curves II, II'). Peaks *1–4* between 4 to 20 eV are the most intense. In spectrum II, they are shifted toward lower energies by 0–0.3 eV relative to the peaks in the $R(E)$ spectrum. Peaks *1–3* in curve II' are shifted toward higher energies. This enhances the discrepancy between the peak positions in the two spectra ε_2 and in the reflection spectra. Also, a considerable difference in the peak intensity is observed. In spectrum II', the amplitudes of peaks *1*, *3*, and *4* are nearly the same, whereas in spectrum II, peak *1* is higher than peaks *3* and *4* by a factor of 1.3 and 1.5, respectively. The height of the peaks in spectrum II is 1.8 (peak *1*), 1.4 (peak *3*), and 1.2 (peak *4*) times that of the corresponding peaks in spectrum II'. At high energies (20–45 eV), both the intensity and the position of the peaks in the ε_2 spectra are in good agreement. A considerable drop in the intensity of the curves is noteworthy: most of the bands are faint.

The discrepancies mentioned above plague the estimation of the band-to-band transition energies and the energy gap E_g in CdF_2. According to our data, E_g is approximately 8.6 eV. Band *2* is apparently associated with the first band-to-band transition; the most intense low-energy band, with free excitons. Then, the binding energy E_b of the most long-wavelength exciton turns out to be ≈1.5 eV, which is excessively high. According to [8], the theory gives $E_g \approx 14.4$ eV at point Γ, which is 5.8 eV higher than our value. The structure of the ε_2 spectra in the range 8–13 eV (peaks *1–3*) is defined mainly by the transitions in the direction Γ*X* from the upper valence bands that are formed by the 2*p* states of F^- to the lower conduction band. Within energy band *4*, the transitions from the semicore bands that are formed by the 4*d* states of Cd^{2+} to the lower conduction band may occur in the vicinity of the point Γ and from the upper valence bands to the lower conduction band, in the vicinity of the point *L*. Peak *5* is due to the transitions from the upper valence bands, and broad peak *6* is conditioned mainly by the transitions from the *d* band into the upper conduction bands. The core band produced by the 2*s* fluorine states is excited at energies $E >$ 37eV. It is natural to consider the origin of the peaks in the ε_2 spectrum in terms of the metastable exciton model; however, no such calculations for CdF_2 have been performed.

The absorption index k appears to be low: $k \le 1.04$ throughout the energy range considered (Fig. 2; curves II, II'). Unlike the bands in the ε_2 spectrum, the peaks $k(E)$

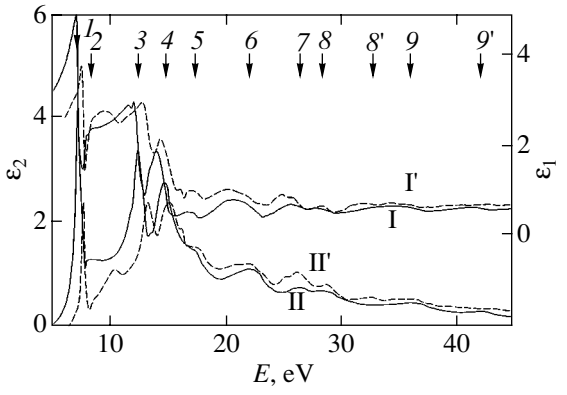

Fig. 1. (I, I') ε_1 and (II, II') ε_2 spectra calculated from the experimental $R(E)$ spectra obtained in (I, II) [4] and (I', II') [5].

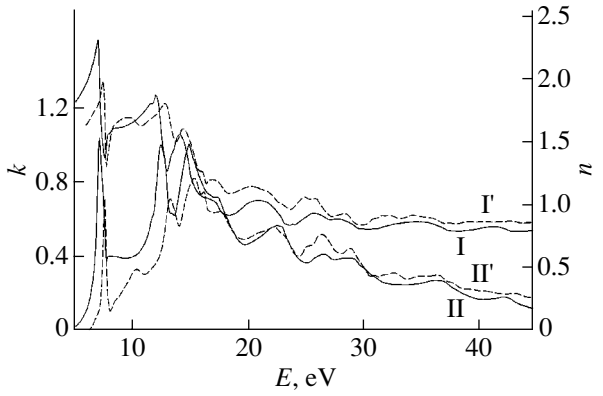

Fig. 2. Spectra of (I, I') n and (II, II') k calculated from the experimental $R(E)$ spectra obtained in (I, II) [4] and (I', II') [5].

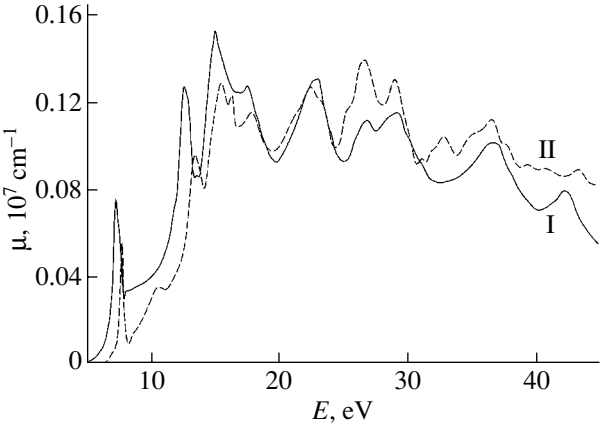

Fig. 3. Spectra of μ calculated from the experimental $R(E)$ spectra obtained in (I) [4] and (II) [5].

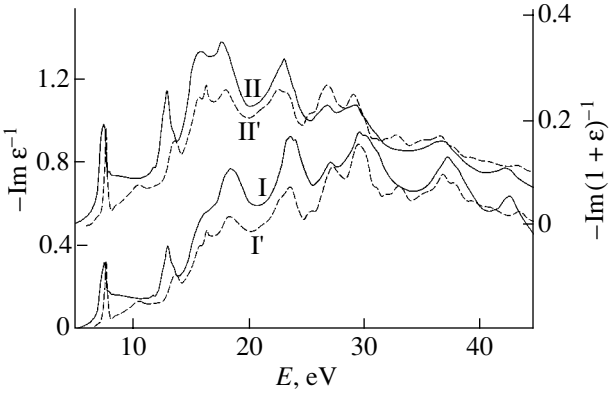

Fig. 4. Spectra of (I, I') $-\mathrm{Im}\varepsilon^{-1}$ and (II, II') $-\mathrm{Im}(1+\varepsilon)^{-1}$ calculated from the experimental $R(E)$ spectra obtained in (I, II) [4] and (I', II') [5].

either do not shift (in the range 6–20 eV) or shift toward lower energies by only 0.1–0.3 eV (20–45 eV) with respect to the peaks in $R(E)$. The absorption coefficient is rather high (Fig. 3): even at 50 eV, $\mu \approx 0.7 \times 10^6$ cm^{-1}. The different intensities of the peaks in the $R(E)$ spectra (calculated in [4, 5]) are highlighted in the spectra of k and μ, which diverge considerably in the intensity distribution of the peaks. For example, in the $\mu(E)$ spectrum calculated from the $R(E)$ spectrum given in [5], peak *7* is the highest ($\mu \approx 1.39 \times 10^6$ cm^{-1}), while in the spectrum calculated in [4] the highest peak is peak *4* ($\mu \approx 1.53 \times 10^6$ cm^{-1}).

The $n(E)$ and $\varepsilon_1(E)$ spectra are similar in structure (Figs. 1, 2; curves I, I'). In each of them, highest peaks *1–4* fall into the energy range 4–15 eV. At higher energies, the analogues of the peaks in the $R(E)$ spectrum are very weak. All bands in the ε_1 spectra are shifted toward lower energies by 0.2–2.4 eV relative to the corresponding peaks in the reflection spectrum (the higher the peak, the larger the shift). The energy positions of the peaks in the n spectra are 0.1–0.5 eV higher than those in the ε_1 spectrum. The peaks calculated in [5] are shifted with respect to the peaks in curves I toward shorter wavelengths by 0.3–0.8 eV (in the range 4–18 eV) and to longer wavelengths by 0.2–0.5 eV (18–45 eV). The intensities of all the bands are in good agreement except for the first peak in curves I' in Figs. 1 and 2, which is lower than the peak in curves I by a factor of ≈1.2.

In the spectra of characteristic volume losses $-\mathrm{Im}\varepsilon^{-1}$, one can easily distinguish four intense peaks at $E_{\mathrm{pv}}^{(1)}$ = 18.4, $E_{\mathrm{pv}}^{(2)}$ = 23.6, $E_{\mathrm{pv}}^{(3)}$ = 29.5, and $E_{\mathrm{pv}}^{(4)}$ = 37.2 eV (Fig. 4, curve I). In curve I', the first three bands appear at the same energies and the last one is shifted by 0.3 eV toward lower energies. It is known that the peaks of the $-\mathrm{Im}\varepsilon^{-1}$ spectra are due to plasmons or the longitudinal components of band-to-band transitions [11]. In the latter case, the transverse components of the transitions are bound to be observed in the $\varepsilon_2(E)$ spectra; however, in the above four bands, the transverse components are either absent or hardly perceptible. Therefore, it is reasonable to assume that the four most intense bands stem from the plasmon excitation. By analogy with the related crystal CaF_2 [10], the peaks at 18.4 eV and 29.5 eV may be associated with the plasma oscillations of the 2*p* and 2*s* electrons in F^-, respectively. The peak at 23.6 eV may be related to the oscillations of the 4*d* electrons in Cd^{2+}. The other peaks of the $-\mathrm{Im}\varepsilon^{-1}$ spectrum, which are shifted by 0.3–0.7 eV toward shorter wavelengths relative to their analogs in the spectrum of ε_2, may be assigned to band-to-band transitions. These shifts define the amount of the transverse–longitudinal split of transitions in CdF_2.

The spectra $-\mathrm{Im}(1+\varepsilon)^{-1}$ of surface losses are 2 to 3 times weaker than the volume loss spectra $-\mathrm{Im}\varepsilon^{-1}$. The peaks in the $-\mathrm{Im}(1+\varepsilon)^{-1}$ spectrum are shifted toward lower energies relative to the peaks in the volume loss spectrum by 0.5–0.8 eV for the analogs of the plasma bands, and by 0.1–0.3 eV for the other peaks. Thus, the bulk-to-surface plasmon energy ratio in CdF_2

varies between 1.02 and 1.04, i.e., within the same interval as in CaF_2.

CONCLUSIONS

For the first time, a complete set of the CdF_2 optical parameters is calculated and their behavior is established. The results of this study make it possible to take a fresh look at the CdF_2 optical spectra and perform much more accurate analysis of the band structure and excitons. We hope that the data obtained will promote the development of new CaF_2-based optoelectronic devices and contribute to the electron theory of solids.

REFERENCES

1. A. I. Ryskin, A. S. Shcheulin, and D. E. Onopko, Phys. Rev. Lett. **80**, 2949 (1998).
2. V. V. Sobolev and V. V. Nemoshkalenko, *Methods of Computer Physics in the Solid-State Theory: The Electronic Structure of Semiconductors* (Naukova Dumka, Kiev, 1988).
3. A. P. Savintsev and A. I. Temrokov, Zh. Tekh. Fiz. **72** (4), 126 (2002) [Tech. Phys. **47**, 497 (2002)].
4. C. Raisin, J. M. Berger, S. Robin-Kandare, *et al.*, J. Phys. C **13**, 1835 (1980).
5. A. J. Bourdillon and J. H. Beaumont, J. Phys. C **9**, L473 (1976).
6. B. A. Orlowski and P. Plenkiewicz, Phys. Status Solidi B **126**, 285 (1984).
7. B. Velicky and J. Masek, Solid State Commun. **58**, 663 (1986).
8. J. P. Albert, C. Jouanin, and C. Gout, Phys. Rev. B **16**, 4619 (1977).
9. V. V. Sobolev, A. I. Kalugin, V. I. Kormilets, and V. Val. Sobolev, J. Wide Bandgap Mater. **8** (10), 87 (2001).
10. V. V. Sobolev, A. I. Kalugin, V. Val. Sobolev, and S. V. Smirnov, Fiz. Tverd. Tela (St. Petersburg) **44**, 836 (2002) [Phys. Solid State **44**, 870 (2002)].
11. D. Pines, *Elementary Excitations in Solids* (Benjamin, New York, 1963; Mir, Moscow, 1965).

Translated by A. Sidorova

Technical Physics, Vol. 49, No. 3, 2004, pp. 342–344. Translated from Zhurnal Tekhnicheskoĭ Fiziki, Vol. 74, No. 3, 2004, pp. 62–64.
Original Russian Text Copyright © 2004 by Baturin, Nikolski, Knyazev, Tchesov, Sheshin.

ELECTRON AND ION BEAMS, ACCELERATORS

Doping of Graphite by an Alkaline-Earth Metal to Reduce the Work Function

A. S. Baturin, K. N. Nikolski, A. I. Knyazev, R. G. Tchesov, and E. P. Sheshin

Moscow Physicotechnical Institute (State University), Institutskiĭ pr. 9, Dolgoprudnyĭ, Moscow Oblast, 141700 Russia

e-mail: roman@lafeet.mipt.ru

Received March 25, 2003; in final form, July 30, 2003

Abstract—A technique for reducing the work function of a field-emission graphite cathode by doping it by an alkaline-earth metal (barium) is suggested. A model of formation of a barium monolayer on the cathode surface is proposed. Field-emission tests show that the operating voltage of the doped cathode is lower than that of the undoped one with the same emission current. *© 2004 MAIK "Nauka/Interperiodica".*

INTRODUCTION

Field-emission cathodes made of carboniferous materials are finding wide application [1] because of their low cost and long lifetime. The basic disadvantage of carbon fibers [2] and natural graphite compared with nanotubes [3] and diamond-like films [4] is a relatively high electron work function, which raises an operating voltage of the cathode. Basically, the operating voltage may be decreased technologically (i.e., by shrinking the cathode–anode gap) or physically and physicochemically. A physical method is, for example, modification of the emitting surface structure by training the cathode [5]. The application of an activator on the cathode in an attempt to decrease the electron work function refers to physicochemical approaches.

In the production of thermionic cathodes [6], the cathode core is usually coated by an activating layer (an alkali, alkaline-earth, or rare-earth metal). A dipole layer formed on the core surface reduces the potential barrier and, hence, the work function. The highest effect is achieved when the thickness of the activator is close to that of a monolayer.

The activator is applied mainly by three methods: (i) metal-vapor deposition, (ii) use of a directed atomic beam, and (iii) diffusion of the activator from the volume of a hot thermionic cathode to the surface. Method (i) provides a metal (activator) monolayer on the core surface. However, when the cathode operates under a pressure of $\sim 10^{-6}$ Torr, ion bombardment due to residual gases destroys the activator and the cathode degrades (its lifetime shortens). In method (ii), the design of the cathode unit is complicated (namely, its dimensions grow) and a part of the power supplied is spent on atomic beam generation. Accordingly, the system as a whole consumes more power. The advantage of method (iii) is that the activator layer is maintained during the cathode operation. However, it is inefficient for field-emission cathodes, because their operating temperature is low.

The aim of this work is to analyze the known methods of activator application and find ways of keeping the activator layer on the field-emission cathode surface during operation.

DOPING TECHNIQUES

Alkali and alkaline-earth metal may be incorporated into the graphite structure to produce intercalation carbon compounds by several methods [7]. One of them is the heating of a graphite powder mixed with a metal to be incorporated in a hermetically sealed ampoule [7]. Such a method is as yet impractical because of troubles associated with preparation of field-emission cathodes. In particular, it remains unclear how one can prepare field-emission cathodes from the final powder product using the conventional methods [8] in such a way that the graphite particles with the activator are not subjected to physicochemical effects. Therefore, test cathodes were made by the method where a graphite plate is impregnated by a salt of a metal to be incorporated with subsequent vacuum annealing at a temperature far exceeding the decomposition temperature of the salt. This method allows the activator to be uniformly distributed over the cathode volume. Auger spectroscopy and secondary ion mass spectrometry data indicated that both the pure metal and its oxide occupy voids. However, no traces of the activator on the surface were found. Field-emission tests showed that the emissivity of the field-emission cathode is improved at relatively high voltages. An explanation may be as follows. Ion bombardment removes the metal oxide from the voids and leads to its decomposition. Metal atoms reach the surface, forming a monolayer of the activator and thereby reducing the electron work function (Fig. 1). However, there exists a reverse process where ion bombardment destroys the activator monolayer, casing the degradation of the emissivity.

1063-7842/04/4903-0342$26.00 © 2004 MAIK "Nauka/Interperiodica"

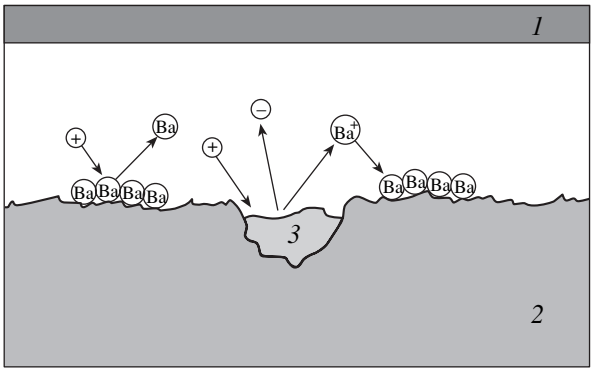

Fig. 1. Formation of a barium monolayer on and its removal from the cathode surface: (*1*) anode, (*2*) graphite cathode, and (3) barium oxide in voids.

SAMPLE PREPARATION

MPG-6 graphite plates were impregnated by solutions of the $BaBr_2$ and $Ba(ClO_4)_2$ salts. After impregnation, the plates were subjected to pulsed annealing under a pressure of 10^{-5} Torr at 1000–1100°C. Note that the melting point of $BaBr_2$ is 857°C; that is, the annealing temperatures used in the experiment were above the melting point. We failed to find the exact value of the melting point for $Ba(ClO_4)_2$: estimates show that it is bound to be higher than 1300°C. Hence, the temperatures reached in the experiment were insufficient for melting $Ba(ClO_4)_2$.

Thus, we expected that $BaBr_2$ will decompose upon vacuum annealing, more volatile Br (its boiling temperature is 59.2°C) will leave the sample, and the graphite matrix will become impregnated by molten Ba.

Further behavior of the barium in the graphite matrix depends on the temperature, according to which one of three processes takes place: barium diffusion from voids to the surface and subsequent barium evaporation, barium diffusion into graphite crystallites, and barium oxidation in the voids. The second and third processes are more favorable, since barium oxide will decompose during cathode operation with the formation of a monolayer on the surface.

The examination of the sample structure after vacuum annealing showed that all the three processes do occur. The barium concentration on the surface is very low and increases with depth. Sometimes, the barium concentration in grains was higher than in voids, indicating barium diffusion into the crystallites.

FIELD-EMISSION TESTS

Field-emission tests of the samples were conducted in the diode-type configuration. The residual pressure in the chamber was ~10^{-6} Torr. Here, we compare the results of field-emission tests for barium-doped samples and pure MPG-6 graphite.

Figure 2 demonstrates series of the *I–V* characteristics for the doped and pure cathodes under the same field-emission test conditions.

The characteristics of the doped cathode are seen to shift markedly toward lower voltages, which testifies that the cathode efficiency (i.e., an anode–cathode voltage that is necessary to achieve a desired emission current) increased.

For applications, an important parameter of a field-emission cathode is long-term stability of the emission current. To study the emission current stability, we applied a dc stabilized voltage of 1400 V between the

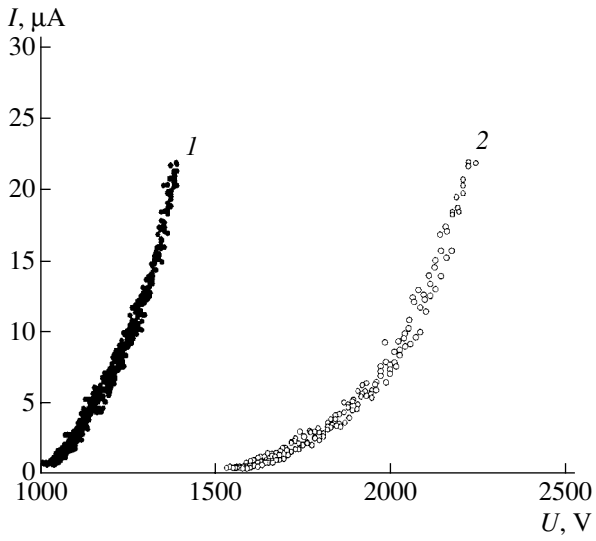

Fig. 2. *I–V* characteristics of field-emission cathodes made of (*1*) barium-doped and (*2*) pure MPG-6 graphite under identical test conditions.

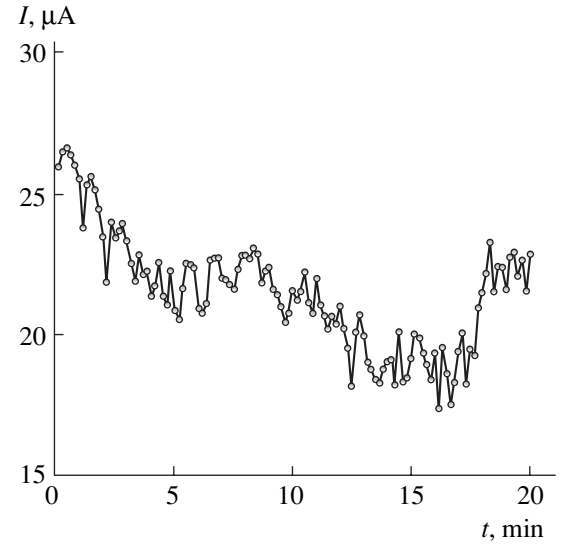

Fig. 3. Time dependence of the emission current for the barium-doped field-emission cathode under a dc voltage of 1400 V.

cathode and anode. Under these conditions, the cathode current was measured for 20 min in 10 s intervals. The time dependence of the emission current (Fig. 3) shows that the decrease in the current within the time of measurement was not very large while its instability was appreciable (more than 20%). Thus, the stabilized voltage conditions are not quite appropriate for cathodes of this type. They may be used in devices with current stabilization.

CONCLUSIONS

Thus, it is shown that doping by an alkaline-earth metal (for example, barium) may reduce significantly the work function. At the current stage of investigation, we succeeded in markedly decreasing the operating voltage. Our results apply not only to graphite. The same behavior may be observed for field-emission cathodes made of carbon fibers and other carboniferous materials. We therefore believe that doping of these materials is a step forward in improving the emissivity of field-emission cathodes.

REFERENCES

1. Kwi Seor Choi, Sang Jin Lee, *et al.*, in *Technical Digest of the International Vacuum Microelectronics Conference IVMC-99, Darmstadt, 1999*, p. 32.
2. E. P. Sheshin, Ultramicroscopy **79**, 101 (1999).
3. J.-M. Bonard, J.-P. A. Châtelain, *et al.*, Appl. Phys. Lett. **73**, 918 (1998).
4. N. I. Sinitsyn, Yu. V. Gulyaev, O. E. Glukhova, *et al.*, Appl. Surf. Sci. **111**, 145 (1997).
5. B. V. Bondarenko, E. P. Sheshin, *et al.*, Radiotekh. Élektron. (Moscow) **30**, 2234 (1985).
6. O. Yu. Maslennikov, *Efficient Activated Thermionic Cathodes* (Mosk. Fiz.-Tekh. Inst., Moscow, 1999).
7. R. Setton, in *Proceedings of the 9th Polish Graphite Conference, Zakopane, 1988*, pp. 531–546.
8. A. S. Baturin, E. P. Sheshin, *et al.*, in *Technical Digest of the IEEE International Vacuum Electron Sources Conference IVESC-2000, Orlando, 2000*, p. 51.

Translated by V. Isaakyan

Technical Physics, Vol. 49, No. 3, 2004, pp. 345–351. Translated from Zhurnal Tekhnicheskoĭ Fiziki, Vol. 74, No. 3, 2004, pp. 65–71.
Original Russian Text Copyright © 2004 by Matveev, Kochkin.

ELECTRON AND ION BEAMS, ACCELERATORS

Energy Spectra and Temperature Distributions of Clusters Produced During Ion-Beam Sputtering of Metals

V. I. Matveev and S. A. Kochkin

Pomor State University, Arkhangelsk, 163006 Russia

e-mail: matveev.victor@pomorsu.ru

Received June 5, 2003

Abstract—A method for evaluating the energy spectra and temperature dependences of the yield of neutral and charged clusters that consist of $N \geq 5$ atoms and are produced by ion bombardment of metals is proposed. The results are presented in the form of simple formulas. Theoretical energy spectra of clusters emitted as a result of bombarding niobium, tantalum, and iron targets by atomic ions of gold or xenon and temperature dependences of the yield of silver clusters produced by bombarding the targets with xenon ions are compared with experimental data. © *2004 MAIK "Nauka/Interperiodica".*

INTRODUCTION

In many cases [1–5], experimental investigation of clustering due to ion-beam sputtering of solids is aimed at revealing mechanisms responsible for the formation of polyatomic particles in sputtering products. Usually (see, e.g., [6–11]), the researchers record the energy spectra and size distributions of neutral and singly charged clusters depending on the target type and the type and current of bombarding particles. Of interest is also the yield of neutral and charged particles versus the target temperature [8], which carries more detailed information about clustering mechanisms. The emission of clusters during ion-beam sputtering is difficult to describe theoretically mostly because of a large number of particles involved. Furthermore, molecular dynamics calculations (see, e.g., [1]) are very tedious, especially for a polyatomic cluster, and hardly reproducible. The difficulties are significantly aggravated when processes that govern the charge composition of sputtering products are included into the simulation (see, e.g., review [5]).

In this paper, we suggest a method for calculating the energy spectra of neutral and charged clusters due to ion-beam bombardment of metals, as well as the energy distributions of these clusters versus the target temperature.

Our approach elaborates upon the physical concepts put forward in [12–15] and the method for evaluating the total yield of clusters [15], which are valid for clusters consisting of $N \geq 5$ atoms.

ENERGY SPECTRUM

Let each of the atoms of a solid (metal) be in an oscillator well of depth Δ and have an eigenfrequency ω. The characteristic period of oscillations is $T = 2\pi/\omega$. Let the velocity of an incident ion be such that the ion and fast recoil atoms, when moving in the metal, experience a great number of collisions in a time $\tau \ll T$. As a result of collisions, the atoms of the metal acquire momenta $\mathbf{q}_i$, where i is the index of the atom. Then, according to [15], the probability of a cluster of N atoms being emitted (as a whole) with a momentum $\mathbf{k}$ is given by

$$W_{\mathbf{k}} = \left| \left\langle \Phi_{\mathbf{k}}(\mathbf{R}) \left| \exp\left(\frac{i}{\hbar} \sum_{i=1}^{N} \mathbf{q}_i \mathbf{R} \right) \right| \Phi_0(\mathbf{R}) \right\rangle \right|^2 \times \exp\left(-\frac{1}{n_0} \frac{1}{2\alpha^2 \hbar^2} \sum_{i=1}^{N} \mathbf{q}_i^2 \right), \quad (1)$$

where $\alpha^2 = m\omega/\hbar$, m is the atomic mass, $\hbar$ is the Planck constant, $n_0 = \Delta/\hbar\omega$, $\Phi_0(\mathbf{R})$ is the wave function of the center of mass of an N-atomic cluster in the ground state, $\Phi_{\mathbf{k}}(\mathbf{R})$ is the wave function of the center of mass of the cluster in the state (from the continuous spectrum) that has the momentum $\mathbf{k}$, and $\mathbf{R}$ is the radius vector of the center of mass.

The center of mass of the cluster is assumed to oscillate with a frequency Ω in a potential well of depth U_N. The well has the meaning of the cluster–metal binding energy, which is proportional to the surface area S_N of the contact between the cluster and the rest of the metal. Then, according to [12–15], $U_N = \sigma S_N = \delta N^{2/3}$, where δ is the binding energy of the cluster per cluster atom (in general, δ differs from the depth Δ of the potential well, where each of the atoms of the solid resides).

Let us use expression (1) to evaluate the energy spectra for this case. We assume that the center of mass of the cluster moves in a spherically symmetric oscilla-

tor potential $U(\mathbf{R})$ cut off at the height U_N:

$$U(\mathbf{R}) = \frac{mN\Omega^2}{2}\mathbf{R}^2$$

for $R < R_N$, where R_N is such that $U(R_N) = U_N$. For $R > R_N$, this potential takes the constant value: $U(\mathbf{R}) = U_N$. Then, we write the wave function $\Phi_\mathbf{k}(\mathbf{R})$ for the center of mass in the state with the momentum $\mathbf{k}$ and energy $E_c + U_N$, where $E_c = \mathbf{k}^2/(2mN)$, in quasi-classical form [16]:

$$\Phi_\mathbf{k}(\mathbf{R}) = \frac{A}{(2\pi\hbar)^{3/2}}\exp\left(\frac{i}{\hbar}\int\mathbf{k}(\mathbf{R})\cdot d\mathbf{R}\right), \qquad (2)$$

where $|\mathbf{k}(\mathbf{R})| = \sqrt{2mN(E_c + U_N - U(\mathbf{R}))}$ and $\mathbf{k}(\mathbf{R}) \longrightarrow \mathbf{k}$ for $R \longrightarrow \infty$.

Assume [12–15] that the well $U(\mathbf{R})$ is deep enough, so that the condition $\hbar\Omega \ll U_N$ is met and we may put $U(\mathbf{R}) \ll U_N$ within the ground state $\Phi_0(\mathbf{R})$. Then, when calculating the matrix element

$$\left\langle \Phi_\mathbf{k}(\mathbf{R})\left|\exp\left(\frac{i}{\hbar}\sum_{i=1}^{N}\mathbf{q}_i\cdot\mathbf{R}\right)\right|\Phi_0(\mathbf{R})\right\rangle$$

in formula (1), one may set $|\mathbf{k}(\mathbf{R})| = \sqrt{2mN(E_c + U_N)} = |\mathbf{k}(0)|$ in the function $\Phi_\mathbf{k}(\mathbf{R})$. As a result,

$$W_\mathbf{k} = \frac{|A|^2}{(\pi mN\hbar\Omega)^{3/2}}\exp\left(-\left(\sum_{i=1}^{N}\mathbf{q}_i - \mathbf{k}(0)\right)^2/(mN\hbar\Omega)\right) \times \exp\left(-\frac{1}{n_0}\frac{1}{2\alpha^2\hbar^2}\sum_{i=1}^{N}\mathbf{q}_i^2\right). \qquad (3)$$

Next, following [15], we average probability (3) over all the states $\mathbf{q}_i$ ($i = (1, 2, \ldots, N)$), making the natural assumption that the magnitudes of $\mathbf{q}_i$ are independent from each other and the directions of $\mathbf{q}_i$ are equiprobable. Consider the probability averaged over the angles $\Omega_{\mathbf{q}_i}$ of the vectors $\mathbf{q}_i$:

$$\overline{W_\mathbf{k}} = \frac{1}{(4\pi)^N}\int\int\ldots\int d\Omega_{\mathbf{q}_1}d\Omega_{\mathbf{q}_2}\ldots d\Omega_{\mathbf{q}_N}W_\mathbf{k}. \qquad (4)$$

To calculate this average, we will take advantage of the expedient proposed in [15]:

$$\exp\left(-\gamma\left(\sum_{i=1}^{N}\mathbf{q}_i - \mathbf{k}(0)\right)^2\right) = \frac{1}{(2\pi)^3}\left(\frac{\pi}{\gamma}\right)^{3/2} \times\int d^3\mathbf{r}\exp\left(-i\left(\sum_{i=1}^{N}\mathbf{q}_i - \mathbf{k}(0)\right)\mathbf{r}\right)\exp\left(-\frac{\mathbf{r}^2}{4\gamma}\right),$$

where $\gamma = 1/(mN\hbar\Omega)$, and use the value of the integral

$$\frac{1}{(4\pi)}\int d\Omega_{\mathbf{q}_i}\exp-(i\mathbf{q}_i\cdot\mathbf{r}) = \frac{1}{qr}\sin(qr).$$

The mathematics simplifies significantly if we assume that all $\mathbf{q}_i$ have the same length (magnitude), $|\mathbf{q}_i| = q$, and randomly distributed directions [12–15]. Then, we obtain

$$\overline{W_\mathbf{k}} = \frac{|A|^2}{(\pi mN\hbar\Omega)^{3/2}}\frac{1}{(2\pi)^3}\left(\frac{\pi}{\gamma}\right)^{3/2} \times\left[\int d^3\mathbf{r}\exp\left(-\frac{\mathbf{r}^2}{4\gamma} + i\mathbf{k}(0)\cdot\mathbf{r}\right)\left(\frac{\sin(qr)}{qr}\right)^N\right] \times\exp\left(-\frac{1}{n_0}\frac{1}{2\alpha^2\hbar^2}Nq^2\right).$$

Next, we use the formula

$$\left(\frac{1}{x}\sin x\right)^N \approx \exp\left(-\frac{Nx^2}{6}\right),$$

which is valid for $N \gg 1$ [15], and arrive at

$$\overline{W_\mathbf{k}} = \frac{|A|^2}{(\pi mN\hbar\Omega)^{3/2}}\frac{1}{(2\pi)^3}\left(\frac{\pi}{\gamma}\right)^{3/2} \times\left[\int d^3\mathbf{r}\exp\left(-\mathbf{r}^2\left(\frac{1}{4\gamma} + \frac{Nq^2}{6}\right) + i\mathbf{k}(0)\cdot\mathbf{r}\right)\right] \times\exp\left(-\frac{1}{n_0}\frac{1}{2\alpha^2\hbar^2}Nq^2\right).$$

The integral in this expression is easy to calculate:

$$\int d^3\mathbf{r}\exp(-\mathbf{r}^2(1/(4\gamma) + Nq^2/6) + i\mathbf{k}(0)\cdot\mathbf{r}) = \frac{\pi^{3/2}}{(1/(4\gamma) + Nq^2/6)^{3/2}}\exp\left(-\frac{k^2(0)}{4(1/(4\gamma) + Nq^2/6)}\right).$$

After averaging, the probability takes the form

$$\overline{W_\mathbf{k}} = \frac{|A|^2}{\pi^{3/2}(mN\hbar\Omega + 2Nq^2/3)^{3/2}} \times\exp\left(-\frac{\mathbf{k}^2(0)}{mN\hbar\Omega + 2Nq^2/3}\right)\exp\left(-\frac{1}{n_0}\frac{1}{2\alpha^2\hbar^2}Nq^2\right). \qquad (5)$$

The total probability $\overline{W_N}$ that the center of mass is in the continuous spectrum is found by integrating $\overline{W_\mathbf{k}}$ over all $\mathbf{k}$ under the condition that the momentum $\mathbf{k}$ is directed outwards, which corresponds to a solid angle of 2π. To this end, we represent $d^3\mathbf{k}$ as $d^3\mathbf{k} = 2\pi k^2 dk =$

$2\pi mN\sqrt{2mN(E_c + U_N)}\,dE$. Then,

$$\overline{W_N} = \int \overline{W_\mathbf{k}} d^3\mathbf{k} = \int_0^\infty \left(\frac{d\overline{W_N}}{dE_c}\right)_1 dE_c, \tag{6}$$

where

$$\left(\frac{d\overline{W_N}}{dE_c}\right)_1 = \overline{W_\mathbf{k}} 2\pi mN\sqrt{2mN(E_c + U_N)}$$

is the energy spectrum of N-atomic clusters, which, upon simple transformations, takes the form

$$\left(\frac{d\overline{W_N}}{dE_c}\right)_1 = |A|^2 \frac{1}{\sqrt{\pi}} \frac{(E_c + U_N)^{1/2}}{\left(\frac{\hbar\Omega}{2} + \frac{2}{3}\frac{q^2}{2m}\right)^{3/2}} \times \exp\left(-\frac{E_c + U_N}{\frac{\hbar\Omega}{2}\frac{2}{3}\frac{q^2}{2m}}\right)\exp\left(-\frac{Nq^2}{2m\Delta}\right).$$

Neglecting the energy $\hbar\Omega/2$ of zero-point oscillations, which is small compared with the energy $\frac{2}{3}\frac{q^2}{2m}$, we find the spectrum in the form

$$\left(\frac{d\overline{W_N}}{dE_c}\right)_1 = |A|^2 \frac{1}{\sqrt{\pi}} \frac{(E_c + U_N)^{1/2}}{\varepsilon^{3/2}} \times \exp\left(-N\frac{3}{2}\frac{\varepsilon}{\Delta} - \frac{E_c + U_N}{\varepsilon}\right), \tag{7}$$

where

$$\varepsilon = \frac{2}{3}\frac{q^2}{2m}, \quad U_N = \delta N^{2/3}.$$

By setting $\overline{W_N}$ given by (6) equal to the expression obtained in [15] (by summing over all bound states $\Phi_n(\mathbf{R})$ of the center of mass and subtracting unity from the sum),

$$\overline{W_N} = \left[1 - \left(1 + \frac{\varepsilon}{U_N}\right)^{-3/2}\right]\exp\left(-N\frac{3}{2}\frac{\varepsilon}{\Delta}\right), \tag{8}$$

we come to

$$|A|^2 = \sqrt{\pi}\left[1 - \left(1 + \frac{\varepsilon}{U_N}\right)^{-3/2}\right]\Gamma^{-1}\left(\frac{3}{2}, \frac{U_N}{\varepsilon}\right),$$

where $\Gamma^{-1}(x, y) = 1/\Gamma(x, y)$ and $\Gamma(x, y)$ is the incomplete gamma function.

Strictly speaking, the above procedure of evaluating $|A|^2$ is valid if $U_N/\varepsilon \longrightarrow 0$. In our case, it is also justified because $\overline{W_N}$ calculated by integrating (6) over the states of the continuous spectrum coincides with the result of summation (see (8)). Eventually, we obtain the energy spectrum of N-atomic clusters in the form

$$\left(\frac{d\overline{W_N}}{dE_c}\right)_1 = \frac{(E_c + U_N)^{1/2}}{\varepsilon^{3/2}\Gamma\left(\frac{3}{2}, \frac{U_N}{\varepsilon}\right)}\left[1 - \left(1 + \frac{\varepsilon}{U_N}\right)^{-3/2}\right] \times \exp\left(-\frac{E_c + U_N}{\varepsilon} - N\frac{3}{2}\frac{\varepsilon}{\Delta}\right). \tag{9}$$

In general, expression (2) for the wave function $\Phi_\mathbf{k}(\mathbf{R})$ refers to the situation where the center of mass of the cluster passes into the continuous spectrum domain far away from the top of the potential well, i.e., when the energy $E_c \gg U_N$ [16, p. 297]. Therefore, expression (9) for the spectrum must be matched to the cluster spectrum at low energies, i.e., at $0 < E_c \ll U_N$. We will derive the low-energy part of the spectrum as follows. In [15], the total probability W_N that the center of mass of an N-atomic cluster passes into the continuous spectrum domain was derived by summing over all possible bound states of the center and subtracting unity form the sum:

$$W_N = \left[1 - \sum_{n=0}^{k_0}\left|\left\langle \Phi_n(\mathbf{R})\left|\exp\left(\frac{i}{\hbar}\sum_{i=1}^N \mathbf{q}_i\cdot\mathbf{R}\right)\right|\Phi_0(\mathbf{R})\right\rangle\right|^2\right] \times \exp\left(-\frac{1}{n_0}\frac{1}{2\alpha^2\hbar^2}\sum_{i=1}^N \mathbf{q}_i^2\right), \tag{10}$$

where summation is performed from $n = 0$ to a certain maximal value $n = k_0$ that refers to the bound state with a maximal energy in the potential well of depth U_N; i.e., $k_0 = U_N/(\hbar\Omega)$.

After calculating the matrix elements, summing over n, and averaging over the vectors $\mathbf{q}_i$, formula (10) yields [15] total probability (8), which is convenient to represent as

$$\overline{W_N} = \left[1 - \left(1 + \frac{\varepsilon}{k_0\hbar\Omega}\right)^{-3/2}\right]\exp\left(-N\frac{3}{2}\frac{\varepsilon}{\Delta}\right).$$

This expression can be recast in the form of the integral of a certain spectral function in simple terms. We assume that k_0 is a variable quantity ($\overline{W_N}$ is then a function of k_0; i.e., $\overline{W_N} = \overline{W_N}(k_0)$) and consider the dependence $k_0 = (E_c + U_N)/(\hbar\Omega)$. Then,

$$\overline{W_N} = \int \frac{d\overline{W_N}}{dk_0} dk_0 = \int_0^\infty \left(\frac{d\overline{W_N}}{dE_c}\right)_2 dE_c,$$

where $(d\overline{W_N}/dE_c)_2$ has the meaning of the energy spec-

trum of an N-atomic cluster:

$$\left(\frac{d\overline{W_N}}{dE_c}\right)_2 = \frac{d\overline{W_N}(k_0)}{dk_0}\frac{dk_0}{dE_c}.$$

Carrying out differentiation and simple transformations, we obtain the energy spectrum of an N-atomic cluster:

$$\left(\frac{d\overline{W_N}}{dE_c}\right)_2 = \frac{3}{2}\left[1+\frac{E_c+U_N}{\varepsilon}\right]^{-5/2} \times \frac{(E_c+U_N)^{1/2}}{\varepsilon^{3/2}}\exp\left(-N\frac{3}{2}\frac{\varepsilon}{\Delta}\right). \quad (11)$$

As follows from the procedure used to derive formula (11), it can be treated as a cluster spectrum only in the immediate vicinity of the boundary between the continuous and discrete states, i.e., when $E_c \ll U_N$. To obtain the spectrum in the entire range of E_c, it is necessary to join the low-energy (expression (11)), and high-energy (expression (9)), parts of the spectrum. Let a desired result of joining have the form

$$\frac{d\overline{W_N}}{dE_c} = f(E_c)|C|^2\left(\frac{d\overline{W_N}}{dE_c}\right)_2 + [1-f(E_c)]\left(\frac{d\overline{W_N}}{dE_c}\right)_1, \quad (12)$$

where the function $f(E_c)$ must be such that $f(E_c) \longrightarrow 1$ when $E_c \ll U_N$ (i.e., when $E_c \longrightarrow 0$) and $f(E_c) \longrightarrow 0$ when $E_c \gg U_N$ (i.e., when $E_c \longrightarrow \infty$).

Then, when E_c varies from 0 to ∞, the full spectrum $d\overline{W_N}/dE_c$ changes smoothly from $(d\overline{W_N}/dE_c)_2$ to the spectrum $(d\overline{W_N}/dE_c)_1$. In this work, the function $f(E_c)$ meeting the above conditions was taken in the form $f(E_c) = \exp[-E_c^2/\varepsilon^2]$. It is clear that such a procedure violates the normalization condition. Therefore, formula (12) is provided with the normalizing factor C such that the full spectrum $d\overline{W_N}/dE_c$ is normalized to the probability $\overline{W_N}$ of escape of an N-atomic cluster, i.e., to $\overline{W_N} = \int_0^\infty (d\overline{W_N}/dE_c)dE_c$. Then,

$$|C|^2 = \left(\int_0^\infty f(E_c)(d\overline{W_N}/dE_c)_1 dE_c\right)\Big/\left(\int_0^\infty f(E_c)(d\overline{W_N}/dE_c)_2 dE_c\right).$$

CHARGE COMPOSITION

To obtain the cluster energy spectra with regard to the charge composition of clusters, we will proceed from the physical concepts [12–15] according to which the charge composition forms during sputtering. In this case, the escape probability $\overline{W_N^Q}$ for an N-atomic cluster that has a charge Qe (e is the electron charge) is given by [15]

$$\overline{W_N^Q} = \overline{W_N}P_N(Q), \quad (13)$$

where $P_N(Q)$ is the probability that the N-atomic cluster escaped has the charge Qe. This probability is described by the standard formula for fluctuation probability [15]:

$$P_N(Q) = \frac{1}{D_N}\exp\left\{-\frac{1}{2}\frac{(Q-Q_0)^2}{\overline{(\Delta Q_N)^2}}\right\}, \quad (14)$$

$$\overline{(\Delta Q_N)^2} = \frac{3^{1/3}}{\pi^{4/3}}\frac{m_e\Theta}{\hbar^2}\left(\frac{V}{N}\right)^{2/3}\gamma^{1/3}N, \quad (15)$$

where the normalizing factor D_N is found by summing over all possible Q ($Q = 0, \pm1, \pm2, \ldots$), m_e is the mass of an electron in the conduction band, V is the cluster volume, Θ is the target temperature, γ is the valence of the metal atoms; and $\overline{(\Delta Q_N)^2}$ is the standard deviation of the cluster charge from an equilibrium value Q_0.

According to [14, 15], the assumption that the equilibrium charge equals zero implies that the Fermi levels in the cluster and metal coincide. Otherwise, asymmetry between negatively and positively charged clusters will be observed, as demonstrated by the experiment [8]; therefore, we assume that the equilibrium charge Q_0 is nonzero. Let us calculate the equilibrium charge Q_0 as a function of the difference $\Delta\mu$ between the Fermi energies in the metal and cluster. With the number N_e of electrons inside the Fermi sphere of radius μ known [17],

$$N_e = N\gamma = \frac{V(2m)_e^{3/2}}{3\pi^2\hbar^3}\mu^{3/2},$$

we obtain the following expression for the equilibrium charge Q_0e:

$$Q_0 = \Delta N_e = 2^{1/2}\frac{Vm_e^{3/2}}{\pi^2\hbar^3}\sqrt{\mu}\Delta\mu = \frac{3^{1/3}}{\pi^{4/3}}\frac{m_e}{\hbar^2}\left(\frac{V}{N}\right)^{2/3}\gamma^{1/3}N\Delta\mu. \quad (16)$$

The expression for $\overline{(\Delta Q_N)^2}$ in the denominator of the exponent in formula (14) needs some comments. The fact that $\overline{(\Delta Q_N)^2}$ tends to zero as the temperature Θ tends to zero is a consequence of applying the Fermi statistics to systems with a macroscopic number of particles or of using the so-called thermodynamic limit ($N \longrightarrow \infty$ and $V \longrightarrow \infty$ with $N/V = \text{const}$). In our case, where the number of particles $N_e = N\gamma$ is, in macroscopic terms, small (while much greater than unity), the

mean-square fluctuation must not exactly equal zero at zero temperatures, because it is necessary to allow for quantum fluctuations. With the corresponding correction to $\overline{(\Delta Q_N)^2}$ in the denominator of the exponent in formula (14) denoted by β, the probability that an N-atomic cluster escaped has the charge Qe will be described by the formula

$$P_N(Q) = \frac{1}{D_N}\exp\left\{-\frac{1}{2}\frac{(Q-Q_0)^2}{\overline{(\Delta Q_N)^2}+\beta}\right\}, \qquad (17)$$

where the parameter β corresponds to quantum fluctuations of the charge at the zero target temperature.

Then, (13) yields a formula for the total probability that an N-atomic cluster escaped has the charge Qe:

$$\overline{W_N^Q} = \left[1-\left(1+\frac{\varepsilon}{U_N}\right)^{-3/2}\right]\exp\left(-N\frac{3}{2}\frac{\varepsilon}{\Delta}\right) \times\frac{1}{D_N}\exp\left\{-\frac{1}{2}\frac{(Q-Q_0)^2}{\overline{(\Delta Q_N)^2}+\beta}\right\}. \qquad (18)$$

Thus, to obtain the energy spectrum $(d\overline{W_N^Q}/dE_c)$ of N-atomic clusters with a charge Qe, one should multiply spectrum (12) by $P_N(Q)$ (see (17)). Eventually, we arrive at a final expression for the energy spectrum of N-atomic clusters with a charge Qe:

$$\frac{d\overline{W_N^Q}}{dE_c} = \left\{f(E_c)|C|^2\left(\frac{d\overline{W_N^Q}}{dE_c}\right)_2 + [1-f(E_c)]\left(\frac{d\overline{W_N^Q}}{dE_c}\right)_1\right\} \times\frac{1}{D_N}\exp\left\{-\frac{1}{2}\frac{(Q-Q_0)^2}{\overline{(\Delta Q_N)^2}+\beta}\right\}. \qquad (19)$$

It should be noted that the energy spectra, as well as the total probabilities $\overline{W_N^Q}$ (cf. [15] and experiment [8]), of neutral clusters depend on the target temperature only slightly, whereas the spectra of charged clusters significantly vary with the target temperature. However, as the temperature increases, they come close to each other.

COMPARISON WITH EXPERIMENTS

Integrating full spectrum (19) over all possible cluster energies E_c yields the total escape probability $\overline{W_N^Q}$ for an N-atomic cluster with a charge Qe. In this sense, $d\overline{W_N^Q}/dE_c$ given by (19) is the absolute value of the spectrum. In experiments, the relative energy spectra I_N^Q of clusters with different numbers of atoms are usually easier to measure. As a rule, the relative energy spectra normalized to unity at $E_c = 0$ are taken:

$$I_N^Q = (d\overline{W_N^Q}/dE_c)/(d\overline{W_N^Q}/dE_c)\Big|_{E_c=0}.$$

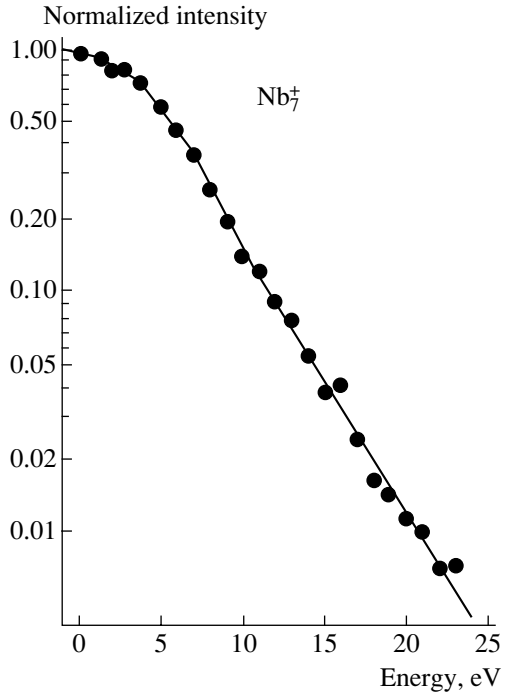

Fig. 1. Relative energy spectrum (normalized intensity) I_7^1 of singly charged Nb_7^+ clusters ($N = 7$) produced by bombarding a niobium target by singly charged 6-keV Au^{-1} ions. Solid line, calculation with the variable parameter q = 270 a.u.; (●), data points [7].

Note that such a normalization, while convenient in experiments, somewhat detracts information being derived. In particular, the dependence on the target temperature disappears, as follows from (19). Figures 1 and 2 show the energy spectra I_7^{+1} of singly charged Nb_N and Ta_N clusters ($N = 7$) produced by bombarding niobium and tantalum targets by singly charged 6-keV gold ions Au^{-1}. Figure 3 demonstrates the relative energy spectra I_N^{+1} of singly charged Fe_N clusters (N = 7–9) that are produced by bombarding an iron target by singly charged 8.5-keV Xe^{+1} ions. To reduce the number of adjusting parameters, we assumed that $\Delta = \delta$ and that this value is equal to the sublimation energy [15]. We found that, for niobium, $\Delta = \delta = 7.47$ eV (the sublimation energy of niobium [18]) and the variable parameter $q = 270$ a.u. (atomic units: $\hbar = m_e = e = 1$); for tantalum, $\Delta = \delta = 8.1$ eV (the sublimation energy of tantalum [18]) and $q = 420$ a.u.; and for iron, $\Delta = \delta = 4.29$ eV (the sublimation energy of iron [18]) and $q = 200$ a.u. For comparison, Figs. 1–3 also show the experimental data from [7, 19, 20]. Figure 3 corroborates the weak

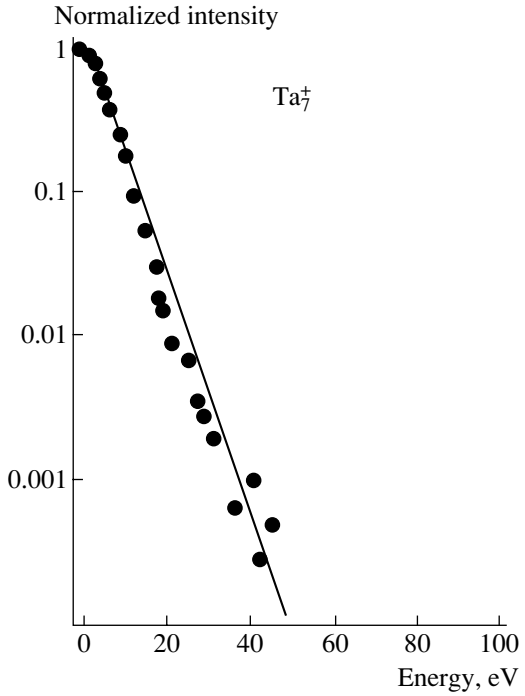

Fig. 2. Relative energy spectrum (normalized intensity) I_7^1 of singly charged Ta_7^{+1} clusters ($N = 7$) produced by bombarding a tantalum target by singly charged 6-keV Au^{-1} ions. Solid line, calculation with the variable parameter q = 420 a.u.; (●), data points [19].

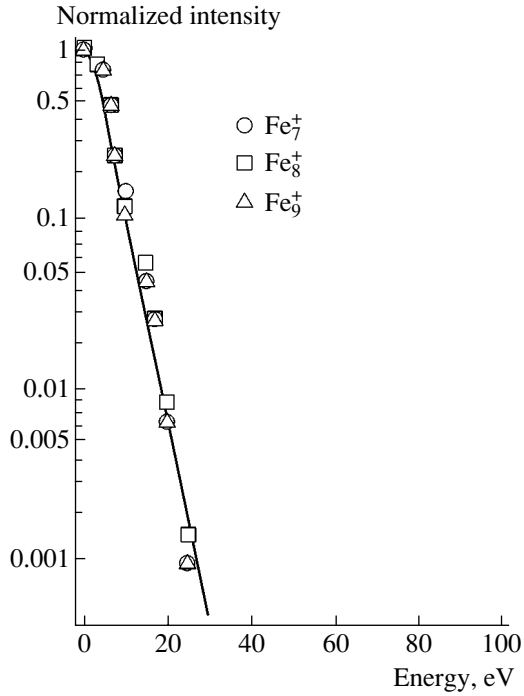

Fig. 3. Relative energy spectra I_N^1 of singly charged Fe_N^1 clusters (N = 7–9) produced by bombarding an iron target with singly charged 8.5-keV Xe^{+1} ions. Solid line depicts three merged curves calculated for N = 7–9 and q = 200 a.u. ○, □, and △ are data points [20].

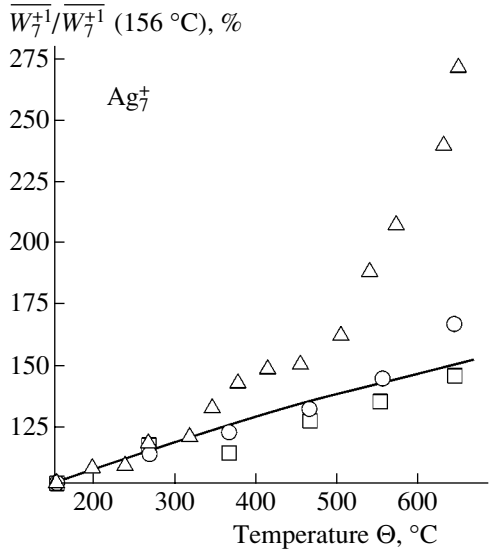

Fig. 4. Temperature dependence for the relative yield of singly charged Ag_7^{+1} clusters ($N = 7$) produced by bombarding a silver target by singly charged 8.5-keV Xe^{+1} ions. Solid line, calculation; ○, □, and △ are three sets of data points [8].

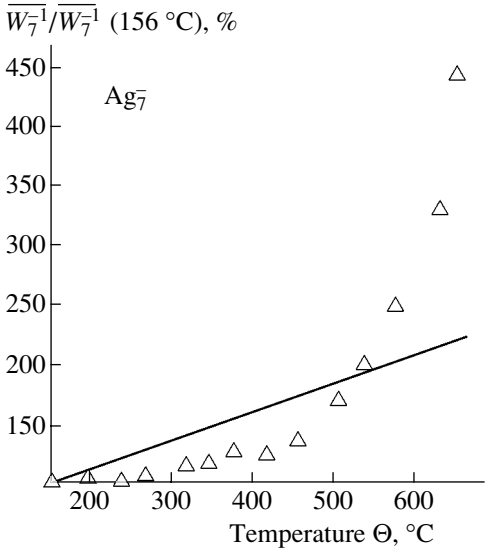

Fig. 5. Temperature dependence of the relative yield for singly charged Ag_7^{-1} clusters ($N = 7$) produced by bombarding a silver target by singly charged 12.5-keV Xe^+ ions: solid line, calculation; △, data points [8].

dependence of the relative energy spectra on the number of particles in a cluster, which follows from (19).

Figures 4 and 5 plot yield (18) against the target temperature Θ for singly charged positive and negative Ag_7 clusters in relation to the yield of the same clusters at Θ = 156°C. The clusters are produced by bombarding a silver target by singly charged Xe^{+1} ions with energies of 8.5 and 12.5 keV, respectively. In other words,

Figs. 4 and 5 show $\overline{W_N^Q}(\Theta)/\overline{W_N^Q}(156°\text{C})$ as a function of temperature at $N = 7$ and $Q = \pm 1$. It was assumed that the difference between the Fermi energies in the metal and hepta-atomic cluster is $\Delta\mu = 0.08$ eV and $\beta = 0.13$. For comparison, Figs. 4 and 5 show the experimental results normalized in the same manner [8]. For positive clusters, three sets of data obtained in different setups were reported [8] (see Fig. 4); for negative clusters, the temperature dependences were taken in the same setup [8] (one set of data in Fig. 5). The spread in the measurements is insignificant. This allows us to conclude that the theoretical results not only qualitatively but also quantitatively agree with the experiment [8], where the total yield of neutral, positive, and negative clusters versus temperature was studied.

ACKNOWLEDGMENTS

This work was supported by the Russian Foundation for Basic Research and the Administration of the Arkhangel'sk Oblast (grant no. 02-02-97503-r2002sever).

REFERENCES

1. *Fundamentals and Application of Sputtering of Solids: Collection of Articles*, Ed. by E. S. Mashkova (Mir, Moscow, 1989) [translated from English].
2. H. H. Andersen, K. Dan. Vidensk. Selsk. Mat. Fys. Medd. **43**, 127 (1993).
3. H. M. Urbassek and W. O. Hofer, K. Dan. Vidensk. Selsk. Mat. Fys. Medd. **43**, 97 (1993).
4. I. A. Baranov, Yu. V. Martynenko, S. O. Tsepelevich, and Yu. N. Yavlinskiĭ, Usp. Fiz. Nauk **156**, 477 (1988) [Sov. Phys. Usp. **31**, 1015 (1988)].
5. *Sputtering by Particle Bombardment*, Ed. by R. Behrisch (Springer-Verlag, New York, 1991; Mir, Moscow, 1998), Vol. 3.
6. Th. J. Colla, H. M. Urbassek, A. Wucher, *et al.*, Nucl. Instrum. Methods Phys. Res. B **143**, 284 (1998).
7. S. F. Belykh, B. Habets, U. Kh. Rasulev, *et al.*, Nucl. Instrum. Methods Phys. Res. B **164–165**, 809 (2000).
8. C. Staudt, R. Heinrich, P. Mazarov, *et al.*, Nucl. Instrum. Methods Phys. Res. B **164–165**, 715 (2000).
9. R. Kissel and H. M. Urbassek, Nucl. Instrum. Methods Phys. Res. B **180**, 293 (2001).
10. S. F. Belykh, V. V. Palitsin, I. V. Veryovkin, *et al.*, Nucl. Instrum. Methods Phys. Res. B **203**, 164 (2003).
11. S. N. Morozov and U. Kh. Rasulev, Nucl. Instrum. Methods Phys. Res. B **203**, 192 (2003).
12. V. I. Matveev and P. K. Khabibullaev, Dokl. Akad. Nauk **362**, 191 (1998) [Dokl. Phys. **43**, 544 (1998)].
13. S. F. Belykh, V. I. Matveev, I. V. Veryovkin, *et al.*, Nucl. Instrum. Methods Phys. Res. B **155**, 409 (1999).
14. V. I. Matveev, Zh. Tekh. Fiz. **70** (8), 10 (2000) [Tech. Phys. **45**, 1063 (2000)].
15. V. I. Matveev, Zh. Tekh. Fiz. **72** (6), 115 (2002) [Tech. Phys. **47**, 767 (2002)].
16. M. L. Goldberger and K. M. Watson, *Collision Theory* (Wiley, New York, 1964; Mir, Moscow, 1967).
17. L. D. Landau and E. M. Lifshitz, *Course of Theoretical Physics*, Vol. 5: *Statistical Physics* (Nauka, Moscow, 1976; Pergamon, Oxford, 1980), Part 1.
18. Ch. Kittel, *Introduction to Solid State Physics* (Wiley, New York, 1976; Nauka, Moscow, 1978).
19. S. F. Belykh, U. Kh. Rasulev, A. V. Samartsev, and I. V. Veryovkin, Nucl. Instrum. Methods Phys. Res. B **136–138**, 773 (1998).
20. A. D. Bekkerman, N. Kh. Dzhemilev, S. V. Verkhoturov, *et al.*, Microchimica Acta: Supplementum **15**, 371 (1998).

Translated by A. Khzmalyan

Technical Physics, Vol. 49, No. 3, 2004, pp. 352–357. Translated from Zhurnal Tekhnicheskoĭ Fiziki, Vol. 74, No. 3, 2004, pp. 72–77.
Original Russian Text Copyright © 2004 by Kotov, Osipov, Samatov, Ivanov, Platonov, Murzakaev, Azarkevich, Medvedev, Shtolts, Timoshenkova.

EXPERIMENTAL INSTRUMENTS AND TECHNIQUES

Properties of Powders Produced by Evaporating CeO_2/Gd_2O_3 Targets Exposed to Pulsed–Periodic Radiation of a CO_2 Laser

Yu. A. Kotov, V. V. Osipov, O. M. Samatov, M. G. Ivanov, V. V. Platonov, A. M. Murzakaev, E. I. Azarkevich, A. I. Medvedev, A. K. Shtolts, and O. R. Timoshenkova

Institute of Electrophysics, Ural Division, Russian Academy of Sciences, ul. Amundsena 106, Yekaterinburg, 620016 Russia

e-mail: kotov@iep.uran.ru

Received June 27, 2003

Abstract—The characteristics (phase composition, grain shape, grain size distribution, and specific surface area) of $Ce_{0.78}Gd_{0.22}O_{2-\delta}$ nanopowders produced by exposing the target to pulsed CO_2 laser radiation are reported. Reasons for a threefold increase in the output of the experimental powder-preparation unit (up to 60 g/h) with the characteristic grain size (≈10 nm) remaining unchanged are discussed. © *2004 MAIK "Nauka/Interperiodica".*

INTRODUCTION

The solid high-temperature electrolyte based on yttria-stabilized zirconia (YSZ) has the highest conductivity (up to ≈0.17 S/cm) among solid electrolytes currently available. However, its high operating temperature (≈1000°C) causes fast degradation of the electrodes and the electrolyte itself, so that the cost of fuel elements becomes unacceptably high. Therefore, improvement of the properties of YSZ-based fuel elements goes in parallel with the search for lower temperature alternatives.

A promising material for medium-temperature solid electrolytes is gadolinium-doped cerium oxide (CeGdO), which has recently been the subject of extensive research [1, 2]. In view of the fact that the conductivity of CeGdO starts rapidly increasing when the grain size becomes <3 μm [3] and that the mechanical strength of the material also grows as the grains become finer, nanometer-grain CeGdO seems the most appropriate for reducing internal losses in fuel elements.

In this work, we report early results concerning the characteristics of Gd-doped CeO nanopowders produced by evaporating the target with pulsed CO_2 laser radiation. The boiling points of CeO_2 (T_b = 3730 K) and Gd_2O_3 (T_b = 3900 K) are considerably lower than those of ZrO_2 (≈4570 K) and Y_2O_3 (≈4710 K) (yttria and zirconia powders were previously obtained by the same technology [3, 4]). Therefore, it was also of interest to trace the effect of the boiling point on the output of the powder preparation unit and on the grain size.

EXPERIMENTAL UNIT

The laser used in our experiments was described in detail in [3, 5]. The only difference from the previous scheme was that a magnetically controlled saturating switch, rather than a diode inductive circuit, was applied to decouple the currents of self-maintained and semi-self-maintained discharges. Accordingly, the radiation pulse waveform slightly changed (Fig. 1).

During operation, the laser was sealed off; i.e., the gas mixture in the pumped space of the laser was not

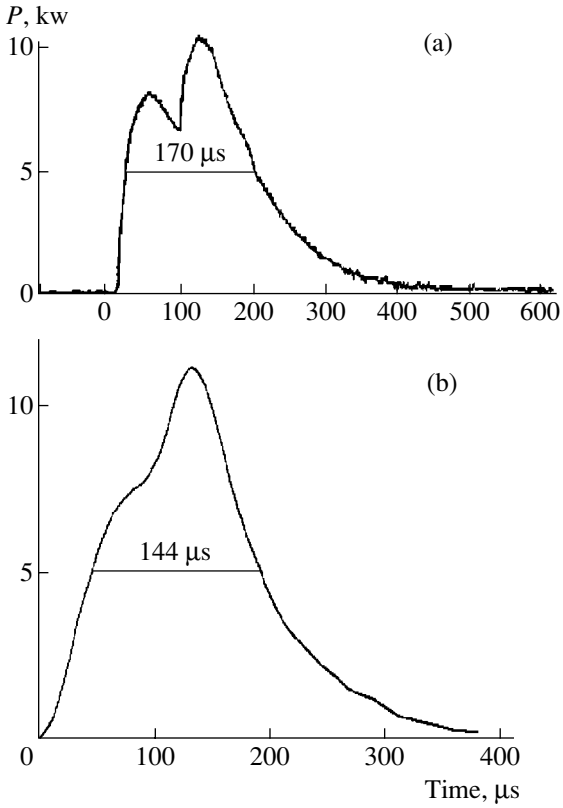

Fig. 1. Waveforms of the CO_2 laser output (a) before and (b) after refining the laser design.

1063-7842/04/4903-0352$26.00 © 2004 MAIK "Nauka/Interperiodica"

changed for several hours until a desired amount of the target was evaporated. Subsequently, the target was replaced and the gas mixture was completely renewed. Therefore, the laser output during operation decreased from 800 to 500 W because of air inleakage to the gas-filled space. Thus, the mean laser output within this time interval was 665 W; the peak output, 11.2 kW; the light spot diameter at the exit window, 35 mm; the FWHM of the laser pulse, 144 μs; the pulse repetition rate, 435 Hz; the efficiency, 8.3%; and the power consumption, 8 kW.

The design of the experimental nanopowder preparation unit is shown in Fig. 2. Laser radiation *10* is focused on target *2* through lens *8*, which simultaneously serves as the entrance window of chamber *3*. Actuator *1* rotates target *2* and moves it in the horizontal plane so that the velocity of travel of the laser beam over the target surface remains constant, providing target evaporation uniformity. As the target is evaporated, it is shifted in the axial direction in such a way that its surface remains in the focal spot plane. The focal length of the KCl lens is 10 cm; the focal spot diameter, 0.45 mm. The laser beam scans the target with a velocity of 20 cm/s; accordingly, the target displacement for a time between the pulses is $D \approx 0.043$ cm. Fan *4* forces air *9* into hermetically sealed evaporator *3* and transports the powder to cyclone *5* and electric filter *6*, where the powder is trapped. The air additionally purified by mechanical filter *7* is applied again to the evaporator by means of the fan. At the target surface, the gas velocity is ≈15 m/s.

TARGET PREPARATION

Targets were prepared from a mixture of CeO_2 and Gd_2O_3 powders to provide a near-optimal composition ($Ce_{0.8}Gd_{0.2}O_{2-\delta}$ [2]) of desired powders. The initial powders were certified by different methods. The initial CeO_2 powders were found to have a specific surface area $S = (2.8 \pm 0.2)$ m^2/g (the BET method, a GKh-1 instrument) and contain 0.25 wt % of adsorbates, which were desorbed completely at 600°C (thermogravimetric analysis (TGA), a Q-1500 instrument). The powder had a cubic structure with a lattice parameter of 0.5411 nm (X-ray diffraction analysis, a DRON-4 diffractometer) in agreement with the ASTM library. No impurities have been detected. SEM analysis (a JSM-T220A microscope) showed that the powder consists of irregularly shaped grains and their agglomerates (Fig. 3a) up to 10 μm across.

The Gd_2O_3 powder had $S = (2.0 \pm 0.2)$ m^2/g and contained up to 0.97 wt % of adsorbates, which were fully desorbed at 700°C. The powder was one-phase and had a cubic lattice with a parameter of 1.0813 nm. As follows from the micrographs (Fig. 3b), the grains are also of irregular shape and are heavily agglomerated (the grain and agglomerate size reaches 5 μm).

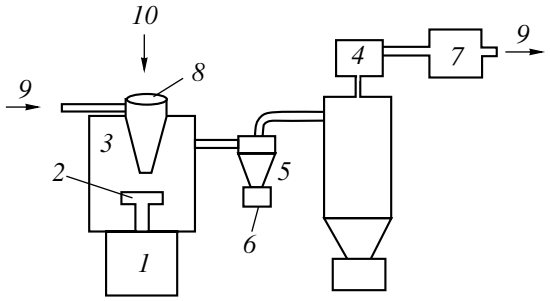

Fig. 2. Design of the nanopowder preparation unit used in the experiments.

When preparing the target, one should take into account that the content of the higher temperature component (Gd_2O_3) in the target evaporation product will be lower than in the as-prepared target [4, 6]. The desired composition $Ce_{0.8}Gd_{0.2}O_{2-\delta}$ meets the weight ratio $CeO_2 : Gd_2O_3 = 0.792 : 0.208$. Since final results of experiments were unknown in advance, we took the initial weight ratio of the components to be 0.654 : 0.346; in other words, the concentration of Gd_2O_3 far exceeded the value calculated. The same proportion was taken for dry powders in view of the TGA data.

The initial powders taken in the above proportion were thoroughly mixed in an LDI-65 disk mill (SiC disks) by sequentially putting the powders (six times) and then the mixture through the mill. Upon mixing, S was equal to 2.46 m^2/g, which agrees well with calculations (2.5 m^2/g).

The mixture obtained was forced down into the evaporating dish of the die by a screw press. The density of the compact was 0.46 that of the crystalline component mixture. Such a target, however, collapsed and was thrown around during evaporation within about 5 min. Therefore, the target was partially sintered, after which it evaporated without disintegration. The output of the unit was 60 g of powder per hour.

RESULTS AND DISCUSSION

A total of 780 g of the powder with a specific surface area $S = (57 \pm 4)$ m^2/g was produced. Sedimentation analysis in isopropyl alcohol showed that the powder contains ≤8 wt% of objects with a size of >200 nm (Fig. 3c). These objects represent a mixture of spherical grains with a diameter of up to 1.5 μm (they seem likely to appear when the liquid bath is splashed on the target) and irregular shaped grains of size to 5 μm (possibly, target fragments). Therefore, in order to improve the quality of the ceramic material, the powder was settled down. After sedimentation, S was found to be (56 ± 4) m^2/g, i.e., remained virtually unchanged, since the precipitation of coarse grains is accompanied by minor agglomeration of the powder.

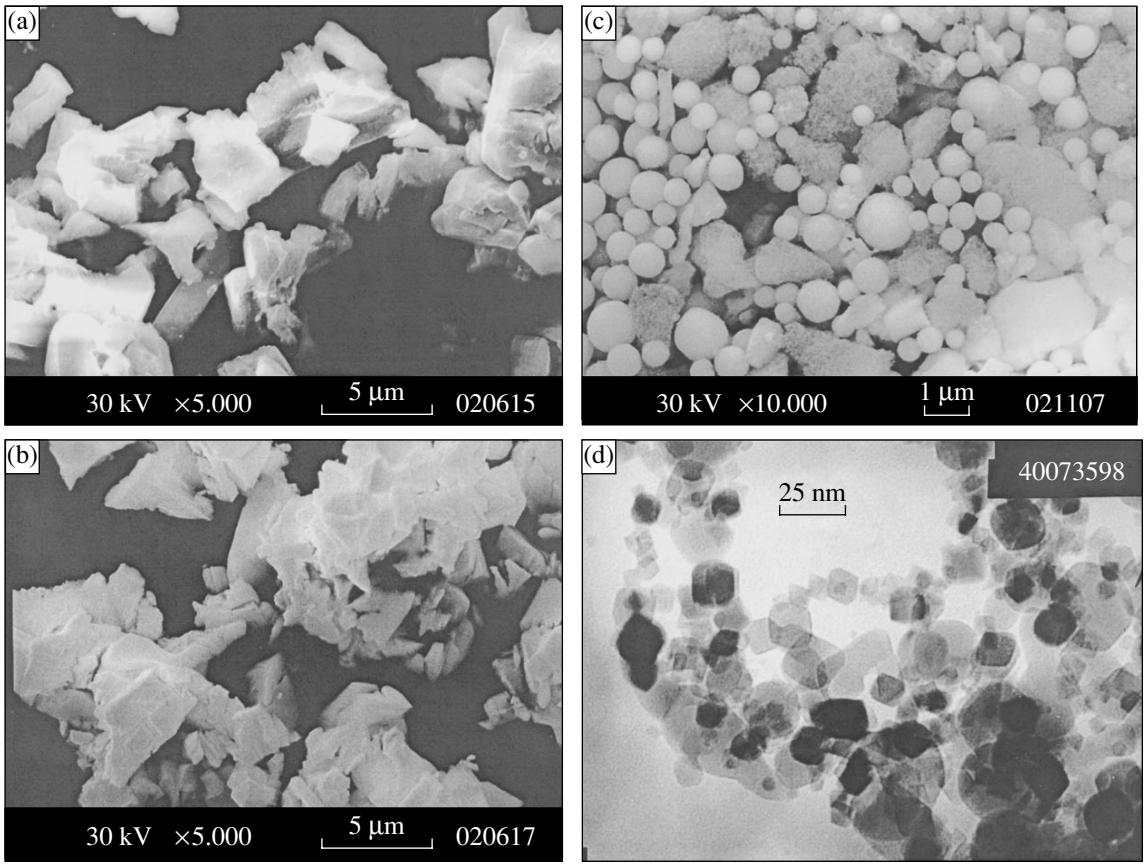

Fig. 3. Micrographs of the grains. (a, b) Initial CeO_2 and Gd_2O_3 powders, respectively; (c) sediment particles; and (d) grains of the settled powder.

TEM (JEM-200) data (Fig. 3d) indicate that the shape of the grains varies from cubic to spherical. The grain size distribution constructed (a total of 1583 grains, Fig. 4) turned out to be close to the lognormal distribution with a geometric mean diameter d_g = 9.4 nm and a variance σ_g = 1.7 nm. In the size range > 40 nm, only single grains with diameters d = 50, 60, 65, 80, and 195 nm were detected; that is, more than 99% of the grains had d < 40 nm (as for YSZ powders prepared earlier [3, 4]).

TGA data suggest that the powder is one-phase and represents the solid solution of Gd in the CeO_2 cubic lattice with a parameter of 0.5424 nm. The grain size evaluated by the Debye–Scherrer method was found to be D = 19 nm. Since coarser grains make a major contribution to the overall grain size and $D > d_g$, one can conclude that the grains are single-crystalline.

Elemental identification (a Jobin Yvon 48 instrument) showed that the composition of the nanopowder is close to the desired one within the measurement accuracy. The content of CeO_2 and Gd_2O_3 oxides (with regard for 2.8 wt% of adsorbates measured by TGA) is, respectively, 78.2% and 21.8%. The significant depletion of the product by gadolinium oxide may be explained by the fact that the heat of vaporization of Gd_2O_3 (it dissociates during vaporization) is roughly 1.5 times higher than that of CeO_2 [7, 8]. To obtain data for the target composition providing a desired ratio Ce/Gd in the solid solution nanopowder, we are currently performing experiments with different component ratios in the target.

As was noted above, the output of the unit was 60 g/h, i.e., three times higher than in the case of YSZ [4]. This is in part because the shape of the pulse applied was somewhat improved (it became shorter), the peak power increased by 10%, and the repetition rate was raised from 400 to 435 Hz. It appears, however, that the basic reason is a considerable reduction of the energy spent to evaporate the mixture. Calculations based on available thermodynamic data for ZrO_2, Y_2O_3, CeO_2, and Gd_2O_3 [7, 8] showed that the energy needed to heat and evaporate a $0.83ZrO_2 + 0.17Y_2O_3$ mixture (which corresponds to 10 YSZ) under adiabatic conditions is $W_{(H+E)} \approx 7.9$ kJ/g and the mixture under study ($0.654CeO_2 + 0.346Gd_2O_3$), $W_{(H+E)} \approx 4.75$ kJ/g. Since the pulse energy remains nearly the same as before (≈1.5 J) and the energy $W_{(H+E)}$ decreased by a factor of ≈1.7, a rise in the output might be expected. The improvement of the laser pulse parameters mentioned above and the noticeably lower boiling points of

the components of the mixture studied compared with the boiling points of the YSZ components are also a factor. A reduction of the boiling point in the case of a bell-shaped pulse (Fig. 1) allows one to maintain the power density on the target that is sufficient for evaporation for a longer time.

It is surprising at first glance that the grain size does not grow with increasing output. Recall that the rate of evaporation of the $0.654CeO_2 + 0.346Gd_2O_3$ (in weight ratio) target is three times higher than that of 10 YSZ ($0.87ZrO_2 + 0.17Y_2O_3$) [4]. However, as follows from estimates based on [9, 10] (see the appendix), the temperature of the target surface irradiated must be higher than the boiling temperature by 1000 K. The vapor flows away from the surface with a velocity on the order of the velocity of sound at pressure of 1.5–2.0 MPa. In the torch, the vapor slows down and its pressure drops to the pressure of the surrounding gas. During the effluence, the degree of condensation is low: about 0.1. Condensation takes place largely when the vapor mixes with the air. At this time, the vapor concentration in both mixtures is roughly the same; hence, the sizes of the grains produced from the mixtures are close to each other.

The pulse energy is one order of magnitude higher than needed to evaporate the amount of the material per pulse (3.8×10^{-5} g). Obviously, the excess energy partially reflects from the target and its remaining part is absorbed and dissipated by the expanding cloud of the vapors and by the condensate. The radiative heating is bound to decrease the vapor concentration before condensation. Accordingly, the grains have no time to grow larger than ≈10 nm because of condensation and, possibly, subsequent coalescence. This suggests that the output of the evaporation process may be raised further. However, efforts in this direction (an increase in the evaporation area) were of no avail. It seems necessary to look into reasons for energy loss (radiation from the torch area, the thermal conductivity of the target, melting of its surface layer, losses in the plasma, the energy of particles leaving the target, etc.) more closely. These issues go beyond the scope of this work and will be discussed later.

CONCLUSIONS

It is shown that the evaporation of the target by a pulsed CO_2 laser is an efficient way of producing weakly agglomerated nanopowders of compounds with a characteristic grain size of ≈10 nm and the narrow grain size distribution. The basic factor governing the output of the powder preparation unit is the specific energy required to vaporize the material. The nanopowders obtained offer possibilities for creating solid electrolytes with a nanodimensional structure.

ACKNOWLEDGMENTS

The authors thank V.M. Tel'nova for conducting experiments with powder settlement and T.M. Demina for taking measurements of the specific surface area.

This work was supported by the ISTC (project no. 2277r) and by the Fundamental Research Program of the Presidium of the Russian Academy of Sciences.

APPENDIX

Estimates of the Evaporation Regime Parameters

(1) According the classification made in [9], a radiation flux of power density ~10^6 W/cm^2 is a medium-power flux. When incident on a material, it triggers the thermal destruction mechanism, where the kinetic energy of evaporation products is small compared with the heat of vaporization. In addition, the effect of vapor flow on the motion of the evaporation front is insignificant, so that they may be considered separately. The evaporation front velocity v and the temperature T_0 of the evaporating surface are found by solving the one-dimensional stationary heat conduction problem:

$$v = \frac{q}{\rho(\Delta H_0 + c_p T_0)}, \quad T_0 = \frac{T_\infty}{\ln(v_\infty / v)}, \qquad (1)$$

where q is the radiation flux absorbed; ρ is the density of the condensate; ΔH_0 is the heat of vaporization at 0 K; c_p is the specific heat at constant pressure of the vapor; v_∞ is the preexponential in the temperature dependence of the rate of evaporation, $v = v_\infty \exp(-T_\infty/T)$; $T_\infty = \Delta H_0 \mu / R$; μ is the molecular mass; and R is the gas constant.

If the liquid phase evaporates, $v = (P_0/\rho)(\mu/2\pi R T_0)^{1/2}$, where P_0 is the saturated vapor pressure at the temperature T_0.

(2) The temperature distribution in the condensate depends on the relationship between the thermal conductivity and the laser radiation absorption coefficient. In metals, the optical flux is completely absorbed in a surface layer ≈0.1 μm thick and the heat conduction mechanism then comes into play. The temperature distribution in this case in exponential if melting is ignored. The heat characteristic penetration depth is given by $l = \kappa/\rho c v$, where κ is the thermal conductivity and c is the specific heat of the condensate.

In ceramic materials, the light penetration depth may be comparable to the wavelength: l = 5–10 μm [11]. The thermal conductivity of ceramic materials is two orders of magnitude lower than that of metals (for example, 2 W/(m K) for ZrO_2 [12] versus 400 W/(m K) for copper). Therefore, for ceramic materials, $l \sim 1$ μm and the situation $l_0 \gg l$ is quite realistic.

In this case, the temperature distribution is the sum of two exponentials: $T(x) = A\exp(-x/l_0) - B\exp(-x/l)$. It peaks at a depth of l. Under the steady-state conditions, the surface temperature and the rate of evaporation do

Table 1

Mixture	μ, g/mol	ΔH_0, kJ/g	T_b, K	ρ, g/cm^3	v_∞, 10^6 m/s	T_∞, 10^3 K	c, J/kg K	c_p, J/kg K	T_0, K	v, m/s	l, μm	m_{calc}, 10^{-5} g
YSZ(*)	111	6.66	4590	2.75	6.32	88.9	598	284	5710	1.09	0.50	8.6
YSZ(**)	111	6.66	4590	2.75	6.32	88.9	598	464	5670	0.97	0.56	7.6
CeGdO(*)	150	4.03	3780	3.65	5.38	72.7	403	202	4790	1.36	0.45	14.2
CeGdO(**)	150	4.03	3780	3.65	5.38	72.7	403	312	4760	1.24	0.50	12.9

Note: Without (*) and with (**) taking into account molecular vibration.

not depend on the temperature distribution. At the same time, the temperature distribution affects the heating duration and the heat stored in the layer heated.

(3) In the calculation, the mixture was replaced by a homogeneous material with averaged parameters μ, ρ, ΔH_0, c, c_p, and T_b (boiling point). These parameters were estimated from the properties of the components in view of their weight percent [7, 8]. We took into consideration that, when boiling, sesquioxides dissociate into three molecules by the reaction $Me_2O_3 = 2MeO + O$ [7]; therefore, the molecular mass was found from the formula $\mu = (g_1/\mu_1 + 3g_2/\mu_2)^{-1}$, where g_1 and g_2 are the weight fractions. The heat of vaporization was taken to be equal to the heat of this reaction (with opposite sign). The specific heat c was calculated by the Dulong–Petit law.

Next, we assumed that the target is compacted to a relative density of 0.5, the thermal conductivity is proportional to the relative density, and half the incident flux is absorbed in the target. The radiation flux is approximated by a rectangular pulse of amplitude 7.9 kW and duration 180 μs. For a focal spot diameter of 0.45 mm, the power density equals 5×10^6 W/cm^2.

(4) Table 1 lists the mean values of the electrophysical parameters, T_0, v, l, and the calculated weight m_{calc} of the material evaporated per pulse. The calculation

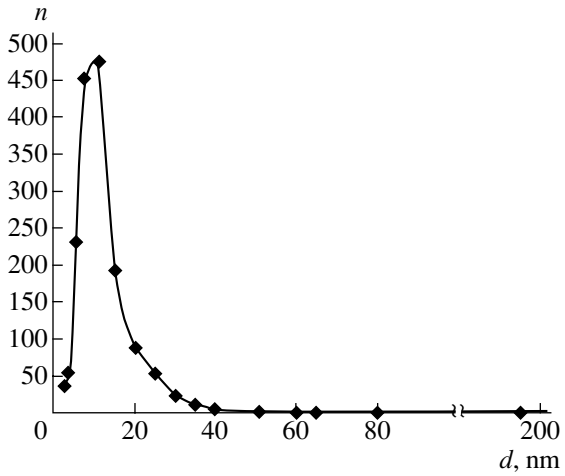

Fig. 4. Grain size distribution in the $Ce_{0.78}Gd_{0.22}O_{2-\delta}$ powder after sedimentation.

was performed for two values of c_p when molecular vibrations are unexcited and totally excited. The real situation is between these two extreme cases.

Provided that half the incident flux is absorbed in the target, the calculated weight of the product exceeds the experimental value by a factor of 5.8 for YSZ and 3.6 for CeGdO. It is likely that the energy is partially lost on the way to the target surface because of radiation scattering and absorption by evaporation products.

(5) Upon evaporation, the nonequilibrium "semi-Maxwellian" velocity distribution of vapor particles becomes equilibrium with parameters T_1, n_1, and velocity u_1. These parameters are hard to determine correctly and are found by solving the kinetic equation. Direct use of results obtained for monoatomic gas [9] fails. Let us therefore assume that the vapor flows with a local acoustic velocity and that a backward flow toward the surface is absent. The parameters are then determined from the equations of conservation of mass flow and energy flow:

$$\rho v = mn_0(kT_0/2\pi m)^{1/2} = mn_1u_1;$$
$$(c_p - R_1/2)T_0 = c_pT_1 + u_1^2/2; \quad u_1^2 = \gamma R_1T_1, \tag{2}$$

where m is the molecular mass, $R_1 = R/\mu$, γ is the adiabatic exponent, $n_0 = P_0/kT_0$ is the concentration of saturated vapor particles at the temperature T_0.

From these equations, we get

$$T_1/T_0 = 1/\gamma; \quad n_1/n_0 = 1/\sqrt{2\pi} = 0.399;$$
$$P_1/P_0 = 0.399/\gamma; \quad P_w = P_1 + \rho_1u_1^2, \tag{3}$$

where P_w is the pressure exerted on the evaporation surface (wall). It is found from the equation of conservation of momentum flux.

(6) The simulation of the saturation temperature T_s at the density n_1 shows that the outgoing vapor is supersaturated; hence, it becomes condensing at once. Until the vapor pressure drops to the environmental pressure, the vapor mixes with the air insignificantly and condensation proceeds adiabatically (if the absorption of the radiation by the vapor is ignored). Under these conditions, the adiabatic equation $dH - VdP = 0$ (H is the enthalpy), the equation of state for a two-phase medium $PV = (1 - x)R_1T$, the equation of phase equilibrium

Table 2.

Mixture	γ	T_1, K	P_1, 10^5 Pa	P_w, 10^5 Pa	ρ_1, kg/m^3	T_s, K	u_1, m/s	x
YSZ(*)	1.359	4201	12.9	30.5	4.10	5291	654	0.124
YSZ(**)	1.192	4754	13.2	28.8	3.71	5299	651	0.090
CeGdO(*)	1.379	3471	16.5	39.3	6.35	4425	515	0.132
CeGdO(**)	1.216	3911	17.0	37.6	5.80	4433	513	0.103

Note: For * and **, see the note to Table 1.

$dp/dT = \Delta H(1 - x)/TV$, and the expression for enthalpy $H = c_p(1 - x)T + cxT - \Delta Hx$ are valid [10]. Here, x is the degree of condensation (the weight fraction of the liquid), ΔH is the heat of phase transition, and V is the volume of a two-phase medium.

Assuming that ΔH is constant and eliminating P and V from the equations, we come to an equation that relates x and T:

$$\frac{dx}{dT} = -\frac{\Delta H + \Delta cT}{\Delta H - \Delta cT}\frac{1-x}{T} + \frac{c}{\Delta H - \Delta cT}, \qquad (4)$$

where $\Delta c = c - c_p$.

It is reasonable to put $x = 0$ at $T = T_s$ as the initial condition. The final temperature equals the boiling temperature T_b. Taking into account that the fractions depend on temperature only slightly, we may write an approximate solution in the form

$$1 - x = \left(\frac{T_b}{T_s}\right)^a + \frac{c}{2\Delta c}\left[1 - \left(\frac{T_b}{T_s}\right)^{a-1}\right];$$
$$a = \frac{\Delta H + \Delta cT_b}{\Delta H - \Delta cT_b}, \qquad (5)$$

where $\Delta H = \Delta H_0 - \Delta cT_b$. The results of simulation are given in Table 2.

It is seen that the temperature and degree of condensation depend markedly on the excitation of molecular vibration. However, the degree of condensation under adiabatic expansion is small. For the most part, the vapor condenses only when it mixes with the air, transferring to it the heat of condensation. During mixing, the particle concentration $n = P/kT$ is nearly the same in both mixtures; hence, the sizes of the particles are also close to each other.

REFERENCES

1. G. M. Christe and F. P. F. van Berkel, J. Solid State Ionics **83**, 17 (1996).
2. Z. Tianshu, P. Hing, H. Huang, *et al.*, J. Solid State Ionics **148**, 567 (2002).
3. V. V. Osipov, Yu. A. Kotov, M. G. Ivanov, *et al.*, Izv. Ross. Akad. Nauk, Ser. Fiz. **63**, 1968 (1999).
4. Yu. A. Kotov, V. V. Osipov, M. G. Ivanov, *et al.*, Zh. Tekh. Fiz. **72** (11), 76 (2002) [Tech. Phys. **47**, 1420 (2002)].
5. V. V. Osipov, M. G. Ivanov, V. V. Lisenkov, *et al.*, Kvantovaya Élektron. (Moscow) **32**, 253 (2002).
6. E. Muller, Ch. Oestreich, U. Popp, *et al.*, in *Proceedings of the 4th Euro-Ceramics Conference, Riccione, 1995*, Vol. 1, pp. 219–224.
7. E. K. Kazenas and D. M. Chizhikov, *Vapor Pressure and Vapor Composition over Oxides of Chemical Elements* (Nauka, Moscow, 1976).
8. P. A. Arsen'ev, L. M. Kovba, and Kh. S. Bagdasarov, *Compounds of Rare-Earth Elements: Systems with Group I–III Element Oxides and Chemistry of Rare Elements* (Nauka, Moscow, 1983).
9. S. I. Anisimov, Ya. A. Imas, G. S. Romanov, and Yu. V. Khodyko, *Effect of High-Power Radiation on Metals* (Nauka, Moscow, 1970).
10. Ya. B. Zeldovich and Yu. P. Raizer, *Physics of Shock Waves and High-Temperature Hydrodynamic Phenomena* (Nauka, Moscow, 1966; Academic, New York, 1967).
11. *Handbook of Optical Constants of Solids*, Ed. by E. D. Palik (Academic, New York, 1985).
12. *Handbook of Physical Quantities*, Ed. by I. S. Grigoriev and E. Z. Meilikhov (Énergoatomizdat, Moscow, 1991; CRC, Boca Raton, 1997).

Translated by V. Isaakyan

Technical Physics, Vol. 49, No. 3, 2004, pp. 358–360. Translated from Zhurnal Tekhnicheskoĭ Fiziki, Vol. 74, No. 3, 2004, pp. 78–80.
Original Russian Text Copyright © 2004 by Volkov, Baiburin, Konnov.

SHORT COMMUNICATIONS

Formation of Silicon Nanospheres in Molten Aluminum

Yu. P. Volkov, V. B. Baiburin, and N. P. Konnov

Saratov State Technical University, Saratov, 410016 Russia

e-mail: bai@sstu.saratov.su

Received June 25, 2003

Abstract—Transmission electron microscopy and electron diffraction data show that, as silicon dissolves in molten aluminum, a great number of silicon nanospheres (from 1.5 nm to several tens of nanometers across) forms in the melt. When these particles are dissolved in toluene, the solution takes on a pale pink color and its transmission coefficient at a wavelength of 300 nm decreases fivefold. In such a solution, a great number of equal-size silicon nanospheres (1.5 nm in diameter) are observed. © *2004 MAIK "Nauka/Interperiodica".*

INTRODUCTION

Nanometer-sized semiconductor structures, specifically, silicon, GaAs, etc., filamentary nanocrystals, are today attracting considerable interest [1]. However, no case of producing spherical silicon nanoparticles has come to our notice.

In this work, we describe the formation of silicon spherical nanoparticles by a method that is based on the well-known phenomenon of silicon dissolution in metal melts (in particular, in aluminum melt) where silicon does not chemically react with the metal [2]. Transmission electron microscopy (TEM) and electron diffraction (ED) data for the silicon nanospheres obtained and the transmission spectrum of the silicon nanoparticles in toluene are reported.

EXPERIMENTAL

A small amount (≈0.04 g) of 99.99% pure aluminum was placed on the surface of a 0.38-mm-thick polished ÉKDB-10-26 Si(111) wafer that was located in a Hitachi HUS 5GB vacuum evaporator kept at a pressure of 10^{-5} Torr. The wafer was heated by passing electric current through it until the metal melted. Once the silicon had dissolved (virtually instantly) in the melt, the current was immediately switched off and the metal was cooled and withdrawn from the evaporator. Then, the Al–Si alloy was etched in a large amount of a 60% solution of reagent-grade HCl in distilled water for 5 days. As a result, we obtained a lump of porous silicon, which was rinsed several times in distilled water to remove the residual acid and water-soluble metal salts. The lump was ultrasonically (44 kHz, 5 min) crushed in distilled water. A drop of the resulting liquid was placed on the microscope grid covered by a 20-nm-thick carbon film, dried in air, and examined in a Hitachi HU-12A transmission electron microscope (the rated resolution 0.2 nm at an accelerating voltage of 75 kV). The silicon lump was also crushed in toluene, and the resulting solution was spun (for 30 min at an acceleration of 800 g) to settle out coarse particles. Then, the supernatant liquid was carefully decanted and its transmission spectrum was recorded with an SF-26 spectrophotometer.

RESULTS AND DISCUSSION

Irregularly shaped fragments of various size, as well as many rounded and spherical particles of size ranging from several nanometers to several thousands of nanometers, were observed. Figures 1a and 1b show TEM micrographs and ED patterns taken of spherical particles formed in the aluminum melt. The EED pattern in Fig. 1b is composed of two patterns: one was taken at a short exposure time to reveal the structure of the inner rings; the other, at a long exposure time to image the outer (less intense) rings. The interplanar spacings calculated for the center of the rings with an accuracy of ≈10% were found to be 0.33 nm (for the (111) reflection), 0.19 nm (220), 0.16 nm (311), 0.12 nm (422), and 0.093 nm (531). Since the diameters of the (211) and (311) rings are close to each other and their brightnesses differ substantially, they seem to merge into one ring. The tabulated values [3] for interplanar spacings in silicon are 0.3138 nm (111), 0.1920 nm (220), 0.1638 nm (311), 0.1108 nm (422), and 0.0918 nm (531).

When the silicon lump disintegrated in toluene, the solution turns pinkish. Figures 2a and 2b show, respectively, TEM images and ED patterns of the silicon particles from the toluene. It is seen that most of the particles are spherical and have an equal size (1.5 nm). The interplanar spacings (calculated for the center of the rings with an accuracy of ≈10%) were found to be 0.312 nm (111), 0.18 nm (220), 0.16 nm (311), 0.104 nm (422), and 0.089 nm (531). Since the diameters of the (211) and (311) rings are close to each other and their brightnesses differ substantially, they seem to merge into one ring. It is also hard to distinguish between the (400), (331), and (422) rings. These find-

1063-7842/04/4903-0358$26.00 © 2004 MAIK "Nauka/Interperiodica"

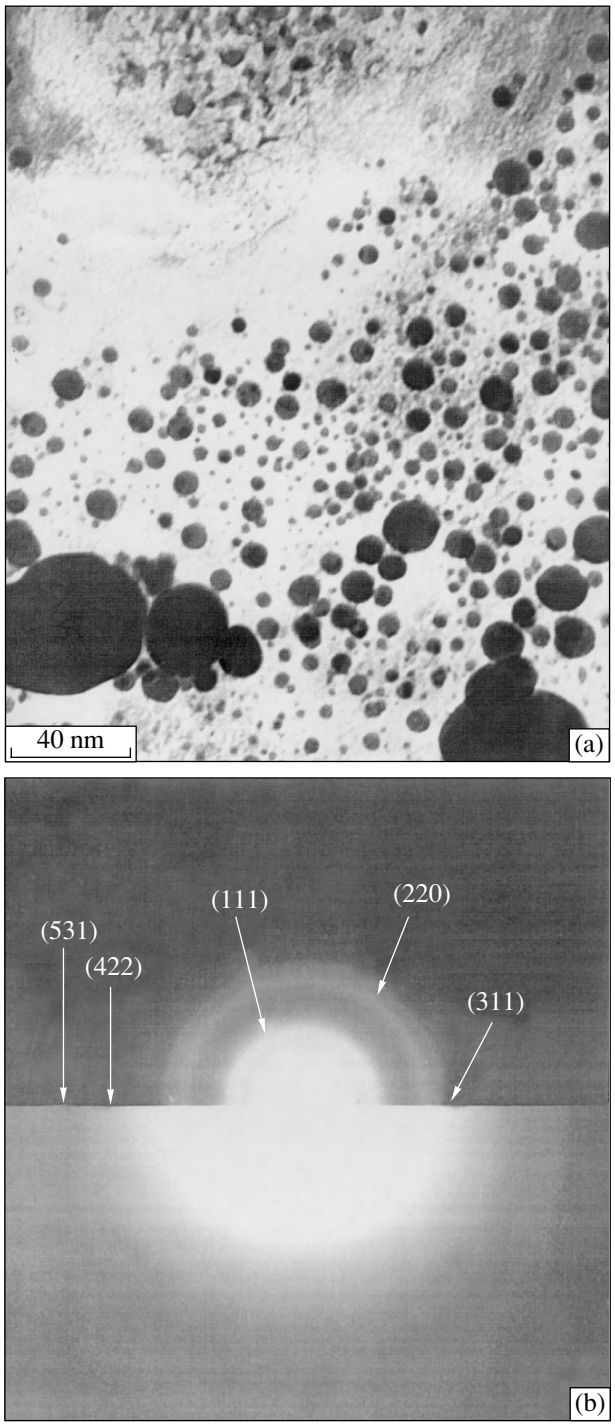

Fig. 1. (a) TEM micrograph of the silicon nanoparticles formed by dissolving silicon in the aluminum melt and (b) ED pattern taken of these particles.

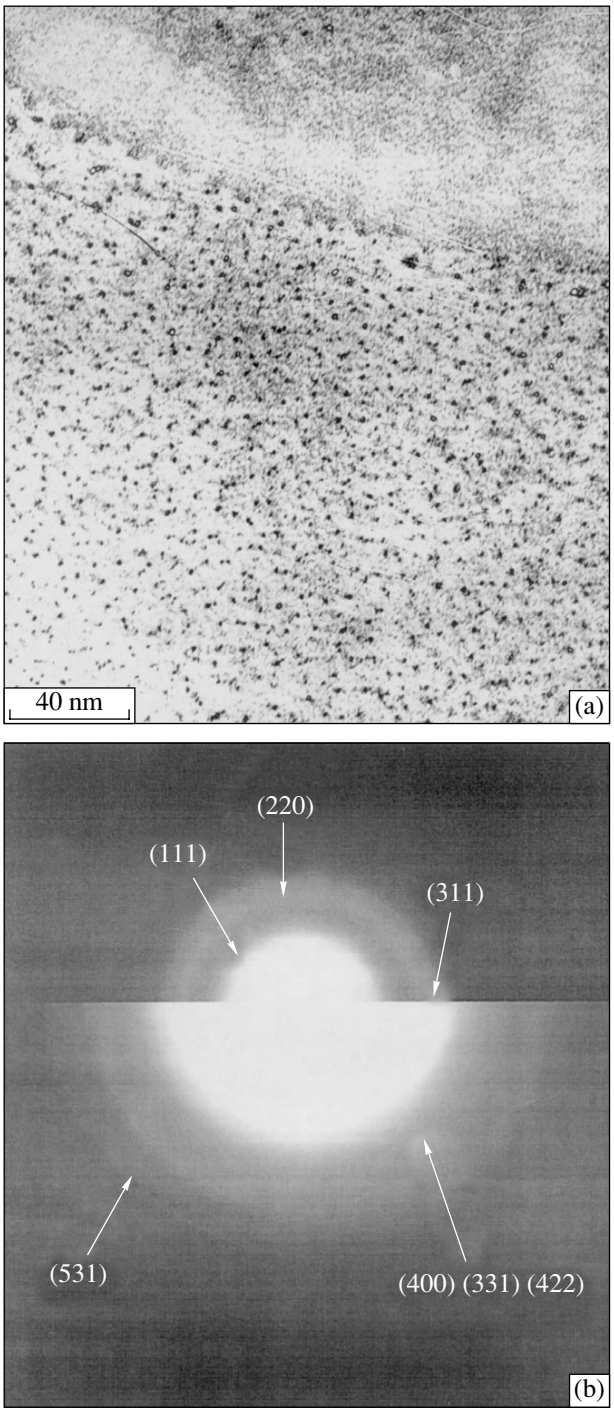

Fig. 2. TEM micrograph of the silicon nanoparticles extracted from the toluene solution and (b) ED pattern taken of these particles.

ings coincide with the tabulated data (within the error of measurement), suggesting that the spherical particles observed are silicon particles.

Figure 3 demonstrates the transmission spectra taken from the solution of the silicon nanospheres in toluene and from pure toluene. At a wavelength of ≈300 nm, the transmission of the solution is roughly five times lower.

For comparison, we studied silicon particles that formed when silicon was dissolved in molten copper (the experimental technique was the same as described above). Copper was chosen because it intensely dis-

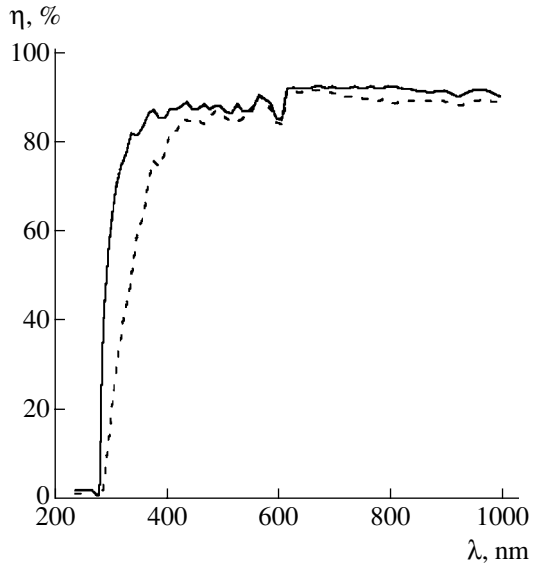

Fig. 3. Optical transmission spectra for pure toluene (continuous curve) and for the solution of the silicon nanoparticles in toluene (dashed line).

solves but does not interact with silicon [2] and contains oxygen in large amounts [4]. After etching the copper–silicon alloy, we obtained a white porous lump, which was free of spherical particles (as demonstrated by TEM examination). The irregular shape of the particles and their white color suggested that this lump consists of silicon oxide, which was confirmed by etching in hydrofluoric acid. One may assume that the oxygen dissolved in copper oxidizes the silicon almost completely, thus preventing the formation of spherical silicon nanoparticles.

Thus, the aluminum melt appears to represent a unique medium where oxygen and other gases that are capable of combining with silicon are present in minor amounts, if at all, and where silicon does not react with the metal. As a result, silicon atoms interact with each other to form spherical particles. The sizes of the fine silicon particles obtained are close to theoretically predicted diameters of Si_{60} silicon fullerenes (1.5 nm) [5]. The coarse particles are likely to be an analogue of carbon soot (so-called white soot), which is known to consist of spherical particles [6].

Further investigation into the structure and properties of the spherical silicon nanoparticles will clear up whether they have a regular fullerene-like structure.

REFERENCES

1. X. Duan and C. M. Lieber, Adv. Mater. **12**, 298 (2000).
2. M. Hansen and K. Anderko, *Constitution of Binary Alloys* (McGraw-Hill, New York, 1958; Metallurgizdat, Moscow, 1962), Vol. 1.
3. L. I. Mirkin, *Handbook of X-ray Analysis of Polycrystalline Materials* (Fizmatgiz, Moscow, 1961; Plenum, New York, 1964).
4. W. Espe, *Werkstoffkunde der Hochvakuumtechnik* (Deutscher Verlag der Wissenschaften, Berlin, 1959; Gosénergoizdat, Moscow, 1962), Vol. 1.
5. Bao-Xing Li, Pei-Lin Cao, and Duan-Lin Que, Phys. Rev. B **61**, 1685 (2000).
6. V. I. Berezkin, Fiz. Tverd. Tela (St. Petersburg) **42**, 567 (2000) [Phys. Solid State **42**, 580 (2000)].

Translated by V. Isaakyan

Technical Physics, Vol. 49, No. 3, 2004, pp. 361–362. Translated from Zhurnal Tekhnicheskoĭ Fiziki, Vol. 74, No. 3, 2004, pp. 81–82.
Original Russian Text Copyright © 2004 by Shpak, Shevchenko, Mel'nik.

SHORT COMMUNICATIONS

Effect of the Lattice Structure of Nickel Nanoparticles on Their Practical Magnetization

A. P. Shpak, A. B. Shevchenko, and A. B. Mel'nik

Kurdyumov Institute of Metal Physics, National Academy of Sciences of Ukraine, pr. Vernadskogo 36, Kiev, 03680 Ukraine

e-mail: abs@imp.kiev.ua

Received August 11, 2003

Abstract—Magnetization of nickel nanoparticles with various lattice structures is studied. Nickel particles with the fcc structure are shown to be magnetically harder than the particles with the icosahedron structure. Easy magnetization axes in the particles are found. © *2004 MAIK "Nauka/Interperiodica".*

The physical properties of nanoparticles with sizes ranging from 10 to 50 Å are of both fundamental and applied interest (as for their practical use, see, e.g., review [1] and Refs. therein). Among them, tiny ferromagnetic particles (nanoobjects with various lattice structures) are attracting special attention. As follows from many experiments and numerical simulations, metal ferromagnetic clusters have usually the bcc, fcc, or icosahedral structure with a fivefold symmetry axis, which is prohibited by translation symmetry in the massive body. It is obvious that the lattice structure, along with the size, influences the magnetic properties of nanoparticles. Therefore, finding a correlation between the lattice structure and magnetic properties of nanoparticles seems topical. In this study, the effect of the lattice structure of Ni nanoparticles on their magnetization is studied.

It is known [2] that small Ni particles have the icosahedral or fcc structure, for which an icosahedron and rhombic dodecahedron, respectively, are spatial subunits of the first coordination sphere. Let us determine stability domains for the nanoparticles. Following [3], we find their specific cohesion energy E_{coh}/E_{bulk} (Fig. 1). Calculation shows that icosahedral particles with the number of atoms N_1 = 13, 55, 147, 309, 561, … (the characteristic sizes are 5 to 25 Å) and face-centered cubic particles with N_2 = 19 (7 Å), 79 (11.1 Å), 135 (13.1 Å), 201 (15.6 Å), 675 (23 Å), … are energetically the most favorable. Note that these values of N for stable states of the particles correspond to configurations with the coordination spheres totally occupied.

When investigating the magnetic properties of the particles, we take into account that the magnetic moment of Ni clusters with N = 55.79 is $m \approx 0.8\mu_B$, where μ_B is the Bohr magneton. For Ni clusters with N = 135, $m \approx 0.7\mu_B$; for $N \geq 147$, $m \approx 0.6\mu_B$.

Thus, the magnetic moments of the most stable atomic configurations of small Ni particles are close to that of bulk nickel. Since the charge density of bulk nickel is almost coincident with the density of spin states [5], the phenomenological expression for the magnetic anisotropy energy of the particle can be written in the form

$$E_a = \frac{\mu_0 q^2}{8\pi N}\sum_{i\neq j}^{N}\left[\frac{2}{r_{ij}} - \frac{1}{|\mathbf{r}_{ij}+\mathbf{r}|} - \frac{1}{|\mathbf{r}_{ij}-\mathbf{r}|}\right], \qquad (1)$$

where μ_0 is the magnetic constant, $q = m/r$, $\mathbf{r} = \mathbf{e}_m r$, $\mathbf{e} = \mathbf{m}/m$, $\mathbf{m}$ is the atomic magnetic moment ($0.8\mu_B$ for N =

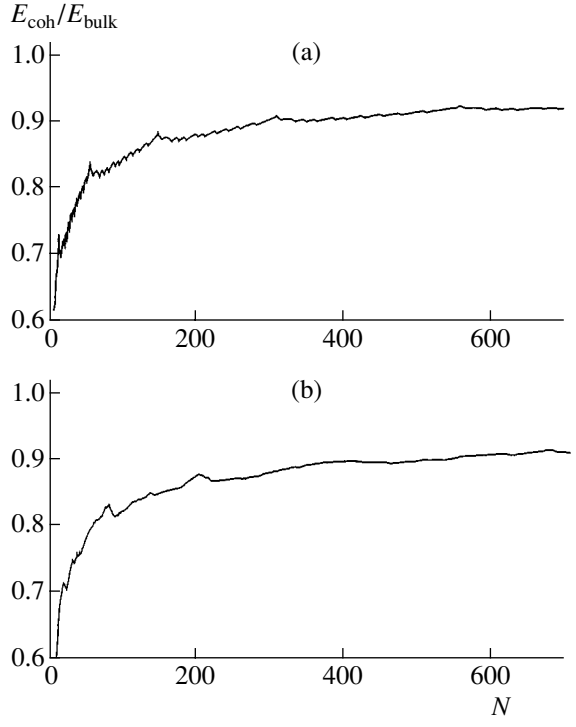

Fig. 1. Specific cohesion energy of Ni nanoparticles vs. the number of constituent atoms: (a) icosahedral particles and (b) particles with the fcc lattice.

1063-7842/04/4903-0361$26.00 © 2004 MAIK "Nauka/Interperiodica"

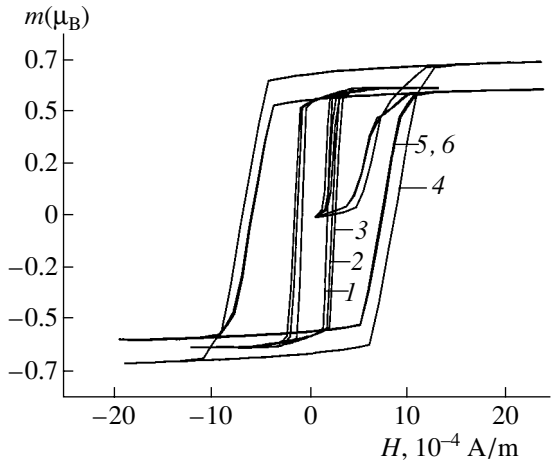

Fig. 2. Magnetization curves for the Ni nanoparticles. N = (*1*) 147, (*2*) 309, (*3*) 561, (*4*) 135, (*5*) 201, and (*6*) 675 (curves *5* and *6* merge together).

55.79, $0.7\mu_B$ for $N = 135$, and $0.6\mu_B$ for $N > 135$), r is the atomic radius, and $\mathbf{r}_{ij}$ is the vector distance between i and j atoms (atoms are viewed as hard spheres).

The particles with $N < 55$ ($N = 13.19$) are disregarded, since their characteristic size 5 Å is smaller than the minimal size of a ferromagnetic particle (10 Å) [5].

The direction of the easy magnetization axis in the nanoparticles is found by minimizing expression (1). Performing minimization by the Monte Carlo method with an angular step $\Delta\varphi = 1.7 \times 10^{-6}$ rad between the easy magnetization axis and the Cartesian axes, we find that the easy magnetization axis for the icosahedral particles represents the fivefold axis of rotational symmetry that passed through the center and opposite vertices of the icosahedron. At the same time, the binary axis of rotational symmetry that connects the central vertices of the rhombic dodecahedron is the easy magnetization axis for the fcc particles.

Using the Monte Carlo method, we also studied the process of magnetization of the nanoparticles (Fig. 2). The amount of hysteresis was determined by averaging hysteresis loops at various directions of the easy magnetization axis and external magnetic field **H**. An angular step between the easy magnetization axis and **H** was 1.7×10^{-6} rad; a step in field, 1.26×10^{-4} A/m. Since E_a varies insignificantly with N, the magnetization curves for the particles in Fig. 2 superpose. This fact outlines the domain of interest in studying nanoparticles. From Fig. 2, it also follows that the icosahedral particles are magnetically softer than the fcc ones. For example, the coercive force ratio for the particles with $N_2 = 147$ and $N_1 = 135$ and 201 are $H_{c135}/H_{c147} \approx 6.2$ and $H_{c201}/H_{c147} \approx 5.4$. The ratio of the initial differential susceptibilities $\chi_a = (dm/dH)|_{H \to 0}$ is $\chi_{a135}/\chi_{a147} \approx 0.2$ and $\chi_{a201}/\chi_{a147} \approx 0.24$. In other words, the lattice symmetry (the symmetry of the icosahedral particles is higher) has an effect on the magnetic properties of nanoparticles and, accordingly, on the properties of materials made of nanoparticles.

Typical ranges of the coercive fields for the icosahedral and fcc particles are, respectively, $(1.3–2.3) \times 10^{-4}$ and $(7–8) \times 10^{-4}$ A/m. These values are rather high, so that both particles may be considered as magnetically hard materials. A jump in the coercive force that is observed in going from the icosahedron particles with $N = 147$ and 561 to the fcc particles with $N = 201$ and 675 is worth noting. The particle size is 15 and 15.6 Å in the former case and 25 and 23 Å in the latter.

REFERENCES

1. I. P. Suzdalev and P. I. Suzdalev, Usp. Khim. **70**, 203 (1999).
2. Yu. I. Petrov, *Clusters and Small Particles* (Nauka, Moscow, 1986).
3. D. Tomanek, S. Mukherjee, and K. H. Bennemann, Phys. Rev. B **28**, 665 (1983).
4. I. Billas, A. Chatelian, and W. Heer, Science **265**, 1682 (1994).
5. S. V. Vonsovskiĭ, *Magnetism* (Nauka, Moscow, 1971; Wiley, New York, 1974).

Translated by V. Isaakyan

Technical Physics, Vol. 49, No. 3, 2004, pp. 363–364. Translated from Zhurnal Tekhnicheskoĭ Fiziki, Vol. 74, No. 3, 2004, pp. 83–84.
Original Russian Text Copyright © 2004 by Antonov, Zhukarev, Polyakov, Skachkov.

SHORT COMMUNICATIONS

Magnetization Vector Field in a Uniaxial Ferromagnetic Film

L. I. Antonov, A. S. Zhukarev, P. A. Polyakov, and D. G. Skachkov

Moscow State University, Vorob'evy Gory, Moscow, 119992 Russia

e-mail: lev@genphys.phys.msu.ru

Received August 11, 2003

Abstract—Analytical models for the magnetization vector field $\mathbf{B}_m$ in a uniaxial ferromagnetic film are studied. Some of them are found to closely approximate $\mathbf{B}_m$ even if the quality factor of the material approaches unity. © *2004 MAIK "Nauka/Interperiodica".*

When theoretically describing states and processes in ferromagnets, one must know the distribution of the magnetization vector or of its components $\mathbf{B}_m$ and $\mathbf{H}_m$ [1]. The description of $\mathbf{B}_m$ or $\mathbf{H}_m$ is usually carried out in terms of simplified models that yield analytical expressions for $\mathbf{B}_m$ and $\mathbf{H}_m$, which is of great importance for applied problems. Although results obtained from the simplified models are of limited utility, they are often applied too broadly without considering errors that may arise.

In this work, we describe the magnetization vector field $\mathbf{B}_m$ in a magnetic film with easy-axis anisotropy in terms of a simple model where a solitary domain wall (DW) separates two semi-infinite domains magnetized normally to the film plane (i.e., the magnetization is aligned with the z axis). It is assumed that the demagnetizing field is equal to the magnetic field produced by an infinitely long strip of width h (h is the film thickness) with a current $J_y = 2Mh$ in the direction of the y axis (in the film plane, the magnetization experiences a jump of $2M$). At points lying at the middle of the DW, the demagnetizing field is given by [2, Eq. (3.2.1), p. 77]

$$B_{mx}(z) = 4M\ln\frac{z+h/2}{z-h/2}, \qquad B_{mz}(z) = 0. \tag{1}$$

The model considered is a significant drawback: the field B_{mx} diverges on the film surface. This field must be known, for example, in order to calculate the "twist" of the magnetization in the DW.

To eliminate this drawback, it is necessary to consider the magnetization distribution in the DW. Let the DW have a width Δ. In such a model, the field $\mathbf{B}_m$ is equivalent to the field between two infinitely long strips that are Δ distant from each other and have codirected currents $J_y = Mh$. The expression for the field B_{mx} at the middle of the DW has the form

$$B_{mx}(z) = 2M\ln\frac{(z+h/2)^2+\Delta^2/4}{(z-h/2)^2+\Delta^2/4}. \tag{2}$$

Assuming that the magnetization inside the DW varies linearly from $-M$ to M and splitting the DW into a set of layers dx of thickness h with currents $di = Mdx$, we obtain

$$B_{mx}(z) = 2M\ln\frac{(z+h/2)^2+\Delta^2}{(z-h/2)^2+\Delta^2} + 4M\frac{(h/2+z)}{\Delta}\arctan\frac{\Delta}{(h/2+z)} - 4M\frac{(h/2-z)}{\Delta}\arctan\frac{\Delta}{(h/2-z)}.$$

Now, assuming that the magnetization obeys the Landau–Lifshitz distribution ($M_z = M(\tanh(x/\Delta)$ and splitting the DW into a set of layers dx with a thickness h and currents $di = Md(\tanh(x/\Delta))$, we arrive at

$$B_{mx}(z) = 2M\int_0^\infty \frac{1}{\cosh^2(x/\Delta)}\ln\frac{(z+h/2)^2+x^2}{(z-h/2)^2+x^2}\frac{dx}{\Delta}. \tag{3}$$

For a periodic array of DWs, the field $\mathbf{B}_m$ may be found under the assumption $\Delta \ll d$, where d is the period of the structure. For such a structure, the field B_{mx} at the middle of the DW is expressed as

$$B_{mx}(z) = B_{mx}^1 + 2M\sum_{n=1}^{\infty}(-1)^n\ln\frac{(z+h/2)^2+(nd/2)^2}{(z-h/2)^2+(nd/2)^2}, \tag{4}$$

where B_{mx}^1 is the demagnetizing field for a solitary DW.

For a curved DW, which arises in dynamic processes, the component B_{mz} of the field $\mathbf{B}_m$ is other than

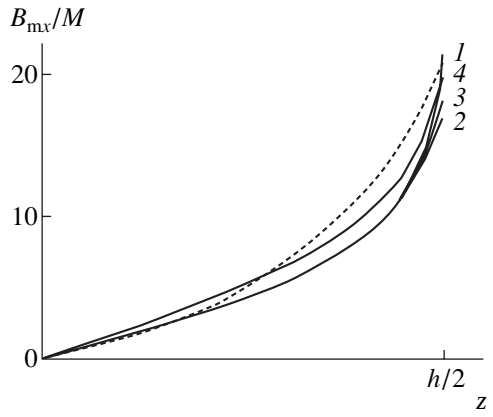

Field B_{mx} calculated by Formulas (1)–(4) and obtained by the dynamic establishment method for a twisted DW (dashed line).

zero. Expressions for the components of the field $\mathbf{B}_m$ can be found by supposing that the field is equivalent to the field of currents passing over the curved surfaces $q(z) - \Delta/2$ and $q(z) + \Delta/2$, where $q(z)$ is the coordinate of the DW center:

$$B_{mx}(z) = 2M \int_{-h/2}^{h/2} \left[\frac{(z-z')}{(z-z')^2 + (q(z)-q(z')+\Delta/2)^2} + \frac{(z-z')}{(z-z')^2 + (q(z)-q(z')-\Delta/2)^2} \right] dz',$$

$$B_{mz}(z) = 2M \int_{-h/2}^{h/2} \left[\frac{(q(z)-q(z')+\Delta/2)}{(z-z')^2 + (q(z)-q(z')+\Delta/2)^2} + \frac{(q(z)-q(z')-\Delta/2)}{(z-z')^2 + (q(z)-q(z')-\Delta/2)^2} \right] dz'.$$

Advanced numerical methods allow one to solve the rigorously stated problem of magnetization vector distribution both in a solitary DW [4] and in a periodic domain structure [5] with any desired accuracy and calculate the field $\mathbf{B}_m$ [6].

The figure compares $\mathbf{B}_m$ calculated by formulas (1)–(4) with the result of numerical calculation by the dynamic establishment method (dashed line) [5]. The ordinate is the component B_{mx} in units of M; the abscissa, the coordinate z from the middle of the film to its surface. The parameters of the film are the quality factor $Q = K/2\pi M^2 = 2$, the thickness $h = 10l$, and the period of the magnetization structure $d = 11l$. Here, $l = (AK)^{1/2}/\pi M$ is the characteristic length of the film and A and K are the anisotropy constant and the constant of exchange interaction, respectively.

As follows from the figure, B_{mx} found from formulas (1)–(4) qualitatively agree with B_{mx} obtained by the numerical method. The mean discrepancy between the field obtained by (4) and that obtained numerically varies from 18% for $Q = 4$ to 45% for $Q = 1$. Thus, the analytical formulas provide a good approximation of $\mathbf{B}_m$ even if the Q factor of a material is close to unity.

REFERENCES

1. L. I. Antonov, I. K. Bol'nykh, Yu. A. Durasova, *et al.*, Preprint No. 1/2000, Mosk. Gos. Univ. im. M. V. Lomonosova (Moscow State University, Moscow, 2000).
2. L. I. Antonov, L. G. Dedenko, and A. N. Matveev, *Solution of Electricity Problems* (Mosk. Gos. Univ., Moscow, 1982).
3. F. V. Lisovskiĭ, *Physics of Magnetic Bubbles* (Sov. Radio, Moscow, 1979).
4. L. I. Antonov, S. G. Osipov, and M. M. Khapaev, Fiz. Met. Metalloved. **55**, 917 (1983).
5. L. I. Antonov, V. V. Ternovskiĭ, and M. M. Khapaev, Fiz. Met. Metalloved. **67**, 55 (1989).
6. L. I. Antonov, G. A. Mironova, E. V. Lukasheva, *et al.*, Preprint No. 2/1999, Mosk. Gos. Univ. im. M. V. Lomonosova (Moscow State University, Moscow, 1999).

Translated by V. Isaakyan

Technical Physics, Vol. 49, No. 3, 2004, pp. 365–366. Translated from Zhurnal Tekhnicheskoĭ Fiziki, Vol. 74, No. 3, 2004, pp. 85–86.
Original Russian Text Copyright © 2004 by Dvinskikh.

SHORT COMMUNICATIONS

Estimating the Spectrum of a Component of a Digital Signal Containing an Intense Interference

V. A. Dvinskikh

Chernyshevsky State University, Saratov, Moskovskaya ul. 155, 410026 Russia

e-mail: cred@sgu.ru

Received August 11, 2003

Abstract—A spectral analysis technique based on approximating a set of counts by a first-degree trigonometric polynomial with a varying frequency of its harmonics. With this technique, the parameters of a signal component that is two orders of magnitude weaker than an interference are estimated at a frequency ratio of 0.82.
© 2004 MAIK "Nauka/Interperiodica".

In experiments, one often needs to estimate the spectrum of a weak periodic component in the presence of an intense harmonic interference. Fast Fourier transformation in this case cannot provide a necessary resolution because of its poor selectivity [1] and the presence of extra noise [2]. Earlier [3], the author suggested a technique for consistent spectral analysis of quasi-periodic oscillations where a set of counts is approximated by a first-degree trigonometric polynomial with a varying frequency of its harmonics. To date, this technique has proved to be efficient in estimating the parameters of components of a digital signal with an intense harmonic interference. In [4], the parameters of a double-period component of oscillations were estimated in the case when the amplitude of this component was five times lower that the basic component amplitude. Therefore, it seems reasonable to extend the technique for a wider range of amplitude and frequency ratios.

The parameters of oscillation harmonics can be appropriately estimated by the spectral analysis technique where a sequence of counts is approximated by a first-degree trigonometric polynomial. Let we have a sequence of counts $x(n)$ ($n = 0, 1, \ldots, N-1$) that may contain harmonics such that their number K and frequencies are unknown but a frequency range expected can be given. We approximate this sequence by a trigonometric polynomial [3] of type

$$y_j(n) = G_j + S_j\sin(nh_j) + C_j\cos(nh_j),$$

$$j = 1, 2, \ldots, L \gg K, \quad n = 0, 1, \ldots, N-1.$$

Here,

$$h_j = \frac{2\pi}{24}(A + rj),$$

A is the starting point of spectral analysis; r is a step; and C_j, S_j, and G_j are to be found by the least-squares method:

$$S_j = (U_{2j}F_{1j} - U_{1j}F_{2j})/W_j; \quad C_j = (V_{1j}F_{2j} - V_{2j}F_{1j})/W_j;$$

$$G_j = (E_{1j} - A_{1j}S_j - A_{2j}C_j)/N.$$

In the above formulas,

$$W_j = V_{1j}U_{2j} - V_{2j}U_{1j}; \quad V_{1j} = B_{1j}A_{0j} - A_{1j}B_{0j};$$

$$V_{2j} = D_{1j}A_{0j} - A_{1j}D_{0j}; \quad U_{1j} = B_{2j}A_{0j} - A_{2j}B_{0j};$$

$$U_{2j} = D_{2j}A_{0j} - A_{2j}D_{0j}; \quad F_{1j} = E_{2j}A_{0j} - E_{1j}B_{0j};$$

$$F_{2j} = E_{3j}A_{0j} - E_{1j}D_{0j},$$

$$A_{0j} = N; \quad A_{1j} = B_{0j} = \sum_{n=0}^{N-1}\sin(nh_1);$$

$$B_{1j} = \sum_{n=0}^{N-1}\sin^2(nh_j); \quad A_{2j} = D_{0j} = \sum_{n=0}^{N-1}\cos(nh_j);$$

$$B_{2j} = D_{1j} = \sum_{n=0}^{N-1}\sin(nh_j)\cos(nh_j);$$

$$D_{2j} = \sum_{n=0}^{N-1}\cos^2(nh_j); \quad E_{1j} = \sum_{n=0}^{N-1}x(n);$$

$$E_{2j} = \sum_{n=0}^{N-1}x(n)\sin(nh_j); \quad E_{3j} = \sum_{n=0}^{N-1}x(n)\cos(nh_1),$$

$$j = 1, 2, \ldots, L.$$

From the maxima of the dependences

$$M_j = \sqrt{S_j^2 + C_j^2}, \quad J = 1, 2, \ldots, L$$

the presence of harmonics in a process studied is established. Then, if necessary, one can determine the coef-

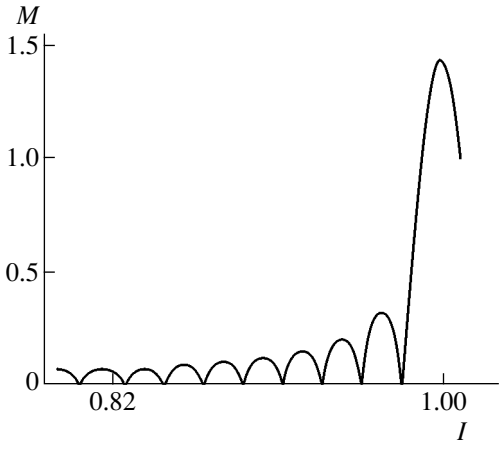

Fig. 1.

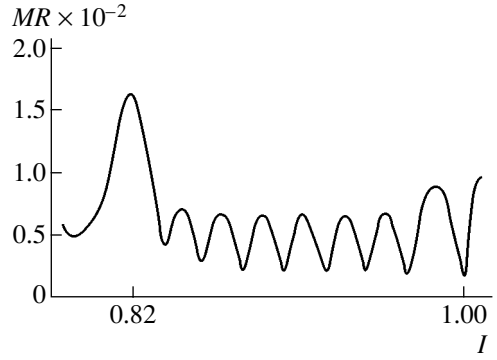

Fig. 2.

ficients of the trigonometric polynomial that correspond to these maxima.

Since the constant component is found simultaneously, associated calculations are carried out without preliminarily memorizing the array of input data, i.e., in real time. Using the technique of approximation by trigonometric polynomial, one may reveal [4] weak frequency components in the presence of an intense harmonic interference. In this case, calculations are performed in two steps. First, spectral analysis is carried out in a given frequency range and the parameters S_1, C_1, and h_1 of the intense harmonic component (interference) are found with the entire spectrum memorized. At the second step, spectral analysis is performed again in the same frequency range of the signal:

$$Z(n) = G_1 + S_1\sin(nh_1) + C_1\cos(nh_1).$$

Next, the spectral components are successively subtracted: $W_{1j} = S_j - Z_{1j}$, $W_{2j} = C_j - Z_{2j}$ ($j = 1, 2, \ldots, L$), and the dependence $MR_j = \sqrt{W_{1j}^2 + W_{2j}^2}$, from which the parameters of weak components are estimated, is calculated.

The author investigated the signal with $a = 2\pi/24$:

$$q(n) = 1000 + \sin(an\sqrt{3}) + \cos(an\sqrt{3})$$
$$+ 0.01\sin(an\sqrt{2}) + 0.01\cos(an\sqrt{2}) + \varepsilon(n),$$
$$n = 0, 1, \ldots, N-1.$$

Figure 1 shows the initial spectrum; Fig. 2, the difference signal spectrum, from which one determines the absolute value of the weak component of interest with an accuracy of 20% or higher (the abscissa is the frequency ratio).

REFERENCES

1. S. L. Marple, Jr., *Digital Spectral Analysis with Application* (Prentice-Hall, New York, 1987; Mir, Moscow, 1990).
2. *Mathematical Methods and Computers: Experimental Design and Data Processing*, Ed. by A. N. Ostanin (Vysshaya Shkola, Minsk, 1986).
3. V. A. Dvinskikh, Zh. Tekh. Fiz. **62** (12), 168 (1992) [Sov. Phys. Tech. Phys. **37**, 1213 (1992)].
4. V. A. Dvinskikh, Pis'ma Zh. Tekh. Fiz. **25** (5), 21 (1999) [Tech. Phys. Lett. **25**, 172 (1999)].

Translated by V. Isaakyan

Technical Physics, Vol. 49, No. 3, 2004, pp. 367–370. Translated from Zhurnal Tekhnicheskoĭ Fiziki, Vol. 74, No. 3, 2004, pp. 87–90.
Original Russian Text Copyright © 2004 by Prudan, Kozyrev, Zemtsov.

SHORT COMMUNICATIONS

Equal-Permittivity States Induced in a Ferroelectric

A. M. Prudan, A. B. Kozyrev, and A. V. Zemtsov

LÉTI St. Petersburg State Electrotechnical University, ul. prof. Popova 5, St. Petersburg, 197376 Russia

e-mail: f@eltech.ru

Received August 11, 2003

Abstract—Conditions under which a ferroelectric subjected to an electric field acquires equal-permittivity paraelectric states at different temperatures are studied. The temperature dependences of the control (inducing) field intensity and feasible permittivity interval (ε_{min}–ε_{max}) are obtained. The effect of intersection of the $\varepsilon(E, T_i)$ characteristics of the ferroelectric in the paraelectric state is analyzed. With the control field and temperature varying consistently, the permittivity ε_i of strontium titanate films and films of the barium titanate–strontium titanate solid solution may be kept constant in a wide (200–320 K) temperature range and, at the same time, changed by more than twofold by varying the electric field. © *2004 MAIK "Nauka/Interperiodica".*

INTRODUCTION

Use of ferroelectric (FE) materials in metal–insulator–metal structures makes it possible to design electrically controlled electronic devices [1]. In ferroelectrics, the field and temperature dependences of the permittivity ε coexist; i.e., $\varepsilon = \varepsilon(E, T)$. From the viewpoint of applications, the temperature sensitivity of the permittivity ($\varepsilon(T)$) and, accordingly, device characteristics is a detrimental factor. A straightforward way of removing this effect is to stabilize the temperature of an FE element or device as a whole. Insertion of a thermostat sometimes degrades the performance of an electronic system. For applications, one needs to devise less hardware-intensive techniques for stabilizing the temperature characteristics of FE components.

In the absence of an external electric action, each paraelectric state of a ferroelectric is known to be assigned a specific value of the permittivity $\varepsilon(T)$. The application of an electric field may change the situation. In particular, if the polarization is constant ($P_i(T) = \text{const}$), all the states have different permittivities. However, when the control field intensity is temperature-invariable ($E_i(T) = \text{const}$), the temperature dependence of the permittivity ($\varepsilon(E_i, T)$) in the paraelectric range becomes nonmonotonic. Pairs of states with the same permittivity $\varepsilon(E_i, T_k) = \varepsilon(E_i, T_l)$ appear. Also, the situation becomes possible where the electric field provides a constant permittivity ($\varepsilon_i(T) = \text{const}$) over a wide temperature range [2]. In this paper, we consider the problem of matching the temperature and control field so as to induce states in a ferroelectric that differ in temperature interval but are indistinguishable in permittivity.

INDUCED STATES OF A FERROELECTRIC

The dielectric properties of a ferroelectric with the second-order phase transition will be described in terms of the Ginzburg–Devonshire formalism. In this approximation, the inverse permittivity ($\alpha = 1/\varepsilon_0\varepsilon$) of a ferroelectric in the paraelectric state is a function of two independent arguments, namely, polarization (P) and temperature (T):

$$\alpha(P, T) = \alpha_0(0, T) + 3\beta P^2, \tag{1}$$

where $\alpha(0, T)$ is the temperature-dependent inverse permittivity in the absence of the control field and β is the constant of first-order dielectric nonlinearity ($\beta = \text{const}(T)$).

The dependence $P(T)$ artificially maintained in the form

$$P^2(T) = P_1^2 - P_2^2(T), \tag{2}$$

where P_1 is a constant and

$$P_2(T) = (3\beta\varepsilon_0\varepsilon(0, T))^{-0.5} \tag{3}$$

is the temperature-dependent component of the polarization, provides both the control of the permittivity $\varepsilon_i(P_1)$ and compensation for its temperature variation ($d\varepsilon_i/dT = 0$). Note that temperature dependence (2) constructed by a step increase in the polarization at a constant temperature (ΔP_T) and a step increase in the temperature at a constant polarization (ΔT_P) meets the applicability condition for relationship (1). The invariant statement of an electric action that induces states indistinguishable in permittivity has the form

$$E^2(T) = E_1^2 + \frac{3}{2}\sqrt[3]{2E_1^4E_2^2(T)} - E_2^2(T), \tag{4}$$

where

$$E_1 = (27\beta\varepsilon_0^3\varepsilon_i^3)^{-0.5}, \tag{5}$$

and

$$E_2(T) = 2(27\beta\varepsilon_0^3\varepsilon^3(0, T))^{-0.5} \quad (6)$$

are the electric field components that provide, respectively, the variation of the permittivity $\varepsilon_i(E_1)$ and maintenance of its constant value ($\varepsilon_i(T)$ = const) in a given temperature range and ε_0 is the absolute dielectric constant.

Thus, basically the permittivity of an FE may be stabilized in a given temperature range and available hardware can implement algorithms (1) and (4), which match the control field and temperature.

A relationship between the temperature interval width T_l–T_k, the range $\varepsilon_i = \varepsilon_{max}$–$\varepsilon_{min}$ of realizable permittivities, and the related range of control field strengths E_{min}–E_{max} is a key issue in the discussed problem of stabilizing the FE permittivity. The search for a correlation between $\Delta\varepsilon_i$ and ΔT and between ΔE and ΔT simplifies greatly if one takes a good look at the behavior of the point of intersection between characteristics $\varepsilon(E, T)$ corresponding to two different temperatures ($T_l < T_k$). Note that the property $\varepsilon(E_C, T_l) = \varepsilon(E_C, T_k)$ of nonlinear FEs could be noticed from earlier experimental data [3, 4]; however, it was overlooked by the researchers and was not explained analytically.

INTERSECTION OF $\varepsilon(E)$ CHARACTERISTICS

In the absence of the control field ($E = 0$), the permittivity $\varepsilon(0, T)$ of a ferroelectric exhibiting the second-order phase transition decreases monotonically with increasing temperature in the paraelectric range ($T > T_C$). The application of an electric field (E_i = const) causes the permittivity to decrease ($\varepsilon(0, T) > \varepsilon(E_i, T)$) and produces a maximum in the curve $\varepsilon(E_i, T)$ in the range $T > T_C$ [3–5]. In this case, pairs of states equal in permittivity appear. The presence of equal values of ε ($\varepsilon(E_i, T_l) = \varepsilon(E_i, T_k)$ in the temperature dependence $\varepsilon(E_i, T)$ means that the field dependences $\varepsilon(E, T_l)$ and $\varepsilon(E, T_k)$ at temperatures T_l and $T_k > T_l$ must intersect.

This conclusion follows from the phenomenological theory of ferroelectricity. Let us use the truncated Ginzburg–Devonshire series where polarization terms to a power higher than the fourth are rejected. Standard differentiation of the series yields a system of algebraic equations that relate the electric field intensity E and inverse permittivity $\alpha = 1/\varepsilon_0\varepsilon(E, T)$ to the magnitude of the polarization vector P of the ferroelectric in the paraelectric state:

$$\begin{cases} E = (\alpha_0 + \beta P^2)P \\ \alpha = \alpha_0 + 3\beta P^2. \end{cases} \quad (7)$$

System (7) is written for two temperatures, $T = T_k$ and $T = T_l < T_k$, and has a positive solution ε_C for the permittivity ($\varepsilon(E_C, T_l) = \varepsilon(E_C, T_k) = \varepsilon_C$),

$$\frac{1}{\varepsilon_C^2} = \frac{4}{3}\left(\frac{1}{\varepsilon^2(0, T_l)} + \frac{1}{\varepsilon(0, T_l)\varepsilon(0, T_k)} + \frac{1}{\varepsilon^2(0, T_k)}\right) \quad (8)$$

and a positive solution E_C for the field intensity,

$$(27\beta(\varepsilon_0\varepsilon(0, T_k))^3)E_C^2 = \left(\frac{\varepsilon(0, T_k)}{\varepsilon_C}\right)^3 + 3\left(\frac{\varepsilon(0, T_k)}{\varepsilon_C}\right)^2 - 4. \quad (9)$$

In combination, these solutions specify the point where the curves $\varepsilon(E, T_l)$ and $\varepsilon(E, T_k)$ intersect. This property is exemplified in Fig. 1, which plots $\varepsilon(E, T_i)$ calculated for strontium titanate (T_C = 40 K, $C_C = 9 \times 10^4$ K, and $\beta = 8.9 \times 10^9$ m^5/C^{2}F [3–5]).

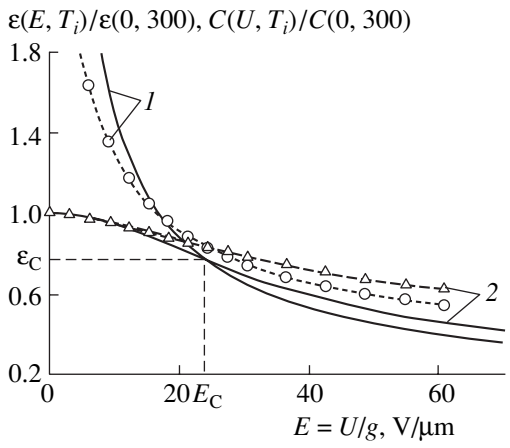

Fig. 1. Calculated permittivity (solid lines) of strontium titanate and the capacitance of the $SrTiO_3$ film plane capacitor (data points) vs. electric field intensity E at T = (*1*) 78 and (*2*) 300 K. U is the control voltage, and g is the electrode gap.

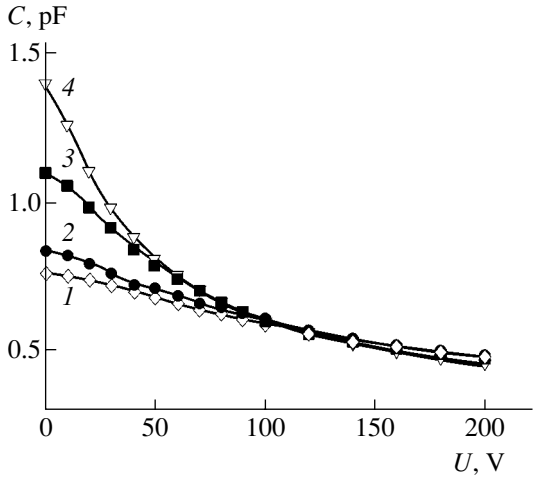

Fig. 2. C–U characteristics of the $Ba_{0.3}Sr_{0.7}TiO_3$ film plane capacitor (T_C = 120 K, Fig. 2) at T = (*1*) 325, (*2*) 305, (*3*) 225, and (*4*) 200 K. The measuring field frequency is f = 1 MHz.

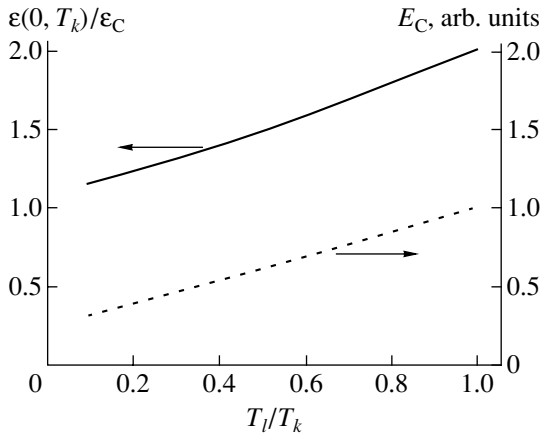

Fig. 3. Coordinates (ε_C, E_C) of the point where two $\varepsilon(E)$ characteristics of strontium titanate intersect vs. the ratio of temperatures (T_l/T_k) at which they were taken.

Pair intersection of the capacitance–voltage characteristics $C = C(U, T_i)$ was observed for plane-parallel metal–insulator–metal structures based on bulk ferroelectrics [4] and for plane capacitors made of $SrTiO_3$ (T_C = 40 K, Fig. 1) and $Ba_xSr_{1-x}TiO_3$ (T_C = 120 K, Fig. 2) films produced by rf magnetron sputtering [6, 7]. It should be noted that the electrode spacing of a plane capacitor is filled with a dielectric nonuniformly and its capacitance depends on the FE permittivity nonlinearly [8]. For this reason, the permittivities are not exactly equal at the point of interaction of the two *C–U* characteristics:

$$\varepsilon(E_C, T_l)/\varepsilon(E_C, T_k) = 1 \pm \Delta.$$

For the planar structures we studied, the correction Δ is small ($\Delta \ll 1$), so that the condition $\varepsilon(E_C, T_l) = \varepsilon(E_C, T_k)$ is met at the point $\{C_C, U_C\}$ in the *C–U* curve (Fig. 1).

The temperature ratio T_l/T_k has a decisive effect on the coordinates of this point (Fig. 3). As follows from (8), the permittivity ε_C takes a minimal value ($\varepsilon_C = 0.5\varepsilon(0, T_k)$) at $T_l/T_k = 1$. The greater the difference between T_k and T_l, the higher the permittivity ε_C. Its ultimate value $\varepsilon_C = 0.87\varepsilon(0, T_k)$ is reached in the limit $T_l = T_C$.

The other coordinate, the field intensity E_C (see (9)), increases with ratio T_l/T_k (Fig. 3), taking a maximal value at $T_l/T_k = 1$:

$$(E_C)_{max} = \frac{4}{3}(3\beta(\varepsilon_0\varepsilon(0, T_k))^3)^{-1/2}. \quad (10)$$

It should also be noted that, when the control field is weak ($E_i < (E_C)_{max}$), the derivative $\partial(\varepsilon(E_i, T))/\partial T$ is negative. At high control fields ($E_i > (E_C)_{max}$), the derivative becomes positive. In the latter case, each of the characteristics $\varepsilon(E, T_i)$ taken in the interval $T_i \in (T_l–T_k)$ is assigned the same range ($\varepsilon_{max}–\varepsilon_{min}$) of realizable permittivities.

Analysis shows that the field dependence $\varepsilon(E, T_k)$, where T_k is a maximal temperature, contains full information about the extrema (ε_{max} and ε_{min}) of permittivities to be stabilized: $\varepsilon_{max} = \varepsilon(0, T_k)$ and $\varepsilon_{min} = (\varepsilon(E_{max}, T_k))$, where E_{max} is the maximum intensity of the control field at $T = T_k$. To be definite, we assume that E_{max} equals the maximum field intensity $(E_C)_{max}$ given by (10). Note that $(E_C)_{max}$ is a physical parameter of a ferroelectric, because it includes only the material constants. It is also significant that the application of the field $(E_C)_{max}$ halves the permittivity ($\varepsilon(0, T_k) = 2(\varepsilon((E_C)_{max}, T_k))$). Such a variation is sufficient for applications.

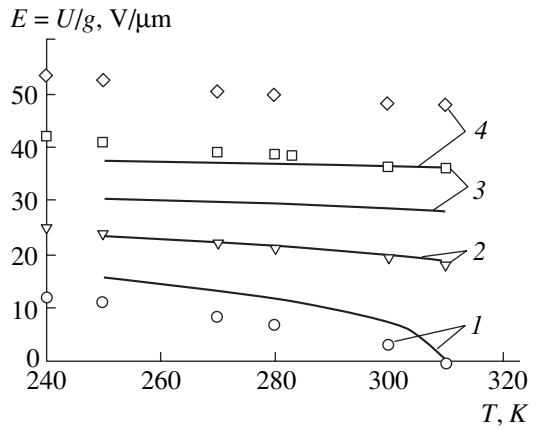

Fig. 4. Temperature behavior of the control field intensity in strontium titanate at which the permittivity ε_i of the bulk sample (solid lines, calculation) and the capacitance C_i of the $SrTiO_3$ film plane capacitor (data points) are kept constant: $C_i/C(0, 310) = \varepsilon_i/\varepsilon(0, 310) =$ (*1*) 1.00, (*2*) 0.83, (*3*) 0.71, and (*4*) 0.62.

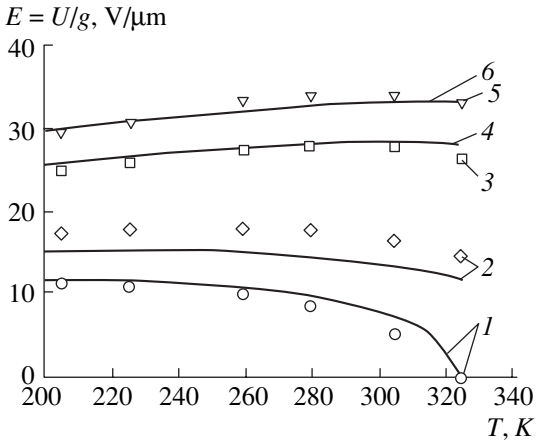

Fig. 5. Temperature behavior of the control field intensity in the barium titanate–strontium titanate solid solution at which the permittivity ε_i of the bulk sample (solid lines, calculation) and the capacitance C_i of the $Ba_{0.3}Sr_{0.7}TiO_3$ film plane capacitor (data points) are kept constant: $C_i/C(0, 310) = \varepsilon_i/\varepsilon(0, 310) =$ (*1*) 1.00, (*2*) 0.83, (3) 0.71, (*4*) 0.55, (*5*) 0.66, and (*6*) 0.50.

DISCUSSION

Experimental temperature dependences of the control field strength that provides a constant permittivity ($\varepsilon_i(T)$ = const) of $SrTiO_3$ are presented in Fig. 4. Even if the temperature interval of interest for applications (220–320 K) is far from the Curie temperature (T_C = 40 K), the control field intensity is several times lower than the critical value ($E_{cr} \sim 200$ V/μm [9]) for FE films. The disagreement between the theoretical and experimental results observed in Fig. 4 is conceivably associated with a nonuniform permittivity of the FE film of the plane capacitor.

The field component $E_2(T)$ (see (6)), which compensates for the temperature dependence of the permittivity, grows with temperature as $E_2 \sim (T - T_C)^{3/2}$. A decrease in the temperature $(T - T_C)$ through using a ferroelectric with high T_C is expected to reduce significantly the E_2 component and resultant intensity (4) of the control field. Experimental data (Fig. 5) for $Ba_{0.3}Sr_{0.7}TiO_3$ film plane capacitors (T_C = 120 K) corroborate this prediction.

To conclude, a control field consistently varying with temperature induces states in a ferroelectric that differ in temperature interval but are indistinguishable in permittivity. The permittivity ε_i of the ferroelectric becomes temperature independent but may be controlled with a field in the range from $\varepsilon_i = \varepsilon_{min}$ to $\varepsilon_i = \varepsilon_{max}$ ($\varepsilon_{max}/\varepsilon_{min} \approx 2$), which is sufficient for applications.

REFERENCES

1. O. G. Vendik, E. K. Golman, A. B. Kozyrev, *et al.*, J. Supercond. **12**, 325 (1999).
2. A. M. Prudan, Cand. Sci. Dissertation (St. Petersburg, 2002).
3. G. V. Belokopytov, I. M. Buzin, I. V. Ivanov, *et al.*, Fiz. Tverd. Tela (Leningrad) **23**, 141 (1981) [Sov. Phys. Solid State **23**, 79 (1981)].
4. J. Dec, W. Kleemann, and B. Westwanski, J. Phys.: Condens. Matter **11**, L379 (1999).
5. J. M. Worlock and P. A. Fleury, Phys. Rev. Lett. **19**, 1176 (1967).
6. E. K. Gol'man, V. E. Loginov, A. M. Prudan, *et al.*, Pis'ma Zh. Tekh. Fiz. **21** (21), 84 (1995) [Tech. Phys. Lett. **21**, 899 (1995)].
7. E. K. Gol'man, V. I. Gol'drin, V. E. Loginov, *et al.*, Pis'ma Zh. Tekh. Fiz. **25** (14), 1 (1999) [Tech. Phys. Lett. **25**, 549 (1999)].
8. O. G. Vendik, S. P. Zubko, and M. A. Nikol'skii, Zh. Tekh. Fiz. **69** (4), 1 (1999) [Tech. Phys. **44**, 349 (1999)].
9. K. Dougherty, J. Drab, M. Brand, *et al.*, Mater. Res. Soc. Symp. Proc. **720**, H2.3.1 (2002).

Translated by A. Khzmalyan

Technical Physics, Vol. 49, No. 3, 2004, pp. 371–377. Translated from Zhurnal Tekhnicheskoĭ Fiziki, Vol. 74, No. 3, 2004, pp. 91–97.
Original Russian Text Copyright © 2004 by Tkachev, Yakovlenko.

SHORT COMMUNICATIONS

Simulation of an Electron Avalanche in Helium

A. N. Tkachev and S. I. Yakovlenko

Institute of General Physics, Russian Academy of Sciences, Moscow, 119991 Russia

e-mail: syakov@kapella.gpi.ru

Received August 11, 2003

Abstract—The parameters of an avalanche generated by an electron in helium at different ratios E/p, where E is the external field strength and p is the pressure, are simulated. The E/p dependences of the ionization rate and Townsend coefficient have maxima at $E/p \approx 1000$ and ≈ 200 V/(cm Torr), respectively. The today's concepts of the electron density distribution in the avalanche are valid only at small values of the reduced strength, $E/p <$ 100 V/(cm Torr). With $E/p >$ 100 V/(cm Torr), the electron density distribution extends along the field. © *2004 MAIK "Nauka/Interperiodica".*

INTRODUCTION

If a gas is under a strong electric field, an accidentally born electron causes exponential electron multiplication, generating an avalanche [1–7]. When the number of the electrons becomes sufficiently large, the resultant plasma begins to distort the external field, causing streamers [1–7]. Streamer modification has recently become the subject of extensive research (see, e.g., [8–13] and Refs. therein). However, the avalanche has been simulated in detail only in nitrogen [14], whereas the avalanche in helium, for which electron–atom collision cross sections are well known, is much more interesting with a view to check the basic statements of the theory.

In [15], we, using the method of multiparticle dynamics, calculated the Townsend coefficients and mean velocities of electrons that multiply in helium in the gap between planar electrodes. It was shown that the notion of the Townsend ionization coefficient remains valid even in high fields if the spacing between the planes is sufficiently large. In this case, the E/p dependence of the Townsend coefficient (E is the external field strength, and p is the pressure) has a maximum at $E/p \approx 200$ V/(cm Torr), which gives rise to the upper branch of the Paschen curve. In [15], the parameters of a single avalanche were not considered. In this work, we fill this gap.

STATEMENT OF THE PROBLEM AND SOLUTION METHOD

The multiplication and runaway of electrons in helium were simulated based on the modified particle method [15–17]. An avalanche-initiating electron was born at the origin and had a randomly directed velocity. Its initial energy obeys the Poisson distribution with a mean value $\varepsilon_0 = 0.2$ eV. At small time steps, the equations of motion were solved for all the electrons and elastic and inelastic collisions with probabilities defined by the cross sections of elementary events were drawn. The cross sections were taken from [18–20], and the approximations of these sections are given in [15].

As a result of the simulation, which took a reasonable amount of time, we managed to trace the electron dynamics within seven to nine characteristic times of electron multiplication: $t \sim (7–9)/\nu_i$, where ν_i is the ionization rate. Upon simulating, the number of electrons in the avalanche reached five thousands. Unfortunately, the method of multiparticle dynamics does not allow researchers to trace an avalanche at times $t \geq 11/\nu_i$, because the time of computation grows exponentially. Therefore, we proceeded as follows.

After the electron dynamics had been simulated, the data obtained were extrapolated to double time. When extrapolating, we assumed that each of the electrons generates a new avalanche and that the new avalanche is identical to the one for which dynamic simulation has been already performed. In other words, it was assumed that the avalanche evolution is a Markovian process. Such an approach is certainly inapplicable if the electric field of an avalanche is comparable to the external field. If the avalanche field is taken to be weak, such an extrapolation can be applied only once for times $t \lesssim (15–18)/\nu_i$.

Using this expedient, we calculated the distributions of ions and electrons in the avalanche, as well as the field produced by the particles, at later time instants. The particle density and the field were calculated in the following way.

Let sets $\{r_j^{(e)}, j \in 1\ldots N\}$ and $\{r_j^{(i)}, j \in 1\ldots N\}$ be the sets of radius vectors for electrons and ions, respectively, at a time t that is the time of completion of simulating electron multiplication in an avalanche. Under the assumption that the process is Markovian, the sets of the electron and ion coordinates at a time $2t$ are, respectively, $\{r_j^{(e)} + r_k^{(e)}, j \in 1\ldots N, k \in 1\ldots N\}$ and

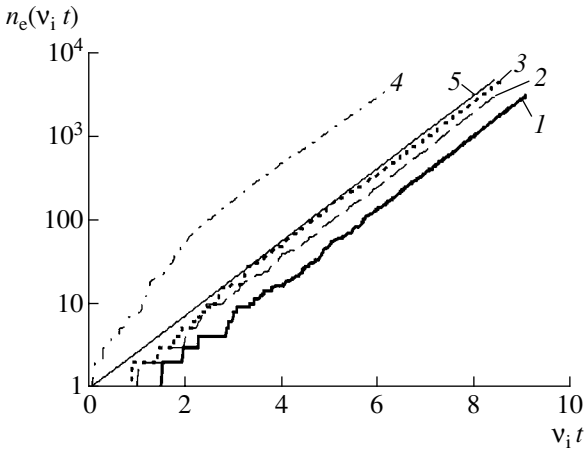

Fig. 1. Number of electrons and ions in the avalanche vs. reduced time $\nu_i t$ for various reduced field strengths: (*1*) E/p = 40 V/(cm Torr), E = 30.4 kV/cm, and $\nu_i = 1.82 \times 10^{10}$ s^{-1}; (*2*) E/p = 71.85 V/(cm Torr), E = 54.6 kV/cm, and $\nu_i = 6.5 \times 10^{10}$ s^{-1}; (*3*) E/p = 160 V/(cm Torr), E = 121.6 kV/cm, and $\nu_i = 2.23 \times 10^{11}$ s^{-1}; and (*4*) E/p = 2.56 kV/(cm Torr), E = 1946 kV/cm, and $\nu_i = 2.91 \times 10^{11}$ s^{-1} (p = 760 Torr). (*5*) Approximating exponential dependence on $\nu_i t$. The value of ν_i is found from the slopes of curves *1–4*.

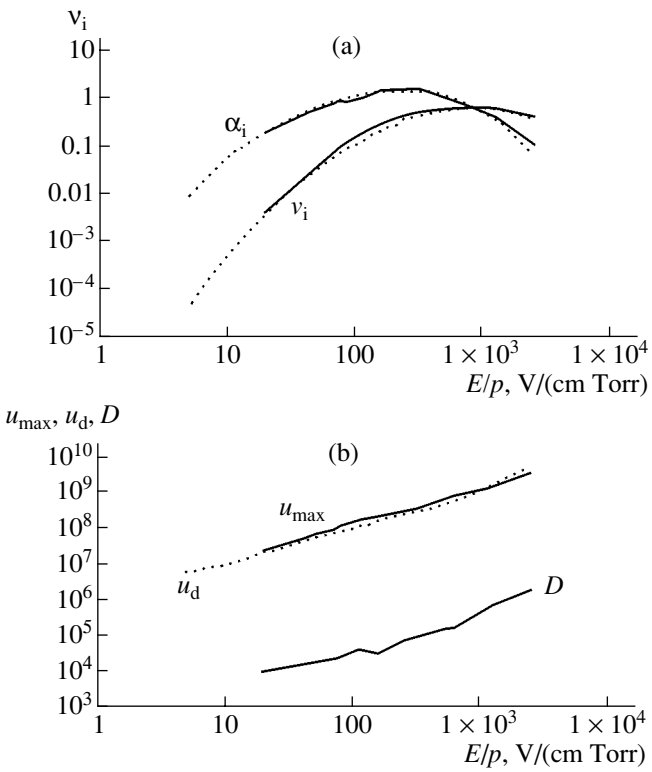

Fig. 2. Avalanche parameters vs. E/p. Solid curves, calculations made in this work (p = 760 Torr); dotted curves, calculations made in [15]. (a) Reduced ionization rate ν_i/p (1/(ns Torr)) and Townsend coefficient α_i (1/(cm Torr)). Solid curves, calculations made in this work (p = 760 Torr); dotted curves, calculations [15] based on the relationship $\nu_i = \alpha_i u_d$, where the Townsend coefficient α_i and the drift velocity u_d were calculated from the steady-state dependences of α_i and u_d on the distance z to the planar cathode for p = 100 Torr. (b) Avalanche propagation velocity (cm/s), drift velocity (cm/s), and coefficient of diffusion D in the transverse direction (cm^2/s). The upper solid curve stands for the propagation velocity u_{max} of the density maximum; dotted curve, for the mean drift velocity u_d of electrons in the process of multiplication.

$\{r_j^{(i)}, j \in 1\ldots N\} \cup \{r_j^{(e)} + r_k^{(i)}, j \in 1\ldots N, k \in 2\ldots N\}$. To calculate the particle density in the cylindrical coordinate system with the Z axis aligned with the external electric field, a 3D grid was constructed. Either interval of distances, $0 \le z \le z_{max}$ and $0 \le \rho \le \rho_{max}$, was split into 20 to 50 meshes of equal size ($z_{max} = 2\max(z_j^{(e,i)})$ and $\rho_{max} = 2\max(\sqrt{(x_j^{e,i})^2 + (y_j^{(e,i)})^2})$ are the maximal values of the particle coordinates at a time $2t$). Then, all the particles in the system were searched through and the number of the particles in each of the meshes was calculated. The density was defined as the number of particles per mesh divided by the mesh volume.

Concurrently, the net field produced by the particles at the Z axis at a time $2t$ was calculated. At given points on the Z axis, the field was calculated as a vector sum of partial (one-particle) Coulomb fields.

RESULTS OF SIMULATION

Ionization rate. The time dependence of the total number of electrons, n_e, and ions, n_i, in the avalanche may be approximated by the expression $n_i = n_e = n_0 \exp(\nu_i t)$, where n_0 is a constant (Fig. 1). The dependences $n_i = n_e$ on $\nu_i t$ are straight lines and have equal slopes at $\nu_i t > 3$. However, the quantities ν_i and n_0 vary significantly with E/p. A series of calculations allowed us to reveal a relationship between the reduced electric field strength E/p and ionization rate ν_i (Fig. 2a).

This relationship was contrasted with results from [15], where the ionization rate was determined by the well-known formula $\nu_i = \alpha_i u_d$, where α_i is the Townsend coefficient and u_d is the drift velocity. In [15], the Townsend coefficient was defined as a factor in the exponent of the exponential function n_i = const $\exp(\alpha_i z)$ (where n_i is the number of ionization events and z is the distance from the cathode) and the drift velocity [15], as the steady-state mean projection of the electron velocity onto the electric field direction: $u_z(z)$ = const = u_d. The values of α_i and u_d set up at $z > (3–5)\alpha_i^{-1}$. Many avalanche-initiating electrons were taken into consideration. The results for ν_i obtained in this work differ from the data in [15] by less than 10%.

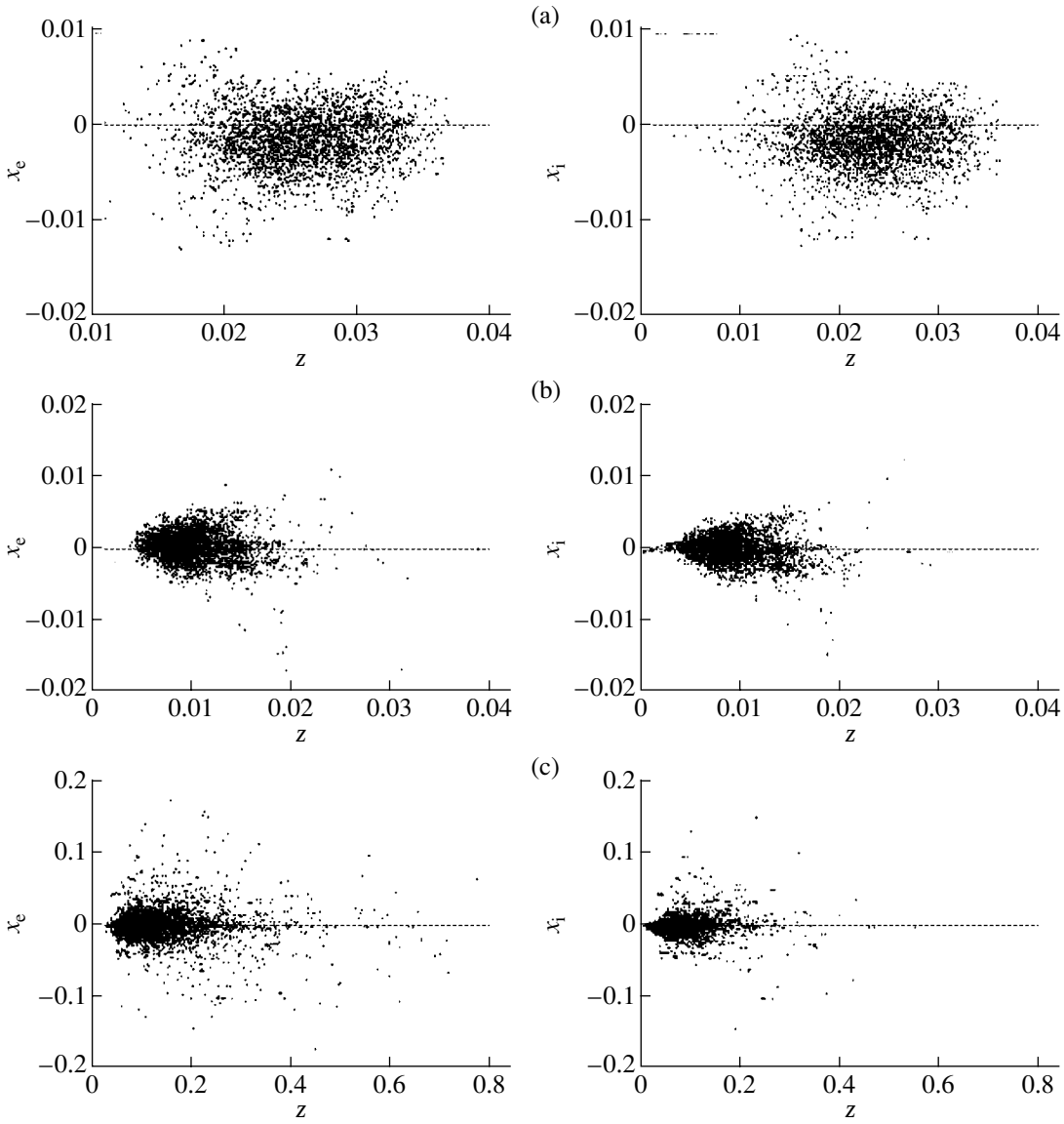

Fig. 3. Projections of the coordinates of the electron ($x_e z$) and ion ($x_i z$) positions (instantaneous patterns) for three field values at the final time instant t of multiparticle dynamics simulation. (a) E/p = 40 V/(cm Torr), E = 30.4 kV/cm, $\nu_i = 1.82 \times 10^{10}$ s^{-1}, and $\nu_i t$ = 9.1; (b) E/p = 160 V/(cm Torr), E = 121.6 kV/cm, $\nu_i = 2.23 \times 10^{11}$ s^{-1}, and $\nu_i t$ = 8.7; and (c) E/p = 2.56 kV/(cm Torr), E = 1946 kV/cm, $\nu_i = 2.91 \times 10^{11}$ s^{-1}, and $\nu_i t$ = 6.16. p = 760 Torr.

We also calculated the propagation velocity of the avalanche $u_{max} = z_{max}(t)/t$, where z_{max} is the position of the density maximum (for details, see below). As follows from Fig. 2b, the density maximum does move with the drift velocity of the electrons according to the present-day concepts [6]. The values of u_{max} and u_d differ by less than 30%.

Figure 2a shows the Townsend coefficients $\alpha_i = \nu_i/u_{max}$ calculated based on the data obtained in this work. As was expected, they agree with the data from [15].

The small discrepancy between our data and those in [15] is likely to be associated with a statistical scatter. In [15], many avalanche-initiating electrons were considered, while here a single electron avalanche is taken into consideration.

Charge density distribution. A set of projections of the ion and electron coordinates onto the plane xz ("instantaneous patterns" shown in Fig. 3) provides a rough idea of the avalanches after the multiparticle dynamics simulation is complete. More detailed information may be derived from the electron density distribution obtained by extrapolating the results of dynamics simulation (Fig. 4).

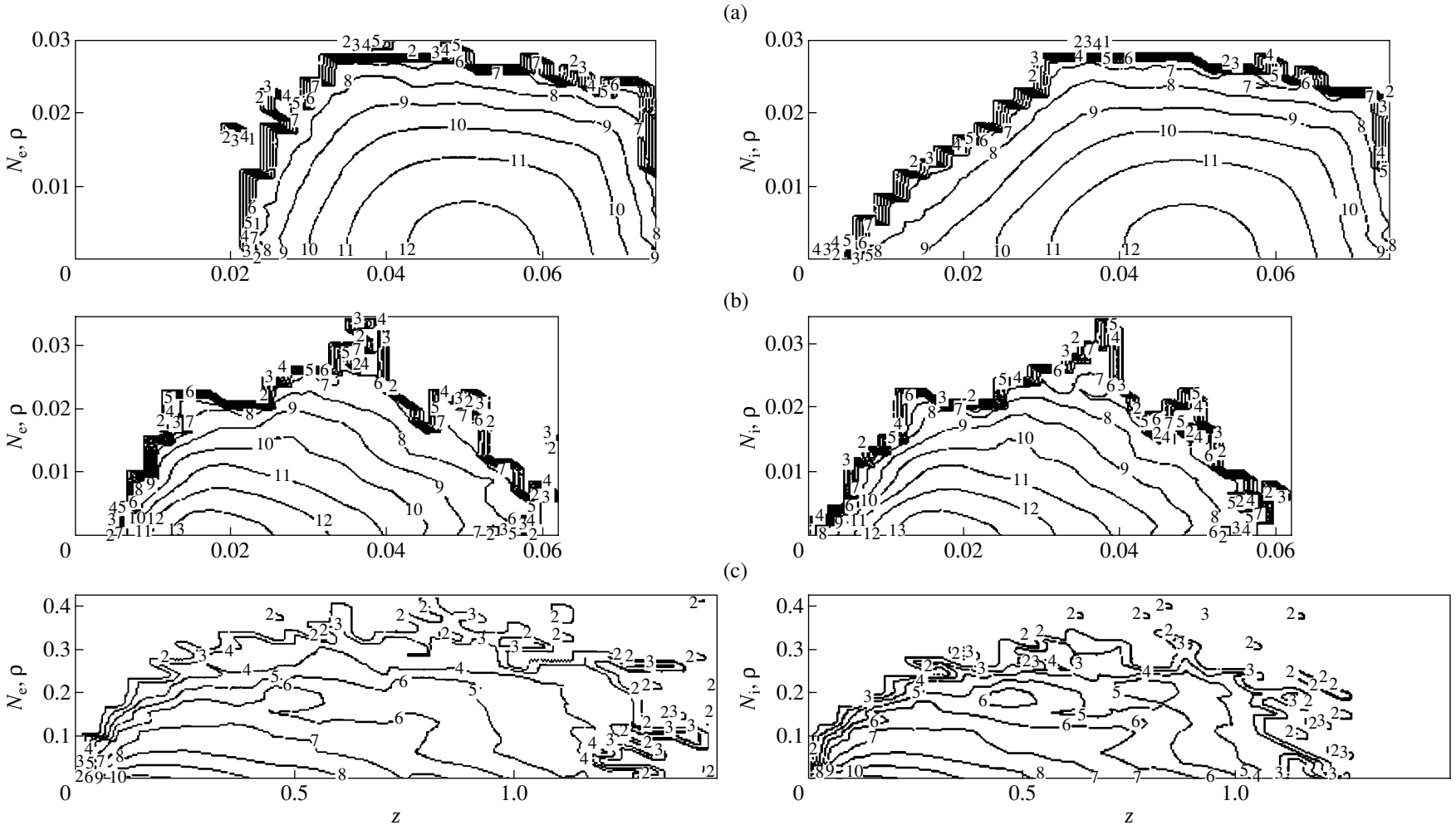

Fig. 4. Electron and ion density isolines for three field values. The initial positions of the particles are found by extrapolating the numerical results for multiparticle dynamics simulation to the double time ($2t$) of multiparticle dynamics simulation under the assumption that the process is Markovian. The parameters are the same as in Fig. 3.

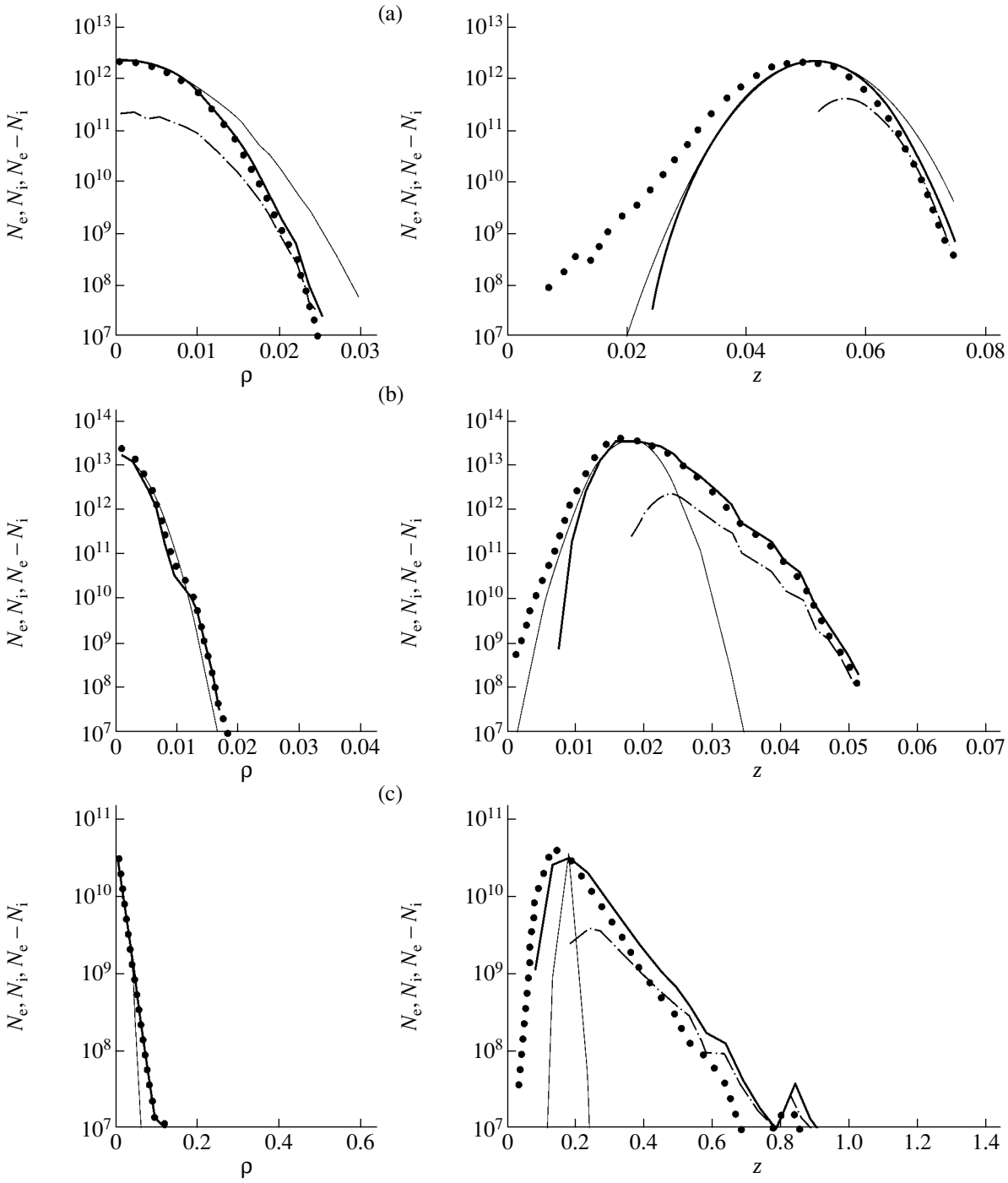

Fig. 5. Electron and ion density distributions (a) across, $N_{e,\,i}(\rho, z = z_{max})$, and (b) along, $N_{e,\,i}(\rho = 0, z)$, the field for three field values. Thick solid curves, electron density distributions N_e; dotted lines, ion density distribution N_i; thin solid curves, distribution given by (1), where $N_{e0}(t)$, $\sigma^2(t)$, and $z_{max}(t)$ serve as adjusting parameters, and dash-and-dot lines, distribution $N_e - N_i$ (positive values). The parameters are the same as in Fig. 3.

The assumption that the electrons multiply, drift, and diffuse leads us to the Gaussian electron density distribution in the coordinate system moving along the field with the drift velocity. The space–time dependence of the electron density in an avalanche initiated by a single electron has the form [6]

$$N_e(t, \rho, z) = N_{e0}(t)\exp\left(-\frac{\rho^2 + (z - z_{max}(t))^2}{\sigma^2(t)}\right), \quad (1)$$

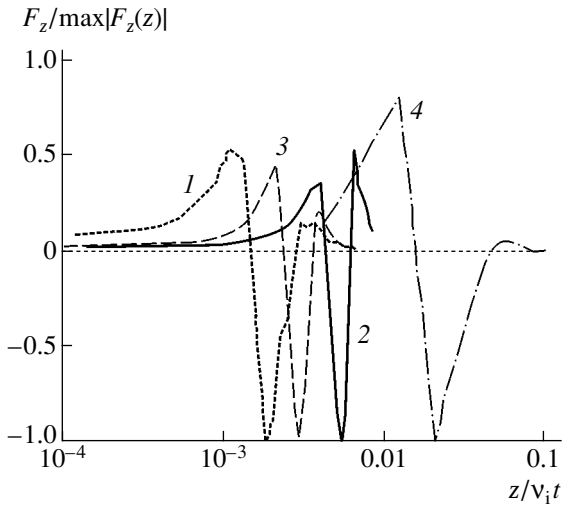

Fig. 6. Distributions of the z component of the electric field produced by the particles along the avalanche axis for three values of the external field. The initial positions of the particles are found by extrapolating the numerical results for multiparticle dynamics simulation to the double time ($2t$) of multiparticle dynamics simulation under the assumption that the process is Markovian. (*1*) E/p = 40 V/(cm Torr), E = 30.4 kV/cm, F_{max} = 2.9 kV/cm, $\nu_i t$ = 9.1, and $\nu_i = 1.82 \times 10^{10}$ s^{-1}; (*2*) E/p = 71.85 V/(cm Torr), E = 54.6 kV/cm, F_{max} = 10.8 kV/cm, $\nu_i t$ = 8.5, and $\nu_i = 6.5 \times 10^{10}$ s^{-1}; (*3*) E/p = 160 V/(cm Torr), E = 121.6 kV/cm, F_{max} = 16.8 kV/cm, $\nu_i t$ = 8.7, and $\nu_i = 2.23 \times 10^{11}$ s^{-1}; and (*4*) E/p = 2.65 kV/(cm Torr), E = 1946 kV/cm, F_{max} = 0.39 kV/cm, $\nu_i t$ = 6.16, and $\nu_i = 2.91 \times 10^{11}$ s^{-1}; p = 760 Torr.

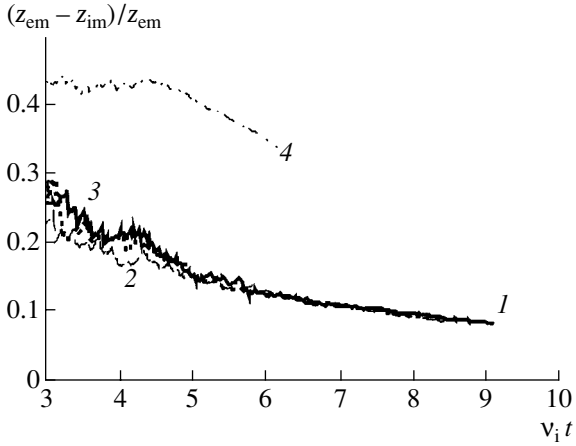

Fig. 7. Dependence of the relative difference $(z_{em} - z_{im})/z_{em}$ between the mean coordinates on the reduced time. (*1*) E/p = 40 V/(cm Torr), E = 30.4 kV/cm, and $\nu_i = 1.82 \times 10^{10}$ s^{-1}; (*2*) E/p = 71.85 V/(cm Torr), E = 54.6 kV/cm, and $\nu_i = 6.5 \times 10^{10}$ s^{-1}; (*3*) E/p = 160 V/(cm Torr), E = 121.6 kV/cm, and $\nu_i = 2.23 \times 10^{11}$ s^{-1}; and (*4*) E/p = 2.56 kV/(cm Torr), E = 1946 kV/cm, and $\nu_i = 2.91 \times 10^{11}$ s^{-1}; p = 760 Torr.

where ρ is the distance to the Z axis aligned with the field, $\sigma^2(t) = 4Dt$, D is the diffusion coefficient, $N_{e0}(t) = (4\pi Dt)^{-3/2}\exp(\nu_i t)$ is the maximum electron density, and $z_{max}(t) = u_d t$.

Expression (1) implies that electron density isolines are concentric circles centered at the point $z = z_{max}$. At a stretch, this is true when E/p is small and N_e is close to the maximal value (Fig. 4a). However, even with E/p = 160 V/(cm Torr), which roughly corresponds to the maximum of the Townsend coefficient, the isolines extend in the Z-axis direction (Fig. 4b). The extension increases with increasing E/p (Fig. 4c).

Comparing the analytical electron density distribution (Fig. 5) with distribution (1) yields the avalanche parameters σ^2 and z_{max} for various E/p. The value of σ was determined from the transverse size $N_e(\rho, z = z_{max})$ of the avalanche; z_{max}, from the distribution along the field, $N_e(\rho = 0, z)$. Based on these values, the E/p dependences of D and u_{max} were constructed (Fig. 2).

From the ion and electron coordinates known, we found the electric field $F(z)$ generated by the particles at the Z axis (Fig. 6). The behavior of its projection $F_z(z)$ (growth, fall into the negative range, and then the transition to the positive range again) coincides qualitatively with the behavior of the projection of the electric field produced by positive and negative charge clouds shifted along the Z axis, the center of the positive charge cloud being shifted relative to the center of the negative charge cloud toward smaller z. In fact, the electron distributions in Fig. 5 are somewhat shifted toward larger z relative to the ion distributions.

It is seen that the plasma field strength is small compared with the strength E of the external avalanche-initiating field at times considered. This is not only because the amount of charges is as yet insufficient at these time instants. Another reason is that the clouds of positive and negative charges overlap considerably. The mean values of the electron, z_{em}, and ion, z_{im}, coordinates differ insignificantly. Moreover, the relative difference of the mean coordinates, $(z_{em} - z_{im})/z_{em}$, drops with time (Fig. 7). The plasma field cannot hold the charges close to each other and is disregarded in the calculation. The fact is that, when multiplying, the electrons cannot be displaced relative to the ions by a distance much greater than that predicted by the inverse Townsend coefficient.

Obviously, since the amount of charges in an avalanche grows exponentially, the plasma field will equal the external field at $t \sim 20/\nu_i$, which meets the well-known criterion of avalanche–streamer transition [1–7].

CONCLUSIONS

Thus, electrons in an avalanche multiply by the exponential law (both in time and in coordinate along the field) even if the reduced field strength E/p is high, $E/p > 200$ V/(cm Torr), when the Townsend multiplica-

tion coefficient and the ionization rate start decreasing. However, today's concepts of the electron distribution in an avalanche are valid only for low values of the reduced field strength, $E/p < 100$ V/(cm Torr).

ACKNOWLEDGMENTS

This work was supported by the International Science and Technology Center (grant no. 1270).

REFERENCES

1. L. B. Loeb, *Fundamental Processes of Electrical Discharges in Gases* (Wiley, New York, 1939; Gostekhizdat, Moscow, 1950).
2. V. L. Granovskiĭ, *Electric Current in Gases* (Gostekhizdat, Moscow, 1952), Vol. 1.
3. P. A. Kaptsov, *Electronics* (Gostekhizdat, Moscow, 1954).
4. A. von Engel, *Ionized Gases* (Clarendon, Oxford, 1955; Fizmatgiz, Moscow, 1959).
5. H. Raether, *Electron Avalanches and Breakdown in Gases* (Butterworths, London, 1964; Mir, Moscow, 1968).
6. É. D. Lozanskiĭ and O. B. Firsov, *Theory of Spark* (Atomizdat, Moscow, 1975).
7. Yu. P. Raizer, *Physics of Gas Discharge* (Nauka, Moscow, 1992).
8. M. C. Wang and E. E. Kunhard, Phys. Rev. A **42**, 2366 (1990).
9. P. A. Vitello, B. M. Penetrante, and J. N. Bardsley, Phys. Rev. E **49**, 5574 (1990).
10. A. A. Kulikovsky, Phys. Rev. E **57**, 7066 (1998).
11. A. Rocco, U. Ebert, and W. Hundsdorfer, Phys. Rev. E **66**, 035102 (2002).
12. M. Arrayás, U. Ebert, and W. Hundsdorfer, Phys. Rev. Lett. **88**, 174502-1 (2002).
13. A. A. Kulikovsky, Phys. Rev. Lett. **89**, 229401 (2002).
14. E. E. Kunhardt, Y. Tzeng, and J. P. Boeuf, Phys. Rev. A **34**, 440 (1986).
15. A. N. Tkachev and S. I. Yakovlenko, Pis'ma Zh. Éksp. Teor. Fiz. **77**, 264 (2003) [JETP Lett. **77**, 221 (2003)].
16. A. N. Tkachev and S. I. Yakovlenko, Proc. SPIE **4747**, 271 (2002).
17. A. N. Tkachev and S. I. Yakovlenko, Laser Phys. **12**, 1022 (2002).
18. E. Krishnakumar and S. K. Srivastava, J. Phys. B **21**, 1055 (1988).
19. D. V. Fursa and I. Bray, Phys. Rev. A **52**, 1279 (1995).
20. J. C. Nickel, K. Imre, D. F. Register, and S. Trajmar, J. Phys. B **18**, 125 (1985).

Translated by V. Isaakyan